Impact of Large, Periodic Deformations on Flow and Transport in Soft Porous Media



Matilde Fiori
St Catherine's College
University of Oxford

A thesis submitted for the degree of
Doctor of Philosophy

Michaelmas 2023

Acknowledgements

I am grateful to my supervisor Chris MacMinn, for the patience, the trust and the support that he has always shown to me, both professionally and personally. And for truly being an example of the knowledgeable and kind researcher I aspire to be.

I would like to thank Satyajit Pramanik, for the inspiring collaborations and the essential inputs and guidance. I would also like to express gratitude towards Sylvie Lorthois and Tanguy Le Borgne, for their interest and insightful inputs on my research and for their warm welcome to share my work with their groups.

I am grateful to the Poromechanics group for the constant support and collaborative spirit, and the stimulating environment they all exposed me to. An essential thank you goes to Callum and Oliver, with whom I could always find support to weather the challenges of the experiments.

I also would like to thank Nick, who, unlike me, never doubted for an instant that I could get to the end of this. And I would like to thank Govind and Gonzalo, for truly being my Oxonian family, and Alexei, Alasdair, Federico, Andrea, Max, Daniele and Francisco for being my buddies in this hard process. A big thanks goes to the Oxford dancing community, for the safe and warm dancing environment that has allowed me to express myself and to keep me sane (to some extent). And I would like to thank the Begbroke crew (Antonio, Govind, Yuan, Gustavo, Ram) for the lovely work environment that brought me to think that I could pursue a DPhil in the first place.

For the last portion of this list, I believe it makes sense to switch to Italian.

Come sempre, grazie a mamma Marina e papà Paolo, perché sono la mia forza e senza di loro non avrei mai nemmeno immaginato di poter arrivare qui. Grazie a zia Titti, per avermi preso sotto la propria ala e per l'immenso valore delle nostre conversazioni.

Grazie a Dennis, perché più cresciamo e più convergiamo nella certezza di esserci sempre e di poter affrontare qualsiasi cosa insieme. Grazie a Sveva, Claudia e Marco, per essere la mia famiglia acquisita. Grazie a Simona, Silvia, Federica, Irene, Elisa, Giulio, Giorgio e Ilaria per l'affetto costante, anche a distanza. Grazie a Beppe, per esserci stato nella fase più difficile di questo percorso.

Non sapere dove andare è una buona premessa per arrivare dappertutto.
[Michela Murgia]

Diventare. Era un verbo che mi aveva sempre ossessionata. Ma me ne accorsi per la prima volta solo in quella circostanza. Io volevo diventare. Anche se non avevo mai saputo cosa.
[Elena Ferrante]

Declaration of Authorship

I, Matilde Fiori, declare that this project, titled 'Impact of Large, Periodic Deformations on Flow and Transport in Soft Porous Media' and the work presented in it are my own. I hereby certify that the work presented in this project is all my own unaided work and that all material obtained from published or unpublished sources of any type, including the internet, have been fully acknowledged at the proper point in the text and included in the list of references.

Signed: Matilde Fiori

Date: 29/11/2023

Abstract

Soft porous media, such as soils, hydrogels, or soft biological tissues, are characterised by a strong coupling between deformation and fluid flow due to complex rearrangements of the pore space. In these materials, the impact of large, periodic loads on the deformation and fluid flow — and the resulting coupling with solute transport — are of particular interest in the context of, for example, physiological flows and the motion of nutrients or contaminants. However, the basic features of this coupling of flow and transport with poromechanical deformation have not previously been systematically investigated. In this thesis, we study this problem using a 1D continuum model based on large-deformation poroelasticity, focusing on a periodically loaded soft porous medium subject to confined compression. We begin by identifying the relevant parameter space and then by exploring the impact of the key dimensionless control parameters on the poromechanical coupling, focusing on those regulating the applied periodic load. We find that the amplitude and period of deformation influence the mechanical response of the material, which can belong to either a slow-loading or a fast-loading regime. Specifically, the deformation is more localised at the piston as the loading period becomes faster relative to the poroelastic timescale, while nonlinear effects are increased as the loading amplitude increases. We then introduce solute transport, including advection, molecular diffusion, and hydrodynamic dispersion. We show that each transport mechanism is affected by the periodic deformation in specific ways during a single loading cycle, and that the poromechanical regimes have a direct impact on the resultant movement of solute over several loading cycles. In analogy with soft biological tissues, we then consider soft porous media divided into one or more layers characterised by different material properties and study the impact of this complex structure on the poromechanical response to large, periodic loads and on the infiltration of solute. We conclude with an experimental campaign where we fabricate and characterise soft porous media to empirically study their poromechanical response to periodic loads and the resultant transport of solute. We compare these results with our model, finding good qualitative agreement. Despite the complexity of the problem, the models and experiments reported in this work are relatively simple, flexible, and generic. Our results therefore provide unique insights on flow and transport in periodically loaded soft porous media, with relevance to a variety of applications and contexts.

Contents

1 Introduction **1**

1.1 Flow and deformation due to periodic loading in a soft porous medium 2

1.2 Solute transport due to periodic loading in a soft porous medium 3

1.3 Flow, deformation and transport due to periodic loading in a layered soft porous medium 5

1.4 Laboratory experiments 6

1.5 Conclusions 6

2 Large-deformation poroelasticity **8**

2.1 Kinematics 8

2.2 Darcy's law 9

2.3 Fluid flow 9

2.4 Mechanical equilibrium 9

3 Flow and deformation due to periodic loading in a soft porous medium **11**

3.1 Introduction 11

3.2 Theoretical model 12

3.2.1 Model problem 12

3.2.2 Kinematics 13

3.2.3 Darcy's law 14

3.2.4 Fluid flow 14

3.2.5 Mechanical equilibrium 15

3.2.6 Elasticity law 15

3.2.7 Initial and boundary conditions 16

3.2.7.1 Initial conditions 16

3.2.7.2 Left boundary 16

3.2.7.3 Right boundary 16

3.2.8 Linear poroelasticity 16

3.2.9 Scaling and summary . . . 17
3.3 Analytical solutions . . . 18
3.3.1 Average porosity . . . 18
3.3.2 Linear poroelasticity: Early-time solution . . . 18
3.3.3 Linear poroelasticity: Full solution . . . 20
3.3.4 Linear poroelasticity: Response to very fast loading (Stokes' second problem) 21
3.3.5 Response to very slow loading (quasi-static solution) . . . 21
3.3.6 Scaling quantities . . . 22
3.4 Numerical solution . . . 22
3.4.1 Comparison with analytical solutions . . . 24
3.5 Parameter study . . . 26
3.5.1 Impact of loading period . . . 26
3.5.2 Impact of loading amplitude . . . 30
3.5.3 Impact of initial porosity . . . 31
3.5.4 FL in biological examples . . . 34
3.6 Conclusions . . . 37

4 Solute transport due to periodic loading in a soft porous medium 39
4.1 Introduction . . . 39
4.2 Theoretical model . . . 42
4.2.1 Model problem . . . 42
4.2.2 Solute transport . . . 42
4.2.3 Initial and boundary conditions . . . 43
4.2.3.1 Initial conditions . . . 43
4.2.3.2 Left boundary . . . 44
4.2.3.3 Right boundary . . . 44
4.2.4 Scaling and summary . . . 44
4.3 Solute transport and mixing . . . 45
4.3.1 Quantification of solute transport and mixing . . . 45
4.3.2 Qualitative impacts of periodic loading on solute transport . . . 46
4.3.3 Impact of diffusion and dispersion coefficients on transport and mixing . . . 49
4.3.4 Quantitative impacts of periodic loading on solute transport . . . 51
4.3.5 Péclet number in biological examples . . . 59
4.4 Conclusions . . . 59

5 Flow, deformation and transport due to periodic loading in a layered soft porous medium **63**

5.1 Introduction . . . 63
5.2 Model problem . . . 65
5.3 Theoretical model . . . 66
5.3.1 Lagrangian model . . . 66
5.3.1.1 Large-deformation poroelasticity . . . 66
5.3.1.2 Solute transport . . . 67
5.3.2 Boundary conditions . . . 68
5.3.2.1 Initial conditions . . . 68
5.3.2.2 Left boundary . . . 68
5.3.2.3 Right boundary: confined compression . . . 68
5.3.2.4 Right boundary: free-flow compression . . . 68
5.3.3 Scaling and summary . . . 69
5.4 Permeability and poroelastic timescale . . . 69
5.5 Results . . . 71
5.5.1 Confined compression . . . 71
5.5.2 Free-flow compression . . . 71
5.5.3 Solute transport . . . 72
5.6 Analogies with biological tissues . . . 75
5.6.1 Articular cartilage . . . 75
5.6.2 Brain tissue . . . 76
5.7 Conclusions . . . 80

6 Laboratory experiments **82**

6.1 Introduction . . . 82
6.2 Experiments . . . 85
6.2.1 Material fabrication . . . 85
6.2.2 Experimental setup . . . 85
6.2.3 Material characterisation . . . 88
6.3 Semi-2D model . . . 90
6.3.0.1 Model problem . . . 91
6.3.0.2 2D solute transport . . . 91
6.4 Experimental results . . . 93
6.4.1 Poromechanical coupling . . . 93
6.4.2 Solute transport . . . 94
6.5 Conclusions . . . 103

7 Discussion and conclusions **106**

7.1 Limitations and future work 108

7.2 Conclusions 110

A **112**

A.1 Constitutive laws 112

A.2 Early time evolution, penetration length, and periodic response to very fast loading . 114

A.3 Transition to the periodic regime 115

A.4 Impact of elasticity and permeability laws at large amplitudes 115

A.5 Dispersive flux 115

A.6 Initial porosity and solute strip width 117

A.7 Numerical methods 120

A.8 Analytical solution for molecular diffusion 123

Bibliography **125**

Chapter 1

Introduction

Soft porous media are common in nature and industry; examples include biological cells and soft tissues, soils and sediments, and paper products and fabrics. Given their high deformability, these materials often experience large deformations that result in nonlinear kinematic and constitutive responses, as considered and discussed by MacMinn et al. (2016) among others.

In many scenarios, soft porous media are exposed to periodic loading. For example, soft tissues in the body can experience pulsating loads from the surrounding blood vessels, or, on a larger scale, can be cyclically loaded during their basic mechanical function. The former scenario has attracted great interest recently as a potential driver of fluid flow in brain tissue (Bojarskaite et al., 2023, Franceschini et al., 2006, Kedarasetti et al., 2020) and the latter is important for load-bearing and fluid flow in cartilage (Cacheux et al., 2023, DiDomenico et al., 2017, Ferguson et al., 2004, Mauck et al., 2003, Riches et al., 2002, Schmidt et al., 2010, Sengers et al., 2004, Zhang, 2011) and bone (Manfredini et al., 1999, Nguyen et al., 2010, Piekarski and Munro, 1977, Witt et al., 2014, Zhang and Cowin, 1994). Periodic loads are also commonly applied in regenerative medicine to improve cell differentiation in scaffolds via mechanotransduction (Amrollahi and Tayebi, 2015, Butler et al., 2000, Gauvin et al., 2011, Grenier et al., 2005, Haj et al., 2009, Kim et al., 1999, Mauck et al., 2000, Peroglio et al., 2018). Soils and sediments experience periodic loading due to seismicity (Bonazzi et al., 2021, Genna and Cividini, 1989, Li et al., 2004, Popescu et al., 2006), vehicle traffic (Hu et al., 2011, Ni and Geng, 2022, Ni et al., 2015), and ocean waves and tides (Cheng, 2016, Karim et al., 2002, Madsen, 1978, Trefry et al., 2019, Yamamoto et al., 1978).

In the geomechanical and biomechanical systems mentioned above, solute transport can have a crucial role. In general, the transport of solutes in porous media is driven by molecular diffusion and by internal fluid flow. In soft porous media, the latter is strongly coupled to external mechanical loads through rearrangement of the pore structure (*e.g.*, Borja and Choo, 2016, Ehlers et al., 2009, Franceschini et al., 2006, Lai et al., 1991, Li et al., 2004, Moeendarbary et al., 2013, Mow et al., 1980, Preziosi et al., 1996, Vuong et al., 2015). Thus, the large and/or periodic deformation of these materials is expected to have an important impact on solute transport. In soils, for example,

compression due to surface loading can induce the spreading of contaminants. In biological tissues, physiological loads drive nutrient transport and waste removal, impacting cell growth and survival.

The impact of large and periodic loads on the complex coupling between flow and deformation in soft porous media — and the implications of this coupling for the transport of solutes — remains relatively unexplored. This thesis takes several key initial steps toward filling these gaps in our understanding. We begin by using an established model to study the poromechanics of large, periodic deformations; in particular, we examine the impact of the loading parameters on the material and fluid response. Then, we couple this model with a model for solute transport in porous media to explore in detail the impact of periodic loading on solute transport and mixing. We explore this problem numerically for the case of homogeneous media and for the case of layered media. The latter is particularly common in the context of biological tissues. Finally, we develop a novel experimental system for studying solute transport in soft porous media. We characterise its basic poromechanical properties and then use it to perform a proof-of-concept study of the impact of uniaxial periodic loading on solute transport in 2D, comparing our experimental results with simulation results.

The thesis is structured as follows. We begin by providing a general introduction to the established theory of large-deformation poroelasticity in Chapter 2. The contents of the subsequent chapters are summarised below.

1.1 Flow and deformation due to periodic loading in a soft porous medium

In Chapter 3, we characterise the response of a soft porous medium to large and periodic loads.

From a poromechanical point of view, periodic loading is fundamentally different from steady loading because the long-time response is inherently oscillatory and therefore time-dependent. Most previous work on periodic loading has focused on internal stress and/or pressure profiles, on macroscopic observables such as surface motion or net inflow or outflow, or on solute concentration profiles. This is a common approach in seismicity (*e.g.*, Biot, 1956a,b, Gajo and Denzer, 2011, Li et al., 2004, Liu et al., 2019), where classical linear poroelasticity captures well the small deformations characteristic of these contexts.

For stiff biological tissues, such as bone and cartilage, linear poroelasticity has been used to model the macroscopic mechanical response and/or the distribution of pore pressure during small periodic deformations (*e.g.*, Kameo et al., 2008, Manfredini et al., 1999, Riches et al., 2002, Yaogeng et al., 2018, Zhang and Cowin, 1994). However, in soft biological tissues and tissue engineering constructs, deformations are usually large and nonlinearities need to be taken into account. Both linear and nonlinear poroelasticity have been used to model the impact of periodic deformations on the transport of solutes, typically by focusing on an application-specific scenario and comparing the concentration profile at the end of loading across a small set of loading conditions (*e.g.*, Ferguson

et al., 2004, Gardiner et al., 2007, Mauck et al., 2003, Sengers et al., 2004, Urciuolo et al., 2008, Vaughan et al., 2013, Zhang, 2011). This approach leaves a consistent gap, since the detailed flow and mechanics of these deformations have not yet been systematically investigated across the full range of properties and loading parameters.

In this chapter, we identify and explore the complete parameter space associated with large, periodic deformations in the context of a 1D model problem. Specifically, we consider a homogeneous medium periodically loaded through a permeable piston at the left boundary (see Figure 1.2 (a)). We use large-deformation poroelasticity to consider a wide range of loading periods and amplitudes. We identify two distinct mechanical regimes, distinguished by whether the loading period is slow or fast relative to the characteristic poroelastic timescale. We develop analytical solutions for slow loading at any amplitude and for infinitesimal amplitude at any period. We use these analytical solutions and a full numerical solution to explore the localisation of the deformation near the permeable boundary as the period decreases and the emergence of nonlinear effects as the amplitude increases. We show that large deformations lead to asymmetry between the loading and unloading phases of each cycle in terms of the distributions of porosity and fluid flux. These results are published in the *Journal of Fluid Mechanics* (Fiori et al., 2023a).

1.2 Solute transport due to periodic loading in a soft porous medium

In Chapter 4, we study the impact of periodic loading on solute transport and mixing.

In porous media, solute transport occurs through three fundamental mechanisms: advection, molecular diffusion, and hydrodynamic dispersion (Bear, 1972, Brenner and Edwards, 1993, Dentz et al., 2011, Gelhar, 1993, Saffman, 1959, Scheidegger, 1961, Whitaker, 1967, 1998). Diffusion is weaker than in a bulk fluid, because of the tortuosity introduced by the pore space (Bear, 1972, Ghanbarian et al., 2013, Tartakovsky and Dentz, 2019). Both advection and dispersion are driven by fluid flow. At the Darcy scale (which is the framework of this study), solute is simply advected with the mean fluid flux (*i.e.*, the Darcy flux). At the pore scale, however, advection is chaotic (Kree and Villermaux, 2017, Lester et al., 2016a, 2013, 2016b, Souzy et al., 2020); these sub-scale deviations from the Darcy-scale mean contribute to hydrodynamic dispersion. In a porous medium, hydrodynamic dispersion is driven by two phenomena: (i) analogous to classical Taylor dispersion in a tube (Brenner and Stewartson, 1980, Marbach and Alim, 2019, Taylor, 1953), pore-scale velocity gradients smear solute profiles along the flow direction, and (ii) the presence of the complex porous structure and its specific morphology introduce a high variability in the fluid streamlines (Datta et al., 2013, de Anna et al., 2013, Dentz et al., 2023, Gouze et al., 2021, Souzy et al., 2020), thus inducing longitudinal and transverse spreading of the solute plume (Delgado, 2007, Gelhar and Axness, 1983, Gelhar et al., 1992, Scheidegger, 1961). In soft porous media, therefore, deformation can impact the

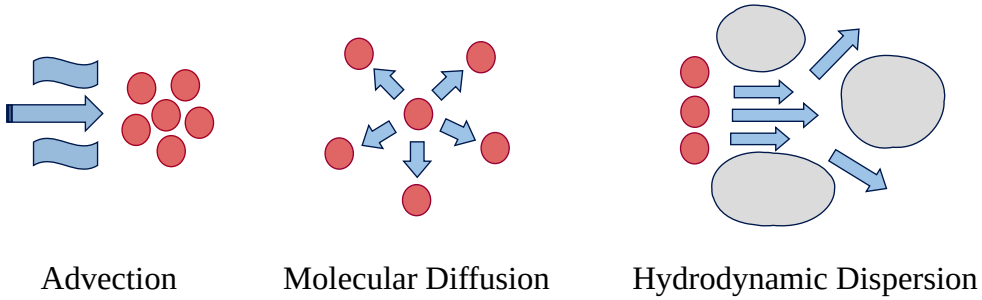

Figure 1.1: Schematic representation of the mechanisms regulating solute transport in porous media: advection, driven by the fluid-flow; molecular diffusion, driven by concentration gradients; and hydrodynamic dispersion, driven both by the fluid flow and by concentration gradients, and originating in the fluid velocity variability in the heterogeneous pore space.

transport of solutes directly by driving a fluid flow, which in turns drives advection and hydrodynamic dispersion, and indirectly by distorting the pore space, thus modifying hydrodynamic dispersion and molecular diffusion.

In geomechanical contexts, deformation-driven transport has been mainly studied for the case of consolidation. In this field, it has been established that the poromechanical coupling affects the transport of solutes, which depends on both the solid and the fluid-flow properties (such as compressibility and packing density (Alshawabkeh and Rahbar, 2006, Bonazzi et al., 2021, Zhang et al., 2013)). However, consolidation is not periodic, and acts on scales that are both spatially and temporally much larger than for biological tissues.

As noted above, periodic loading is common in the context of biological tissues, where it is known to enhance the transport of nutrients (*e.g.*, DiDomenico et al., 2017, Ferguson et al., 2004, Gardiner et al., 2007, Schmidt et al., 2010, Witt et al., 2014, Zhang, 2011, Zhang and Szeri, 2008). Similarly, periodic deformations enhance the infiltration of solute species in hydrogels (Albro et al., 2008, Vaughan et al., 2013) and scaffolds for tissue engineering (Cortez et al., 2016, Fan et al., 2016, Kumar et al., 2018, Mauck et al., 2003), where the correlation between loading parameters, nutrient transport, and cell survival is of particular interest. In these materials, however, hydrodynamic dispersion is rarely mentioned or considered (Sengers et al., 2004), despite the importance of advection relative to diffusion in many scenarios (quantified by the Péclet number, as discussed in Chapter 4). The poromechanics of periodic loading in this context have been studied to some extent, as described in the introduction of Chapter 4, but no study has linked the poromechanics of periodic loading to the resultant advection, diffusion, and dispersion of solutes across a broad spectrum of loading parameters.

In Chapter 4, we address this aspect by including the mechanisms of transport in porous media into large-deformation poromechanics. We do so by expanding the model developed in Chapter 3 to incorporate the transport and mixing of a passive solute, which we place in a strip at the right end of the domain (as shown in Figure 1.2 (b)). Based on results from Chapter 3 — regarding the

impact of periodic deformation on the displacement, porosity, and fluid flux throughout the domain — we analyse the effect of these mechanical quantities on solute transport and mixing. First, we characterise the separate roles of advection, molecular diffusion, and hydrodynamic dispersion during one loading cycle. We also explore the roles of the diffusion and dispersion coefficients, taking them to be constant. We then consider the mechanical regimes described in Chapter 3 — from slow to fast loading (relative to the poroelastic timescale) and from small to large amplitude — and quantify their impact on solute mixing and spreading. Overall, we show that the effect of periodic compression on solute motion is irreversible and can be controlled by tuning the loading parameters.

1.3 Flow, deformation and transport due to periodic loading in a layered soft porous medium

In Chapter 5, we add a level of complexity to our previous studies, by considering heterogeneous media. Because of their specific physiological function (Fung, 2013), soft tissues can often feature a heterogeneous structure, with multiple layers characterised by different mechanical and fluid-flow properties (Federico and Herzog, 2008a, Gu et al., 1999, Krishnan et al., 2003, Malandrino et al., 2009, Park et al., 2003, Pierce et al., 2013, 2016, Reynaud and Quinn, 2006). In some diseases, such as osteoarthritis in articular cartilage (Stender et al., 2017) or Alzheimer's disease in brain matter — which originates from abnormal accumulation of stiff and impermeable plaques (Hu et al., 2023, Mattana et al., 2017, Palombo et al., 2018) — this defined structured is lost or altered. In general, models of soft tissues include the details of the division in layers (Federico and Grillo, 2012, Federico and Herzog, 2008a, Gao et al., 2015, Gastaldi et al., 2018, Maleki et al., 2020, Tomic et al., 2014, Wu et al., 2016); however, the effect of the layers on the material poromechanical response to periodic loads, and their poromechanical role with respect to the emergence of diseases that alter the layer distribution, have not been investigated so far. Moreover, in tissue engineering scaffolds, a layered structure is known to favour the survival and proliferation of cells (Camarero-Espinosa et al., 2016b, Karpiak et al., 2012, Lee et al., 2015, Mesallati et al., 2013, Ng et al., 2006, Sano et al., 2018, Zhu et al., 2014). Despite being widely employed, layered scaffolds are still missing a deep understanding of the physical reasons why a periodically loaded layered structure may be favourable for cell and tissue development with respect to a homogeneous one.

From a poromechanical point of view, each layer can have a different poroelastic timescale, and thus a different response to a given rate of loading, as we consider in detail for homogeneous media in Chapter 3, and for its impact on the transport of solutes in Chapter 4. In Chapter 5, we explore the impact of a layered structure on the poromechanical response to periodic loading. We divide the material in two layers with different permeabilities and compare their response to the one experienced by a homogeneous medium with the same effective permeability and under the same loading conditions. The layered media are studied under confined compression (see Figure 1.2 (c)),

as in Chapters 3 and 4 for homogeneous media, and under free-flow compression, where the right boundary is permeable (see Figure 1.2 (d)). For each loading scenario, we study the impact of the layered structure on the deformation and fluid flow, and consequently on solute transport. We then consider two specific examples of layered biological tissues, articular cartilage and brain matter, and pathological alterations of their structure due to osteoarthritis and Alzheimer's disease, respectively.

1.4 Laboratory experiments

The nontrivial coupling between deformation and fluid flow in soft porous media has been the object of significant interest in experimental campaigns (see for example (Beavers et al., 1975, Hewitt et al., 2016a, Lanir et al., 1990, Lutz et al., 2021, Parker et al., 1987, Paterson et al., 2019)). However, the effect of this coupling on the transport of solutes has not been investigated experimentally in any detail. Some studies have observed the macroscopic long-term absorption or desorption of solutes from periodically loaded hydrogels (Albro et al., 2008, Mauck et al., 2003, Urciuolo et al., 2008, Vaughan et al., 2013); however, these hydrogel blocks do not allow the local observation of the solute spreading within the medium, which is essential to link solute transport to the local poromechanics.

In Chapter 6, we propose and develop an experimental system for studying flow, deformation and solute transport in a soft porous medium subject to periodic loads. Our system consists of a confined-compression experiment, where a soft, quasi-2D porous medium (with a thickness considerably smaller than the other dimensions) is periodically loaded via a permeable piston in an otherwise impermeable chamber. As a model material, we fabricate soft, porous "sponges" out of polydimethylsiloxane (PDMS). We characterise the basic mechanical and fluid-flow properties of these PDMS sponges, such as their stiffness, permeability and initial porosity. We then conduct a set of proof-of-concept experiments in which we inject a blob of dye into the centre of a sponge and apply periodic deformations with several combinations of parameters. We provide a qualitative comparison between these preliminary experimental results and the predictions of a quasi-2D extension of our model from Chapter 4, which we solve numerically. We show a schematic representation of the semi-2D model and the experimental setup in figure 1.3.

1.5 Conclusions

In Chapter 7, we summarise our key findings and consider them from a broader perspective. We comment on the applications of our results, as well as their limitations. We stress the complexity of the experiments, discussing their potential and limitations, and providing a detailed description of the future work needed for a quantitative experimental campaign.

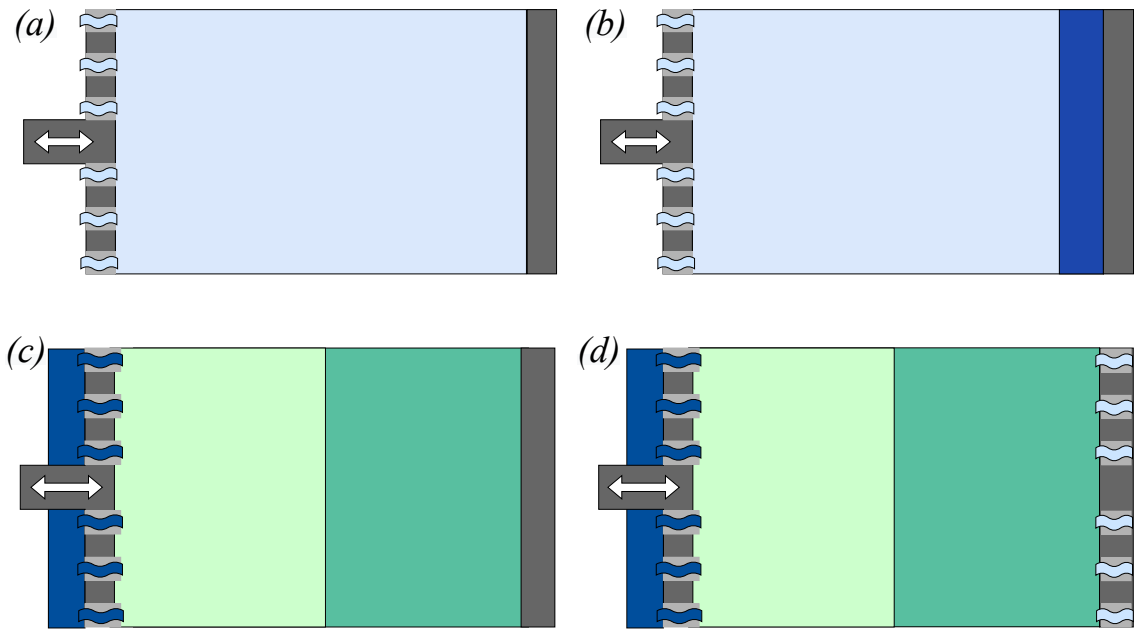

Figure 1.2: Schematic representation of the scenarios studied numerically in this thesis. A generic soft porous medium is shown in light blue. All cases involve periodic, uni-axial loading via displacement controlled motion (white arrows) of the permeable left boundary. Dark blue regions represent areas occupied by solute. We begin studying (a) the response of a homogeneous medium; in the same medium, we then examine (b) the transport and mixing of solute, initially located in a strip at the right end of the domain; we then (c, d) split the domain into two regions, each characterised by a different permeability (indicated as shades of green), and observe the infiltration of solutes from the permeable boundary. Scenarios (a), (b), and (c) are in confined compression, where the right boundary is impermeable. Scenario (d) is free-flow compression, where the right boundary is permeable.

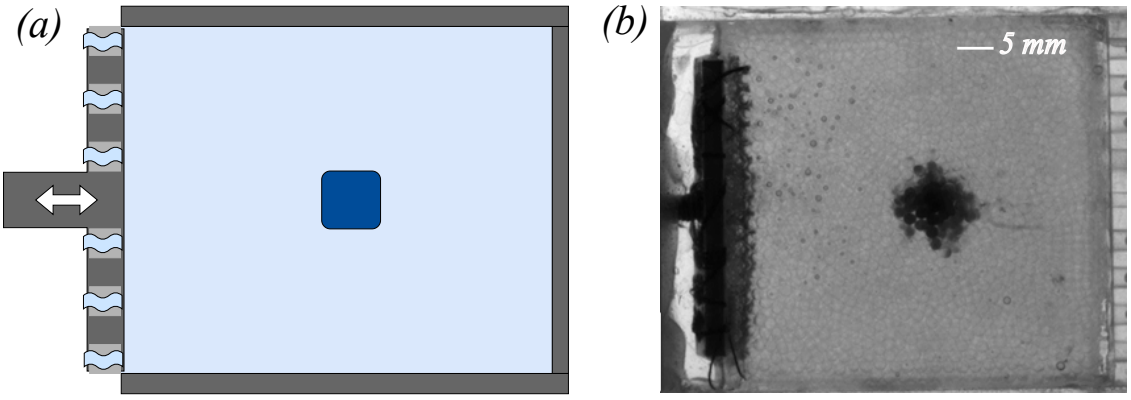

Figure 1.3: (a) schematic representation of the semi-2D problem, involving 1D poromechanics and 2D solute transport, and (b) a snapshot of an experiment. In (b), the medium is a PDMS sponge, as described in detail in Chapter 6. The solute is the dark blob in the middle of the image.

Chapter 2

Large-deformation poroelasticity

In this chapter, we provide a brief review of the established theory of large-deformation poroelasticity, as outlined in MacMinn et al. (2016) and used in the rest of the thesis. This theory assumes a fully saturated medium. Note that we use an Eulerian reference frame in the models in Chapters 3, 4 and 6, in which the medium is homogeneous and the Eulerian formulation is straightforward and intuitive for physical interpretation. In Chapter 5, we model heterogeneous media that are divided into two or more layers characterised by different permeabilities. Since the permeability is a material property, the model in that chapter is reformulated in a Lagrangian framework, which is attached to the solid skeleton.

2.1 Kinematics

We work in an Eulerian reference frame, where the solid displacement field is $\mathbf{u_s}(\mathbf{x},t) = \mathbf{x} - \mathbf{X}(\mathbf{x},t)$, with $\mathbf{X}(\mathbf{x},t)$ the reference position of the material point that at time t occupies the position $\mathbf{x}$. We choose $\mathbf{X}(\mathbf{x},0) \equiv \mathbf{x}$ so that $\mathbf{u_s}(\mathbf{x},0) = 0$, in which case the initial configuration is the reference configuration. We denote the true volume fractions of fluid and solid by ϕ_f and ϕ_s, respectively, where $\phi_f + \phi_s = 1$.

The deformation is characterised by the deformation gradient tensor $\mathbf{F} = [\mathbf{I} - (\boldsymbol{\nabla}\mathbf{u_s})^\mathsf{T}]^{-1}$, where $\mathbf{I}$ is the identity tensor, $(\square)^\mathsf{T}$ denotes the transpose, and $(\square)^{-1}$ denotes the inverse. The Jacobian determinant $J = \det(\mathbf{F}) = \lambda_1\lambda_2\lambda_3$ measures the local volume change, where $\det(\square)$ denotes the determinant and λ_1^2, λ_2^2, and λ_3^2 are the eigenvalues of $\mathbf{F}\cdot\mathbf{F}^\mathsf{T}$.

For incompressible constituents and uniform initial porosity $\phi_{f,0}$, the Jacobian determinant is linked to the porosity according to

$$J(\mathbf{x},t) = \frac{1-\phi_{f,0}}{1-\phi_f(\mathbf{x},t)}. \tag{2.1}$$

Local continuity for the solid phase reads

$$\frac{\partial \phi_s}{\partial t} + \boldsymbol{\nabla}\cdot(\phi_s\mathbf{v_s}) = 0 \quad \text{or} \quad \frac{\partial \phi_f}{\partial t} - \boldsymbol{\nabla}\cdot[(1-\phi_f)\mathbf{v_s}] = 0, \tag{2.2}$$

where the solid velocity $\mathbf{v_s}(\mathbf{x}, t)$ is related to the solid displacement via

$$\mathbf{v_s} = \frac{D\mathbf{u_s}}{Dt} \equiv \frac{\partial \mathbf{u_s}}{\partial t} + \mathbf{v_s} \cdot \boldsymbol{\nabla} \mathbf{u_s} = \frac{\partial \mathbf{u_s}}{\partial t} \cdot \mathbf{F}. \tag{2.3}$$

Considering a single incompressible fluid, continuity for the fluid phase reads

$$\frac{\partial \phi_f}{\partial t} + \boldsymbol{\nabla} \cdot (\phi_f \mathbf{v_f}) = 0, \tag{2.4}$$

where $\mathbf{v_f}(\mathbf{x}, t)$ is the fluid velocity.

2.2 Darcy's law

We assume that the movement of the fluid relative to the solid skeleton is described by Darcy's law,

$$\phi_f(\mathbf{v_f} - \mathbf{v_s}) = -\frac{k(\phi_f)}{\mu} \boldsymbol{\nabla} p, \tag{2.5}$$

where $k(\phi_f)$ is the permeability of the solid skeleton, μ is the dynamic viscosity of the fluid, and p is the fluid (pore) pressure, and where we have neglected gravity. We have taken the permeability $k(\phi_f)$ to be a function of current porosity only. The model requires an appropriate choice of permeability law. We discuss this choice in more detail in Chapter 3 and extend this formulation to include a non-uniform initial permeability $k_0(X)$ in Chapter 5.

2.3 Fluid flow

Combining equations (2.2) and (2.5), we arrive at the nonlinear flow equations:

$$\frac{\partial \phi_f}{\partial t} + \boldsymbol{\nabla} \cdot \left[\phi_f \mathbf{q} - (1 - \phi_f) \frac{k(\phi_f)}{\mu} \boldsymbol{\nabla} p \right] = 0 \quad \text{and} \quad \boldsymbol{\nabla} \cdot q = 0, \tag{2.6}$$

where the total flux q is

$$\mathbf{q} \equiv \phi_f \mathbf{v_f} + (1 - \phi_f) \mathbf{v_s}. \tag{2.7}$$

The fluid velocity and the solid velocity are then given by

$$\mathbf{v_f} = \mathbf{q} - \frac{1 - \phi_f}{\phi_f} \frac{k(\phi_f)}{\mu} \boldsymbol{\nabla} p \quad \text{and} \quad \mathbf{v_s} = \mathbf{q} + \frac{k(\phi_f)}{\mu} \boldsymbol{\nabla} p. \tag{2.8}$$

2.4 Mechanical equilibrium

The true (Cauchy) total stress $\boldsymbol{\sigma}$ is supported jointly by the fluid phase and the solid phase. The total stress can be decomposed into a contribution from the fluid pressure p and a contribution from Terzaghi's effective stress $\boldsymbol{\sigma'}$,

$$\boldsymbol{\sigma} = \boldsymbol{\sigma'} - p\mathbf{I}, \tag{2.9}$$

where we adopt the sign convention of tension being positive. Neglecting inertia and body forces, mechanical equilibrium can then be written

$$\boldsymbol{\nabla} \cdot \boldsymbol{\sigma} = \boldsymbol{\nabla} \cdot \boldsymbol{\sigma'} - \boldsymbol{\nabla} p = 0. \tag{2.10}$$

The effective stress is the portion of the total stress that contributes to deformation of the solid skeleton. The effective stress and the deformation are linked through a suitable constitutive law. We take the solid skeleton to be elastic, with no viscous or dissipative behaviours. We discuss our choice of elasticity law — comparing it to other constitutive laws — in Chapter 3.

With appropriate initial and boundary conditions and constitutive functions, equations (2.6) and (2.10) comprise a closed model for the evolution of the porosity. In Chapter 3, we simplify the model above to 1D and introduce constitutive functions and boundary conditions in to the context of a uniaxial model problem.

Chapter 3

Flow and deformation due to periodic loading in a soft porous medium

3.1 Introduction

In this chapter, we focus on the poromechanics of large, periodic loading in soft porous media. These materials are exposed to periodic deformations in a variety of natural and industrial scenarios, as we have outlined in Chapter 1. In the context of periodic loading due to seismicity, frequencies are high enough for inertia to play a dominant role. As a result, seismic response is typically dominated by the propagation of compressional and shear acoustic waves (*e.g.*, Biot, 1956a,b, Gajo and Denzer, 2011, Li et al., 2004, Liu et al., 2019). In contrast, ocean waves and tides are typically associated with a low enough frequency that inertia can be ignored (*e.g.*, Cheng, 2016, Madsen, 1978, Yamamoto et al., 1978). Instead, these studies typically focus on the pressure and stress profiles within seabed sediments in response to periodic fluctuations in hydrostatic pressure. The sediment is usually taken to be semi-infinite, the associated deformations are assumed to be small, and the response is often dominated by compressibility. Tidal forcing in coastal aquifers has similar features (*e.g.*, Trefry et al., 2019).

Our primary motivation here is tissue mechanics, where inertia and compressibility are usually negligible but moderate to large deformations are common. In this regime, poroelasticity is physically diffusive with a characteristic poroelastic relaxation time. Zhang and Cowin (1994) showed that the magnitude and distribution of pore pressure depend strongly on the loading period, introducing the ratio of the loading period to the poroelastic relaxation time as a key dimensionless control parameter. In cartilage and hydrogel scaffolds, several studies noted that faster loading (shorter loading period) is associated with larger fluid velocities that are localised near the surface, whereas slower loading (longer loading period) is associated with intermediate fluid velocities that penetrate more deeply (DiDomenico et al., 2017, Gardiner et al., 2007, Kameo et al., 2008, Urciuolo

et al., 2008, Vaughan et al., 2013). Gardiner et al. (2007) further noted that, for small deformations, the magnitude of the fluid velocity is roughly proportional to the loading amplitude, whereas the penetration depth is relatively insensitive to amplitude. Despite this extensive previous work, many basic features of flow and deformation due to periodic loading have not yet been systematically studied, in part because most of the above studies have focused on relatively narrow regions of the associated parameter space and/or on relatively small sets of specific results. For example, kinematic and constitutive nonlinearities (characteristic of large deformations and nonlinear constitutive behavior, respectively) become increasingly important as the amplitude grows, but the emergence of these nonlinearities has not been investigated. Moreover, the impact of the deformation on the magnitude and profile of the fluid flux — directly relevant to the transport of solutes— have not been examined.

Here, we study the confined compression of a soft porous medium over a wide range of loading periods (from very slow to very fast) and amplitudes (from infinitesimal to moderate/large) in the context of a simple one-dimensional model problem. Following MacMinn et al. (2016), our large-deformation poroelastic model is kinematically rigorous and includes both deformation-dependent permeability and nonlinear elasticity. We characterise the motion of the fluid and the solid throughout the loading cycle, focusing on the evolution of porosity and fluid flux, which are particularly relevant for the transport of solutes. We develop a series of analytical solutions that describe loading with small amplitude but arbitrary period (Section 3.3.2–3.3.4) and loading with large period but arbitrary amplitude (Section 3.3.5). We then solve the full problem numerically and compare with our analytical results. We use these solutions to examine the transition from very slow loading to very fast loading and from infinitesimal to large amplitudes, as well as the role of the initial porosity. Finally, we discuss the relevance of these results to some specific biological and biomedical scenarios. These results are published in the *Journal of Fluid Mechanics* (Fiori et al., 2023a).

3.2 Theoretical model

Our theoretical model is based on large-deformation poroelasticity (also referred to as biphasic theory in biomedical communities), as outlined in Chapter 2.

3.2.1 Model problem

We consider a one-dimensional sample of soft porous medium of relaxed length L and relaxed porosity (fluid fraction) $\phi_{f,0}$. The left boundary of the medium is permeable and located at $x = a(t)$ (moving); the right boundary is impermeable and located at $x = L$ (fixed in place) (Figure 3.1). We impose a periodic, displacement-driven loading via the position of the left boundary,

$$a(t) = \frac{A}{2}\left[1 - \cos\left(\frac{2\pi t}{T}\right)\right], \tag{3.1}$$



Figure 3.1: We consider a 1D sample of soft porous medium of relaxed length L, subject to a periodic, displacement-driven loading at its left boundary (white arrows). The left boundary is permeable, thus allowing fluid flow in or out (blue squiggles) to accommodate the loading. The right boundary is impermeable and fixed in place.

where A and T are the amplitude and period of the loading, respectively. Macroscopically, the deformation is strictly compressive in the sense that $a(t) \geq 0$.

We consider deformations ranging from small to large macroscopic nominal strain (-0.4% to -20% or $0.004 \leq A/L \leq 0.2$), with commensurate macroscopic changes in bulk (total) volume. We assume that the fluid and the solid phases are individually incompressible, so that the total volume of solid is constant and any change in bulk volume must correspond to a change in total pore (fluid) volume via a rearrangement of the pore structure and an influx or an efflux of fluid at the left boundary. Incompressibility of both phases is often assumed in the context of soft porous media, in particular for biological tissues (*e.g.*, (Ehlers et al., 2009, Mauck et al., 2003, Pierce et al., 2013, Vuong et al., 2015, Zhang and Szeri, 2007)). Note that, for a granular material like sand, the incompressibility of the solid phase is justified by comparing the bulk modulus of the material of the individual grains to the typical pore pressure. For moderate to large deformations, pore pressures are comparable to the stiffness of the skeleton, which, for sand packs, is considerably lower than the bulk modulus of silica (Bowles, 1988). For gels and tissues, the bulk modulus of the solid constituent is less well defined because the solid "grains" or "fibers" can be molecular. However, incompressibility is a standard part of the theory of ideal elastomeric gels (Cai and Suo, 2012, Hong et al., 2008, Li et al., 2012) and has been confirmed experimentally for cartilage (Bachrach et al., 1998).

3.2.2 Kinematics

In the Eulerian reference frame described in Chapter 2, with solid displacement field $\mathbf{u_s} = \mathbf{x} - \mathbf{X}(\mathbf{x}, t)$ and reference position $\mathbf{X}(\mathbf{x}, t)$, we similarly take the reference configuration to be the relaxed configuration, or $\mathbf{X}(\mathbf{x}, 0) \equiv \mathbf{x}$ so that $\mathbf{u_s}(\mathbf{x}, 0) = 0$. Recall that ϕ_f and ϕ_s are the true volume fraction of fluid and solid respectively, and that $\phi_f + \phi_s = 1$. In this case, flow and deformation are uniaxial, such that

$$\mathbf{u_s} = u_s(x,t)\hat{\mathbf{e}}_\mathbf{x},\ \mathbf{v_s} = v_s(x,t)\hat{\mathbf{e}}_\mathbf{x},\ \mathbf{v_f} = v_f(x,t)\hat{\mathbf{e}}_\mathbf{x}, \tag{3.2}$$

where u_s, v_s, and v_f are the x-components of the solid displacement field and the solid and fluid velocity fields, respectively, and $\hat{\mathbf{e}}_\mathbf{x}$ is the unit vector in the x-direction.

In 1D, the local state of deformation is fully characterised by the Jacobian determinant $J = (1 - \partial u_s/\partial x)^{-1}$. Therefore, assuming incompressible constituents and uniform initial porosity $\phi_{f,0}$, the local change in volume is linked to the change in porosity and to the displacement field according to

$$J(x,t) = \frac{1-\phi_{f,0}}{1-\phi_f} \quad \rightarrow \quad \frac{\partial u_s}{\partial x} = \frac{\phi_f - \phi_{f,0}}{1-\phi_{f,0}}. \tag{3.3}$$

Continuity in 1D can be derived as:

$$\frac{\partial \phi_f}{\partial t} + \frac{\partial}{\partial x}(\phi_f v_f) = 0 \quad \text{and} \quad \frac{\partial \phi_f}{\partial t} - \frac{\partial}{\partial x}[(1-\phi_f)v_s] = 0, \tag{3.4}$$

which together imply that the total flux $q = \phi_f v_f + (1-\phi_f)v_s$ is uniform in space, $\partial q/\partial x = 0$.

3.2.3 Darcy's law

In 1D, Darcy's law is expressed as

$$\phi_f(v_f - v_s) = -\frac{k(\phi_f)}{\mu}\frac{\partial p}{\partial x}, \tag{3.5}$$

where $k(\phi_f)$ is the permeability of the solid skeleton, μ is the dynamic viscosity of the fluid, and p is the fluid (pore) pressure, and neglecting gravity. We use a normalised Kozeny-Carman relation for deformation-dependent permeability (MacMinn et al., 2016):

$$k(\phi_f) = k_0 \, \frac{(1-\phi_{f,0})^2}{\phi_{f,0}^3} \, \frac{\phi_f^3}{(1-\phi_f)^2}, \tag{3.6}$$

where $k_0 \equiv k(\phi_{f,0})$ is the reference permeability. Kozeny-Carman permeability is a common choice for gels and soft tissues (Gao and Cho, 2022, Malandrino et al., 2014, Rahbari et al., 2017, Sacco et al., 2014). We compare it with a simpler power-law formulation in Appendix A.1, showing that the two are qualitatively and quantitatively similar and are expected to produce similar behavior.

3.2.4 Fluid flow

The 1D formulation of the nonlinear flow equations is:

$$\frac{\partial \phi_f}{\partial t} + \frac{\partial}{\partial x}\left[\phi_f q - (1-\phi_f)\frac{k(\phi_f)}{\mu}\frac{\partial p}{\partial x}\right] = 0 \quad \text{and} \quad \frac{\partial q}{\partial x} = 0, \tag{3.7}$$

where the total flux q is again

$$q \equiv \phi_f v_f + (1-\phi_f)v_s. \tag{3.8}$$

The Darcy-scale fluid velocity and solid velocity are:

$$v_f = q - \frac{1-\phi_f}{\phi_f}\,\frac{k(\phi_f)}{\mu}\frac{\partial p}{\partial x} \quad \text{and} \quad v_s = q + \frac{k(\phi_f)}{\mu}\frac{\partial p}{\partial x}. \tag{3.9}$$

and the local fluid flux is

$$q_f = \phi_f v_f. \tag{3.10}$$

3.2.5 Mechanical equilibrium

In 1D, Equation (2.10) implies that

$$\frac{\partial \sigma'}{\partial x} = \frac{\partial p}{\partial x}, \tag{3.11}$$

where σ' is the xx component of $\boldsymbol{\sigma}'$.

3.2.6 Elasticity law

For confined compression in 1D, as considered here, any elasticity law can be written in the form $\sigma' = \sigma'(\phi_f)$. Thus, Equation (3.7) can be rewritten as a nonlinear advection-diffusion equation:

$$\frac{\partial \phi_f}{\partial t} + \frac{\partial}{\partial x}\left[\phi_f q - D_f(\phi_f)\frac{\partial \phi_f}{\partial x}\right] = 0 \quad \text{and} \quad \frac{\partial q}{\partial x} = 0, \tag{3.12}$$

where the nonlinear composite constitutive function

$$D_f(\phi_f) = (1-\phi_f)\frac{k(\phi_f)}{\mu}\frac{\mathrm{d}\sigma'}{\mathrm{d}\phi_f} \tag{3.13}$$

is the poroelastic diffusivity.

Hencky elasticity is a simple nonlinear hyperelasticity model that considers logarithmic strains ("true strains" or "Hencky strains") to capture kinematic nonlinearity (Hencky, 1931), and which is commonly used to model soft rubbers and foams (Anand, 1979, Hencky, 1933, Xiao and Chen, 2002) and sometimes for soft biological tissues (Fraldi et al., 2018, Marchesseau et al., 2010). Hencky elasticity is convenient for our present purposes because (i) it reduces to linear elasticity for small strains and (ii) it uses the same two elastic parameters as linear elasticity. It is straightforward to replace Hencky elasticity in the present formulation with a different elastic behavior, such as a Neo-Hookean model, as appropriate for the problem/material of interest. Neo-Hookean elasticity is commonly used as a simple model for soft tissues (*e.g.* (Ehlers et al., 2009, Sengers et al., 2004)); in the present context, we expect Hencky elasticity to provide a qualitatively similar mechanical response (see Appendix A.1).

For a uniaxial deformation, the relevant component of the effective stress tensor for Hencky elasticity is (Auton and MacMinn, 2018, MacMinn et al., 2016)

$$\sigma' = \mathcal{M}\frac{\ln(J)}{J} = \mathcal{M}\left(\frac{1-\phi_f}{1-\phi_{f,0}}\right)\ln\left(\frac{1-\phi_{f,0}}{1-\phi_f}\right), \tag{3.14}$$

where $\mathcal{M} = \mathcal{K} + \frac{4}{3}\mathcal{G}$ is the p-wave or oedometric modulus, expressed here in terms of the bulk modulus and shear modulus of the solid skeleton, $\mathcal{K}$ and $\mathcal{G}$ respectively.

With appropriate initial and boundary conditions, equations (3.12), (3.13), and (3.14) form a closed model for the evolution of the porosity.

3.2.7 Initial and boundary conditions

Finally, we specify appropriate initial and boundary conditions for the solid skeleton and for the fluid. As noted above, we locate the left and right boundaries of the solid at $x = a(t)$ and $x = L$, respectively.

3.2.7.1 Initial conditions

Equation (3.1) suggests that $a(0) = 0$. The solid is therefore initially relaxed and the initial porosity is uniform and equal to the relaxed porosity,

$$u_s(x, 0) = 0 \quad \text{and} \quad \phi_f(x, 0) = \phi_{f,0}. \tag{3.15}$$

3.2.7.2 Left boundary

For $t > 0$, we apply a displacement-controlled mechanical loading at the left boundary, which is therefore a moving boundary (see Equation 3.1). The associated boundary conditions are

$$u_s(a, t) = a(t) \quad \text{and} \quad v_s(a, t) = \frac{\mathrm{d}a}{\mathrm{d}t}. \tag{3.16a}$$

The left boundary is also permeable, so we take

$$p(a, t) = 0, \tag{3.16b}$$

where we measure pressure relative to atmospheric.

3.2.7.3 Right boundary

The right boundary is impermeable and fixed in place, such that

$$u_s(L, t) = v_s(L, t) = v_f(L, t) = 0. \tag{3.17}$$

This condition and the requirement that q be uniform in space (see the end of Section 3.2.2 and Equation 3.7) together imply that $q \equiv 0$, meaning that there is no net flow through any cross-section. Equation (3.8) then requires that

$$v_f = -\frac{(1 - \phi_f)}{\phi_f} v_s, \tag{3.18}$$

meaning that the fluid and the solid always locally move in opposite directions.

3.2.8 Linear poroelasticity

For comparison with the fully nonlinear model, we linearise the relations above to arrive at linear poroelasticity, which is valid for infinitesimal deformations, $(\phi_f - \phi_{f,0})/(1 - \phi_{f,0}) = \partial u_s/\partial x \ll 1$. In this limit, Equation (3.7) reduces to the linear-poroelastic diffusion equation,

$$\frac{\partial \phi_f}{\partial t} - \frac{\partial}{\partial x}\left(D_{f,0} \frac{\partial \phi_f}{\partial x} \right) \approx 0, \tag{3.19}$$

where Hencky elasticity reduces to linear elasticity,

$$\sigma' \approx \mathcal{M}\,\frac{\partial u_s}{\partial x} = \mathcal{M}\left(\frac{\phi_f - \phi_{f,0}}{1-\phi_{f,0}}\right), \tag{3.20}$$

and $D_{f,0} = k_0\mathcal{M}/\mu$ is the constant linear-poroelastic diffusivity. With appropriate initial and boundary conditions, Equation (3.19) is a closed linear model for the evolution of the porosity.

In the linear poroelastic model, the initial conditions and the boundary conditions for the right boundary are again equations (3.15) and (3.17), respectively. The linearised boundary conditions for the left boundary are

$$u_s(0,t) \approx a(t) \quad \text{and} \quad v_s(0,t) \approx \frac{\mathrm{d}a}{\mathrm{d}t}, \tag{3.21}$$

where $a(t)$ is again given by Equation (3.1). Note that these conditions are linearized relative to equations (3.16) by virtue of being applied at $x = 0$ rather than at $x = a(t)$.

3.2.9 Scaling and summary

We make the above problem dimensionless via the scaling

$$\tilde{x} = \frac{x}{L},\ \tilde{u}_s = \frac{u_s}{L},\ \tilde{t} = \frac{t}{T_{\mathrm{pe}}},\ \tilde{\sigma}' = \frac{\sigma'}{\mathcal{M}},\ \tilde{p} = \frac{p}{\mathcal{M}},\ \tilde{k} = \frac{k(\phi)}{k_0},\ \tilde{v}_f = \frac{v_f}{L/T_{\mathrm{pe}}},\ \tilde{v}_s = \frac{v_s}{L/T_{\mathrm{pe}}}, \tag{3.22}$$

where $T_{\mathrm{pe}} = L^2/D_{f,0} = \mu L^2/(k_0\mathcal{M})$ is the classical poroelastic timescale, which is the characteristic diffusion time for the relaxation of pressure over a distance L. Now taking $q \equiv 0$, as required by the boundary conditions (see Section 3.2.7.3), the nonlinear flow equation can be rewritten in dimensionless form as

$$\frac{\partial \phi_f}{\partial \tilde{t}} - \frac{\partial}{\partial \tilde{x}}\left[\tilde{D}_f(\phi_f)\frac{\partial \phi_f}{\partial \tilde{x}}\right] = 0 \tag{3.23}$$

with nonlinear-poroelastic diffusivity

$$\tilde{D}_f = \frac{D_f}{D_{f,0}} = (1-\phi_f)\tilde{k}(\phi_f)\frac{\mathrm{d}\tilde{\sigma}'}{\mathrm{d}\phi_f}, \tag{3.24}$$

elasticity law

$$\tilde{\sigma}' = \left(\frac{1-\phi_f}{1-\phi_{f,0}}\right)\ln\left(\frac{1-\phi_{f,0}}{1-\phi_f}\right), \tag{3.25}$$

initial conditions

$$\tilde{a}(0) = 0,\ \phi_f(\tilde{x},0) = \phi_{f,0},\ \tilde{v}_f(\tilde{x},0) = \tilde{v}_s(\tilde{x},0) = 0, \tag{3.26}$$

left boundary conditions

$$\tilde{u}_s(\tilde{a},\tilde{t}) = \tilde{a}(\tilde{t}) = \frac{\tilde{A}}{2}\left[1 - \cos\left(\frac{2\pi\tilde{t}}{\tilde{T}}\right)\right],\ \tilde{v}_s(\tilde{a},\tilde{t}) = \frac{\mathrm{d}\tilde{a}}{\mathrm{d}\tilde{t}},\ \text{and} \quad \tilde{p}(\tilde{a},\tilde{t}) = 0, \tag{3.27}$$

and right boundary conditions

$$\tilde{u}_s(1,\tilde{t}) = \tilde{v}_s(1,\tilde{t}) = \tilde{v}_f(1,\tilde{t}) = 0, \tag{3.28}$$

where $\tilde{A} = A/L$ and $\tilde{T} = T/T_{\mathrm{pe}}$. We consider only dimensionless quantities below, dropping the tildes for convenience.

The above 1D model describes flow and mechanics in a poroelastic medium subject to periodic loading. The kinematics are rigorous and nonlinear, the elasticity law is Hencky elasticity, and the permeability law is the Kozeny-Carman relation. The full and linearised problems share the same three dimensionless control parameters: the dimensionless amplitude and period of the loading, A and T, and the relaxed porosity $\phi_{f,0}$.

3.3 Analytical solutions

We next develop three different analytical solutions to the linear-poroelastic problem, which are valid for small deformations ($A \ll 1$), and to the full problem for slow deformations ($T \gg 1$) at any amplitude (*i.e.*, the quasi-static limit). As formulated in Section 3.2.8, the linear-poroelastic problem implies linearised kinematics, linear elasticity, and constant permeability, and thus a constant and uniform poroelastic diffusivity. We also solve the full problem numerically in general.

3.3.1 Average porosity

We begin by deriving some basic kinematic results for the average porosity. The macroscopic total volume at any instant is $1 - a(t)$, whereas the total volume of solid is constant and equal to $1 - \phi_{f,0}$. As a result, the total volume of fluid is $\phi_{f,0} - a(t)$ and the spatially averaged porosity is

$$\langle \phi_f \rangle(t) = \frac{\phi_{f,0} - a(t)}{1 - a(t)}. \tag{3.29}$$

The average of $\langle \phi_f \rangle(t)$ in time over any integer number of loading cycles is then

$$\langle \overline{\phi_f} \rangle = \frac{1}{mT} \int_{nT}^{(n+m)T} \langle \phi_f \rangle \, \mathrm{d}t = 1 - \frac{1 - \phi_{f,0}}{\sqrt{1 - A}} \tag{3.30}$$

for any $n \geq 0$ and integer $m \geq 1$. Note that both the spatial and overall averages are smaller than $\phi_{f,0}$ for $a > 0$ and $A > 0$ because the loading has a nonzero mean (*i.e.*, $\bar{a} = A/2 > 0$), so the medium is on average compressed.

3.3.2 Linear poroelasticity: Early-time solution

The linear problem posed in Section 3.2.8 can be rewritten as a bounded linear diffusion problem for the displacement. When the loading begins, information about the motion of the left boundary propagates into the domain via poroelastic diffusion. At early times, before this information has had time to reach the right boundary, the response is the same as if the medium were semi-infinite in the x direction. The corresponding semi-infinite diffusion problem involves applying the right boundary

conditions at $x \to \infty$. This early-time ("et") solution can be derived via Laplace transform and written as a convolution integral,

$$u_{s,\mathrm{et}}(x,t) = \frac{\pi A}{T}\int_0^t \operatorname{erfc}\left(\frac{x}{2\sqrt{\tau}}\right)\sin\left[\frac{2\pi(t-\tau)}{T}\right]\,\mathrm{d}\tau. \tag{3.31}$$

The corresponding porosity field can be derived from Equation (3.31) via Equation (3.3), and is given by

$$\phi_{f,\mathrm{et}}(x,t) = \phi_{f,0} - (1-\phi_{f,0})\frac{\pi A}{T}\int_0^t \frac{1}{\sqrt{\pi\tau}}\exp\left(-\frac{x^2}{4\tau}\right)\sin\left[\frac{2\pi(t-\tau)}{T}\right]\,\mathrm{d}\tau. \tag{3.32}$$

This solution is valid until the deformation spans the domain. Introducing the penetration length $\delta_{\mathrm{et}}(t)$ as the distance from the left boundary over which the change in porosity has exceeded a threshold, the nature of the problem and the structure of the solution suggest that $\delta_{\mathrm{et}}(t) \sim 2\sqrt{t}$. We confirm this reasoning in Appendix A.2. Thus, the above solution is valid for $\delta_{\mathrm{et}} \lesssim 1 \to t \lesssim 1/4$.

Having originated from linear poroelasticity, the above solution is limited to small deformations ($A \ll 1$). Naively, this solution is valid for any loading period T; however, sufficiently small values of T also violate the assumption of small deformations because deformation of size $\sim A$ are localised to a region of size $\sim \delta_{\mathrm{et}}(t)$ at early times. As a result, we expect the maximum strain near the left boundary to be roughly of size $\max[a(t)/\delta_{\mathrm{et}}(t)] \sim A/\sqrt{T}$. More precisely, Equation (3.32) can be used to show that the extreme values of $\phi_{f,\mathrm{et}}$ will always occur at the left boundary and that the evolution of $\phi_{f,\mathrm{et}}$ at the left boundary is given by

$$\phi_{f,\mathrm{et}}(0,t) = \phi_{f,0} - (1-\phi_{f,0})A\sqrt{\frac{\pi}{T}}\,\mathcal{I}(t/T), \tag{3.33}$$

where

$$\mathcal{I}(y) = C(2\sqrt{y})\sin(2\pi y) - S(2\sqrt{y})\cos(2\pi y) \tag{3.34}$$

and C and S are the Fresnel cosine and sine integrals, respectively. The extreme values of $\phi_{f,\mathrm{et}}$ are then given by

$$\min(\phi_{f,\mathrm{et}}) = \phi_{f,0} - (1-\phi_{f,0})A\sqrt{\frac{\pi}{T}}\,\mathcal{I}_{\max}, \tag{3.35}$$

and

$$\max(\phi_{f,\mathrm{et}}) = \phi_{f,0} - (1-\phi_{f,0})A\sqrt{\frac{\pi}{T}}\,\mathcal{I}_{\min}, \tag{3.36}$$

where $\mathcal{I}_{\max} = \mathcal{I}(698/1909) \approx 0.9491$ and $\mathcal{I}_{\min} = \mathcal{I}(310/353) \approx -0.5406$ are the maximum and minimum values of $\mathcal{I}$, respectively. Strictly, the above solution is non-physical for parameter combinations for which the porosity decreases to 0 or increases to 1, corresponding to $\min(\phi_{f,\mathrm{et}}) = 0$ and $\max(\phi_{f,\mathrm{et}}) = 1$, respectively. In practise, these solutions become inaccurate for much less extreme parameter combinations as kinematic and constitutive nonlinearities become increasingly important. Hewitt et al. (2016b) showed that very fast monotonic compression of a soft porous medium can lead to extreme localisation near the piston in the form of a "bloated" low-porosity boundary layer,

the formation and evolution of which depends sensitively on the particular constitutive functions $k(\phi_f)$ and $\sigma'(\phi_f)$. We avoid these extreme loading conditions in the present study, focusing instead on scenarios that are likely to have more biological relevance. The above results confirm that the maximum local strain is indeed of size $A/\sqrt{T}$, suggesting that the above solution and the linear model in general are valid for $A \ll \sqrt{T}$. A similar condition can be derived by noting that, in the linear-poroelastic case, the boundary conditions at the left are applied at $x = 0$ rather than at $x = a(t)$ (see Equation (3.21)). Thus, the validity of the linear-poroelastic model requires that the error in this linearisation, which is $\sim A$, must be negligible relative to the poroelastic diffusion length associated with the deformation, which is $\sim \sqrt{T}$.

3.3.3 Linear poroelasticity: Full solution

The original bounded linear diffusion problem can be solved analytically via separation of variables. The resulting linear-poroelastic ("lpe") displacement field is

$$u_{s,\mathrm{lpe}}(x,t) = a(t)(1-x) - \sum_{n=1}^{\infty} 2A \sin(n\pi x) \frac{[2e^{-n^2\pi^2 t} - 2\cos(\frac{2\pi t}{T}) + n^2\pi T \sin(\frac{2\pi t}{T})]}{n\pi(4 + n^4\pi^2 T^2)}. \tag{3.37}$$

The corresponding porosity field can be derived from Equation (3.37) via Equation (3.3) and is given by

$$\phi_{f,\mathrm{lpe}}(x,t) = \phi_{f,0} - (1-\phi_{f,0}) \left\{ a(t) + \sum_{n=1}^{\infty} 2A \cos(n\pi x) \frac{[2e^{-n^2\pi^2 t} - 2\cos(\frac{2\pi t}{T}) + n^2\pi T \sin(\frac{2\pi t}{T})]}{(4 + n^4\pi^2 T^2)} \right\}. \tag{3.38}$$

The corresponding fluid velocity field can be derived by taking the time derivative of Equation (3.37) to obtain the solid velocity and then using Equation (3.18) to arrive at

$$v_{f,\mathrm{lpe}}(x,t) = -\frac{(1-\phi_{f,0})}{\phi_{f,0}} \left\{ \dot{a}(t)(1-x) - \sum_{n=1}^{\infty} 4A \sin(n\pi x) \frac{[-n^2\pi e^{-n^2\pi^2 t} + \frac{2}{T}\sin(\frac{2\pi t}{T}) + n^2\pi \cos(\frac{2\pi t}{T})]}{n(4 + n^4\pi^2 T^2)} \right\}. \tag{3.39}$$

Like the early-time solution, this solution provides a good approximation for $A \ll 1$ and for $A \ll \sqrt{T}$. Also like the early-time solution, this solution provides general insight into the poromechanical response of the system to periodic loading. The expression for $\phi_{f,\mathrm{lpe}}$ can be divided into three parts:

1. a uniform quasi-static part proportional to $a(t)$, which is the linearised form of the nonlinear quasi-static solution derived below;

2. an early-time transient that decays exponentially in time at a rate that is independent of A and T; and

3. a periodic forced response with period T.

The early-time transient captures the early-time solution derived above, which spans the domain after a time $t \approx 1/4$ and then decays exponentially relative to the periodic forced response that dominates the solution thereafter. Going forward, we focus on this periodic regime. We show in Appendix A.3 that the same reasoning also applies for large deformations.

3.3.4 Linear poroelasticity: Response to very fast loading (Stokes' second problem)

As noted above, the response at early times will be confined to a region of size $\sim \sqrt{t}$, spreading diffusively until the entire domain is engaged, at which point the response will evolve exponentially toward its periodic regime. However, the oscillations in the periodic regime will be confined to a region of size $\sim \sqrt{T}$ (or $\sim A$ if larger, but recall that linear poroelasticity requires that $A \ll \sqrt{T}$). Thus, if the period is sufficiently small (*i.e.*, $\sqrt{T} \ll 1$), the material near the piston will oscillate while the far field exists in a state of static compression. This response to very fast loading is well known from Stokes's classical "second problem", in which oscillations diffuse into a semi-infinite domain with an amplitude that decays exponentially in space, much like an evanescent wave. The corresponding analytical solution to linear poroelasticity for the periodic response to very fast loading ("vf") is

$$u_{s,\mathrm{vf}}(x,t) = \frac{A}{2}\left[1 - x - \exp\left(-x\sqrt{\frac{\pi}{T}}\right)\cos\left(\frac{2\pi t}{T} - x\sqrt{\frac{\pi}{T}}\right)\right] \tag{3.40}$$

and

$$\begin{aligned}\phi_{f,\mathrm{vf}}(x,t) = \phi_{f,0} - (1-\phi_{f,0})\frac{A}{2}\Bigg\{1 - \sqrt{\frac{\pi}{T}}\exp\left(-x\sqrt{\frac{\pi}{T}}\right) \\ \left[\cos\left(\frac{2\pi t}{T} - x\sqrt{\frac{\pi}{T}}\right) - \sin\left(\frac{2\pi t}{T} - x\sqrt{\frac{\pi}{T}}\right)\right]\Bigg\},\end{aligned} \tag{3.41}$$

where the first two terms in $u_{s,\mathrm{vf}}$ and in $\phi_{f,\mathrm{vf}}$ give the static far-field compression, which is also the (linearised) overall mean compression. This solution confirms that the oscillations will be increasingly localised near the piston as T decreases, featuring near-piston oscillations with an amplitude proportional to $1/\sqrt{T}$ that decay exponentially in space over a characteristic distance $\sqrt{T}$. This solution is illustrated and discussed further in Appendix A.2.

3.3.5 Response to very slow loading (quasi-static solution)

In the full linear-poroelastic solution above, the porosity and displacement fields (equations 3.37 and 3.38) converge to the quasi-static limits $\phi_{f,\mathrm{lpe}}(x,t) \to \phi_{f,0} - (1-\phi_{f,0})a(t)$ and $u_{s,\mathrm{lpe}} \to a(t)(1-x)$ as $T \to \infty$. This limit is a uniform state of strain in which poroelastic transients are fast relative to the loading period, and are therefore negligible. The fully nonlinear problem can be solved analytically

in the same limit by taking $\partial\phi_f/\partial t \to 0$. The resulting quasi-static ("qs") solution is

$$u_{s,\mathrm{qs}}(x,t) = \frac{a(t)}{1-a(t)}(1-x), \tag{3.42}$$

$$\phi_{f,\mathrm{qs}}(t) = \frac{\phi_{f,0}-a(t)}{1-a(t)}, \tag{3.43}$$

and

$$v_{f,\mathrm{qs}}(x,t) = -\left[\frac{1-\phi_{f,0}}{\phi_{f,0}-a(t)}\right]\left\{\frac{1-x}{[1-a(t)]^2}\right\}\dot{a}(t). \tag{3.44}$$

This solution is kinematically exact for arbitrarily large values of A, but is only valid for $T \gg 1$. Note that this expression for $\phi_{f,\mathrm{qs}}$ is the same as the one in Equation (3.29) for $\langle\phi_f\rangle(t)$ because the quasi-static porosity is spatially uniform and must therefore be equal to the average porosity.

3.3.6 Scaling quantities

In the absence of a net flow, fluid motion is directly related to changes in porosity. Hence, we present our solutions and results below in terms of the *change* in porosity with respect to the overall average porosity,

$$\Delta\phi_f \equiv \phi_f - \langle\overline{\phi_f}\rangle. \tag{3.45}$$

This mean change in porosity accounts for the non-zero mean compression.

The various results above suggest simple scaling relationships for the magnitudes of $\Delta\phi_f$ and v_f in terms of the dimensionless control parameters A and T. In particular, the magnitude of $\Delta\phi_f$ is captured by the spatially averaged change in porosity at mid-cycle,

$$\Delta\phi_f^M = \left|\langle\Delta\phi_f\rangle(T/2)\right| = \frac{\phi_{f,0}-A}{1-A} - \langle\overline{\phi_f}\rangle. \tag{3.46}$$

The quasi-static solution suggests that appropriate scales for the magnitude of the solid and fluid velocity are

$$v_s^* = \frac{2A}{T}, \tag{3.47}$$

and

$$v_f^* = \left(\frac{1-\phi_{f,0}}{\phi_{f,0}}\right)\frac{2A}{T}. \tag{3.48}$$

An appropriate scale for the fluid flux is therefore

$$q_f^* = \phi_{f,0}v_f^*. \tag{3.49}$$

3.4 Numerical solution

We solve the full nonlinear problem (Section 3.2.9) numerically in `MATLAB` using a Chebyshev spectral method in space and an implicit Runge-Kutta method in time, as described in more detail in Appendix A.7. We provide an example code in (Fiori et al., 2023b). In Figure 3.2, we illustrate the

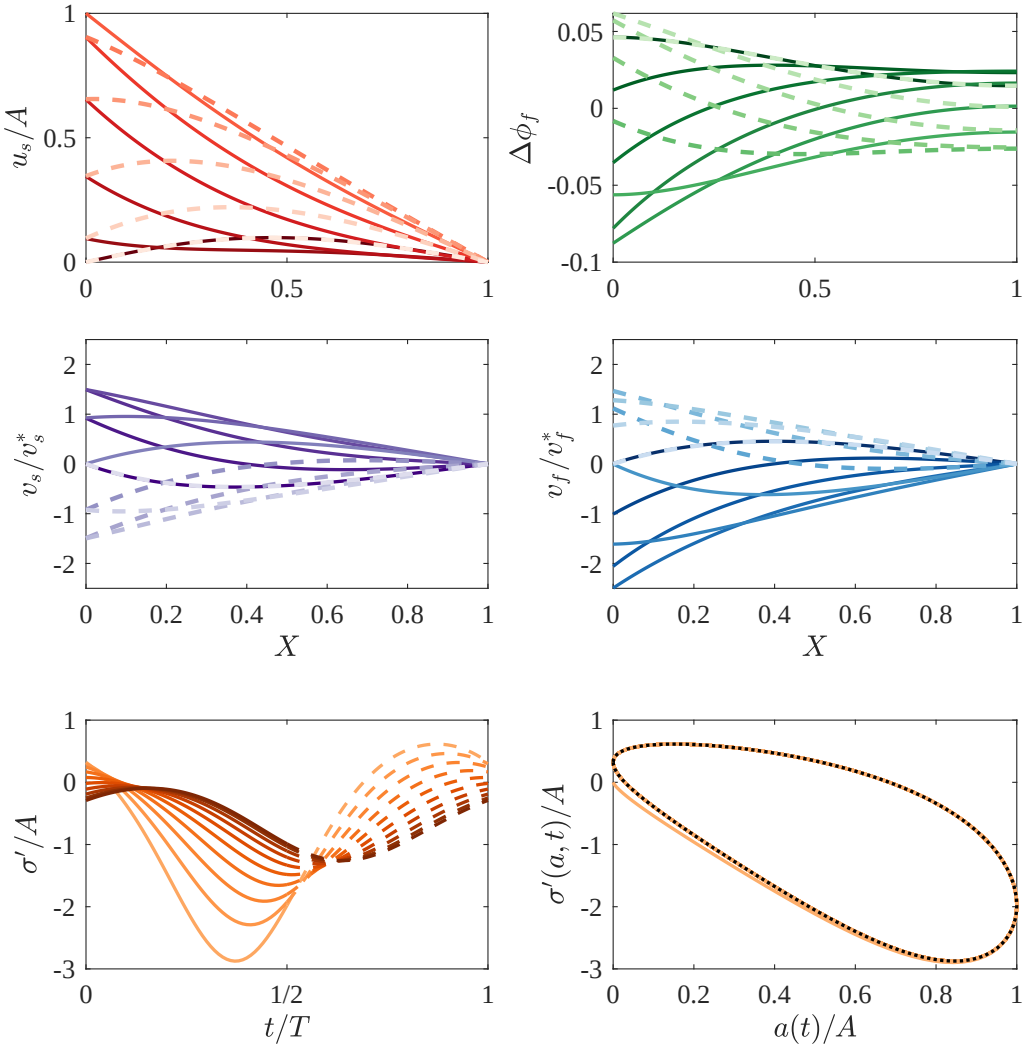

Figure 3.2: Response of a high-porosity medium ($\phi_{f,0} = 0.75$) to periodic loading at high amplitude ($A = 0.2$) and moderate period ($T = 0.3\pi$). In the first two rows, we show the evolution of u_s, $\Delta\phi_f$, v_s, and v_f (all normalised) at times $t = nT$ to $(n+1)T$ in increments of $0.1T$ (dark to light) during one cycle in the periodic regime, where n is an integer. In the first two rows, we plot all fields against the Lagrangian spatial coordinate $X = x - u_s(x,t)$ for visual clarity. In the left column of the third row, we plot σ' against t at fixed values of X from 0 to 1 (light to dark). In the right column of the third row, we plot a phase portrait of $\sigma'(a,t)$ against $a(t)$ for $t = 0$ to $t = 20T$, emphasising the last cycle (dotted black). In all plots but the lower right panel, we distinguish between the loading half of the cycle ($\dot{a}(t) > 0$; solid curves) and the unloading half of the cycle ($\dot{a}(t) < 0$; dashed curves).

basic phenomenology of the response of a high-porosity medium ($\phi_{f,0} = 0.75$) to periodic loading at large amplitude ($A = 0.2$) and moderate period ($T = 0.3\pi$) for one cycle in the periodic regime.

All quantities considered — displacement, change in porosity, solid velocity, fluid velocity, and effective stress — are largest in magnitude at the left boundary, where the medium is forced, and smallest in magnitude at the right boundary, where the medium is stationary, with a magnitude envelope that decreases monotonically from left to right. The displacement and both velocities vanish at the right boundary, as required. Note that these features depend greatly on the boundary conditions for both the solid and the fluid. The flow and deformation will focus toward boundaries where inflow and outflow are permitted, which here is the left side. Reversing the permeability of the two boundaries (*i.e.*, an impermeable moving boundary and a permeable fixed boundary) would instead focus the flow and deformation toward the right side, roughly reversing the spatial profile of $\Delta\phi_f$ and producing a much more uniform profile of v_f. However, the latter scenario is identical to the present one when viewed from a moving frame that follows the left boundary, $x' = 1 + a(t) - x$.

The third row of Figure 3.2 shows the effective stress normalised by the nominal strain at maximum compression, σ'/A. The left column shows that the response is out of phase with the loading, with a phase shift that varies with the Lagrangian spatial coordinate $X = x - u_s(x,t)$. For example, the stress at the left boundary leads the motion of the left boundary by about $0.15T$ (*i.e.*, the moment of maximum $|\sigma'(a,t)|$ occurs about $0.15T$ before the moment of maximum $a(t)$), whereas the stress at the right boundary lags the motion of the left boundary by a similar amount. In addition, the material near the left boundary experiences strong compression during most of the loading phase ($\sigma' < 0$ for $\dot{a} > 0$) and mild tension during much of unloading ($\sigma' > 0$ for $\dot{a} < 0$). This hysteresis is highlighted by the large area enclosed by the loop in the phase portrait (right column), and it originates in the stronger relative role of viscous drag during moderate to fast loading.

Most of the features illustrated in Figure 3.2 are qualitatively consistent with linear poroelasticity, although the quantitative accuracy of linear poroelasticity depends on the deformation parameters as discussed in the next section. A key qualitative feature introduced by nonlinearity is that the response during loading is not necessarily symmetric with the response during unloading. For example, the minimum values of $\Delta\phi_f(a,t)$ and $v_f(a,t)$ are much larger in magnitude than their maximum values and the stress loop is not symmetric about any axis. We explore this asymmetry in more detail in Section 3.5.

3.4.1 Comparison with analytical solutions

We next compare the numerical solution to the linear-poroelastic and nonlinear quasi-static analytical solutions described in Section 3.3, each of which is appropriate for a specific range of A and T. The aim of this comparison is to quantify these ranges of validity and to examine the convergence of the numerical results to each of these special cases. To do so, we calculate all three solutions

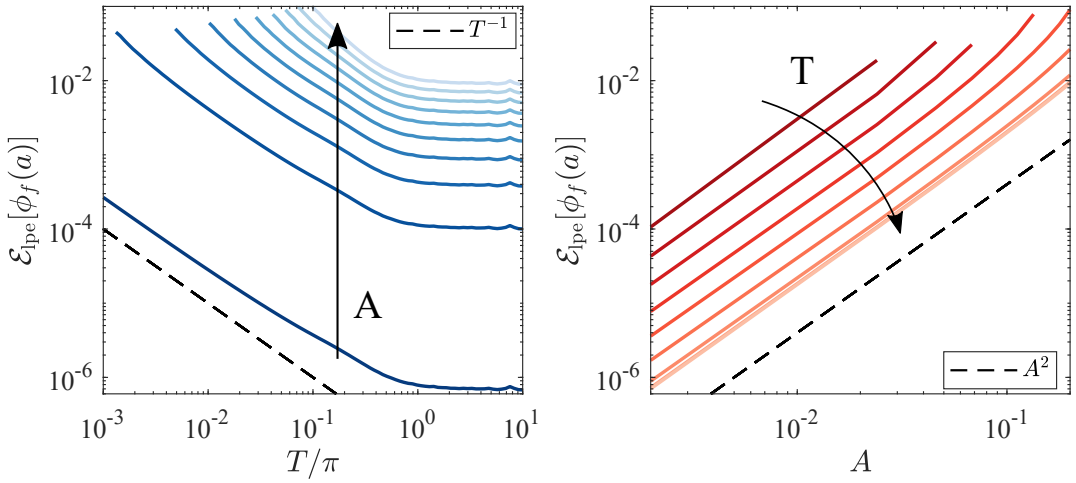

Figure 3.3: Root-mean-square relative difference between the full numerical solution and the linear-poroelastic analytical solution (from Equation 3.38) based on $\phi_f(a,t)$ during one cycle in the periodic regime. On the left, we plot the difference against T for fixed values of A ranging from 0.02 to 0.2 (dark to light). On the right, we plot the same difference against A for fixed values of T ranging from 0.001π to 10π (dark to light).

over a wide range of A and T and then calculate the root-mean-square (RMS) relative difference between the numerical and linear-poroelastic solutions (Figure 3.3), and between the numerical and nonlinear quasi-static solutions (Figure 3.4). We calculate these differences using $\phi_f(a,t)$ during one cycle in the periodic regime. In both figures, we plot these differences against T for several values of A (left panels) and then against A for several values of T (right panels).

As expected, Figure 3.3 shows good agreement between the numerical and linear-poroelastic solutions for small deformations, worsening as A increases. The difference scales with A^2 for a given value of T (right panel), as expected from linear poroelasticity, which is first-order in strain. The difference is insensitive to T for $T \gtrsim 1$, but scales as T^{-1} for faster periods. Decreasing T leads to increasingly strong localisation at the left boundary, and hence increasingly large deformations, even for small A, as expected from the early-time and very-fast analyses above (Section 3.3.2–3.3.4). We explore this localisation in more detail in Section 3.5.

As expected, Figure (3.4) shows good agreement between the numerical and nonlinear quasi-static solutions for large periods, worsening as T decreases. The difference scales with T^{-1} for $T \gtrsim 1$ and with $T^{-1/2}$ for shorter periods (left panel); The difference also scales with A (right panel), consistent with the scaling of the non-quasi-static terms in Equation (3.38). Based on these results, we distinguish between "slow loading" (SL; $T \gtrsim \pi$), where spatial variations in porosity are relatively small, and "fast loading" (FL; $T \lesssim 0.1\pi$), where spatial variations in porosity are relatively large. For very slow loading ($T \gg 1$), the porosity is uniform and the response is quasi-static (see

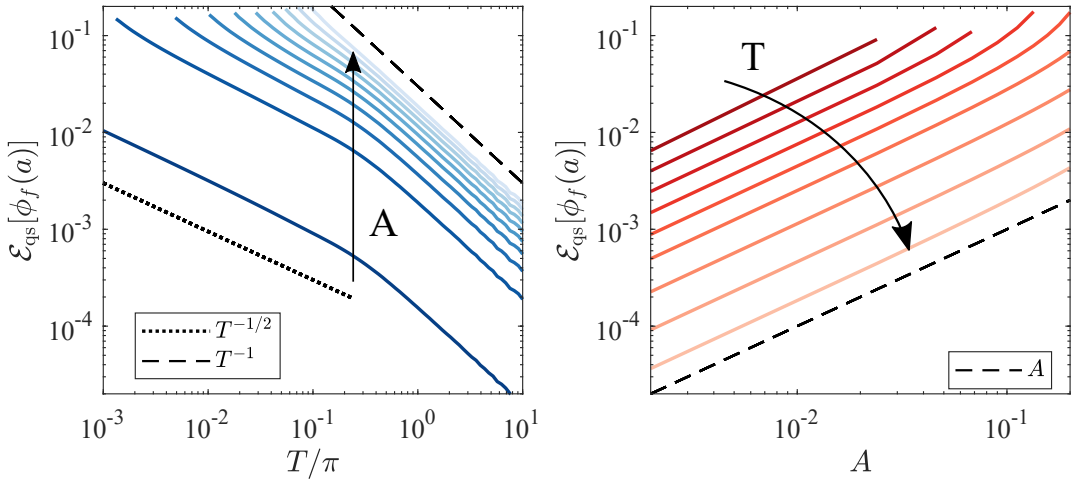

Figure 3.4: Root-mean-square relative difference between the full numerical solution and the nonlinear quasi-static solution (from Equation 3.43) based $\phi_f(a,t)$ during one cycle in the periodic regime. On the left, we plot the difference against T for fixed values of A ranging from 0.02 to 0.2 (dark to light). On the right, we plot the same difference against A for fixed values of T ranging from 0.001π to 10π (dark to light).

Section 3.3.5). For very fast loading ($T \ll 1$), the oscillations are localised near the left boundary and the right portion of the medium is in a state of static compression (see Section 3.3.4).

3.5 Parameter study

We next examine and compare the poroelastic response for SL and FL as a function of T, A, and $\phi_{f,0}$. We focus on the evolution of u_s, ϕ_f and $q_f = \phi_f v_f$ in space and in time, and on the phase behavior of $\sigma'(a,t)$. We conclude by considering the parameter ranges that would be relevant to various biological examples.

3.5.1 Impact of loading period

To visualise the distinct poromechanical responses for FL and SL, and the transition between them, we plot u_s, $\Delta\phi_f$, and q_f (all normalised) over one cycle in the periodic regime for $\phi_{f,0} = 0.75$, $A = 0.1$, and four different values of T — two for FL (left two columns) and two for SL (right two columns) (Figure 3.5).

The first row of Figure 3.5 shows that, for FL (*i.e.*, $T = 0.03\pi$ and 0.1π), the displacement is highly nonlinear in X (and in x), with substantial differences between the loading and unloading phases. As T increases, transitioning into SL (*i.e.*, $T = 1\pi$ and 10π), the displacement is increasingly linear in X and converges toward the quasi-static solution, which is fully determined by the

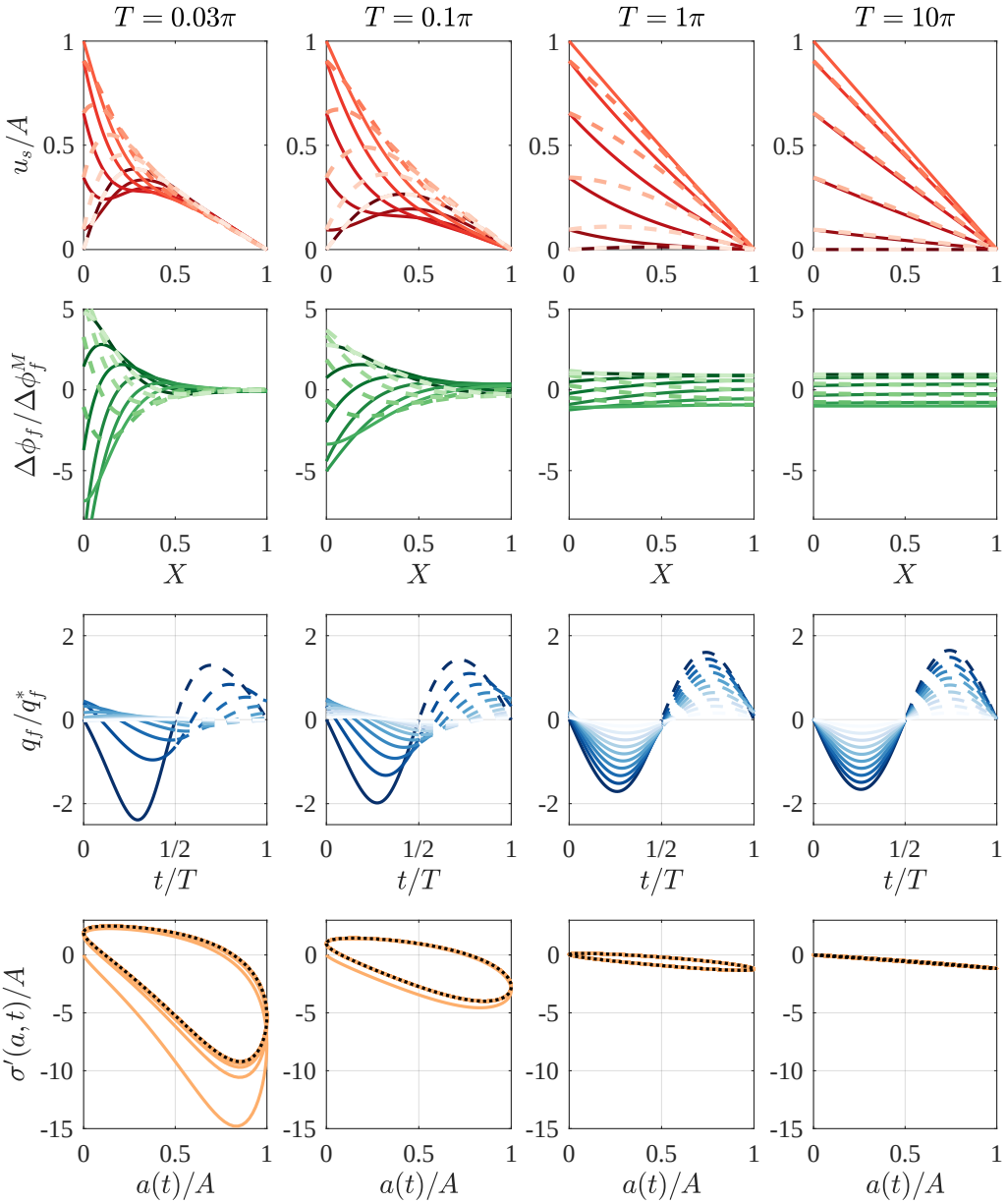

Figure 3.5: Evolution of normalised u_s (first row) and $\Delta\phi_f$ (second row) at times $t = nT$ to $(n+1)T$ in increments of $0.1T$ (dark to light), where n is an integer, during one cycle in the periodic regime for $A = 0.1$, $\phi_{f,0} = 0.75$, and $T = 0.03\pi$ (first column), 0.1π (second column), π (third column), and 10π (fourth column). As in Figure 3.2, we plot all fields in the first two rows against the Lagrangian spatial coordinate $X = x - u_s(x,t)$ for clarity. In the third row, we plot normalised q_f against t for ten different values of X from 0 to 1 (dark to light). We distinguish between the loading half of the cycle ($\dot{a} > 0$; solid curves) and the unloading half of the cycle ($\dot{a} < 0$; dashed curves). In the last row, plot phase portraits of $\sigma'(a,t)$ against $a(t)$ from $t = 0$ to $t = 20T$, emphasising the last cycle (dotted black).

instantaneous value of a and is thus symmetric between loading and unloading. For all values of T, the displacement is of characteristic size A at the left and vanishes at the right.

For SL, $\Delta\phi_f$ is uniform in space and varies only in time, as per the quasi-static solution. The medium is in a uniform state of compression, fully determined by the instantaneous value of a and thus symmetric between loading and unloading and fully relaxed at the beginning/end of each cycle. As T decreases, transitioning into FL, $\Delta\phi_f$ becomes increasingly localised near the left boundary and also increasingly asymmetric between loading and unloading (Figure 3.5, second row, left column). For FL, the medium experiences a substantial amount of tension in the left portion of the domain during unloading, despite the overall mean compression. Tension emerges for FL because this regime is, by definition, one where the rate of loading is much faster than the poroelastic relaxation time, so the left boundary must *pull* the medium to the left during unloading. The right portion of the domain experiences an overall more limited range of porosities and remains compressed throughout the cycle, never reaching a state of tension or even full unloading. The latter feature is also visible in the corresponding displacement fields.

The fluid flux $q_f = \phi_f v_f$ is particularly relevant to the transport of solutes since it drives advection. Fluid leaves the domain during the loading phase of the cycle ($q_f(x = a, t) = q_f(X = 0, t) < 0$ when $\dot{a} > 0$) and enters the domain during unloading. For SL, q_f is entirely in-phase with the loading, but opposite in sign. For FL, the peak value of q_f in the interior exhibits a lag relative to the peak value of $\dot{a}$, and this lag increases with x. Note that the fluid flux is orders of magnitude larger for FL than for SL because the rate of loading is orders of magnitude faster, but this variation is largely scaled out by normalisation with $q_f^*(\phi_{f,0}, A, T) \propto T^{-1}$, per Equation (3.49) (Figure 3.5, third row).

The extreme values of q_f at the left boundary are larger in loading than in unloading, but progressively more symmetric as T increases. This asymmetry is a result of the kinematic and constitutive nonlinearity of large deformations. We show in Appendix A.4 that this asymmetry originates in the nonlinear kinematics of large deformations, meaning that it emerges from the nonlinear model during large deformations even with linear elasticity and constant permeability. This asymmetry is then strongly amplified by deformation-dependent permeability (relative to constant permeability) and slightly suppressed by Hencky elasticity (relative to linear elasticity). The latter occurs because Hencky elasticity stiffens in compression, resulting in a larger poroelastic diffusivity and therefore weaker localisation during loading (see also Appendix A.1).

The asymmetry between loading and unloading is also highlighted by the evolution of $\sigma'(a, t)$ (Figure 3.5, fourth row). For FL, $\sigma'(a, t)$ exhibits hysteresis: for the same value of $a(t)$, the value of $\sigma'(a, t)$ is considerably higher in magnitude during loading than during unloading (and tensile during much of the unloading phase). This hysteresis decreases as T increases, such that, for SL, $\sigma'(a, t)$ is modest in magnitude, fully compressive, and symmetric between loading and unloading

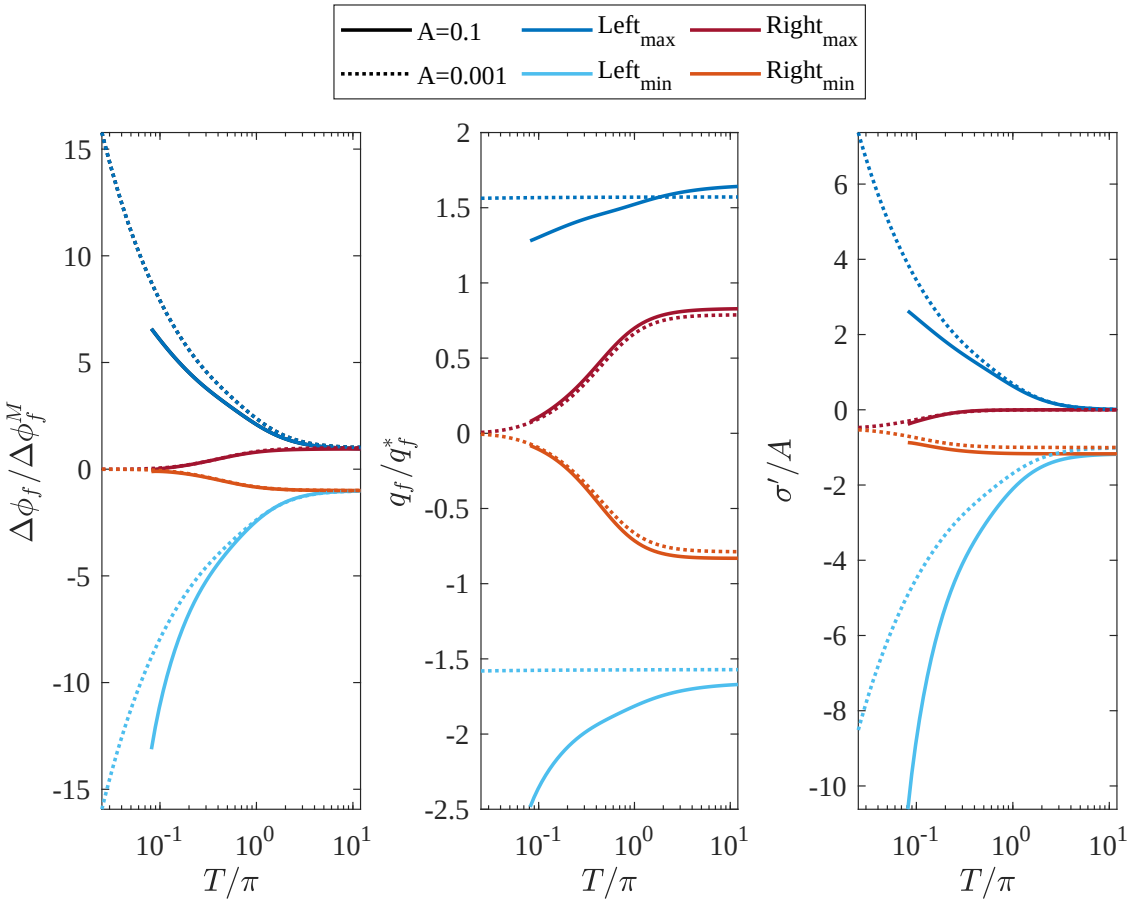

Figure 3.6: We illustrate the transition from FL to SL as T increases by plotting the normalised maximum and minimum values $\Delta\phi_f$ (first column), q_f (second column), and σ' (third column) against T for $A = 0.1$ (solid lines) and $A = 0.001$ (dotted lines) during the periodic regime. We show the maximum values (dark colours) and minimum values (light colours) of all three quantities at the left boundary ($X = 0$, blue curves), of $\Delta\phi_f$ and σ' at the right boundary ($X = 1$, red curves), and of q_f at the material midpoint ($X = 1/2$, red curves).

(*i.e.*, non-hysteretic); as a result of the latter, the phase portrait for SL is a single curve (rather than a loop). These phase portraits also illustrate the convergence to the periodic regime: in all cases, the overall response grows less extreme as the transient component decays exponentially over the first $\sim T^{-1}$ cycles.

Since a key difference between SL and FL is that the deformation is uniformly distributed in the former and localised toward the left in the latter, we study the emergence of this localisation to further quantify the transition from SL to FL. In Figure 3.6, we plot the normalised maximum and minimum values of $\Delta\phi_f$, q_f, and σ' at the left boundary ($X = 0$) and then either at the right boundary ($X = 1$) for $\Delta\phi_f$ and σ' or at the material mid-point ($X = 1/2$) for q_f. The latter is necessary because q_f vanishes at $X = 1$. We consider a range of periods T at two fixed values of A for $\phi_{f,0} = 0.75$.

Figure 3.6 shows that, for SL, the deformation is uniform, varying only in time. The maxima and minima of both $\Delta\phi_f$ and σ' remain separate, but their left and right values converge. The flux q_f remains linear in space, even for SL (see Section 3.3.5). As T decreases, the deformation is progressively localised at the left, such that the right is increasingly static. At the right, the maximum and minimum values of $\Delta\phi_f$ and q_f converge to zero while the maximum and minimum values of σ' converge to weak compression, as also illustrated in Figure 3.5.

We find that a small-amplitude deformation ($A = 0.001$) and a large-amplitude deformation ($A = 0.1$) exhibit qualitatively similar features. However, large deformations lead to an increasingly strong asymmetry between the maxima and minima of all quantities at the left boundary as T decreases. In particular, the curves are biased downward, such with higher magnitudes reached in loading (minima) than in unloading (maxima). This asymmetry is does not occur for small deformations, for which the maxima and minima of all quantities are symmetric in magnitude. Note also that the maxima of $\Delta\phi_f$ and σ' increase as T decreases for both values of A, whereas the maximum of q_f is independent of T for small deformations but decreases with T for large deformations, consistent with Figure 3.5.

3.5.2 Impact of loading amplitude

We next examine the impact of loading amplitude A on the poromechanical response. We first assess the interaction between amplitude and period by plotting $\Delta\phi_f$ against X at mid-cycle for two different values of T (one for SL and one for FL) and for five different values of A, ranging from small to large deformations ($A = 0.002$ to 0.2; fig. 3.7). The left panel in Figure 3.7 shows that, for SL, the non-normalised value of $\Delta\phi_f$ is uniform in X and increases with A, as expected. For FL, the non-normalised value of $\Delta\phi_f$ is increasingly non-uniform with X as A increases. Relative to the SL case, the deformation is increasingly amplified at the left boundary and suppressed at the right boundary (recall that the mean value of $\Delta\phi_f$ is independent of T). The right panel shows the same results, but now normalised by $\Delta\phi_f^M$ (Equation (3.46)). By definition, all of the SL curves collapse onto $\Delta\phi_f/\Delta\phi_f^M = -1$ ($\Delta\phi_f^M$ is the magnitude of the quasi-static change in porosity at mid-cycle). The FL curves also nearly collapse onto a master curve, suggesting that this normalisation scales out the leading-order impact of A, even for large deformations for FL. The largest deviations from this collapse are near the left boundary, where nonlinearities are particularly pronounced.

In Figure 3.8, we focus on FL by fixing $T = 0.1\pi$ and plotting the evolution of $\Delta\phi_f$, q_f, and $\sigma'(a,t)$ for three different values of A, ranging from small to large deformations. We find that increasing A amplifies the asymmetry in the extreme values of $\Delta\phi_f$ and q_f at the left boundary in loading and unloading, as noted in Figure 3.6. The normalisation scales out the leading-order impact of A on all of these quantities, as noted in Figure 3.7; the non-normalised values of all three quantities would vary by two orders of magnitude across this range of A. As A increases,

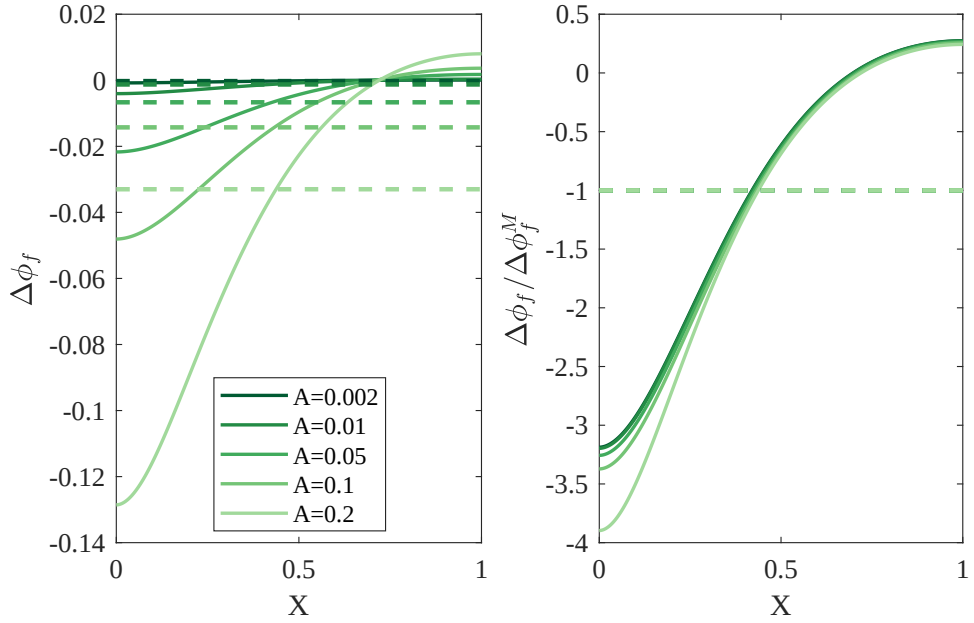

Figure 3.7: Profiles of $\Delta\phi_f$ at mid-cycle during the periodic regime for $\phi_{f,0} = 0.75$ and for five values of A ranging from small to large deformations (dark to light), each for two different periods: $T = 0.1\pi$ (FL; solid) and $T = 10\pi$ (SL; dashed). The left and right panels are non-normalised and normalised, respectively, showing that this normalisation scales out the leading-order impact of A on $\Delta\phi_f$.

$\sigma'(a,t)$ exhibits more hysteresis and larger normalised magnitudes, in accordance with the amplified asymmetry.

We further explore the impact of A in Figure 3.9 by plotting the normalised maxima and minima of $\Delta\phi_f$, q_f, and σ' at the left and at the right, as in Figure 3.6, but now against A for two different values of T, showing the smooth transition from small deformations ($A \lesssim 0.01$) to large deformations ($A \gtrsim 0.01$). For small deformations, the normalised maxima and minima of all quantities at the left and at the right become independent of A, and the extreme values of $\Delta\phi_f$ and q_f become symmetric. For SL, $\Delta\phi_f$ and σ' become uniform in space, such that their normalised left and right values are equal and depend only weakly on A for the largest deformations shown here (*e.g.*, $A \gtrsim 0.1$). For FL, the values of all three quantities at the left become increasingly asymmetric and biased downward as A increases.

3.5.3 Impact of initial porosity

Finally, we consider the initial porosity $\phi_{f,0}$. In Figure 3.10, we plot the distribution of $\Delta\phi_f$ at mid-cycle for three different values of $\phi_{f,0}$ for fixed $A = 0.01$ and for two different values of T, one for FL ($T = 0.1\pi$) and SL ($T = 10\pi$). For both SL and FL, the non-normalised values of $\Delta\phi_f$ (left panel) increase in magnitude as $\phi_{f,0}$ decreases because the same change in total volume is a larger

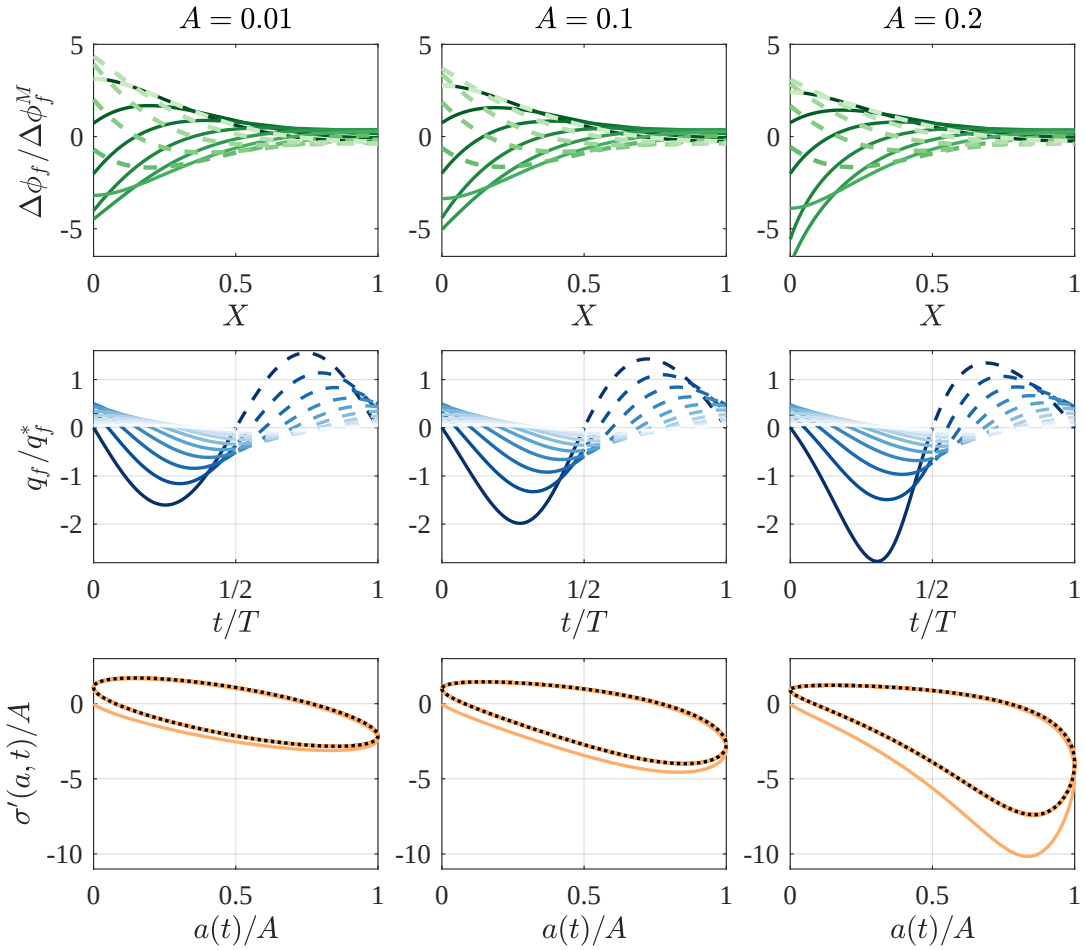

Figure 3.8: Evolution of normalised $\Delta\phi_f$, q_f, and $\sigma'(a,t)$ for $\phi_{f,0} = 0.75$, $T = 0.1\pi$, and $A = 0.01$ (first column), 0.1 (second column), and 0.2 (third column). In the first row, we plot $\Delta\phi_f$ against the Lagrangian spatial coordinate $X = x - u_s$ at times $t = nT$ to $(n+1)T$ in increments of $0.1T$ (dark to light) during one cycle in the periodic regime. In the second row, we plot q_f against t for ten different values of X from 0 to 1 (dark to light); we distinguish between loading ($\dot{a} > 0$; solid curves) and unloading ($\dot{a} < 0$; dashed curves). In the last row, we plot phase portraits of $\sigma'(a,t)$ against $a(t)$ from $t = 0$ to $t = 20T$, emphasising the last cycle (dotted black lines).

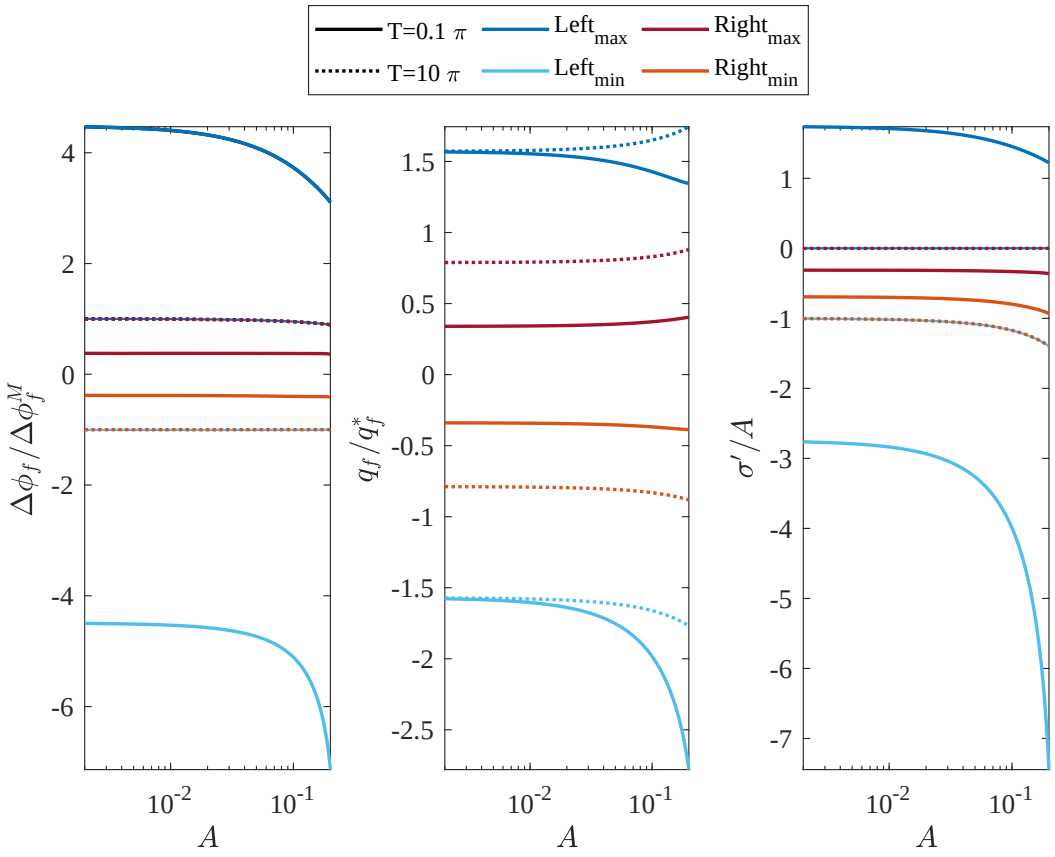

Figure 3.9: We illustrate the transition from small to large deformations as A increases by plotting the normalised maximum and minimum values $\Delta\phi_f$ (first column), q_f (second column), and σ' (third column) against A for $T = 0.1\pi$ (solid lines) and $T = 10\pi$ (dotted lines) during the periodic regime. We show the maximum values (dark colours) and minimum values (light colours) of all three quantities at the left boundary ($X = 0$, blue curves), of $\Delta\phi_f$ and σ' at the right boundary ($X = 1$, red curves), and of q_f at the material midpoint ($X = 1/2$, red curves).

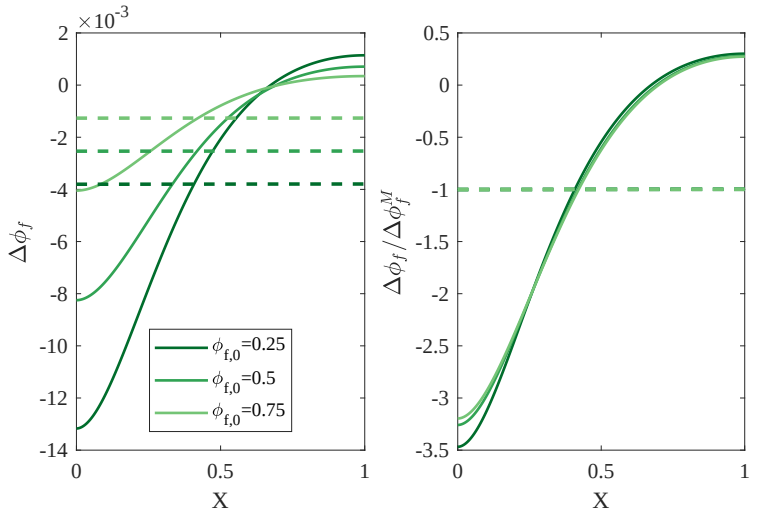

Figure 3.10: Impact of $\phi_{f,0}$ on $\Delta\phi_f$ at mid-cycle in the periodic regime for $A = 0.1$ and for two different periods: $T = 0.1\pi$ (FL; solid) and 10π (SL; dashed). We show results for three values of $\phi_{f,0}$ (increasing from dark to light). We plot the non-normalised value of $\Delta\phi_f$ on the left and the normalised value on the right.

portion of the initial fluid volume. The right panel shows that normalisation by $\Delta\phi_f^M$ scales out the leading-order impact of varying $\phi_{f,0}$ on $\Delta\phi_f$, again with small deviations at the left boundary for FL, when nonlinearities are most pronounced.

We next plot the evolution of $\Delta\phi_f$ and σ' in time for $A = 0.01$ and $T = 0.1\pi$ for the same three values of $\phi_{f,0}$ (fig. 3.11), confirming that normalisation scales out the primary impact of $\phi_{f,0}$ on $\Delta\phi_f$ and on $\sigma'(a,t)$.

3.5.4 FL in biological examples

We conclude by considering appropriate parameter ranges for several examples of periodic loading in soft biological tissues (Table 3.1). Based on these values, we calculate the poroelastic timescale T_{pe} and the relative dimensionless loading period $\tilde{T} = T/T_{\mathrm{pe}}$ for each example to understand the ranges of relevance for $\tilde{A}$, $\tilde{T}$ and $\phi_{f,0}$.

Table 3.1 indicates that, for a variety of soft tissues, deformations are in the range of the dimensionless amplitudes $\tilde{A}$ considered here, with nearly all being near the upper end. The range of $\phi_{f,0}$ is slightly wider than the range considered here, but we showed in Section 3.5.3 that this value has little impact on the normalised mechanical response of the medium. The range of poroelastic timescales T_{pe} and respective loading frequencies suggest that dimensionless loading periods $\tilde{T}$ span a wide range, with many corresponding to FL. These values justify our analysis and underscore the importance of characterising the nonlinearity of large poromechanical deformations during FL in particular.

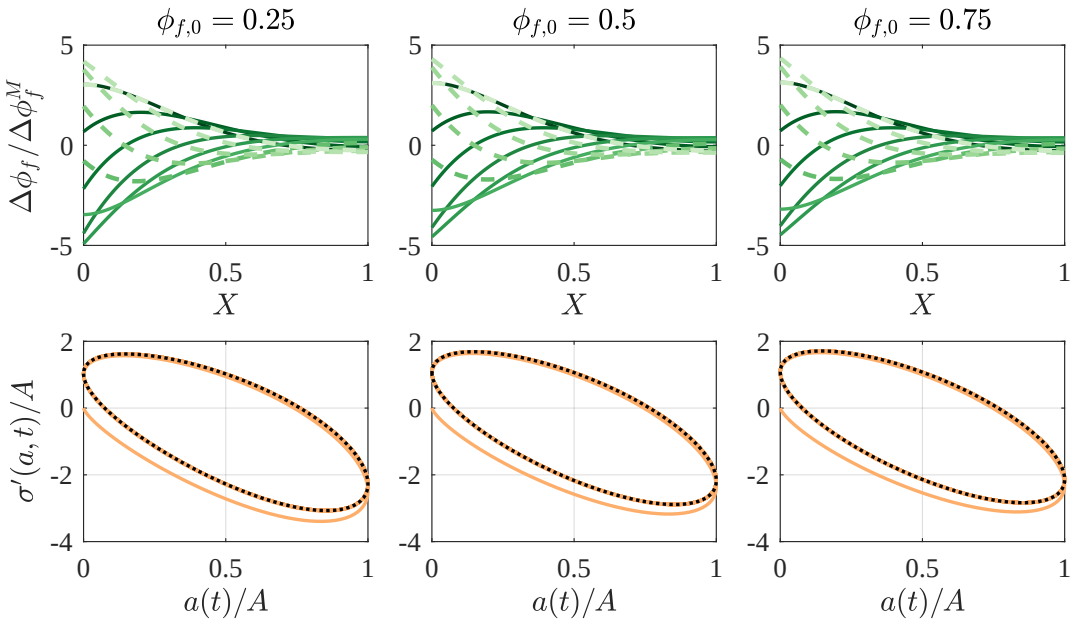

Figure 3.11: Impact of $\phi_{f,0}$ on the evolution of $\Delta\phi_f$ and $\sigma'(a,t)$ for $A = 0.01$, $T = 0.1\pi$, and $\phi_{f,0} = 0.25$ (first column), 0.5 (second column), and 0.75 (third column). In the first row, we plot $\Delta\phi_f$ against the Lagrangian spatial coordinate $X = x - u_s$ at times $t = nT$ to $(n+1)T$ in increments of $0.1T$ (dark to light) during one cycle in the periodic regime, and we distinguish between loading ($\dot{a} > 0$; solid curves) and unloading ($\dot{a} < 0$; dashed curves). In the second row, we plot phase portraits of $\sigma'(a,t)$ against $a(t)$ from $t = 0$ to $t = 20T$, emphasising the last cycle (dotted black lines).

Tissue	L [m]	$\tilde{A} = A/L$	$\phi_{f,0}$	k_0 [m^2]	$\mathcal{M}$ [Pa]	T_{pe} [s]	Typical loading frequency [Hz]	$\tilde{T} = T/T_{\text{pe}}$
Brain ECM (Kedarasetti et al., 2020)	2×10^{-4}	0.1 – 0.2	0.2	2×10^{-15}	2×10^{3}	≈ 10	0.3 – 10	0.003π – 0.1π
Cartilage (Ferguson et al., 2004)	2×10^{-3}	≈ 0.15	0.8	7.5×10^{-18}	5×10^{6}	$\approx 10^{2}$	0.001 – 0.1 (sitting) 0.1 – 1 (running)	0.03π – 3π 0.003π – 0.03π
Intervertebral Disk (Anulus F.) (Ferguson et al., 2004)	10^{-2}	≈ 0.15	0.7	7.5×10^{-19}	2.5×10^{6}	$\approx 5 \times 10^{4}$	2×10^{-5} (wake cycle) 0.001 – 0.1 (sitting) 0.1 – 1 (running)	0.3π $6 \times 10^{-5}\pi$ – $6 \times 10^{-3}\pi$ $6 \times 10^{-6}\pi$ – $6 \times 10^{-5}\pi$
Cartilage Scaffold (bioreactor) (Sengers et al., 2004)	2×10^{-3}	$0 - 0.15$	0.9	10^{-17}	10^{5}	$\approx 4 \times 10^{3}$	0.001 – 1	0.0001π – 0.1π

Table 3.1: Material and loading pararameters for some examples of biological media.

3.6 Conclusions

We have provided an analysis of the poromechanical coupling between large deformations and fluid flow in a periodically loaded soft porous medium. To do so, we used a kinematically rigorous 1D continuum model with Hencky elasticity and Kozeny-Carman permeability. In particular, we examined the roles of the three dimensionless control parameters: the initial porosity $\phi_{f,0}$, the loading amplitude A, and the loading period T.

We began by deriving several analytical solutions from linear poroelasticity — an early-time solution, a full solution, and a solution for the response to very fast loading (Stokes's second problem) — as well as a quasi-static solution to the fully nonlinear problem. The former are valid for small deformations, which corresponds to $A \ll 1$ and also, less obviously, to $A \ll \sqrt{T}$. The quasi-static solution is valid for very slow loading ($T \gg 1$) but arbitrarily large amplitudes. We then compared these solutions with our numerical results, highlighting the existence of two mechanical regimes: slow loading (SL), where the loading is much slower than the poroelastic relaxation time T_{pe}, and fast loading (FL), where the loading is much faster than T_{pe}.

We then showed that the material response to SL ($T \gtrsim \pi$) is an increasingly uniform deformation throughout the domain, approaching the quasi-static solution for very slow loading. For FL ($T \lesssim 0.1\pi$), the deformation is nonuniform and increasingly localised near the left boundary. In the limit of very fast loading, this localisation is such that the left portion of the medium oscillates while the right portion is in a state of static compression. We showed that FL is also characterised by asymmetry between loading and unloading, with a larger change in porosity and higher fluid flux magnitudes during loading (when fluid is squeezed out) than during unloading (when fluid is sucked back in). This asymmetry originates in the kinematic nonlinearity of large deformations and is amplified by the localisation of the deformation near the left boundary as T decreases (itself a linear effect) and by the nonlinearity of deformation-dependent permeability as A increases. Thus, this asymmetry emerges from the fast and large deformation of an elastic and initially homogeneous medium, and is therefore purely poromechanical; it does not occur during slow loading. Asymmetry between quasi-static loading and unloading can instead result from wall friction in confined geometries and/or constitutive hysteresis due to microstructural changes, as has been observed experimentally for some soft porous media (*e.g.*, Hewitt et al., 2016b, Lutz et al., 2021, Sobac et al., 2011).

Through the analysis on the fluid flow at different fixed material points in the domain, we also showed that faster loading leads to an increasing delay in the interior of the domain relative to the motion of the left boundary. Although the motion of the fluid itself is reversible, these features are likely to have an important impact on irreversible phenomena. For example, these results have interesting implications for the deformation-driven transport and mixing of solutes, which we consider in detail Chapter 4.

The evolution of the stress at the left boundary as a function of the piston position revealed that, for faster loading and larger deformations, the force required to compress the medium is much larger than the force required to pull it back. This asymmetry occurs because the viscous drag associated with outflow compresses the medium against the outlet, reducing the permeability and resisting further fluid expulsion, whereas the viscous drag associated with inflow stretches the medium away from the outlet, increasing the permeability and easing further fluid influx.

Finally, we showed that a larger initial porosity $\phi_{f,0}$ leads to much lower fluid fluxes that can be accounted for by normalisation.

Our results elucidate the local and global poromechanical behaviour of soft porous media during periodic loading over a wide range of $\phi_{f,0}$, A, and T. Having used relatively generic constitutive models, we expect our qualitative insights to be robust across a wide range of media; however, it is straightforward to adapt our approach to other constitutive models (see Appendix A.1).

Chapter 4

Solute transport due to periodic loading in a soft porous medium

4.1 Introduction

In this chapter, we focus on the impact of large, periodic deformations on solute transport and mixing in porous media. These deformations — addressed in detail in Chapter 3 — drive solute transport through the poromechanical coupling in nontrivial ways.

In the context of deformation-driven solute transport, consolidation is the simplest loading case, and its impact on the transport of solutes is mostly studied in geomechanical applications (see for example, (Fox, 2007a,b, Pu et al., 2018)). In consolidation, solute spreading is enhanced by larger deformations (Lewis et al., 2009, Peters and Smith, 2002), with shorter breakthrough times observed for higher compressibility, fluid fraction, and degree of saturation (Alshawabkeh and Rahbar, 2006, Bonazzi et al., 2021, Zhang et al., 2013). In the presence of a viscous instability in a poroelastic medium, the transport of the invading fluid is also impacted by the deformations, resulting in a faster breakthrough for softer and more loosely packed media (Tran and Jha, 2020). These observations are limited to the non-periodic nature of consolidation and to timescales and loading parameters typical of soils. Fundamental differences between consolidation and periodic loading for solute transport are related to single flux contributions and their summation or competition in each (reversed) phase of the cycle. Hence, the same principles reported above need to be adapted to the context of periodic loading. This has been considered for aquifers, where chaotic advection due to periodic tidal phenomena enhances solute transport (Trefry et al., 2019, Wu et al., 2020) and, more generally, for small-deformation poroelasticity (Bonazzi et al., 2021), observing the impact of a limited range of frequencies on the final solute spreading. However, these studies linked the poromechanical coupling due to periodic loading to the global solute transport, while its local impact still needs to be characterised.

Periodic loading promotes the transport of solutes in biological tissues, (*e.g.*, DiDomenico et al., 2017, Ferguson et al., 2004, Gardiner et al., 2007, Schmidt et al., 2010, Witt et al., 2014, Zhang,

2011, Zhang and Szeri, 2008), hydrogels (Albro et al., 2008, Vaughan et al., 2013) and scaffolds for tissue engineering (Cortez et al., 2016, Fan et al., 2016, Kumar et al., 2018, Mauck et al., 2003). In these materials, increasing the loading amplitude and/or decreasing the loading period induces a transition from diffusion-dominated to advection-dominated regimes (Urciuolo et al., 2008) and a more prominent role of hydrodynamic dispersion (Sengers et al., 2004). A decreasing loading period also leads to localisation of flow and deformation near permeable boundaries, and the resulting higher velocity magnitudes near the surface in the case of faster loading have been correlated with higher solute spreading (DiDomenico et al., 2017, Gardiner et al., 2007, Urciuolo et al., 2008, Vaughan et al., 2013).

In general, despite the established role of hydrodynamic dispersion in driving the transport of solutes in porous media, dispersion is rarely included in biomechanical models. One context where dispersion is widely agreed to be important is brain microcirculation (Kelley and Thomas, 2023). In the network formed by the brain blood vessels, dispersion is a result of the shear-induced radial concentration gradients in single vessels (*e.g.* (Berg et al., 2020, Bojarskaite et al., 2023, Marbach and Alim, 2019, Sharp et al., 2019, Troyetsky et al., 2021)) and of the progressive bifurcation of each vessel in smaller branches (*e.g.* (Goirand et al., 2021, Zimmerman and Tartakovsky, 2020)). This network of vessels can be modelled at the continuum scale as an effective porous medium.

For other biological tissues or gels, dispersion is rarely considered, because of two main assumptions. First, fluid flow is often assumed to be slow, implying that transport mainly occurs via diffusion. However, the Péclet number, for tissues and gels subject to fast $(0.1 - 1Hz)$ and large $(10 - 20\%)$ deformations, is usually higher than 1 and hence already in the dispersion-dominated regime (Delgado, 2007). With an analogous argument, Davit et al. (2013) showed the importance of including dispersion in models for solute transport in biofilms. Furthermore, the advection-dominated regimes reported in literature (and cited above) are compared to diffusion-dominated regimes, *de facto* implying high fluid fluxes overcoming diffusive timescales. For completeness' sake, we provide examples of Péclet numbers for some examples of soft tissues and scaffolds for tissue engineering in Table 4.2. Following the general theories of transport in porous media, if the Péclet number is large enough to generate advection, then it also generates dispersion, assuming a large enough dispersivity α. The second argument against including dispersion in tissues and gels is based on α itself, assumed to be negligible. This is because, in granular materials, the dispersivity is generally scaled with the pore size (Kree and Villermaux, 2017, Liang et al., 2018, Oswald and Kinzelbach, 2004, Saffman, 1959), which is considered too small to originate dispersive phenomena in soft tissues and gels. Indeed, the pore size in the extracellular matrix of most tissues is small (for example, around 6 nm for cartilage (Mow et al., 1984)), and can be of the same size as large solute molecules (or smaller) (DiDomenico et al., 2018, Maroudas, 1970), originating solid-solute friction (Ateshian and Weiss, 2013, Yao and Gu, 2007). However, the presence of other components

in the tissues, such as collagen fibres, originates a "mesoscale" (Federico and Herzog, 2008a) of larger pores (100-150 nm in cartilage (Levick, 1987, Maroudas, 1975)), where even the larger solutes can pass (DiDomenico et al., 2017, 2018) and hence be subject to dispersion. This is true for double-porosity scaffolds and gels as well, where additional channels and/or macroscopic pores are included to enhance fluid-flow throughout the scaffold depth (Buijs et al., 2010, Lee et al., 2015, Mesallati et al., 2013). As a further argument, we hypothesise that, even in pores that are small compared to the solute molecules, the absence of velocity gradients in a single pore does not exclude velocity variations and streamline alterations in the overall network, which could originate longitudinal and transverse dispersion. This hypothesis is consistent with the quantification of tortuosity in several soft tissues (Hrabe et al., 2004, Maroudas, 1970, Zhang and Szeri, 2005).

To sum up, solute transport in periodically loaded highly-deformable porous media has been addressed with various approaches and assumptions. Although covering several types of soft porous media (soils, tissues, hydrogels, and scaffolds) and a range of loading frequencies and deformation magnitudes (small and large amplitudes), the majority of the available data refers to specific case studies. Moreover, the impact of hydrodynamic dispersion remains relatively unexplored and therefore poorly understood.

Here, we study the transport and mixing of solutes due to arbitrarily large, periodic deformations of a soft porous medium. For the flow and deformation, we adopt a one-dimensional, large-deformation poroelasticity model that includes rigorous nonlinear kinematics, deformation-dependent permeability and Hencky elasticity for the solid skeleton. In Chapter 3, we developed this model and used it to explore the poromechanics of large-amplitude periodic loading. Here, we introduce an additional model for solute transport, with contributions from advection, molecular diffusion, and hydrodynamic dispersion. A parameter study of how this complex coupling impacts each transport mechanism is necessary and still missing in the context of highly deformable porous media.

We begin by studying the individual evolution of advection, molecular diffusion, and hydrodynamic dispersion during one cycle of loading. We then consider the impact of several parameters on solute transport and mixing over longer time periods and/or larger number of loading cycles. Initially, we analyse the role of the transport coefficients, specifically diffusion and dispersion coefficients. We then focus on the loading parameters, which are responsible of tuning the material mechanical response, as explored in detail Chapter 3. In particular, we report the impact of a wide range of loading amplitudes and periods on each transport mechanism and observe how transport depends on the poromechanical response through its impact on local fluid flow.

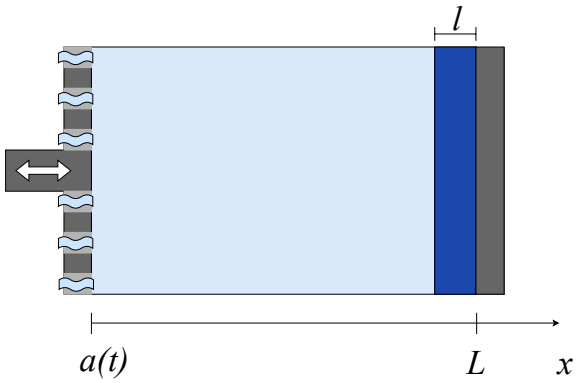

Figure 4.1: We consider a 1D sample of soft porous medium of relaxed length L, subject to a periodic, displacement-driven loading at its left boundary (white arrows). The left boundary is permeable, thus allowing fluid flow in or out (blue squiggles) to accommodate the loading. The solute is initially localised against the right boundary in a strip of width l (dark blue). We take the right boundary to fixed and impermeable.

4.2 Theoretical model

Our model combines large-deformation poroelasticity with solute transport and mixing. The coupling between periodic deformations and solute movement occurs primarily via the fluid flow, which is originated by the former and responsible for the latter.

4.2.1 Model problem

We consider the same one-dimensional sample of soft porous medium (of relaxed length L and relaxed porosity $\phi_{f,0}$) as described in Chapter 3. The poromechanics of this scenario are presented and analysed in detail in Chapter 3. We now introduce a strip of solute of initial width l located at the right boundary. In this chapter, we focus on the impact of this periodic, displacement-driven deformation on the evolution of the solute stripe (Figure 4.1).

4.2.2 Solute transport

We denote the true local solute concentration in the fluid phase by c (amount of solute per unit fluid volume). The solute is assumed to be passive and charge-neutral, with no chemical or other interaction with the solid and fluid phases, so that neither the fluid properties nor the solid properties depend on c. The flow and mechanics are then independent of the transport problem.

In 1D, conservation of mass for the solute can be written (*e.g.* (Scheidegger, 1961)):

$$\frac{\partial}{\partial t}(\phi_f c) + \frac{\partial}{\partial x}\left[\phi_f c v_f - \phi_f \mathcal{D}\frac{\partial c}{\partial x}\right] = 0. \tag{4.1}$$

The first term in the square brackets is the solute flux due to advection, which occurs here entirely in response to the deformation. The second term in the square brackets combines molecular diffusion

and hydrodynamic dispersion. These fluxes are weighted by the porosity ϕ_f since solute movements only occur in the fluid phase. The coefficient $\mathcal{D}$ can be written as:

$$\mathcal{D} = \mathcal{D}_m + \mathcal{D}_h, \tag{4.2}$$

where $\mathcal{D}_m$ and $\mathcal{D}_h$ are the coefficients of molecular diffusion and hydrodynamic dispersion, having taken the latter to be Fickian. Dispersion, in which pore-scale velocity gradients and the tortuosity of the pore space lead to macroscopic spreading of solute, depends sensitively on flow conditions and the details of the pore structure in ways that are not yet fully understood, even for rigid porous media (Dentz et al., 2018, 2023). The most widely used model for the macroscopic dispersive flux is Fickian, as above, with a velocity-dependent dispersion coefficient given by (Brenner and Edwards, 1993, Gelhar, 1993, Whitaker, 1998)

$$\mathcal{D}_h = \alpha|v_f - v_s|, \tag{4.3}$$

where α is the longitudinal dispersivity. Note that $\mathcal{D}_h$ is proportional to $|v_f - v_s|$, unlike advection, because dispersion is driven by flow of fluid through the pore structure (if $v_f = vs \neq 0$, there will be advection but no dispersion). Note also that the sign of the advective flux depends on the direction of the flow, whereas the signs of the diffusive and dispersive fluxes do not. Note finally that α is typically taken to be a constant material property for a given pore structure. In a deforming porous medium, and particularly for moderate to large deformations, it is likely that α should be deformation-dependent to account for the evolving pore structure. However, this coupling has not yet been studied, and will be the subject of future work. Here, we take α to be constant for simplicity.

4.2.3 Initial and boundary conditions

Here we recall initial and boundary conditions for the solid skeleton and the fluid (which are the same as in Chapter 3) and specify them for the solute. Recall that the left and right boundaries of the solid are at $x = a(t)$ and $x = L$, respectively, with $a(0) = 0$.

4.2.3.1 Initial conditions

Equation (3.1), implies that $a(0) = 0$, and thus that the initial porosity is uniform and equal to the relaxed porosity, with the fluid and solid initially at rest:

$$\phi_f(x, 0) = \phi_{f,0} \text{ and } u_s(x, 0) = v_f(x, 0) = v_s(x, 0) = 0. \tag{4.4}$$

We take the solute to be initially localised against the right boundary in a strip of width l and concentration c_0, such that

$$c(x, 0) = \frac{c_0}{2} \left\{ \tanh \left[s(x - L + l) \right] + 1 \right\}, \tag{4.5}$$

where s is a steepness parameter.

4.2.3.2 Left boundary

For $t > 0$, the boundary conditions applying the displacement-controlled loading at the left boundary are

$$u_s(a,t) = a(t), \quad \text{and} \quad v_s(a,t) = \frac{\mathrm{d}a}{\mathrm{d}t} \quad \text{and} \quad p(a,t) = 0. \tag{4.6}$$

We take the fluid outside of the domain to be "clean", such that

$$c(a,t) = 0. \tag{4.7}$$

4.2.3.3 Right boundary

The right boundary is fixed and impermeable, which implies

$$u_s(L,t) = v_s(L,t) = v_f(L,t) = 0 \quad \text{and} \quad \left.\frac{\partial c}{\partial x}\right|_{x=L} = 0. \tag{4.8}$$

4.2.4 Scaling and summary

For the poromechanics, we apply the same non-dimensionalization as in Chapter 3 (see Equation (3.22)) We scale quantities related to solute transport as

$$\tilde{c} = \frac{c}{c_0},\ \tilde{l} = \frac{l}{L},\ \tilde{\alpha} = \frac{\alpha}{L}. \tag{4.9}$$

We report here full problem in dimensionless form, with

$$\frac{\partial \phi_f}{\partial \tilde{t}} - \frac{\partial}{\partial \tilde{x}}\left[\tilde{D}_f(\phi_f)\frac{\partial \phi_f}{\partial \tilde{x}}\right] = 0, \tag{4.10}$$

where $\tilde{D}_f$ is the nonlinear-poroelastic diffusivity

$$\tilde{D}_f = \frac{D_f}{D_{f,0}} = (1-\phi_f)\tilde{k}(\phi_f)\frac{\mathrm{d}\tilde{\sigma}'}{\mathrm{d}\phi_f}, \tag{4.11}$$

and

$$\frac{\partial}{\partial \tilde{t}}(\phi_f \tilde{c}) + \frac{\partial}{\partial \tilde{x}}\left[\phi_f \tilde{c}\tilde{v}_f - \phi_f \mathrm{Pe}^{-1}\tilde{\mathcal{D}}\frac{\partial \tilde{c}}{\partial \tilde{x}}\right] = 0. \tag{4.12}$$

The scaled coefficient $\tilde{D}$ reads:

$$\tilde{\mathcal{D}} = \frac{\mathcal{D}}{\mathcal{D}_m} = 1 + \tilde{\alpha}\mathrm{Pe}|\tilde{v}_f - \tilde{v}_s|, \tag{4.13}$$

where $\mathrm{Pe} = \frac{L^2/T_{\mathrm{pe}}}{\mathcal{D}_m} = \frac{k_0\mathcal{M}}{\mu\mathcal{D}_m}$ is the Péclet number, which quantifies the importance of deformation-driven advection relative to molecular diffusion. The initial conditions are:

$$\tilde{a}(0) = 0,\ \phi_f(\tilde{x},0) = \phi_{f,0},\ \tilde{v}_f(\tilde{x},0) = \tilde{v}_s(\tilde{x},0) = 0, \tag{4.14}$$

and

$$\tilde{c}(\tilde{x},0) = \frac{1}{2}\{\tanh\left[\tilde{s}(\tilde{x} - 1 + \tilde{l})\right] + 1\}, \tag{4.15}$$

where we have taken $\tilde{s} = sL = 60$. The left boundary conditions are

$$\tilde{u}_s(\tilde{a},\tilde{t}) = \tilde{a}(\tilde{t}) = \frac{\tilde{A}}{2}\left[1 - \cos\left(\frac{2\pi\tilde{t}}{\tilde{T}}\right)\right], \; \tilde{v}_s(\tilde{a},\tilde{t}) = \frac{\mathrm{d}\tilde{a}}{\mathrm{d}\tilde{t}}, \quad \tilde{p}(\tilde{a},\tilde{t}) = 0, \text{ and } \quad \tilde{c}(\tilde{a},\tilde{t}) = 0, \tag{4.16}$$

and the right boundary conditions read

$$\tilde{u}_s(1,\tilde{t}) = \tilde{v}_s(1,\tilde{t}) = \tilde{v}_f(1,\tilde{t}) = 0, \quad \text{and } \left.\frac{\partial\tilde{c}}{\partial\tilde{x}}\right|_{\tilde{x}=1} = 0. \tag{4.17}$$

where $\tilde{A} = A/L$ and $\tilde{T} = T/T_{\mathrm{pe}}$. Below, we consider only dimensionless quantities, dropping the tildes for convenience.

The above 1D model describes flow, mechanics, and solute transport in a poroelastic medium subject to periodic deformations. The kinematics are rigorous and nonlinear, the elasticity law is Hencky elasticity, and the permeability law is the Kozeny-Carman formula. Solute transport occurs via advection, molecular diffusion, and hydrodynamic dispersion.

Below, we solve this system numerically in MATLAB as described in Appendix A.7.

4.3 Solute transport and mixing

4.3.1 Quantification of solute transport and mixing

We begin with some qualitative examples that illustrate the contribution of each transport mechanism. We then assess solute transport and mixing quantitatively via two metrics:

1. the travel distance (or mixing length) δ, which is the distance travelled by the left edge of the concentration profile (Figure 4.2).

2. the degree of mixing χ, which measures the degree of homogenisation and is related to the spatial variance of the concentration profile about its center of mass. χ can range from 0 to 1, where the former corresponds to no mixing (typical of the initial state) and the latter is characteristic of a completely mixed configuration. Following the analysis of Jha et al. (2011), we express the degree of mixing in terms of the variance of the solute concentration. Considering the weighted average $\langle * \rangle_{\phi_f}$ defined as

$$\langle * \rangle_{\phi_f} = \frac{\int \phi_f * \,\mathrm{d}x}{\int \phi_f \,\mathrm{d}x}, \tag{4.18}$$

the variance of the concentration profile is

$$\sigma^2(t) = \langle c^2 \rangle_{\phi_f} - \langle c \rangle^2_{\phi_f}. \tag{4.19}$$

Our definition of the spatial averaging and $\sigma^2(t)$ are the generalised form of those defined in (Jha et al., 2011), allowing us to define the degree of mixing as

$$\chi(t) = 1 - \frac{\sigma^2(t)}{\sigma^2_{\max}}, \tag{4.20}$$

where $\sigma^2_{\max} = \sigma^2(t=0)$ in this case.

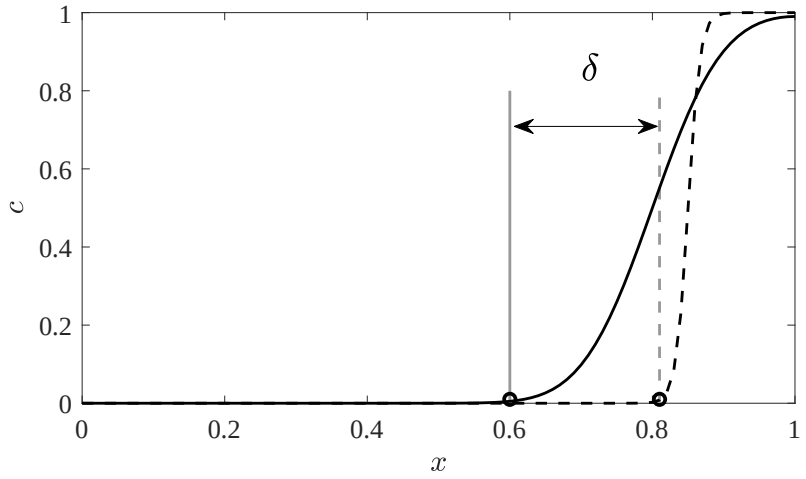

Figure 4.2: Schematic representation of the mixing length δ, which measures the distance traveled by the left edge of the concentration profile during the time t. We adopt the most suitable definition when the solute is initially localised in a finite strip (see, for example, (Tan and Homsy, 1988) or (Mishra et al., 2008)), and calculate $\delta(t)$ by choosing a small threshold concentration c_δ and then finding the leftmost position $x_{\delta(t)}$ where that concentration occurs. Then, $\delta(t) = |x_{\delta(t)} - x_{\delta(0)}|$. Here, we show $c(x, 0)$ (dashed curve), $c(x, t)$ (solid curve), and the corresponding $\delta(t)$. In the results shown below, we take $c_\delta = 0.01$.

4.3.2 Qualitative impacts of periodic loading on solute transport

We begin by isolating and comparing the solute transport mechanisms. To illustrate the contribution of each mechanism, we plot the corresponding fluxes at $x = 1 - l$, which is the initial left edge of the concentration profile, during five loading cycles in the slow-loading regime (Figure 4.3). During loading, the three fluxes all have the same sign, implying that the solute is carried in the same direction (to the left) by all of the mechanisms. During unloading, however, the flow changes direction and the advective flux changes sign (now to the right), whereas the diffusive and dispersive fluxes do not (still to the left). As a result, the amount of net transport depends on the difference between advection and the diffusive and dispersive fluxes. The contribution from diffusion and dispersion is very strong at early times and quickly fades, as the initially sharp concentration gradient fades.

We next plot the evolution of the full concentration profile during one cycle (Figure 4.4). We split the cycle into two phases, loading and unloading, and plot four intermediate times for each. We consider four cases: molecular diffusion only, in which $A = 0$ (no loading); advection only, in which $\mathrm{Pe}^{-1} = \alpha = 0$; advection and molecular diffusion only, in which $\alpha = 0$; and the general case, including all the mechanisms. The case of diffusion only (Figure 4.3, top left) involves no deformation, such that solute spreading is driven only by concentration gradients and $\delta \propto \sqrt{t}$. When a deformation is applied (which is the case for all the other three panels), two main factors impact the movement of the solute: the velocity of the fluid and solid phases, driving advection and

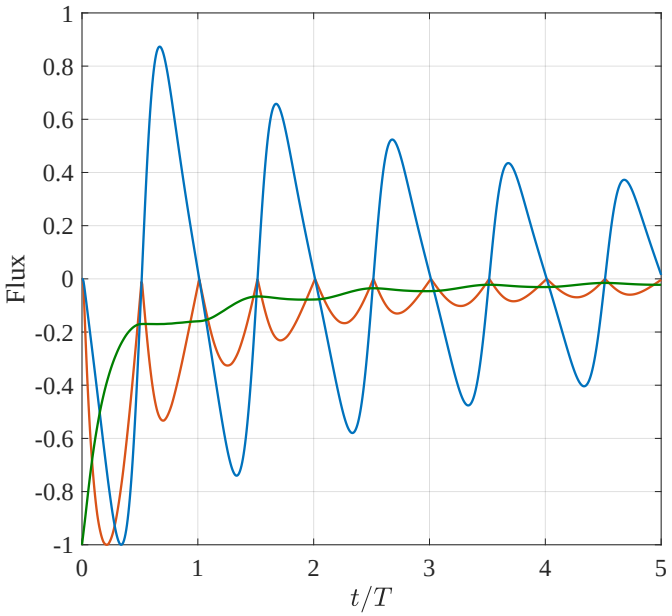

Figure 4.3: Magnitudes of the three fluxes regulating solute transport — advection (blue), molecular diffusion (green), and hydrodynamic dispersion (red) — at $x = 0.95$ over 5 loading cycles. The parameters are: $A = 0.4, T = 6\pi, \alpha = 0.025, \mathrm{Pe}^{-1} = 10^{-5}$. Note that A and α are chosen to be higher than in the rest of the simulations to better illustrate the role of dispersion.

hydrodynamic dispersion, and the changing porosity ϕ_f, which is a weighting factor for diffusion and dispersion. When the domain is squeezed, the porosity decreases, thus inducing two main effects: (i) each transport mechanism is weighted by a lower factor; (ii) the solute profile spreads, since the same quantity of fluid (and solute) must now occupy a larger macroscopic area, thus weakening concentration gradients. These phenomena reverse during unloading. The latter phenomenon is most obvious in the case of advection only (Figure 4.3, top right), where the motion of the solute is perfectly reversible and $\delta = 0$ at the end of the loading cycle. Hence, loading weakens molecular diffusion (Figure 4.3, bottom left), because the diffusive flux is proportional to (i) the current fluid fraction ϕ_f and (ii) the concentration gradient $\frac{\partial c}{\partial x}$, both of which decrease due to compression. The impact of the deformation on diffusion is also visible in Figure 4.3, where the diffusive flux exhibits weak oscillations rather than decreasingly smoothly and monotonically. As a result, the final travel distance δ is higher for the case of diffusion only (no loading) than during periodic loading without dispersion. When dispersion is included (Figure 4.3, bottom right), transport is greatly amplified by dispersion despite the weak suppression of diffusion, because loading induces high fluid velocities, counterbalancing the effect.

We next consider several quantitative measures of transport and mixing.

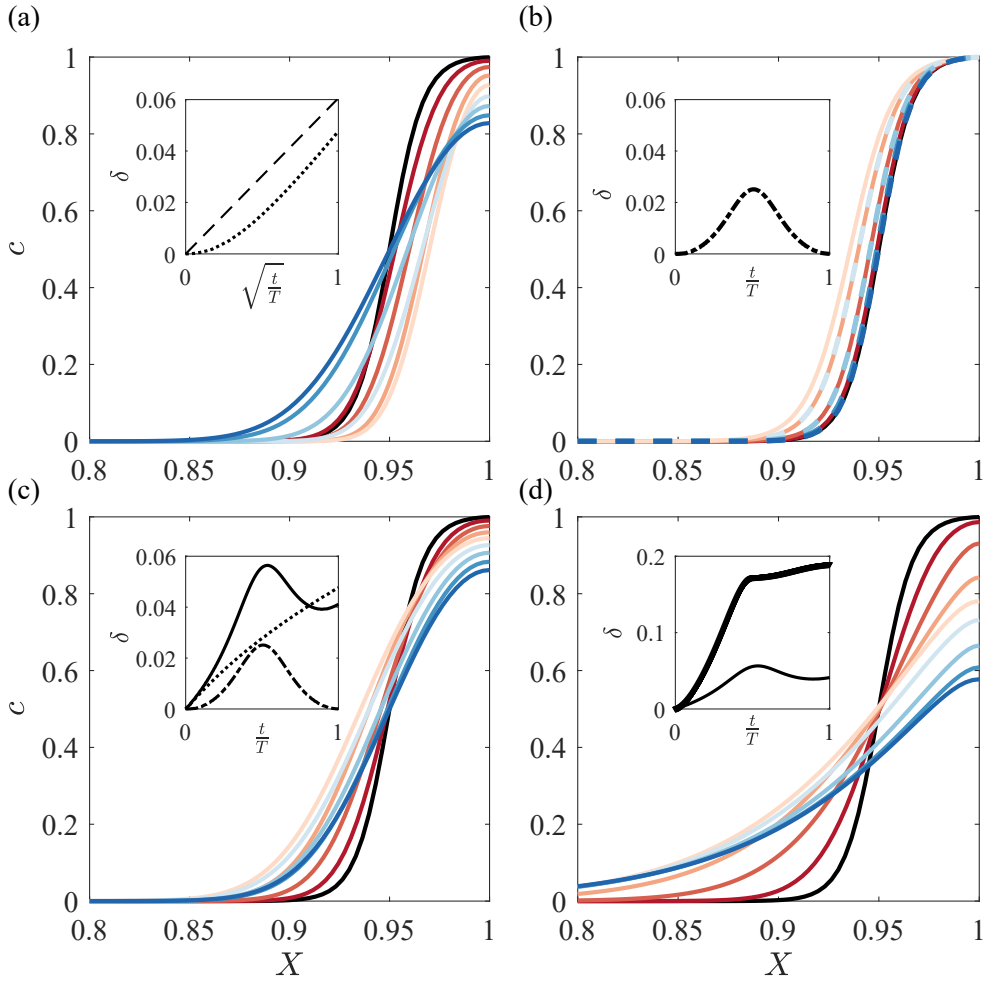

Figure 4.4: Evolution of the concentration profile during one cycle (red to blue) for four cases: (a) molecular diffusion with no loading ($A = \alpha = 0, \mathrm{Pe}^{-1} = 3 \times 10^{-5}$); (b) advection only ($A = 0.4, \mathrm{Pe}^{-1} = \alpha = 0$); (c) advection and molecular diffusion ($A = 0.4, \mathrm{Pe}^{-1} = 3 \times 10^{-5}, \alpha = 0$); (d) advection, molecular diffusion, and hydrodynamic dispersion ($A = 0.4, \mathrm{Pe}^{-1} = 3 \times 10^{-5}, \alpha = 0.025$). We split the evolution into two phases, loading (first half of the cycle, dark to light red) and unloading (second half, light to dark blue). The initial profile is shown in black. For each case, we also show the evolution of δ throughout the loading cycle (insets), where the dotted curves are diffusion only (with the dashed reference line to show the linearity with $\sqrt{t/T}$), the dash-dot curves are advection only, the thinner black curves advection and diffusion, and the thick black curve is advection, diffusion, and dispersion. All four cases are for $T = 6\pi$. Note that A and α are chosen to be higher than in the rest of the simulations, to better illustrate the role of dispersion.

Parameter	Baseline value	Other values examined
Pe^{-1}	3×10^{-5}	3×10^{-8}, 3×10^{-6}, 3×10^{-4}.
α	10^{-2}	10^{-5}, 10^{-3}, 10^{-1}.

Table 4.1: Summary of the values of the coefficients explored.

4.3.3 Impact of diffusion and dispersion coefficients on transport and mixing

In general, δ and χ depend on (i) the loading parameters, and (ii) the properties that characterise the specific coupling between the solutes and medium, specifically the coefficients regulating hydrodynamic dispersion and molecular diffusion, α and Pe^{-1}; the initial value of the porosity in the domain, $\phi_{f,0}$; the initial total width of the solute strip l. In this section, our goal is to isolate the role of α and Pe^{-1}. For this reason, we restrict our analysis to the slow-loading case, fixing $A = 0.1$, $T = 6\pi$, $\phi_{f,0} = 0.75$ and $l = 0.05$, and consider 5 loading cycles. We study the impact of $\phi_{f,0}$ and l on δ and χ in Appendix A.6.

The scaled values of dispersion and diffusion coefficients explored are in the range of those proposed by Sengers et al. (2004) for cartilage constructs. We define a baseline case by specifying values for α and Pe^{-1}, as reported in Table 4.1. This baseline case also fixes the parameters used in Section 4.3.4. Note that this baseline is arbitrary, and is chosen to ensure that, in the slow-loading regime, diffusion is stronger than dispersion. In fast-loading, the values of α and Pe^{-1} chosen for the baseline lead to dispersion-dominated regimes. We quantify the predominance of either mechanism on the other one using the flux ratio $q_{\mathrm{disp}}/q_{\mathrm{diff}}$ which we define in Section 4.3.4. The cases for lowest and highest $q_{\mathrm{disp}}/q_{\mathrm{diff}}$ in the whole parametric study are reported in Appendix A.5.

The effect of changing the two coefficients, Pe^{-1} for molecular diffusion and α for hydrodynamic dispersion, are shown in Figure 4.5 and 4.6, respectively. All the curves are oscillatory, with maxima at the highest-compression states and minima in the relaxed states. The observed fluctuations are related to the two phenomena described in the first qualitative analysis in Section 4.3.2 (alterations in domain porosity and changes in the direction of the advective flux during compression and relaxation) that indicate, overall, how the solute transport is linked to the deformation. For both constants, higher values promote the spreading and mixing of the solute. This behaviour is expected, since higher coefficients enhance the respective fluxes. In both cases, moreover, below a certain value of each parameter curves are not significantly altered; this is again as anticipated, since the formulation $\mathrm{Pe}^{-1} + \alpha|v_f - v_s|$ shows that, as one of the two coefficients becomes negligible, the other mechanism dominates. Note that enhancing one of these constants while suppressing the other provides a tool to isolate the effect of hydrodynamic dispersion or molecular diffusion while keeping the advective fluxes active.

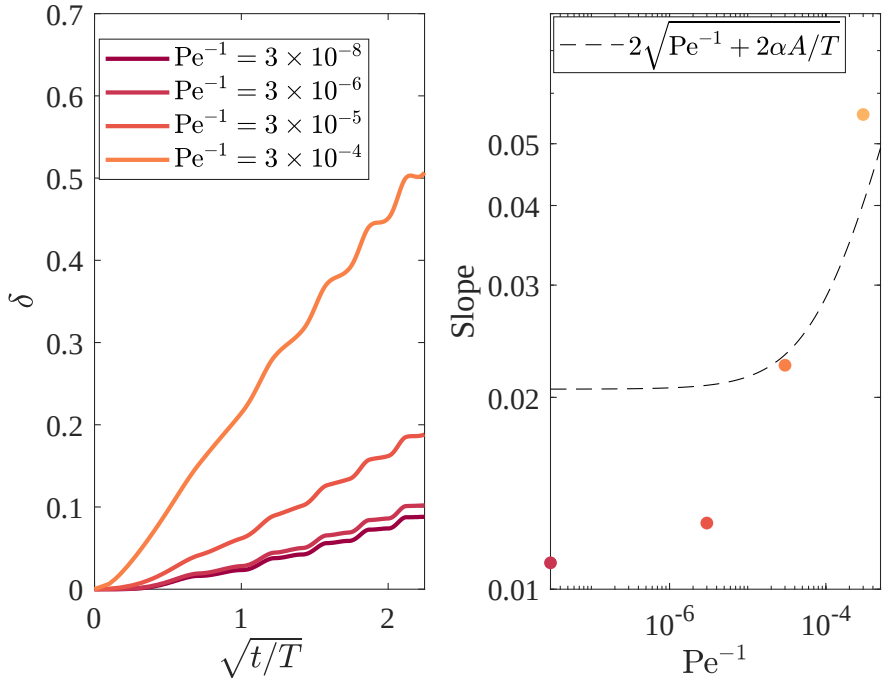

Figure 4.5: Left: impact of Pe^{-1} on the evolution of δ with t. Right: slope of each of the curves showed on the left as a function of Pe^{-1}. The black dashed line shows an approximate theoretical prediction of the slope.

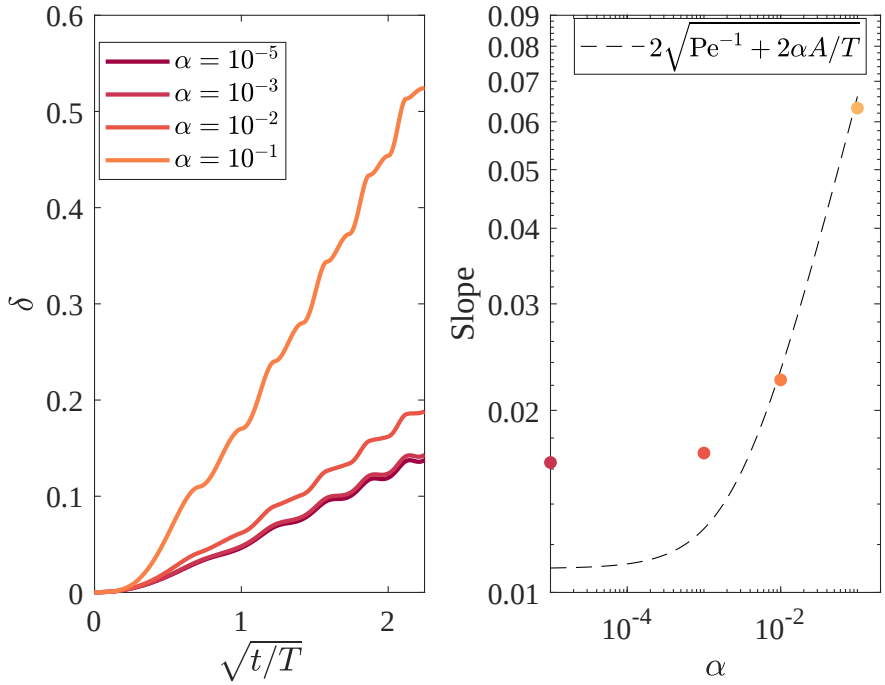

Figure 4.6: Left: impact of α on the evolution of δ with t. Right: slope of each of the curves showed on the left as a function of α. The black dashed line shows an approximate theoretical prediction of the slope.

4.3.4 Quantitative impacts of periodic loading on solute transport

Since our goal in this part is to describe the effects of the loading parameters A and T, we fix Pe^{-1}, α, $\phi_{f,0}$ and l to baseline values (Table 4.1) for the material parameters. To help interpret these results, we first provide a summary of the key findings of Chapter 3 before proceeding to analyse solute transport and mixing.

Poromechanical response to periodic loading

As reported extensively in Chapter 3, during slow loading ($T \gg 1$), the deformation has time to propagate throughout the medium and the response is quasi-static for any amplitude. The porosity is uniform in space through the cycle, returning to its undeformed value at the end of each cycle. During fast loading ($T \ll 1$), the timescale of the applied deformation is faster than the response of the medium. The deformation is nonuniform in space and increasingly localised near the left (permeable) boundary as the period decreases. The left portion of the domain experiences both compression and tension, while the right portion is in compression at all times. For very fast loading, the deformation is entirely localised near the left boundary and right portion of the medium is in static compression. As the amplitude of the deformation increases, the change in porosity at the left boundary with respect to the relaxed state becomes increasingly asymmetric, with a larger decrease in porosity (compression) during loading than the respective increase (tension) during unloading.

This behaviour impacts solute transport through the motion of the fluid and through the changes in porosity, as discussed above. To analyse the fluid flow, we recall a convenient scaling quantity:

$$q_f^* = \phi_{f,0} v_f^* = (1 - \phi_{f,0}) \frac{2A}{T}, \tag{4.21}$$

which is appropriate to normalise the fluid flux q_f. Moreover, we define the ratio between dispersive and diffusive fluxes

$$\frac{q_{\text{disp}}}{q_{\text{diff}}} = \alpha \text{Pe} |v_f - v_s|, \tag{4.22}$$

which is useful to understand the relative importance of these two mechanisms.

In Figure 4.7, we show the impact of T on the normalised fluid flux q_f/q_f^* (driving advection) and on the ratio between the dispersive and diffusive flux $q_{\text{disp}}/q_{\text{diff}}$ for a fixed (large) amplitude A. In Figure 4.8, we show the impact of A for a fixed (fast) period $T = 0.1\pi$. As should be expected, the fluid flux exhibits localisation for fast loading and asymmetry in loading and unloading for large amplitudes. For $q_{\text{disp}}/q_{\text{diff}}$, the strength of dispersion relative to diffusion scales like A/T, through their impact on v_f and v_s (see (4.22)).

Solute transport for different loading amplitude and period

We showed in 4.3.2 how the three transport mechanisms act individually on the initial concentration profile. We now expand this analysis to understand the role of A and T. In Figure 4.9, we show

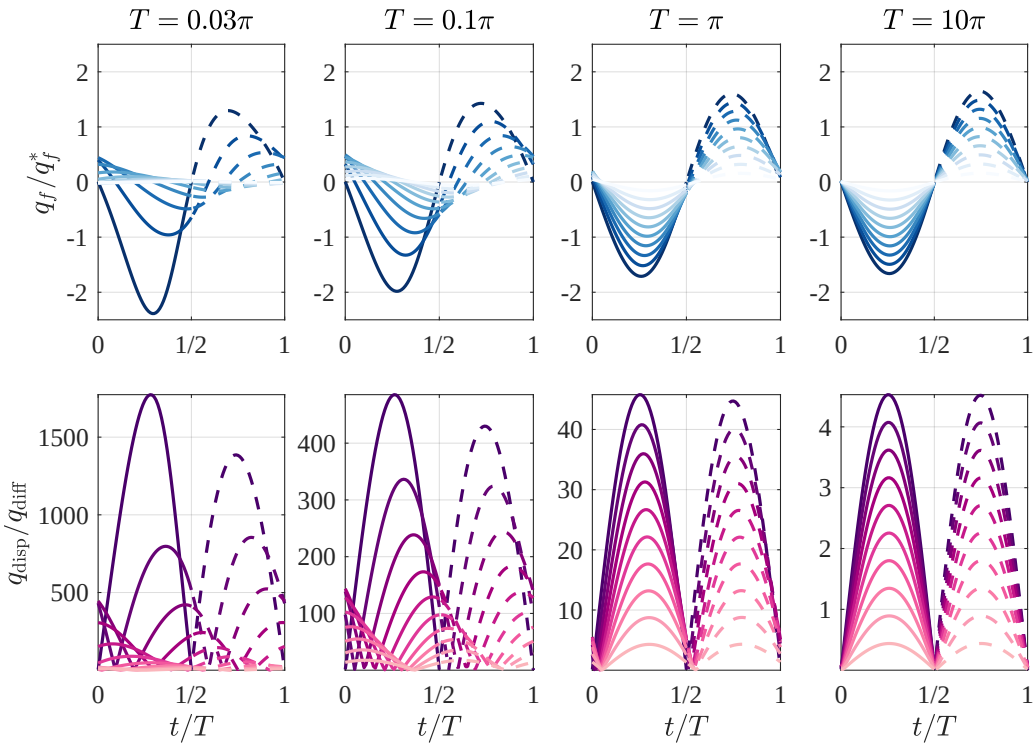

Figure 4.7: Normalised fluid flux q_f/q_f^* (first row) and $q_{\mathrm{disp}}/q_{\mathrm{diff}}$ (second row) against t for ten different values of X from 0 to 1 (dark to light) during one cycle in the periodic regime for $A = 0.1$, $\phi_{f,0} = 0.75$, and four different values of T (columns). We distinguish between the loading half of the cycle ($\dot{a} > 0$; solid curves) and the unloading half of the cycle ($\dot{a} < 0$; dashed curves).

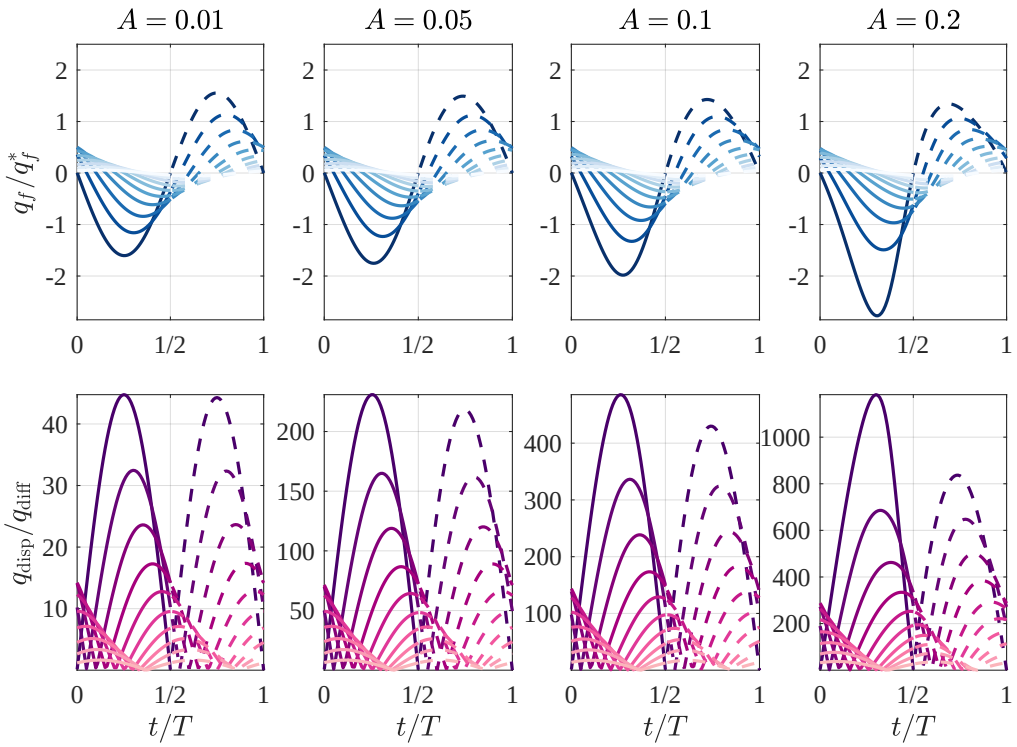

Figure 4.8: Normalised fluid flux q_f/q_f^* (first row) and $q_{\mathrm{disp}}/q_{\mathrm{diff}}$ (second row) against t for ten different values of X from 0 to 1 (dark to light) during one cycle in the periodic regime for $T = 0.1\pi$, $\phi_{f,0} = 0.75$, and four different values of A (columns). We distinguish between the loading half of the cycle ($\dot{a} > 0$; solid curves) and the unloading half of the cycle ($\dot{a} < 0$; dashed curves).

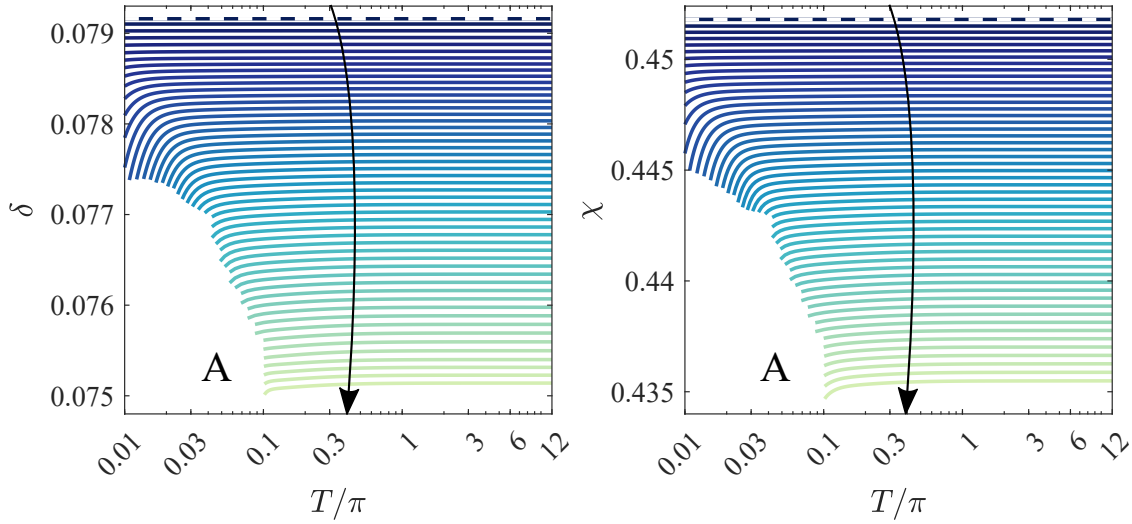

Figure 4.9: Travel distance (left) and degree of mixing (right) after a total loading observation time $t_{\text{tot}} = t_{\text{l}} + t_{\text{r}} = 12\pi + 1$ for several combinations of A and T with advection and molecular diffusion ($\alpha = 0$). Amplitudes are equally spaced from $A = 0.004$ to $A = 0.2$ (dark to light), while periods are selected to ensure an integer number of loading cycles. This constraint leads to periods ranging from $T = 0.01\pi$ applied for 1200 cycles to $T = 12\pi$ applied for 1 cycle. Dashed lines correspond to the diffusion only case ($A = 0$). Note that the minimum porosity in the domain occurs near the piston and is a monotonically decreasing function of T; each curve here ends on the left at the period for which the porosity at the piston vanishes and the simulations fail.

the travel distance δ and the degree of mixing χ when only advection and molecular diffusion are active ($\alpha = 0$) and over a wide range of T — from fast to slow loading — and for several values of A — from small to large deformations. In Figure 4.11, we consider the same parameter space, this time adding the contribution of hydrodynamic dispersion. In both cases, we fix the total observation time to $t_{\text{tot}} = t_{\text{l}} + t_{\text{r}} = 12\pi + 1$: we apply the periodic load for $t_{\text{l}} = 12\pi$ and, after the last cycle, we let the system relax for $t_{\text{r}} = 1$, so that the material is in a relaxed (rather than deformed) state at the moment when δ and χ are evaluated.

During one loading cycle, we illustrated in 4.3.2 that the contribution of advection is reversible, independently of A and T. However, the loading amplitude and period affect the fluid content and distribution, altering the stretching of the solutes and consequently the concentration gradients. Hence, molecular diffusion and hydrodynamic dispersion are expected to vary with A and T. Firstly, the loading parameters affect the porosity. During the loading time, ϕ_f is on average lower than the initial value $\phi_{f,0}$, because the loading has a non-zero mean — the medium is on average compressed. The average porosity $\langle\overline{\phi}\rangle$ over m cycles depends on A and is given by:

$$\langle\overline{\phi_f}\rangle = \frac{1}{mT}\int_{nT}^{(n+m)T} \langle\phi_f\rangle \, \mathrm{d}t = 1 - \frac{1-\phi_{f,0}}{\sqrt{1-A}}, \tag{4.23}$$

as we noted in Chapter 3. Note that $\langle\overline{\phi}\rangle$ decreases with A but is independent of T. We expect

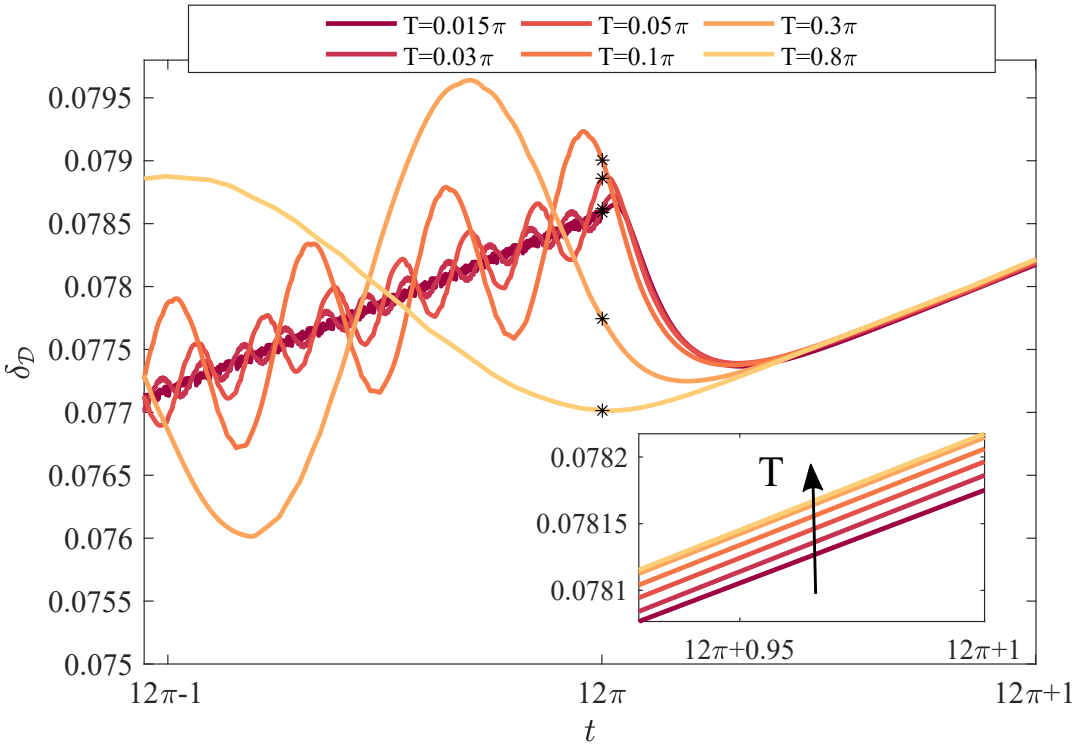

Figure 4.10: Evolution of δ over time at the end of a long series of cycles for six values of the shortest T considered, ranging from $T = 0.15\pi$ to $T = 0.8\pi$, with only advection and molecular diffusion. The inset panel focuses on the very last portion of the plot above for visual clarity. Black stars mark the end of the last cycle of periodic loading and the beginning of the medium relaxation to the undeformed state.

smaller values $\langle\overline{\phi}\rangle$ to suppress transport and mixing both directly, by decreasing the porosity, and indirectly, by stretching the concentration gradients, as noted above. Figure 4.9 shows that δ and χ decrease weakly with A and are essentially independent of T for all but the smallest values of T, as expected. Note that, for moderately large amplitudes and very short periods, both δ and χ decrease with T. This effect is not related to $\langle\overline{\phi}\rangle$, which is independent of T. We explore this behaviour in Figure 4.10 by plotting the evolution of δ over time for a fixed amplitude $A = 0.06$ and for several values of T between $T = 0.015\pi$ and $T = 0.8\pi$. For the slowest case ($T = 0.8\pi$), δ is minimum at the end of the loading time $t_\mathrm{l} = 12\pi$ (marked by a black star) and then increases due to diffusion during the relaxation time $t_\mathrm{r} = 1$. For smaller values of T, δ initially decreases during t_r. This drop is due to the additional constant state of compression induced for very fast loading (*e.g.*, $T \lesssim 0.1\pi$). Since the deformation is faster than the medium response, the domain is never fully relaxed while subject to the cyclic loading, and the effective periodic deformation is summed to a state of constant compression, which contributes to an additional stretch of the concentration gradients and further suppresses solute movements. Once the loading stops, the additional relaxation and the consequent reimbibition of fluid slow down the spreading of the solutes, with a decrease in δ that is stronger

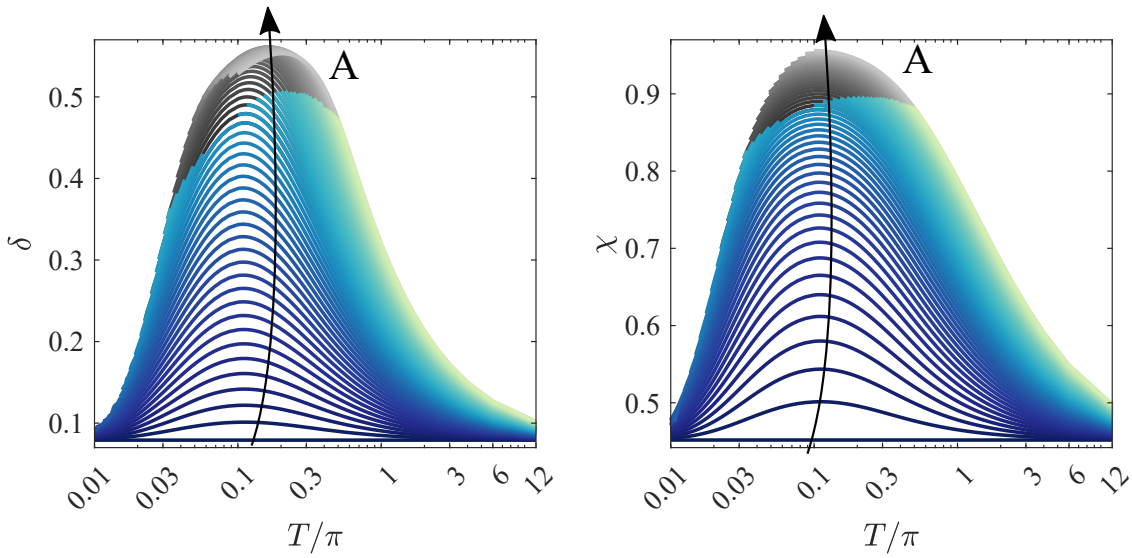

Figure 4.11: Travel distance (left) and degree of mixing (right) against A (increasing dark to light) and T with all three transport mechanisms simultaneously active (with $\mathrm{Pe}^{-1} = 3 \times 10^{-}5$ and $\alpha = 0.01$). Amplitudes and periods are the same as in Figure 4.9. Portions shown in grey-scale indicate simulations where the solute reaches the left boundary and begins to leave the domain.

and longer for a higher state of additional compression.

We next repeat this analysis, but now including hydrodynamic dispersion with $\alpha = 0.01$ (Figure 4.11). Both δ and χ are greatly enhanced by dispersion relative to the results in Figure 4.9 in all regions of the plot. Lower values of δ and χ occur in the SL regime, defined by periods approximately larger than π. When approaching FL (for $T \lesssim \pi$, from right to left in the plot), as the deformation gets faster and larger, the spreading and mixing of the solutes noticeably increase, until a peak is reached for $T \approx 0.1\pi$. Note that the values of δ in the peak region are almost one order of magnitude larger than without dispersion (Figure 4.9). For $T \lesssim 0.1\pi$, δ and χ decrease as T decreases. Across the full range of T, δ and χ increase with A. This trend can be linked to the impact of A and T on the advective flux q_f and on the ratio between the dispersive and diffusive flux $q_{\mathrm{disp}}/q_{\mathrm{diff}}$, shown in Figure 4.7 and 4.8. For large values of T (*e.g.* Figure 4.7, fourth column), the deformation is uniform and very slow, and $q_{\mathrm{disp}}/q_{\mathrm{diff}}$ is low, especially towards the right (lighter lines), where the solute is positioned. Diffusion dominates over dispersion, even with a large amplitude ($A = 0.1$). As T decreases (*e.g.* Figure 4.7, third and second columns), $q_{\mathrm{disp}}/q_{\mathrm{diff}}$ progressively increases. In fast-loading, the entire domain is characterised by a very high $q_{\mathrm{disp}}/q_{\mathrm{diff}}$, and thus, large values of δ and χ. For even faster loading periods, however, the deformation is increasingly localised at the left boundary: Figure 4.7 (first column), shows that both q_f/q_f^* and $q_{\mathrm{disp}}/q_{\mathrm{diff}}$ are orders of magnitude larger at the left boundary (darkest curves) than near the right boundary (lightest curves). Therefore, the region occupied by the solutes is increasingly not engaged in the deformation: as T further decreases δ and χ converge back toward their diffusion-only values. These observations are

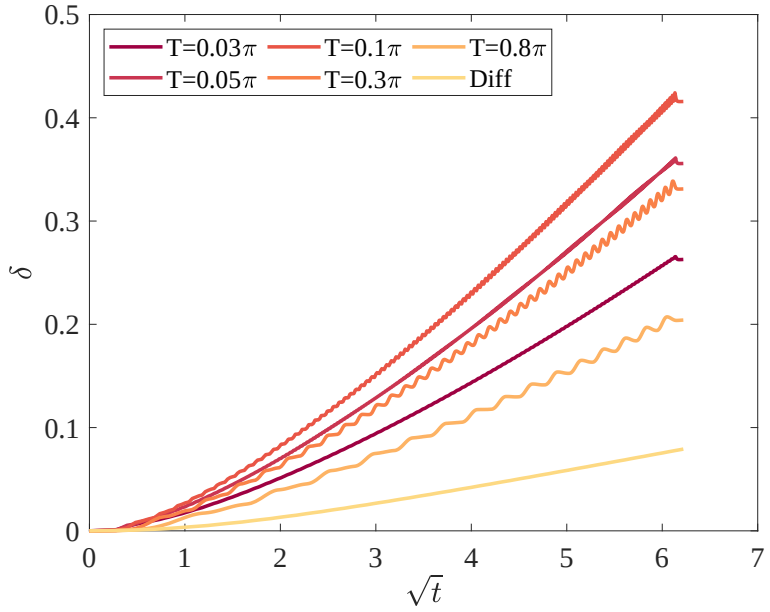

Figure 4.12: Evolution of δ over the entire loading time for $A = 0.06$ and for five values of T, as indicated, when advection, molecular diffusion and hydrodynamic dispersion are simultaneously active. We also show the case of diffusion only (no loading, lightest curve).

examined in more detail in Figure 4.12, where we plot the evolution of δ throughout the loading time for a fixed amplitude and for several periods between $T = 0.03\pi$ and $T = 0.8\pi$, thus covering the region crossing the peak. In all cases, delta exhibits oscillations on top of a roughly diffusive growth. As T decreases, the magnitude of the oscillations that δ experiences progressively decreases, consistent with the deformation being increasingly localised at the left. Hence, for the fastest cases, (*e.g.*, $T < 0.1\pi$), the final value of δ decreases as T decreases.

In Figure 4.13, we isolate the impact of loading amplitude and period on δ and χ normalising them by the respective values of A/T. Note that, to isolate the role of dispersion, we subtract the respective values of δ_D and χ_D — calculated for the case of advection-diffusion only (plotted in Figure 4.9). For $T \gtrsim \pi$, normalised values collapse. In this regime, the simple nature of the flow and deformation suggests that dispersion scales approximately as A/T. For $T \lesssim 0.1\pi$, the normalised values of $\delta - \delta_D$ and $\chi - \chi_D$ depend on T. The suppressed spreading in this region is due to the increasing localisation as T decreases. Following our results in Chapter 3, we report here the analytical solution for the Darcy flux in response to very fast loading (in the limit of linear poroelasticity, from Stokes's classical "second problem"):

$$\phi_f |v_{f,\mathrm{vf}} - v_{s,\mathrm{vf}}|(x,t) = -v_{s,\mathrm{vf}}(x,t) = -\frac{\pi A}{T}\left[\exp\left(-x\sqrt{\frac{\pi}{T}}\right)\sin\left(\frac{2\pi t}{T} - x\sqrt{\frac{\pi}{T}}\right)\right], \tag{4.24}$$

where the subscript ("vf") stands for "very fast" ($T \ll 1$). Equation (4.24) suggests that, in this regime, the amplitude of the Darcy flux decays exponentially with distance from the left boundary,

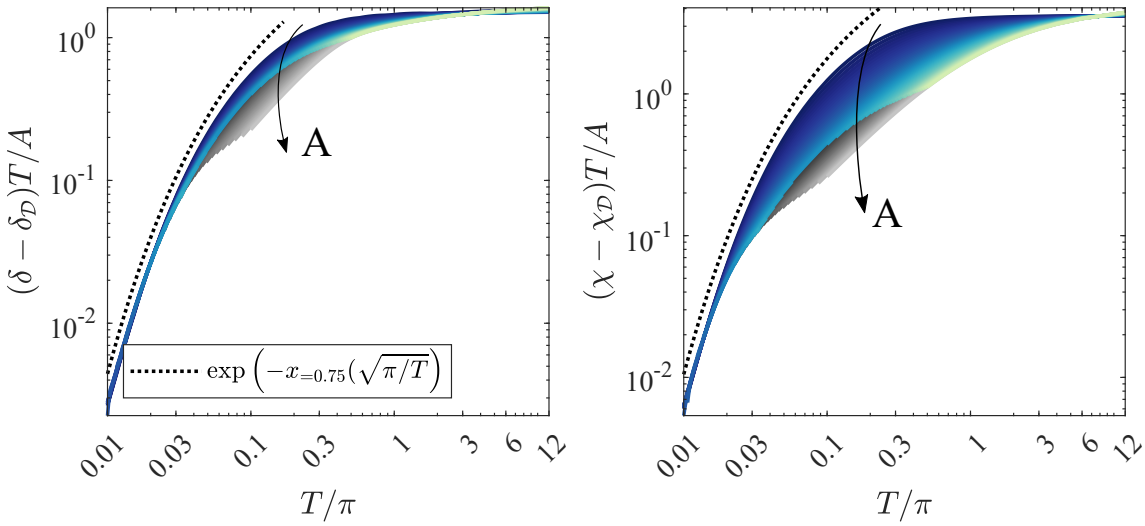

Figure 4.13: Travel distance (left) and degree of mixing (right) against A (increasing dark to light) and T, normalised by A/T with all three transport mechanisms simultaneously active. The values of δ_D and χ_D from the case of advection-diffusion only ($\alpha = 0$) are subtracted from the respective values of δ and χ. Amplitudes and periods are the same as in Figure 4.9. Portions shown in grey-scale indicate simulations where the solute reaches the left boundary and begins to leave the domain.

and also with $T^{-1/2}$. Figure 4.13 suggests that dispersion scales in the same way with T in this regime, having taken $x = 0.75$. Hence, Figure 4.13 highlights two competing mechanisms: progressively faster loading enhances dispersion by promoting large fluxes in general, but also progressively localises the flow and deformation, suppressing the flux (and thus dispersion) near the right boundary. The competition between these two behaviours is the origin of the maximum values of δ and χ with T. Note that, near the peak, normalised $\delta - \delta_D$ and $\chi - \chi_D$ slightly decrease with A. This is again the effect of the progressively lower $\langle\overline{\phi}\rangle$, similarly to what is seen in Figure 4.9. However, when considering Figure 4.11, this tendency is hidden by the high fluid and solid velocity reached in this regime for high values of A, which overall enhance dispersion, being the dispersion coefficient D_h the dominant factor.

In summary, this analysis reveals the link between transport fluxes and loading parameters and, consequently, with the poromechanics of periodic loading. We identify three principal regions of the amplitude-period domain shown in Figure 4.11:

- $T > \pi$: as the deformation is slow, molecular diffusion is of the same order as hydrodynamic dispersion; solute movements are roughly proportional to A and inversely proportional to T. Since these two parameters control the velocity fields, faster and larger deformations progressively increase the role of dispersion over diffusion.

- $0.1\pi < T < \pi$: the increasing localisation of the deformation at the left boundary leads

to high fluid velocities. This means that, for the same amplitude, as we decrease T the flux $|v_f - v_s|$ reaches higher peaks, highly promoting hydrodynamic dispersion, which is the dominant mechanism for this region.

- $T < 0.1\pi$: the travel distance decreases again as T shortens, for constant values of A. This is due to the strong localisation of the deformation and fluid flow near the left boundary as T further decreases. In this region, therefore, molecular diffusion progressively prevails over dispersion.

Note that the values of δ and χ depend on the specific values of the diffusion and dispersion coefficients chosen. This means that, in our plots in Figure 4.11, varying Pe^{-1} and α would impact the width and height of each region (in particular, of the central peak). However, the position and the general features characterising the the three regions is purely related to the poromechanics of periodic loading, and is expected to be independent of the coefficients.

4.3.5 Péclet number in biological examples

We conclude by reporting typical loading parameters, material properties and diffusion coefficients for several examples of soft biological tissues (Table 4.2). Based on these values, we calculate the Péclet number as defined in 4.2.4 (which quantifies the importance of deformation-driven advection relative to molecular diffusion), and the effective Péclet number $\mathrm{Pe}_{\mathrm{eff}} = \mathrm{Pe} \times A/T$, to understand the range of loading amplitudes and frequencies where advection and dispersion are likely to be non-negligible. For simplicity, we calculate these values considering a moderate amplitude, $A = 0.1$.

4.4 Conclusions

We proposed physical insights on solute transport and mixing in a periodically compressed soft porous medium under large deformations. To do so, we used a 1D continuum model, formulated following a rigorous nonlinear kinematic approach and considering Hencky elasticity as constitutive law for the solid skeleton. Overall, we demonstrated that the characteristic rearranging of the porous structure — resulting in a strong coupling between mechanical loads and fluid flow — originates phenomena that are not reversible, despite the cyclic nature of the applied load.

Our analysis is linked to our findings reported in Chapter 3: according to the loading period, the deformation can belong to either a slow-loading regime – in which the displacement and porosity are uniformly spread throughout the domain – or a fast-loading regime – in which the same variables have highly nonlinear and non-uniform behaviours. Fast deformations are characterised by higher fluid velocity magnitudes, constant compression until the loads are released (because of the time needed to propagate the deformation deep inside the domain), and fluid fluxes that become higher in the loading than in unloading phase as the loading amplitude A is increased. Hence, we analysed

Tissue	L [m]	$\tilde{A} = A/L$	k_0 [m^2]	$\mathcal{M}$ [Pa]	T_{pe} [s]	Typical loading frequency [Hz]	$\tilde{T} = T/T_{\text{pe}}$	$\mathcal{D}_m$[m$^2/s$]	Pe	$\text{Pe}_{\text{eff}} = \text{Pe} \times \tilde{A}/\tilde{T}$
Brain ECM (Kedarasetti et al., 2020)	2×10^{-4}	0.1	2×10^{-15}	2×10^{3}	≈ 10	0.3 – 10	0.003π – 0.1π	1.4×10^{-10}	≈ 30	$\approx 30 - 10^3$
Cartilage (Ferguson et al., 2004) (Gardiner et al., 2007) (DiDomenico et al., 2017)	2×10^{-3}	0.1	7.5×10^{-18}	5×10^{6}	$\approx 10^2$	0.001 – 0.1 (sitting) 0.1 – 1 (running)	0.03π – 3π 0.003π – 0.03π	5×10^{-12}	$\approx 7 \times 10^3$	$\approx 10^2 - 10^3$ $\approx 10^3 - 10^5$
Intervertebral Disk (Anulus F.) (Ferguson et al., 2004)	10^{-2}	0.1	7.5×10^{-19}	2.5×10^{6}	$\approx 5 \times 10^4$	2×10^{-5} (wake cycle) 0.001 – 0.1 (sitting) 0.1 – 1 (running)	0.3π $6 \times 10^{-5}\pi$ – $6 \times 10^{-3}\pi$ $6 \times 10^{-6}\pi$ – $6 \times 10^{-5}\pi$	5×10^{-12}	$\approx 4 \times 10^2$	$\approx 40 - 2 \times 10^3$ $\approx 2 \times 10^3 - 2 \times 10^5$ $\approx 2 \times 10^5 - 2 \times 10^6$
Cartilage Scaffold (bioreactor) (Sengers et al., 2004)	2×10^{-3}	0.1	10^{-17}	10^{5}	$\approx 4 \times 10^3$	0.001 – 1	0.0001π – 0.1π	10^{-11}	$\approx 10^2$	$\approx 4 \times 10^{-1} - 4 \times 10^2$

here how this different mechanical behaviour related to the loading parameters influences solute transport and mixing.

In the first part, we studied the nature of the concurring transport phenomena and how they act in the same direction in the loading phase — from right to left — while only advection changes direction in the unloading phase (Figure 4.3). We then observed one stimulation cycle, concentrating on the loading and unloading phase separately. For each phase, we compared the evolution of the solute concentration profile for four cases: (i)) molecular diffusion only (no deformation applied); (ii) transport for pure advection, in which diffusion and dispersion coefficients are set to zero; (iii) a combination of advection and molecular diffusion; (iv) a general case where all the transport mechanisms are active. From the analysis of the individual cases, we were able to justify the shape of the concentration profile according to the mathematical formulation of each transport contribution. Moreover, for all the cases with a deformation applied, the impact of a changing porosity was observed to spread the concentration profile during loading and contracting it back during unloading.

In the analysis of medium and solute parameters, we showed that individually increasing the coefficients of molecular diffusion and hydrodynamic dispersion leads to a more mixed and spread solute profile, since each of the two mechanisms is alternatively promoted. In this way, it is possible to reach a state where one mechanism is negligible compared to the other, thus being able to isolate it and couple it with advection.

We then proceeded to a quantitative overview considering two variables — travel distance and degree of mixing — and comparing them for the different loading conditions. In the first part, we fixed the material parameters and investigated how the slow- or fast-loading regimes impact on the way the solute spreads and mixes in the domain. Our plots of travel distance and degree of mixing for different combinations of amplitudes and periods allowed us to identify three main regions of solute transport regimes: (i) a region where molecular diffusion prevails but slowly starts to compete with hydrodynamic dispersion — characterising the slow-loading mechanical regime — where the influence on the spatial and temporal mixing of amplitudes and periods is small (but increasingly more important as T decreases); (ii) a region where hydrodynamic dispersion is the leading mechanism — extending in the fast-loading regime roughly between $T = \pi$ and $T = 0.1\pi$, where high values of fluid velocity and high asymmetries in the dispersive flux lead to very high levels of solute spreading and mixing; (iii) a region where molecular diffusion becomes prominent again — characterising very fast loading, at $T < 0.1\pi$ — because the high localisation of the deformation at the left boundary reduces the intensity of the dispersive flux at the right boundary, limiting the spread of the solutes located there.

Our results have two important applications: the prediction and control of solute concentration profiles. The former might be convenient in those cases where all the conditions are fixed (*e.g.* to

predict nutrient distributions in biological tissues *in vivo*), while the latter could provide relevant support in the optimization of the stimulation and material features to reach a desired final solute profile (*e.g.*, when designing scaffolds and bioreactors for tissue engineering).

Future modelling work may involve a dependency of the diffusion and dispersion coefficients on the porosity distribution. It is in fact still unclear if a reduced fluid fraction impacts their values, and if this needs to be taken into account for a better understanding of how the deformation affects solute transport. To improve this insight, we aim to perform an experimental campaign, as described in Chapter 7.

Chapter 5

Flow, deformation and transport due to periodic loading in a layered soft porous medium

5.1 Introduction

Soft biological tissues are an important class of soft porous media, and can often feature a layered structure. For this reason, in this chapter, we study the poromechanics and solute transport in layered soft porous media.

In some soft biological tissues, a structure with different layers originates in the orientation of collagen fibres, aligned to provide higher strength and elasticity in specific directions for purposes of load bearing (Fung, 2013). Articular cartilage, for example, is divided throughout its thickness into three zones — superficial, middle, and deep — each characterised by a different orientation of the collagen fibres (Poole et al., 2001). Layers can also arise from differences in density; for example, recent studies on brain matter have stressed the presence of a paravascular space — a highly permeable and highly porous region surrounding blood vessels — and its essential role in the flow of cerebrospinal fluid through the tissue (Iliff et al., 2012, Rasmussen et al., 2022).

The solid-mechanical role of these complex layered architectures is generally well understood. In articular cartilage, the different layers lead to depth-dependent mechanical properties and constitutive responses (Krishnan et al., 2003, Park et al., 2003). However, these layers also play an important fluid-mechanical role in tissues (Federico and Herzog, 2008a, Gu et al., 1999, Malandrino et al., 2009, Reynaud and Quinn, 2006). The presence of a fibre bundle enhances the overall permeability along the fibre direction, while reducing the permeability along the transverse direction (Federico and Herzog, 2008a,b). The complex hydraulic structure of articular cartilage is thought to play a role in maximising the pore pressure at the articular surface (Krishnan et al., 2003, Park et al., 2003, Pierce et al., 2013, 2016), essential to maintaining lubricating properties (Ateshian, 2009) and to protecting the tissue from fracturing (Dabiri and Li, 2013). Overall, authors agree on the importance

of the different layers in defining the biphasic response, with the need for theoretical models to introduce layer-specific permeability tensors (Federico and Grillo, 2012, Gao et al., 2015, Gastaldi et al., 2018, Maleki et al., 2020, Tomic et al., 2014) or depth-dependent permeability functions (Federico and Herzog, 2008a, Wu et al., 2016). The layered structure could be essential to the survival and health of tissues, since alterations of the layered structure are often associated with pathological and/or damaged conditions. For example, while in healthy cartilage pore pressure supports more than 90% of the applied load in compression (Soltz and Ateshian, 1998), damaged cartilage (such as osteoarthritic cartilage) exhibits an increase in permeability and a significant reduction of the pore pressure (Hwang et al., 2008). The fraction of the load carried by the solid matrix is consequently larger, contributing to a potential positive feedback of further damage (Hwang et al., 2008, Stender et al., 2017). In osteoarthritic cartilage, the overall division in layers is lost or modified, resulting in altered distributions of loads and pore pressure (Stender et al., 2017).

Changes in the pore pressure and consequent fluid permeation due to a modified layered structure are expected to affect the transport of solutes as well; this is a fundamental aspect to the health of cartilage, given its avascular nature. Through gradients in pore pressure, the layered structure in cartilage influences the solute movements (Zhang and Szeri, 2007), while the depth-dependent permeability promotes corresponding depth-dependent enhanced solute uptake under dynamic load, due to the inhomogeneous profiles of fluid velocity and pressure (Zhang, 2011) and depth-dependent diffusion coefficients (Arbabi et al., 2015, Ateshian and Weiss, 2010, DiDomenico et al., 2017). A better understanding of the coupling between poromechanics and solute transport in layered soft porous media could also help explaining the advancing of diseases such as Alzheimer's disease. Alzheimer's disease originate from an abnormal accumulation of amyloid-β plaques, which leads to the softening of brain tissue via neuronal cell death and the degradation of the extracellular matrix (Murphy et al., 2011). Simultaneously, the disease also leads to increased stiffness (Hu et al., 2023) and decreased permeability in other regions due to the accumulation of plaques, which have a rigid core surrounded by a lipid layer (Mattana et al., 2017, Palombo et al., 2018). The latter disease-induced changes could be responsible for a positive feedback mechanism suppressing the clearance of amiloyd-β residues, with further plaque accumulations. Overall, these changes in the poromechanical properties of damaged compared to healthy tissues are likely to change the tissue poromechanics, especially since these tissues are physiologically subject to large periodic loads.

A full characterisation of the poromechanical properties of layered soft porous media could also assist in applications related to tissue engineering. For example, it is still very challenging to develop tissue-engineered replacements of articular cartilage to restore the fundamental lubricating and support functions (Sánchez-Téllez et al., 2017). The replacements are usually based on hydrogel scaffolds in which cells are implanted and then subject to periodic mechanical loading (Camarero-Espinosa et al., 2016a). In these constructs, a heterogeneous structure has been observed to provide

essential benefits: hydrogels with several different layers mimic the compressive properties of cartilage (Karpiak et al., 2012, Zhu et al., 2014) and, most importantly, scaffolds with regions of enhanced fluid-flow (Mesallati et al., 2013) or presenting a cartilage-like structure with three zones demonstrated that cell growth can be favoured by the layered architecture. Hence, significant effort has been directed toward fabricating scaffolds with heterogeneous structures (Sano et al., 2018), such as hydrogels with two layers of different densities (Ng et al., 2006), hydrogels with a gradient in permeability (Gurkan et al., 2014), or where the permeability is tuned through microchannels and microgrooves (Lee et al., 2015, Mesallati et al., 2013). These complexly layered scaffolds are still missing a detailed investigation of their mechanical behaviour.

No study has approached the physics of a poroelastic medium with layered poromechanical properties when subject to periodic deformations, which are common for soft biological tissues and scaffolds for tissue engineering. Here, we fill this gap investigating the role of spatial structure — specifically, layering — on the poromechanical response of a generic soft porous medium under large periodic loads. To do so, we reformulate the model from Chapter 3 in a Lagrangian framework, dividing the domain into two or more region of different permeability. We apply fast periodic loading (relative to the poroelastic timescale) and compare the response of the layered media to that of a homogeneous medium. Motivated by two examples of soft biological tissues (articular cartilage and brain matter), we consider two loading cases: (i) confined compression (CC), and (ii) free-flow compression (FFC). CC is commonly applied to articular cartilage and cartilage substitutes, whereas FFC can be used to represent brain matter between a pulsating arteriolar vessel and the respective venule. In both CC and FFC, we take the solutes to be outside of the domain and infiltrating from the left boundary into the solute-free domain. For each loading scenario, we consider deformation (via the porosity field), flow (via the Darcy flux), and solute transport (via the total solute flux). We also consider the rate at which solute enters the domain from the left boundary. We conclude by considering a simplified representation of the changes to the original layered structure of (i) articular cartilage (AC) and (ii) brain tissue (BT) that would result from osteoarthritis and amyloid-β plaques (AβPs), respectively. We analyse the impact of these changes on the mechanics and fluid-flow through the medium.

5.2 Model problem

We consider a 1D soft porous medium divided in two layers. The medium is subject to a periodic displacement-driven load applied via a permeable piston at the left boundary and the right boundary is fixed, as in the cases discussed in Chapter 3. By changing the right boundary conditions for fluid flow, we compare two scenarios: confined compression (CC), where the right boundary is impermeable, and free-flow compression (FFC), where fluid flow is allowed at the right boundary. In both scenarios, the concentration of solutes in the reference configuration is assumed to be zero,

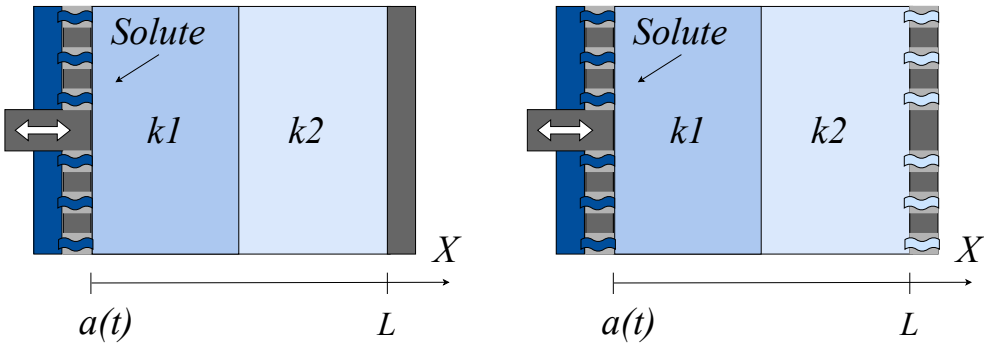

Figure 5.1: Schematic representation of a layered medium (where k_1 and k_2 are two given permeabilities) subject to confined compression (CC, left) and free-flow compression (FFC, right). In both cases, the piston at the left is permeable and applies a periodic displacement-driven load, whereas the right boundary is impermeable in CC and permeable in FFC. Solute enters the domain from the left.

with solute entering the domain from the left boundary. A schematic diagram of the two cases is shown in Figure 5.1.

5.3 Theoretical model

In the framework of the model described in Chapter 3, we make two changes: (i) we take the initial permeability to be a function of space and (ii) we apply two different sets of boundary conditions, for CC and FFC respectively. For purposes of the former, which introduces a spatially varying material property, we reformulate the model from Chapter 3 in a Lagrangian frame.

5.3.1 Lagrangian model

5.3.1.1 Large-deformation poroelasticity

We report here the Lagrangian formulation of the model used in Chapter 3. In the Lagrangian frame, the model is written in terms of nominal quantities, such as the nominal porosity $\Phi_f = J\phi_f$, which measures the current fluid volume per unit reference total volume.

The Lagrangian solid displacement field is $\mathbf{U_s}(\mathbf{X}, t) = \mathbf{x}(\mathbf{X}, t) - \mathbf{X}$, with $\mathbf{x}(\mathbf{X}, t)$ the current position (*i.e.*, the position at time t) of the material point with reference position $\mathbf{X}$. Our reference configuration is once again the relaxed configuration, where $\mathbf{x}(\mathbf{X}, 0) = \mathbf{X}$, so that $\mathbf{U_s}(\mathbf{X}, 0) = 0$.

The Jacobian determinant is $J = 1 + \partial U_s/\partial X$. For incompressible constituents and uniform initial porosity $\phi_{f,0}$, the local change in volume relates to the change in porosity as

$$J(X,t) = 1 - \Phi_{f,0} + \Phi_f \quad \rightarrow \quad \frac{\partial U_s}{\partial X} = \Phi_f - \Phi_{f,0}. \tag{5.1}$$

Continuity can be written as:

$$\frac{\partial \Phi_f}{\partial t} + \frac{\partial}{\partial X}(W_f) = 0, \tag{5.2}$$

where W_f is the nominal flux of fluid through the solid skeleton. The latter is given by Darcy's law, which reads

$$W_f = -\frac{1}{J}\frac{k(X,\phi_f)}{\mu}\frac{\partial p}{\partial X}, \tag{5.3}$$

We again choose a normalised Kozeny-Carman relation for the permeabiliy law, where $k_0 \equiv k(X,\phi_{f,0})$ is the permeability of the initial state, as described below.

In 1D, mechanical equilibrium reads:

$$\frac{\partial s}{\partial X} = 0, \tag{5.4}$$

where s is the nominal total stress. The nominal effective stress is:

$$s' = s + p. \tag{5.5}$$

Once again, we take the elasticity law to be Hencky elasticity:

$$s' = \mathcal{M}\frac{\ln(J)}{J}, \tag{5.6}$$

where $\mathcal{M}$ is the p-wave modulus. Combining equations (5.2)— (5.5), we arrive at the nonlinear flow equations:

$$\frac{\partial \Phi_f}{\partial t} - \frac{\partial}{\partial X}\left[\frac{1}{J}\frac{k(X,\phi_f)}{\mu}\frac{\partial p}{\partial X}\right] = 0 \quad \text{and} \quad \frac{\partial s'}{\partial X} = \frac{\partial p}{\partial X}. \tag{5.7}$$

Note that the net flux q and the fluid and solid velocities (v_f and v_s respectively) are the same in Eulerian and Lagrangian space. Since

$$q = W_f(X = L) = \phi_f(v_f - v_s), \tag{5.8}$$

it is easy to derive that

$$v_s = q - W_f \quad \text{and} \quad v_f = \phi_f q - \left(\frac{1-\phi_f}{\phi_f}\right) v_s. \tag{5.9}$$

With appropriate initial and boundary conditions, the above formulations close the Lagrangian model.

5.3.1.2 Solute transport

The model for solute transport is analogous to the one presented in Chapter 4. In a Lagrangian frame, conservation of mass for the solute (with local solute concentration c) can be written

$$\frac{\partial(\Phi_f c)}{\partial t} + \frac{\partial}{\partial X}\left[cW_f - \frac{1}{J}\phi_f \mathcal{D}\frac{\partial c}{\partial X}\right] = 0, \tag{5.10}$$

where the diffusivity reads

$$\mathcal{D} = \mathcal{D}_m + \mathcal{D}_h = \mathcal{D}_m + \alpha\left|\frac{W_f}{\phi_f}\right|. \tag{5.11}$$

5.3.2 Boundary conditions

5.3.2.1 Initial conditions

We define the left and right boundaries of the solid to be at $X = 0$ and $X = L$, respectively. The mechanics initial conditions are unchanged to the case illustrated in Chapter 3 and Chapter 4. In Lagrangian coordinates, they read:

$$\Phi_f(X, 0) = \phi_{f,0} \quad \text{and} \quad U_s(X, 0) = W_f(X, 0) = 0. \tag{5.12}$$

We take the initial concentration of the solute to be $c(X, t) = 0$.

5.3.2.2 Left boundary

For both CC and FFC, for $t > 0$, we apply the same displacement-controlled mechanical loading at the left boundary, as described in the previous chapters. In the Lagrangian frame, this implies

$$v_s(X = 0, t) = \dot{a}(t) \quad \rightarrow \quad W_f(X = 0, t) = q(t) - \dot{a}(t), \tag{5.13}$$

with

$$a(t) = \frac{A}{2}\left[1 - \cos\left(\frac{2\pi t}{T}\right)\right]. \tag{5.14}$$

For CC, $q = 0$ and $W_f(X = 0, t) = -\dot{a}(t)$. At this boundary, we take $c(X = 0, t) = c_0$.

5.3.2.3 Right boundary: confined compression

For CC, the right boundary is once again impermeable and fixed in place, such that

$$U_s(L, t) = W_f(L, t) = 0. \tag{5.15a}$$

For the solute, this implies

$$\left.\frac{\partial c}{\partial X}\right|_{X=L} = 0. \tag{5.15b}$$

5.3.2.4 Right boundary: free-flow compression

In the case of FFC, the right boundary is fixed in space but permeable. This implies:

$$v_s(L, t) = 0 \quad \rightarrow \quad W_f(L, t) = q(t). \tag{5.16}$$

In this case, $v_f(L, t) \neq 0$. We take the pressure to be zero at both boundaries:

$$p(0, t) = p(L, t) = 0. \tag{5.17}$$

This implies that the effective stress s' must be equal at both boundaries. In Equation (5.7), this leads to:

$$\Phi_f(0, t) = \Phi_f(L, t). \tag{5.18}$$

We assume that the fluid at the right side of the domain is free of solute, with $c(L, t) = 0$.

5.3.3 Scaling and summary

Similarly to our Eulerian formulation, the non-dimensionalization to the evolution equations is

$$\tilde{X} = \frac{X}{L},\ \tilde{U}_s = \frac{U_s}{L},\ \tilde{t} = \frac{t}{T_{\mathrm{pe}}},\ \tilde{s}' = \frac{s'}{\mathcal{M}},\ \tilde{p} = \frac{p}{\mathcal{M}},\ \tilde{k} = \frac{k(\phi)}{k_0},\ \tilde{W}_f = \frac{W_f}{L/T_{\mathrm{pe}}},\ \tilde{q} = \frac{q}{L/T_{\mathrm{pe}}}, \tag{5.19}$$

and

$$\tilde{c} = \frac{c}{c_0},\ \tilde{\alpha} = \frac{\alpha}{L},\ \tilde{\mathcal{D}} = \frac{\mathcal{D}}{\mathcal{D}_m} = 1 + \tilde{\alpha}\mathrm{Pe}\left|\frac{\tilde{W}_f}{\phi_f}\right|. \tag{5.20}$$

The full problem can then be rewritten in dimensionless form as

$$\frac{\partial \Phi_f}{\partial \tilde{t}} - \frac{\partial}{\partial \tilde{X}}\left(\tilde{W}_f\right) = 0 \tag{5.21}$$

and

$$\frac{\partial(\Phi_f \tilde{c})}{\partial \tilde{t}} + \frac{\partial}{\partial \tilde{X}}\left[\tilde{c}\tilde{W}_f - \frac{1}{J}\phi_f \mathrm{Pe}^{-1}\tilde{\mathcal{D}}\frac{\partial \tilde{c}}{\partial \tilde{X}}\right] = 0, \tag{5.22}$$

with initial conditions

$$\tilde{a}(0) = 0,\ \Phi_f(\tilde{X}, 0) = \phi_{f,0},\ \tilde{W}_f(\tilde{X}, 0) = \tilde{v}_s(\tilde{X}, 0) = 0,\ \tilde{c}(\tilde{X}, 0) = 0. \tag{5.23}$$

The scaled left boundary conditions for both CC and FFC read:

$$\tilde{U}_s(0, \tilde{t}) = \tilde{a}(\tilde{t}) = \frac{\tilde{A}}{2}\left[1 - \cos\left(\frac{2\pi \tilde{t}}{\tilde{T}}\right)\right],\ \tilde{W}_f(0, \tilde{t}) = q(\tilde{t}) - \dot{\tilde{a}}(t) \quad \text{and} \quad \tilde{c}(0, \tilde{t}) = 1, \tag{5.24}$$

where $\tilde{A} = A/L$ and $\tilde{T} = T/T_{\mathrm{pe}}$. The right boundary conditions for CC are

$$\tilde{U}_s(1, \tilde{t}) = \tilde{W}_f(1, \tilde{t}) = 0 \quad \text{and} \quad \left.\frac{\partial \tilde{c}}{\partial \tilde{x}}\right|_{\tilde{x}=1} = 0, \tag{5.25}$$

while for FFC they are

$$\tilde{W}_f(1, \tilde{t}) = \tilde{q}(\tilde{t}), \quad \Phi(1, t) = \Phi(0, t), \quad \text{and} \quad \tilde{c}(1, t) = 0, \tag{5.26}$$

Below, all quantities are dimensionless and we drop the tildes for convenience.

5.4 Permeability and poroelastic timescale

For each scenario — CC and FFC — we compare three media: (i) a homogeneous medium, (ii) a medium where the left half has a higher permeability than the right half ("$k_H - k_L$") and (iii) a medium where the left half has a lower permeability than the right half ("$k_L - k_H$"). For the latter two scenarios, we implement this layering by imposing a relaxed permeability that varies within the medium. To avoid discontinuities, we use a hyperbolic tangent to smoothly transitions from one permeability value the second one. A schematic representation of the permeability function in the different cases examined here is shown in Figure 5.2.

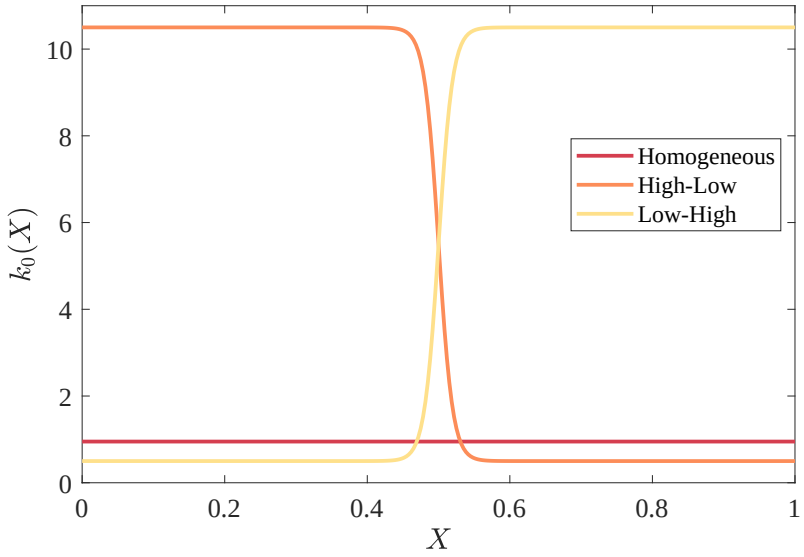

Figure 5.2: Initial permeability for the three types of medium considered in this work: (i) homogeneous case, (ii) $k_H k_L$ case, and (iii) $k_L k_H$ case. k_0 is a function of the spacial coordinate X.

The poroelastic timescale T_{pe} is inversely proportional to the permeability, so layers with different values of initial permeability will have different poroelastic timescales. As shown in Chapter 3, the response of a medium to periodic loading depends on the ratio of the lodaing period T to T_{pe}. Hence, for the same T, layers with different T_{pe} will propagate the deformation throughout the domain at different speeds. For very different permeabilities, for example, one layer could be in the SL regime while the adjacent layer could be in the FL regime. For very slow loading, however, both layers would respond quasi-statically and therefore in the same way as the homogeneous medium considered in Chapter 3. Therefore, we consider here two representative values of the initial permeability, k_H and k_L, and loading periods T for which both layers respond in FL. We fix $k_L = 0.5$ and $k_H = 10.5$. To provide a comparison with a homogeneous medium, we choose the respective permeability to be $2k_0^{-1} = \frac{1}{k_L} + \frac{1}{k_H} = 0.95$. For all cases, we consider moderate amplitudes of $A = 0.1$ and periods in the fast-loading regime, taking $\Phi_0 = 0.75$.

Note that in a physical medium a change in permeability would be caused by a change in pore structure that may also correlate with a change in stiffness, as discussed in Section 5.1. A change in stiffness would impact the response via a change to the poroelastic timescale and in other ways. We focus here on the poroelastic timescale as the most important factor in the response to fast or very fast loading. Also, we focus on the permeability rather than the stiffness because we assume the volume changes to occur mostly by fluid efflux and influx, rather than by deformations of the solid skeleton.

5.5 Results

This section presents numerical results for the three media compared here — homogeneous, $k_H k_L$, and $k_L k_H$ — for each loading scenario. Analogously to Chapter 3, we show the change in porosity (still defined as $\Delta\phi_f \equiv \phi_f - \langle\overline{\phi_f}\rangle$) and the Darcy flux $W_f = \phi(v_f - v_s)$. We normalise these quantities with $\Delta\phi_f^M$ and $W_f^* = \phi_0(v_f^* - v_s^*)$ (where $\Delta\phi_f^M$, v_f^* and v_s^* are defined as in Chapter 3). Note that these normalising quantities are the same for all three media. We also show the total solute flux $c_{\text{flux}} = cW_f - \frac{1}{J}\phi_f \mathcal{D}\frac{\partial c}{\partial X}$. Throughout, we take $\text{Pe}^{-1} = 3 \times 10^{-5}$ and $\alpha = 0.01$.

5.5.1 Confined compression

In Figure 5.3, we show the change in porosity, the normalised Darcy flux W_f/W_f^* and the solute flux c_{flux} for fixed amplitude $A = 0.1$ and period $T = 0.08\pi$ for a homogeneous medium in comparison to the layered media $k_H k_L$ and $k_L k_H$. The layered media present a physically different response than the homogeneous medium. Both cases show some localisation of the deformation on the left half of the domain, whereas the right half of the domain exhibits lower engagement. Specifically, as shown in the first row of Figure 5.3, in the $k_H k_L$ case, the high permeability near the piston localises the deformation in the left half of the domain, but spreads it uniformly. The second half of the domain is subjected to a slightly less uniform compression. In the case of the $k_L k_H$ medium, the high resistance to fluid flow of the first layer localises the deformations more aggressively within the left half, toward the piston. The low permeability in this case induces large changes in porosity near the piston during both loading and unloading in the very superficial areas, causing a significant part of the fluid motion to happen superficially. The right half of the domain deforms almost uniformly, and less overall. This leads to fluxes that are respectively less and more delayed for $k_H k_L$ and $k_L k_H$ with respect to the homogeneous case, as seen in the second row of Figure 5.3. The distribution and the local magnitudes of the fluid and solute fluxes are altered for both layered media in comparison with the homogeneous case.

Overall, the deformation of the medium is altered by the presence of the layers, with higher localisation but different distributions of deformations, fluid fluxes and solute fluxes in the layered media than in the homogeneous case.

5.5.2 Free-flow compression

For free-flow compression, we take again $A = 0.1$ and $T = 0.08\pi$. Figure 5.4 shows that, for a homogeneous medium, the response to FFC is mirrored in the left and right halves of the domain. This is true for $\Delta\phi_f$ and W_f/W_f^* which, in FFC, is symmetric at the two boundaries (following Equation (5.8)). Consequently, for the layered media, $\Delta\phi_f$ is equivalent and opposite at the two boundaries. The regions of low permeability localise deformations at their respective boundaries, while the regions of high permeability spread the deformations. The magnitude of the Darcy fluxes

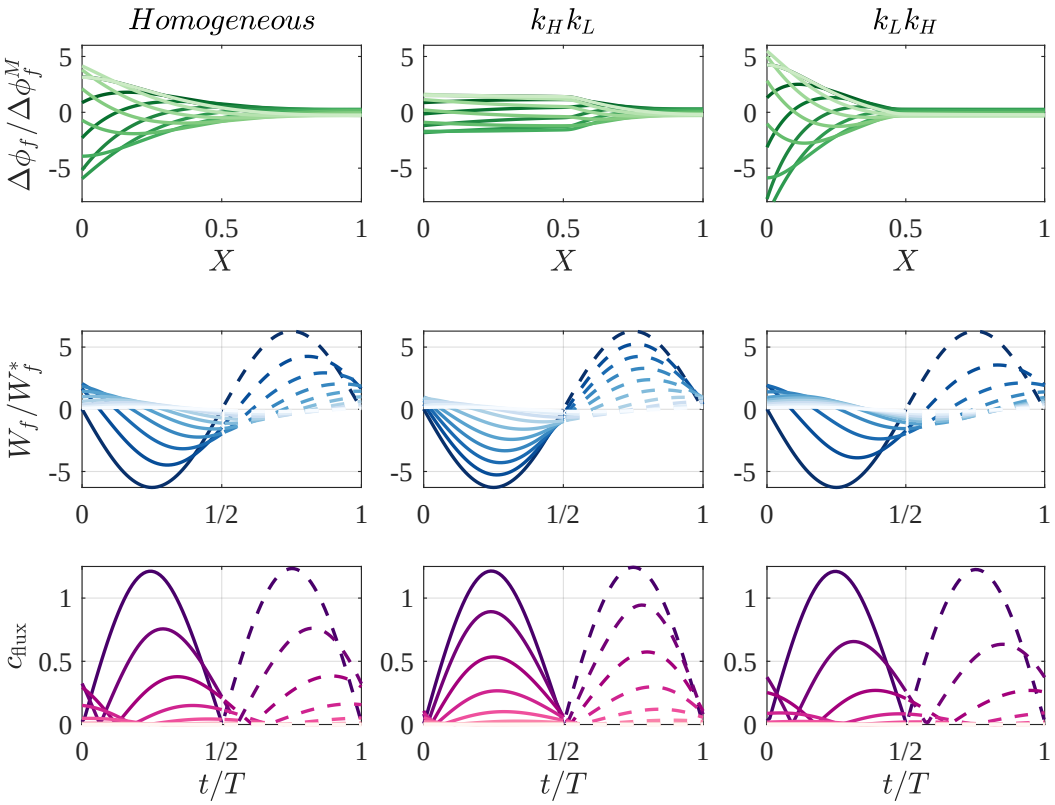

Figure 5.3: Evolution of $\Delta\phi_f$ (first row) at times $t = nT$ to $(n+1)T$ in increments of $0.1T$ (dark to light), where n is an integer, during one cycle in the periodic regime for $A = 0.1$, $\phi_{f,0} = 0.75$, and $T = 0.08\pi$, for the homogeneous case (first column), the $k_H k_L$ case (second column), and the $k_L k_H$ case (third column). In the second and third row, the normalised W_f/W_f^* and c_{flux} are plotted against t for ten different values of X from 0 to 1 (dark to light). We distinguish between the loading half of the cycle ($\dot{a} > 0$; solid curves) and the unloading half of the cycle ($\dot{a} < 0$; dashed curves).

and solute fluxes is respectively larger and smaller for the $k_H k_L$ medium and the $k_L k_H$ medium than for the homogeneous medium. Therefore, the presence of two layers impacts the distribution of the deformations, fluid fluxes and solute fluxes with respect to a homogeneous medium. The order of the layers, moreover, changes the fluid flow throughout the domain.

5.5.3 Solute transport

We next perform a simple comparison of solute transport in a homogeneous medium and layered media for CC, where only the left boundary is permeable to the fluid and solutes, and for FFC, where both boundaries are permeable. In all cases, the concentration in the domain is initially zero and solutes are infiltrating from the left boundary. We compare solute transport in the three media by plotting the final concentration profiles achieved after a fixed number of cycles for three values of T.

Figure 5.5 shows that, for CC, in fast loading the concentration for the homogeneous and the

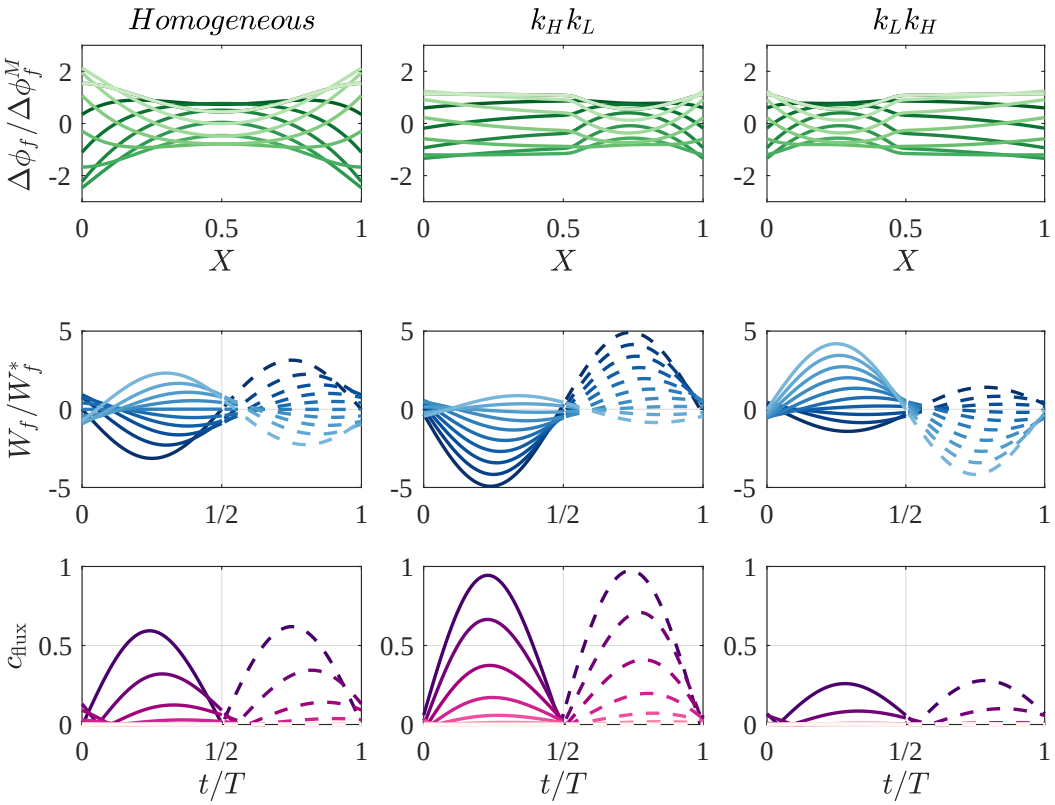

Figure 5.4: Evolution of $\Delta\phi_f$ (first row) at times $t = nT$ to $(n+1)T$ in increments of $0.1T$ (dark to light), where n is an integer, during one cycle in the periodic regime for $A = 0.1$, $\phi_{f,0} = 0.75$, and $T = 0.08\pi$, for the homogeneous case (first column), the $k_H k_L$ case (second column), and the $k_L k_H$ case (third column). In the second and third row, the normalised W_f/W_f^* and c_{flux} are plotted against t for ten different values of X from 0 to 1 (dark to light). We distinguish between the loading half of the cycle ($\dot{a} > 0$; solid curves) and the unloading half of the cycle ($\dot{a} < 0$; dashed curves).

$k_L k_H$ case is comparable, while it is higher for the $k_H k_L$ case. As T increases, the three concentration profiles progressively overlap, since all media progressively approach the slow-loading regime. For FFC, the $k_H k_L$ case again promotes the spreading of the solutes compared to a homogeneous medium, while the $k_L k_H$ case suppresses it. In this loading scenario, the overlap of the three solute profiles is reached for considerably large values of T (*e.g.* $T = 100\pi$). Note that, in FFC and unlike in CC, the flow field depends on the permeability field even for quasi-static compression because the permeability determines the partitioning of the outflow between the left and right boundaries.

These results show that solute transport is affected by the division in layers. The higher transport of solutes for the $k_H k_L$ cases could explain the presence of a higher permeability layer next to the areas of solute delivery (for example, arteries and arterioles) for some biological tissues, such as in the case of the paravascular space near the brain matter (see 5.6.2). Moreover, these results could support the design of scaffolds for tissue engineering to optimise the delivery of nutrients throughout the material thickness.

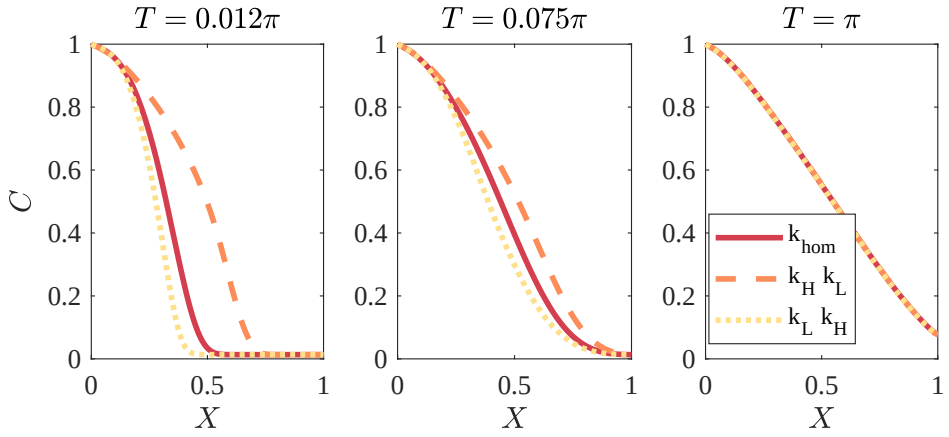

Figure 5.5: Final concentration profiles after 60 cycles with $A = 0.05$, $\phi_{f,0} = 0.75$, for $T = 0.012\pi$ (first column), for $T = 0.075\pi$ (second column) and for $T = \pi$ (third column), comparing the homogeneous case, the $k_H k_L$ case, and the $k_L k_H$ case in CC.

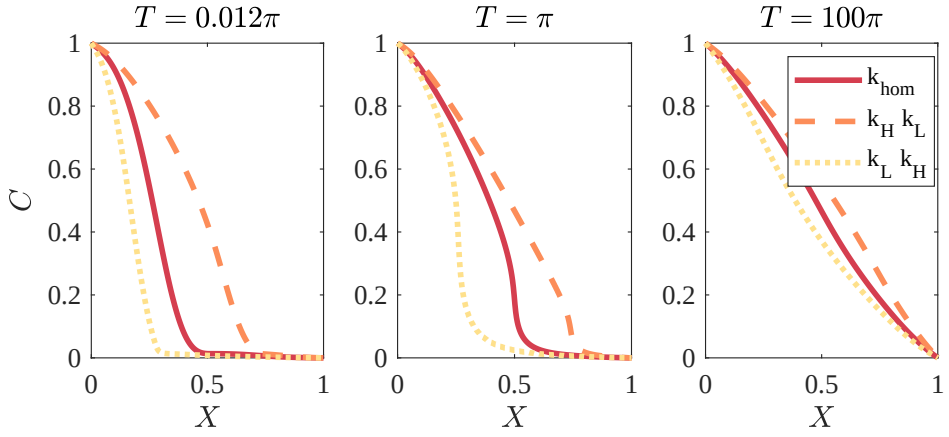

Figure 5.6: Final concentration profiles after 60 cycles with $A = 0.05$, $\phi_{f,0} = 0.75$, for $T = 0.012\pi$ (first column), for $T = \pi$ (second column) and for $T = 100\pi$ (third column), comparing the homogeneous case, the $k_H k_L$ case, and the $k_L k_H$ case in FFC.

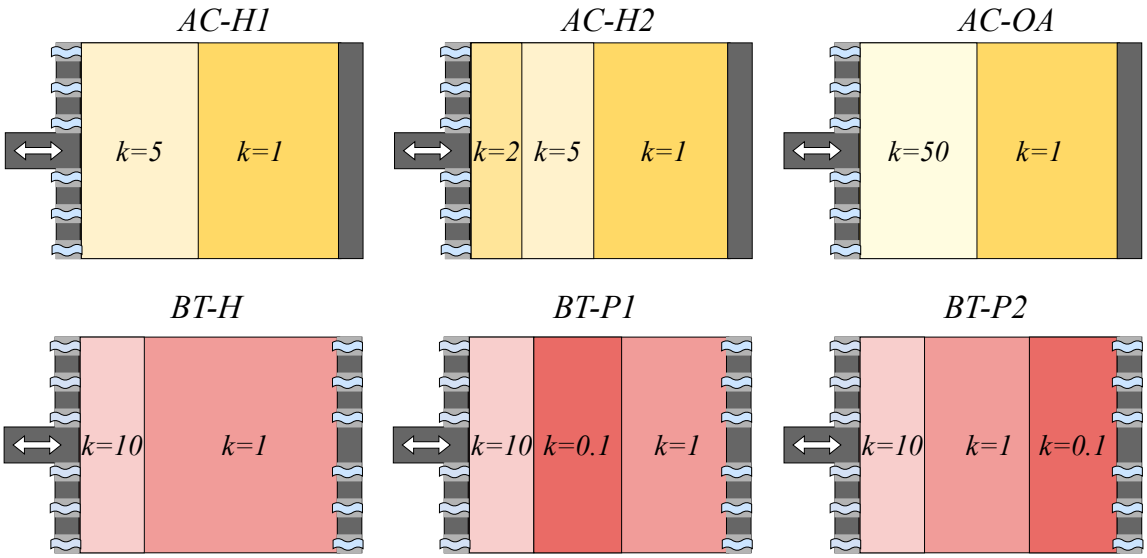

Figure 5.7: Schematic representation of the permeability distributions and values used for the analogies with healthy and damaged AC and BT. In the first row, $AC1$ and $AC2$ represent two models for healthy AC according to the data from (Chen et al., 2001) and (Maroudas and Bullough, 1968) respectively, while OA is the case of osteoarthritic cartilage. The loading case considered is CC. In the second row, BT-H represents a healthy brain system, with the PVS and the BT only. The cases BT-P1 and BT-P2 represent two different scenarios of brain space with $A\beta P$ either in the middle or at the end of the domain. This scenario is modelled with FFC. In all models,darker colors correspond to lower permeability k_0.

5.6 Analogies with biological tissues

We conclude our study of layering presenting two analogies with layered biological tissues, and their alterations under pathological conditions. We compare distributions of permeability qualitatively similar to (i) healthy *versus* osteoarthritic articular cartilage (AC) in Section 5.6.1, and (ii) healthy brain tissue (BT) *versus* brain tissue presenting amyloid-β plaques (AβPs) in Section 5.6.2. The goal is to study the qualitative impact of each disease on the poromechanical coupling. Hence, we use our previously discussed loading cases — CC for cartilage and FFC for the brain — and divide each domain into layers corresponding to the healthy and pathological configurations (as reported in the literature). A schematic summary of the cases considered is shown in Figure 5.7.

5.6.1 Articular cartilage

In AC, the division into the three zones is well understood and has been extensively characterised in terms of mechanical properties. However, the permeability of each layer depends on both the presence and alignment of the collagen fibres, and on the density of large and negatively charged proteoglycan molecules. The latter is also heterogeneous throughout the thickness, increasing from the surface to the bottom of the tissue (Maroudas, 1968, Maroudas and Bullough, 1968). Available experimental data are extremely variable; some studies measured low permeability at the surface,

high permeability in the middle zone, and very low permeability in the deep zone (Maroudas and Bullough, 1968), concluding that the tight packing of the superficial fibres would lead to a lower permeability despite the lower amount of proteoglycans. Other studies, however, measured a monotonically decreasing permeability from the superficial to the deep zone (Chen et al., 2001). For the sake of completeness, we consider both scenarios — AC-H1 and AC-H2, respectively — as potentially representative of the healthy tissue. We take the first case to be a two-layer medium with the permeability being five times larger in the superficial zone than in the deep zone (AC-H1), following the data reported in (Chen et al., 2001). For the second case, we consider three layers by splitting the superficial zone into two separate layers, the permeability being two times larger and fives times larger in the superficial and interior zones, respectively, than in the deep zone (AC-H2). Both scenarios are compared to an unhealthy case featuring a superficial layer with greately enhanced permeability (*e.g.*, ten times the permeability of the healthy case), representing damage associated with osteoarthritis. A schematic description of these three cases considered is shown in Figure 5.7. The loading parameters for CC are $T = 0.01\pi$ and $A = 0.1$, in the range of the physiological parameters reported in Chapter 3.

Figure 5.8 shows the two representations of healthy articular cartilage (first two columns), and the unhealthy ostheoarthritic case (third column). The first row of Figure 5.8 shows that a higher superficial permeability induces a more quasi-static response of the medium, with smaller magnitudes of the deformations at the surface; $\Delta\phi_f$ is more uniform and more symmetric between loading and unloading. The articular surface is supposed to sustain a large part of the deformation (favoured by its specific fibre alignment), helped by the large pore pressure developed in this layer, which also favours lubrication (see Section 5.1). This shielding effect (or, localisation) is reduced in the damaged tissue. A lower localisation leads to a more uniform response for the Darcy flux and the solute flux (Figure 5.6.1, second and third rows): the fluid in the medium is more easily expelled, loosing the damping effect that a healthy articular cartilage is supposed to provide. This could potentially impact nutrient supply and waste removal in the tissue.

5.6.2 Brain tissue

The region of interest considered in the study of the brain is the portion sandwiched between a representative arteriole and a representative venule. In simple terms, nutrients leave arterioles and reach the brain tissue by passing through the paravascular space (PVS). Waste substances, on the contrary, are cleared from the brain tissue through their recollection in the venules, which forms a circuit known as the glymphatic system (Iliff et al., 2012). We model this portion as a one-dimensional porous medium divided into a high permeability region — the PVS — and a lower permeability region — the brain tissue, BT (Kedarasetti et al., 2020). The arterioral wall pulsates, thus loading the domain periodically. The end of the domain is assumed to coincide with the venule

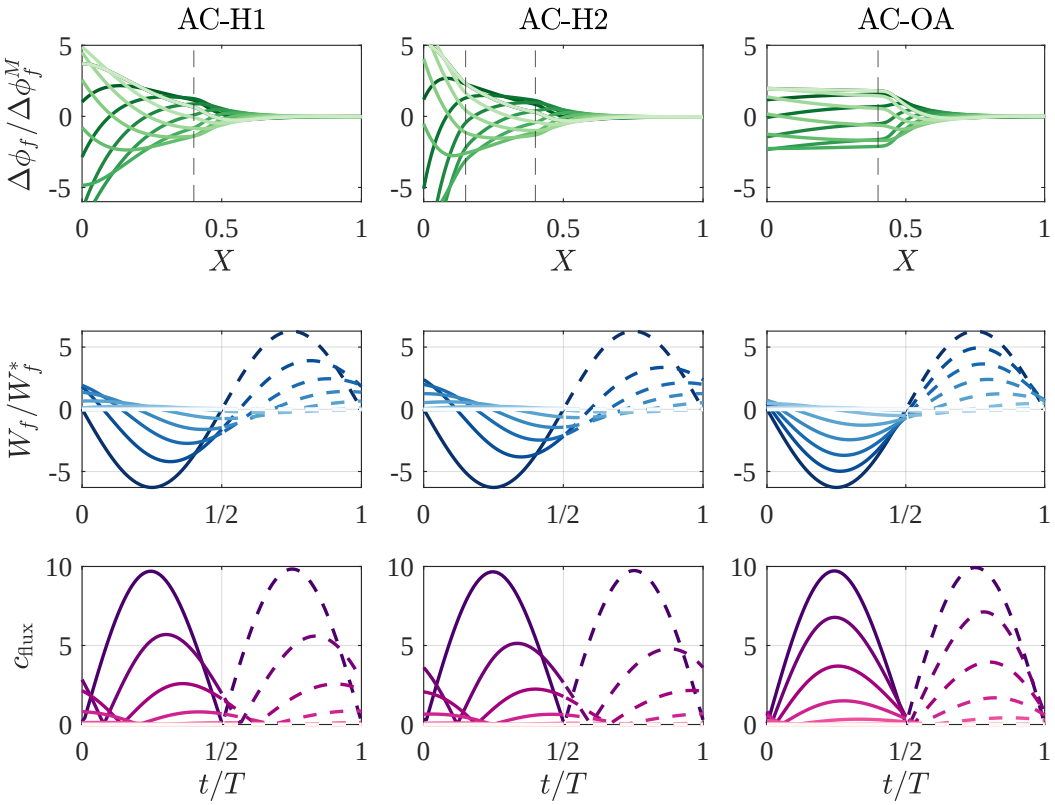

Figure 5.8: Evolution of $\Delta\phi_f$ (first row) at times $t = nT$ to $(n+1)T$ in increments of $0.1T$ (dark to light), where n is an integer, during one cycle in the periodic regime for $A = 0.1$, $\phi_{f,0} = 0.75$, and $T = 0.01\pi$, for two representations of healthy cartilage (first and second column), and osteoarthritic cartilage (third column). In the second and third row, the normalised W_f/W_f^* and c_{flux} are plotted against t for ten different values of X from 0 to 1 (dark to light). We distinguish between the loading half of the cycle ($\dot{a} > 0$; solid curves) and the unloading half of the cycle ($\dot{a} < 0$; dashed curves).

wall, which is far enough away for the periodic displacement to be zero; the clearance of the waste substances at the end of the domain is modelled with free flow at the right boundary.

This model of a healthy brain portion is compared with an altered structure of the tissue, corresponding to an accumulation of amyloid-β plaques (AβP). These tissue alterations consist of abnormal depositions of proteins, associated with neuronal degenerations such as Alzheimer's disease. Plaques have a structure that is irregular, heterogeneous, and extremely variable — in shape, composition and location in the brain (Walker, 2020) (see some examples in Figure 5.9). Despite their variability, studies on the properties of amyloids (which are the main components of the plaques) can provide estimations of the plaque properties. Amyloids are long fibrillar masses, composed of straight and unbranching fibres with a tensile strength comparable to steel (Smith et al., 2006). A key feature that makes these compounds very resistant to degradation is their strong hydrophobic nature (van Gils et al., 2020). Since their core is high in lipid content, we model these plaques with a lower permeability than the surrounding brain tissue.

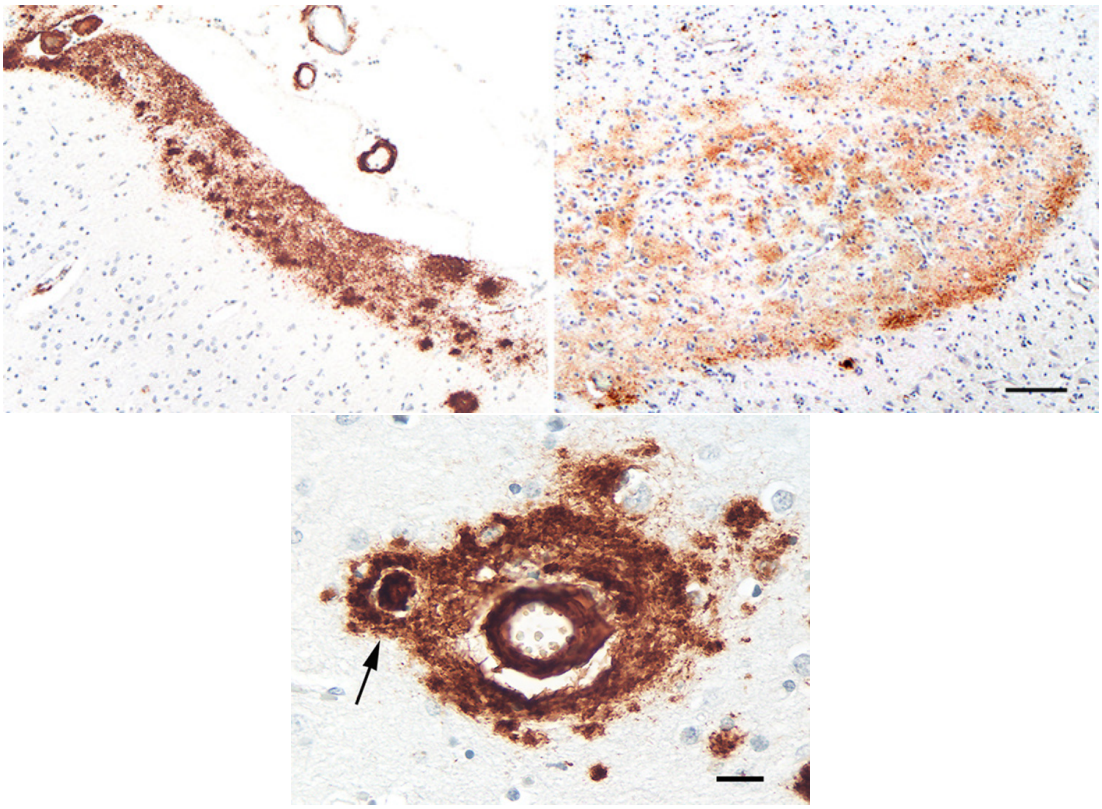

Figure 5.9: Examples of AβP (brown) in the case of Alzheimer's disease. The first row (where the scale bar for both images is 100 μm) shows subpial cortical plaques, while the second row (with scale bar of 20 μm) emphasises the proximity of the cortical plaque to a blood vessel (which is indicated by the arrow). Images are reproduced from Walker (2020).

We compare a simplified representation of the healthy brain tissue — with only the PVS and the BT — with two scenarios including the presence of AβPs, one where the plaque is next to the PVS and one where it is located further into the domain (in analogy with the examples shown in Figure 5.9). For the healthy tissue, we consider values of the permeability according to the ones used in the work by Kedarasetti et al. (2020), where the value in the PVS is reported to be ten times larger than the value in the BT. Given the absence of data for the permeability of the AβPs, we assume it to be one tenth that of in the BT. Through this simple and qualitative model, we aim to observe how the altered structure might further affect the glymphatic system by damaging the mechano-fluid coupling, boosting the positive feedback loop and leading to further plaque accumulation.

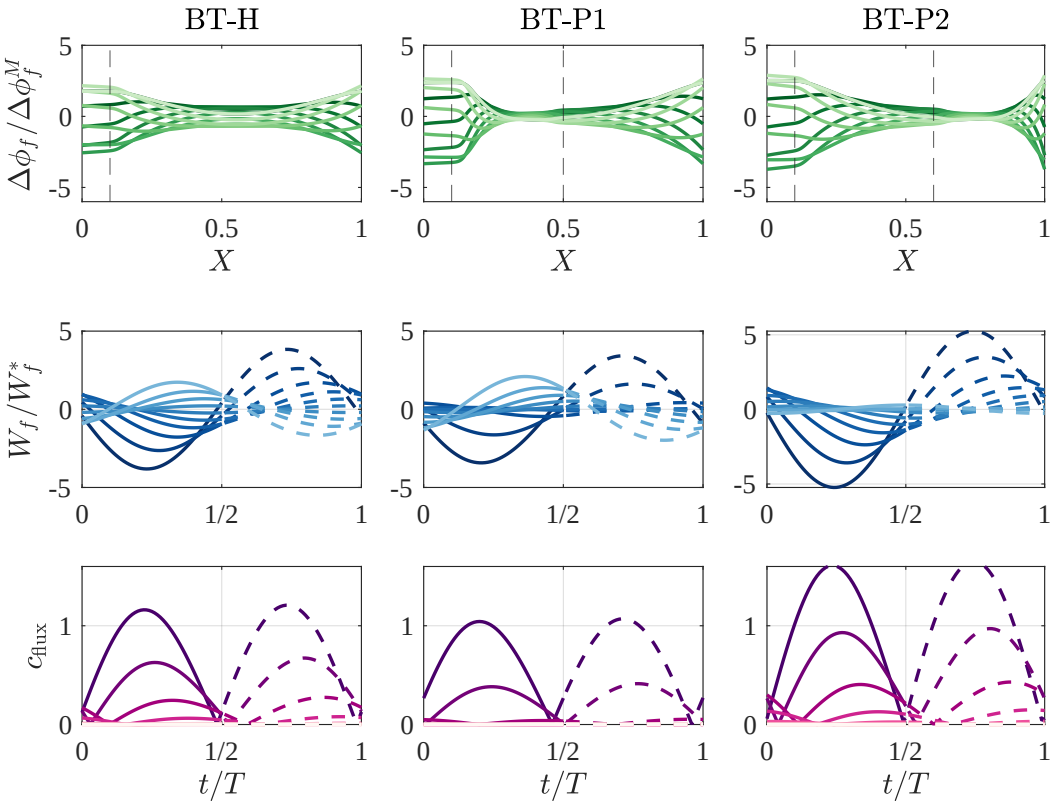

Figure 5.10: Evolution of $\Delta\phi_f$ (first row) at times $t = nT$ to $(n+1)T$ in increments of $0.1T$ (dark to light), where n is an integer, during one cycle in the periodic regime for $A = 0.1$, $\phi_{f,0} = 0.75$, and $T = 0.1\pi$, for a healthy brain tissue (first column) and two representations of brain tissue with AβPs (first and second column). In the second and third row, the normalised W_f/W_f^* and c_{flux} are plotted against t for ten different values of X from 0 to 1 (dark to light). We distinguish between the loading half of the cycle ($\dot{a} > 0$; solid curves) and the unloading half of the cycle ($\dot{a} < 0$; dashed curves).

In Figure 5.10, we show the impact of the presence of a low-permeability plaque on the poromechanical response to a periodic FFC load of amplitude $A = 0.1$ and period $T = 0.05\pi$ (which are nondimensionalised loading parameters in the range of the ones considered in (Kedarasetti et al., 2020)). Porosity, Darcy flux and solute flux are deeply altered by the presence of a low-permeability

layer. The first row of Figure 5.10 shows that $\Delta\phi_f$ in the unhealthy scenarios is subject to significantly higher jumps than in the healthy brain, with reduced deformations in the low permeability regions and enhanced deformations in the surrounding regions due to the low deformability of the plaques. This additional deformation could potentially lead to cell damage. In the second and third row, we observe that W_f and c_{flux} are also altered by the presence of the plaque, both in terms of the flux magnitudes and for their distribution throughout the domain. In particular, in BT-1, solute fluxes are significantly lower than in the healthy case. These fluid and transport flow alterations could lead to difficulties in clearing amyloid-β residuals and further accumulations of these harmful solutes, thus leading to progressive degeneration.

5.7 Conclusions

In this chapter, we used a simple one-dimensional model to consider the impact of layering on the response of a soft porous medium to large periodic deformations. Different layers are modelled in the medium via a spatially varying initial permeability. In this way, we compare three general scenarios: a homogeneous medium, a medium with a higher permeability in the left half and a lower permeability in the right half ($k_H k_L$), and a medium with a lower permeability in the left half and a higher permeability in the right half ($k_L k_H$). The model is based on large deformation poroelasticity and formulated in a Lagrangian frame, to facilitate the inclusion of a spatially heterogeneous permeability. For each medium, we compared two loading scenarios: (i) confined compression (CC), where the piston at the left is permeable and the fixed boundary at the right is impermeable, and (ii) free-flow compression (FFC), where both the piston and the fixed boundary are permeable. The former loading case is widely used to test articular cartilage and to mechanically stimulate cartilage scaffolds, while the latter is representative of the region of brain matter sandwiched between a pulsating arteriole and a venule.

For CC, both the $k_H k_L$ case and the $k_L k_H$ case modify the localisation of the deformations at the piston in fast loading with respect to the homogeneous medium. In the former, the response is overall more uniform, while in the latter localisation is enhanced. Local magnitudes of Darcy fluxes and solute fluxes are slightly modified compared to the homogeneous case. For FFC, the response of the homogeneous medium is mirrored with respect to its centre. In $k_H k_L$ and $k_L k_H$, the deformation is mirrored with respect to each other. The low permeability halves of each domain experience lower changes in porosities, while the high permeability halves deform more. The solute flux is respectively enhanced in $k_H k_L$ and suppressed $k_L k_H$ with respect to the homogeneous case.

To conclude this general study, we provided a simple analysis of the infiltration of the solutes from the left boundary in each loading case and for each medium, after a fixed number of cycles applied for three values of T. In all scenarios, the $k_H k_L$ and $k_L k_H$ media promote respectively the highest and lowest solute infiltration in fast loading. The solute profile for all three media progressively

overlap as T increases. This convergence is seen for low values of T (*e.g.*, $T = \pi$) in CC, and for high values of T (*e.g.*, $T = 100\pi$) in FFC.

From this general analysis, we can conclude that, both in CC and in FFC, the presence of two layers with different permeabilities and their order in the domain affects the distribution of the deformations, fluid fluxes and transport fluxes in response to periodic loads. In particular, a result of this alteration is visible on the transport of solutes, which is dependent on the spacial architecture. An important implication of these results is that the poromechanical response and the transport of solutes in a medium can be controlled and tuned with an appropriate design of the medium structure. For example, even a simple model like the one presented here could help designing scaffolds for tissue engineering to ensure specific deformation and flux conditions and an adequate supply of the nutrients throughout the domain.

Finally, we proposed simplified models of healthy *versus* damaged biological tissue for articular cartilage and brain tissue. In the case of cartilage, two possible healthy distributions of permeability layers were compared with a hypothetical case of highly enhanced superficial permeability, corresponding to the damages induced by osteoarthritis. For the brain, a simplified structure representing the paravascular space and the brain tissue was compared with two configurations presenting a low permeability layer — positioned in two different locations — representing an amyloid-β plaque. For both tissues, a damaged permeability distribution leads to an altered poromechanical response that modifies the original localisation and magnitudes of the deformations — possibly dangerously loading the living cells — and the fluid and transport flows, possibly impacting the transport of nutrients and the clearance of waste and harmful substances. This analysis could provide poromechanical insights for the understanding of the progression of these diseases, and potentially of other ones. For example, another cartilageneous structure whose layered structure is often damaged is the intervertebral disk. In the intervertebral disk, there are two main layers: the nucleus polposus — a homogeneous and highly hydrated core — and the anulus fibrosus — a concentric region surrounding the nucleus with fibres aligned obliquely (Jensen, 1980) to adapt to the complex directionality of the loads (Marini and Ferguson, 2014). In an injured intervertebral disk, the nucleus experiences a reduction in water content, thus becoming stiffer, less permeable and more solid-like (Inoue and Espinoza Orías, 2011). The permeability is altered in the anulus fibrosus, with consequent changes in fluid flow and nutrient transport(Gu et al., 1999). An overall lower pore pressure propagates preexisting cracks, where stresses tend to concentrate (Wognum et al., 2006). Given its geometry and spacial organisation, the intervertebral disk would have to be modelled in two dimensions; hence, future work could imply the extension of the model in 2D to study the impact of an altered layered structure in more complex biological tissues.

Chapter 6

Laboratory experiments

6.1 Introduction

The nontrivial coupling between deformation and fluid flow in soft porous media has been the object of significant interest in experimental campaigns. However, the effect of this coupling on the transport of solutes has not been observed experimentally. In this chapter, we design, construct and test an experimental system for studying the transport of solutes in a soft porous medium subject to periodic loads.

Several standard techniques are available for the experimental characterisation of flow and solute transport in rigid porous media, where the heterogeneity of the flow has been linked to the specific structure of the porous network (Bordoloi et al., 2022, Datta et al., 2013, Holzner et al., 2015). A common method to visualise the details of the flow is via refractive index matching and laser-induced fluorescence (LIF) (for example, (Brouzet et al., 2022, Catania et al., 2008, Kree and Villermaux, 2017, Roth et al., 2021)). Especially at the pore scale, fluorescence allows a precise quantification of mixing and dispersion of solutes in two dimensional (Borgman et al., 2023, de Anna et al., 2014) and in three dimensional bead packs (Kree and Villermaux, 2017), with a detailed comparison with the stretching laws for mixing and chaotic advection in the latter (Heyman et al., 2020, Souzy et al., 2020).

At the Darcy scale, a unique quantification of the solute concentration requires a calibration phase, because the scale of the field of view includes both the fluid in the pores and the solid and is hence heterogeneous. This light intensity calibration enables to apply Beer-Lambert's law to a wide variety of solutes; usually, food dyes and other non-fluorescent dyes are employed (Corapcioglu and Fedirchuk, 1999, McNeil et al., 2006, Neupauer et al., 2021, Roth et al., 2021, Sahu and Neufeld, 2023), with some exceptions (Catania et al., 2008, Roth et al., 2021). This method has been used to track breakthrough curves under steady (Basilio Hazas et al., 2023, Brouzet et al., 2022, Corapcioglu and Fedirchuk, 1999, McNeil et al., 2006, Sahu and Neufeld, 2023) or pull-push flows (Neupauer et al., 2021, Roth et al., 2021).

In rigid media, the solid fraction is fixed, and the evolution of concentration distribution is driven by fluid flow and by molecular diffusion. In a periodically deformed medium, the geometry – and, potentially, the topology – of the pore network vary continuously and heterogeneously throughout the medium. A proper calibration, and consequently, a quantitative tracking of the Darcy-scale solute concentration are hence more challenging: as we showed in our numerical results in Chapter 4, the concentration profiles at any point during the deformation depend on the respective change in porosity, fluid velocity distribution and evolving pore structure. Therefore, we provide here a first step for this complex analysis, with a characterisation of the longitudinal and transverse spreading of the initial solute profile and compare it with the results from our theoretical model.

Previous experiments on soft porous media have employed different types of media. Polyurethane foams and sponges — readily available and durable — have been used to study the coupling between flow and deformation in a uni-axial setting by tracking the motion of the solid, but not the fluid (Beavers et al., 1975, Lanir et al., 1990, Lutz et al., 2021, Parker et al., 1987). The opaque nature of these materials prohibits visual observation of flow and solute transport. An alternative system for studying flow and deformation in soft porous media is a packing of hydrogel particles or beads. These packings are soft and elastic, and can be assumed to behave collectively as a homogeneous medium (Hewitt et al., 2015, 2016a, MacMinn et al., 2015). They are also transparent and naturally index-matched with water, enabling direct visualisation of solute transport (Harshani et al., 2016). However, these beads are non-cohesive and therefore cannot support tension. The ability to support tension is essential in several contexts, including biological applications. Moreover, hydrogel beads might absorb part of the solutes introduced in the aqueous environment, and potentially have an osmotic response to the presence of the solutes. Hydrogel blocks are usually employed to quantify the absorption or desorption of solutes after long loading times (Albro et al., 2008, Mauck et al., 2003, Urciuolo et al., 2008, Vaughan et al., 2013). These materials have low stiffness but very low permeability and very small pores (in the order of micrometers). Hence, a direct visualisation of flow and transport (and, in particular, of hydrodynamic dispersion) in the pores is challenging, because of the small size of the pore network.

Recently, several studies fabricated a variety of porous media made of Polydimethylsiloxane (PDMS), a silicon polymer known for its thermal and mechanical stability, hydrophobicity, and biocompatibility (Zhu et al., 2017). One reported method employs a sacrificial structure – serving as a template for the pore network – that can be dissolved with water once the PDMS has solidified. The sacrificial template can consist of either ordinary granulated sugar (Choi et al., 2011, King et al., 2009, Zhang et al., 2013), caramel slabs (Zhou et al., 2018), sugar fibres (Lee et al., 2012), 3D printed sugar patterns (He et al., 2015), or salt (Zhao et al., 2014). These PDMS "sponges" have several advantages: they are approximately transparent, cohesive and with tunable pore network (according to the sacrificial structure employed in the fabrication). Hence, we use this established

protocol to fabricate PDMS sponges with a macroscopic pore network and low stiffness. Instead of ordinary sugar, which have irregular shapes, we use sugar spheres of different diameters that allow us to achieve media with a controlled pore size. In this way, we can achieve media with different porosities and permeabilities. The stiffness of these media can be also tuned independently of the pore geometry. We fabricate the sponges so that their thickness is small relative to the other dimensions. In this way, we can assume that they behave effectively like a two-dimensional medium, as often applied in similar setups (Rolle et al., 2009, Ye et al., 2015) or in Hele-Shaw cells (de Anna et al., 2013, MacMinn et al., 2015).

These new soft porous media are used here to observe experimentally solute transport in response to periodic deformations that are either small or large, and either slow or fast. We begin the experiments with a material mechanical characterisation, performed with methods reported in literature (Beavers et al., 1975, Hewitt et al., 2016a, Lanir et al., 1990, Lutz et al., 2021, Parker et al., 1987, Paterson et al., 2019); in particular, the stiffness of the media is assessed through force-displacement curves, and the deformation-dependent permeability is measured using Darcy's law and at different compressive strains. The transport of the solutes in the PDMS sponges is then experimentally characterised by injecting an approximately round patch of dye in the middle of the sponge and tracking its spreading in the two dimensions throughout a defined total time. We first characterise the case of molecular diffusion only, where no load is applied. Then, we compare the evolution of the solute patch and the longitudinal and transverse travel distance in each loading scenario.

Our second goal in this study is to provide an experimental validation for the model presented in Chapter 4. For this purpose, we formulate here a "semi-2D" version of the model. This model aims to capture the behaviour of these "quasi-two-dimensional" PDMS sponges when subject to confined compression. The semi-2D model, therefore, neglects variations across the thickness of the medium and assumes that in confined compression the poromechanics of the sponge is approximately one-dimensional (since no flow is allowed in the transverse direction), while the solute transport driven by concentration gradients is two-dimensional, since the dye is injected as a round blob. With an estimation of the molecular diffusion and hydrodynamic dispersion coefficients, we show that our model qualitatively captures the solute movements in response to representative loading parameters.

The chapter is organised as follows. We begin with the experimental campaign, which consists of three main steps: (i) fabrication of appropriate materials, (ii) design of the experimental setup and protocol, and (iii) material characterisation. We then formulate the semi-2D theoretical model used in the comparison with the experimental data. Finally, we present the experimental results and compare them with the numerical ones, for the model validation.

6.2 Experiments

We describe here the experimental protocol, including the material fabrication, the experimental setup and material characterisation.

6.2.1 Material fabrication

A square mold ($50 \times 50 \times 8 \pm 0.5$ mm) is filled with sucrose granules (hsconline). A permeable aluminium piston is positioned against one side of the mould. Liquid PDMS (SYLGARD™ 184 Silicone Elastomer Kit; Dow) is then prepared, poured in the mold, and left to cure for at least 72 hours at room temperature (22°C). Note that, after the PDMS polymerisation, the permeable piston is embedded in the material, avoiding the need for any special clamping solution. When the solidification is complete, the material is removed from the mold and submerged in water to dissolve the sugar, leaving behind a PDMS sponge. The pore structure of the resulting sponge will comprise the volume originally occupied by the sucrose granules. We focus on spherical sugar granules with a nominal diameter of 1.5 mm, but similar granules can be purchased in a range of sizes, with the possibility to tune pore size, porosity and permeability in the sponge. The stiffness of the sponge is controlled in part by the pore structure and in part by the stiffness of the PDMS, which is itself controlled by the ratio of base to crosslinker and by the curing conditions. We focus here on a ratio of 12.5 to 1 and cure at room temperature. An example sponge is shown in Figure 6.1, illustrating the stages of fabrication and the use of two different granule sizes to produce a heterogeneous sponge with two layers. The final relaxed dimensions of the sponge are expected to be the same as for the mold.

6.2.2 Experimental setup

The experimental set-up is shown in Figure 6.2. A transparent rectangular quasi-2D chamber (with a thickness of 8 ± 0.1 mm, considerably smaller than its length and width) is constructed from laser-cut acrylic components. The chamber consists of two transparent parallel plates that position and sandwich the sponge to prevent out-of-plane deflections, which are separated by four impermeable spacers of the same thickness as the sponge, delimiting the left, right, bottom and top boundaries (which are taken to be the same as in our model). We load the sponge with a piston inserted through a water-tight port in the left spacer (see Figure 6.3, right). The chamber is clamped together and secured to an external plate with four screws. The upper plate of the chamber is leveled horizontally (within ± 5 degrees) to avoid any influence of gravity. The fluid-permeable piston embedded in the sponge is connected to the piston, which is attached to a displacement-controlled actuator (M-229.26S stepper linear actuator, connected to a C-663.12 stepper motor controller; PI). Images are recorded through a CMOS camera (ACA4096-30UM; Basler), with an image resolution of 14 pixels per mm at a frame rate of 2 frames per second.

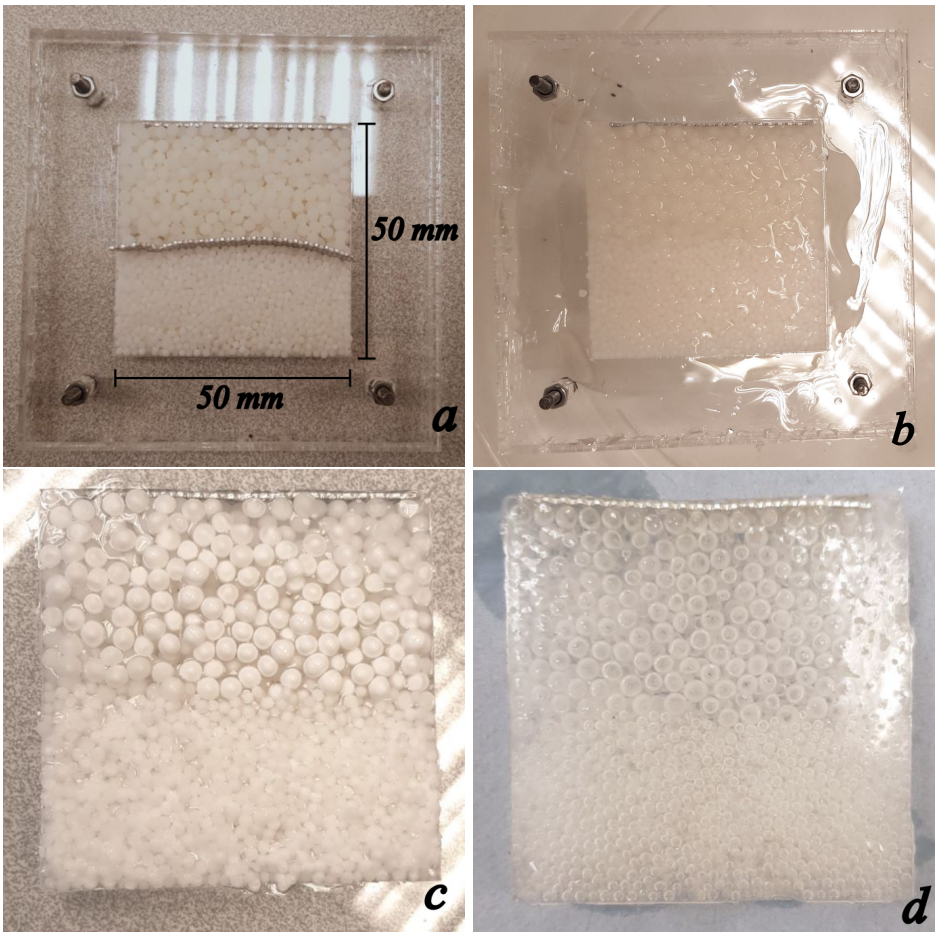

Figure 6.1: Stages of material fabrication. (a) the sugar granules are placed in the $50\times50\times8\pm0.5$ mm mold. (b) the mold is flooded with PDMS and left to cure. The permeable aluminium piston is placed in the mould and results embedded in the polymer. Note that a heterogeneous sponge is shown here, layering sugar granules with different diameters. (c) The cured material is removed from the mold and washed to dissolve the sugar granules, resulting in (d) a soft, porous and permeable PDMS sponge.

In the assembled setup, the actuator is connected to the loading arm using a low-friction cylinder-sliding guide mechanism comprising a delrin cylinder and a stainless-steel guide. This mechanism ensures a loading transmission entirely along the axis of operation of the actuator. The part of the permeable piston embedded in the sponge is sewed to a permeable aluminium piston, attached to the rest of the arm (see Figure 6.3, left). To mitigate sliding friction between the PDMS and the front and back plates of the chamber, a thin sheet of hydrated gelatine is positioned between the sponge and each plate. After placing the sponge and closing the chamber, the latter is filled with water through sealable apertures in the spacers connected to an external reservoir through tubes (see Figure 6.3, right).

Before starting the experiment, a defined amount of dyed water is injected from a syringe through a hole in the right boundary, which is then sealed. A custom-written code (MATLAB 2022b) is used

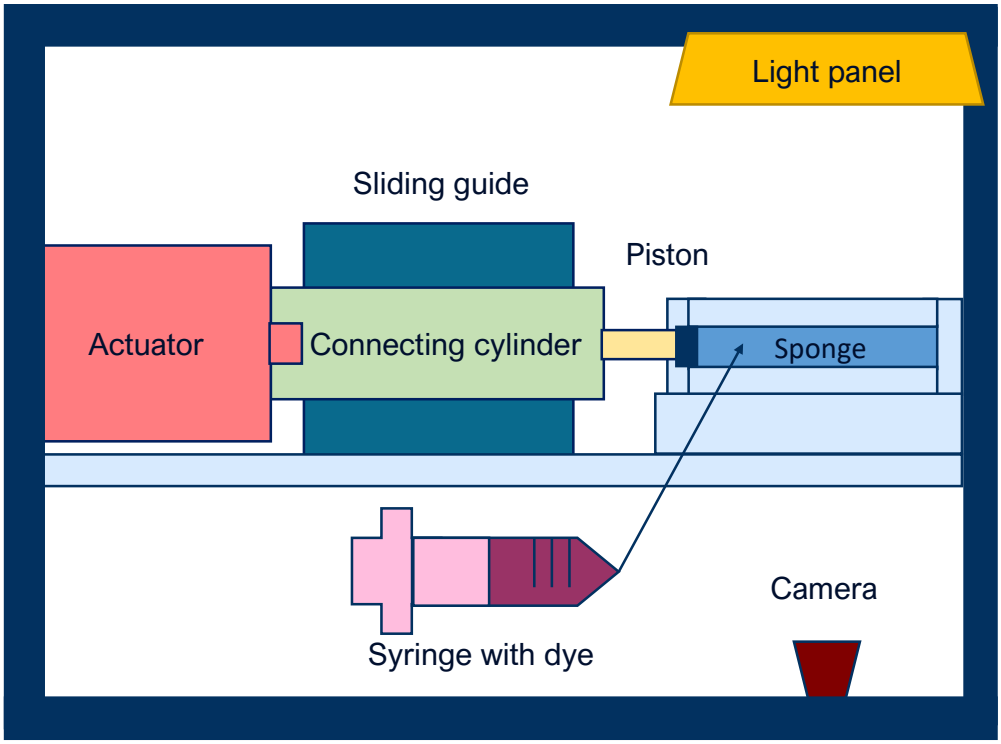

Figure 6.2: Experimental setup. The sponge is placed in a quasi-2D transparent chamber, filled with water. A permeable grid-like piston is embedded in the sponge and connected through the loading arm to the actuator applying the periodic deformation. The actuator transmits the loads via a low-friction cylinder-sliding guide system, to avoid any off-axis load. A defined amount of dye is injected from a syringe through a hole in the right boundary. Images are recorded with a camera. The cell is back-lit with a light panel. The synchronization of stimulation and imaging is achieved by controlling both the actuator and the camera from a PC with a code written for the purpose. A top view of the real testing chamber is shown in Figure 6.3.

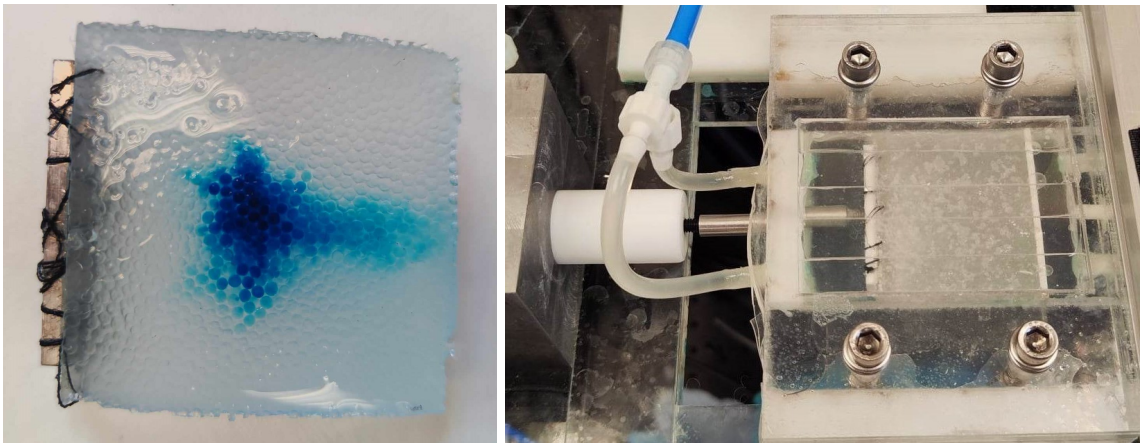

Figure 6.3: Left: the sponge is shown with the permeable piston sewed to the loading arm. The sponge has been injected with blue dye that has diffused into the pore space. Right: detail of the final sponge placed in the loading chamber and compressed via the piston.

to synchronise the actuator motion to the camera output. The actuator is programmed to impose a triangular-wave displacement at the left boundary, with a constant velocity $\dot{a} = 2A/T$ in the first half of each cycle and $-2A/T$ in the second half of each cycle. The whole experiment — where solute transport is observed through the camera output video in relation to the applied periodic displacement — is performed in confined compression.

6.2.3 Material characterisation

To compare experimental data with the predictions of our model, mechanical and fluid-flow properties – such as porosity, stiffness, and permeability – are required.

We measure the initial porosity of the material by dividing the total volume of sugar spheres by the total volume of the sample. The total volume of sugar spheres is measured by dividing the total weight of the packing by the weight of a single granule (to give the number of granules) and then multiplying by the volume of a single granule. To assess the repeatability of our fabrication procedure, we fabricate the same type of sponge three times and then taking the average and standard deviation of the three porosity values. We find a relaxed porosity of $\phi_{f,0} = 0.70 \pm 0.03$. This value suggests that the packing of sugar spheres is denser than a random close packing (0.64), but looser than a face-centered crystal arrangement (0.74), suggesting that the packing generally follows a random arrangement, with some portions following a local ordered crystal packing.

We estimate the p-wave modulus of the material with a force-displacement test in a separate setup. A force sensor (3132 - Micro Load Cell (0-780g) - CZL616C; Robotshop) is placed at the bottom of the chamber and a quasi-static periodic load is prescribed at the piston. The stress is calculated from the measured force divided by the cross-sectional area of the sponge, $A_s = 8 \pm 0.5$ mm.

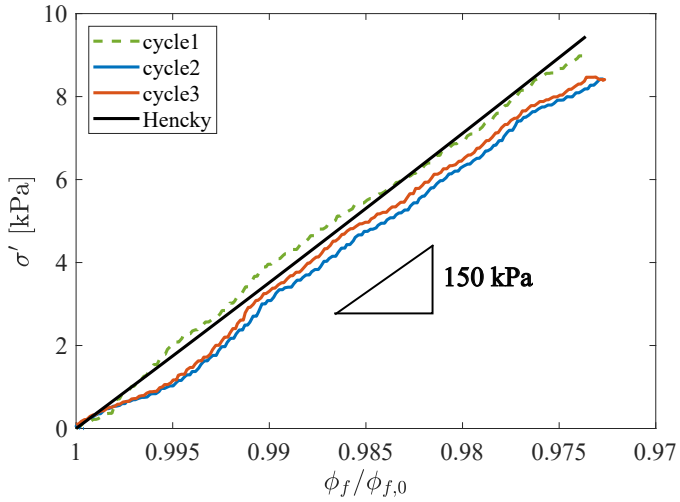

Figure 6.4: Example of a stress-porosity test on a PDMS sponge, performed in the loading phase. The data from the first loading cycle (dashed line) are discarded in the calculations. For comparison, we include theoretical values calculated with Hencky elasticity, with $\mathcal{M} = 150$ kPa (black line).

The nominal strain $\epsilon = a(t)/L_x$ is the change in length per unit original length. The porosity is then calculated as $\phi_f = (\phi_{f,0} + \epsilon)/(1 + \epsilon)$. We plot the stress against porosity from a typical experiment in Figure 6.4, demonstrating roughly linear and repeatable elastic behavior up to moderate strains. In this range of strains, the behaviour is well captured by Hencky elasticity (Figure 6.4, black line). To avoid hysteretic behaviour, we consider the second and third loading cycles only. We average the p-wave modulus from five tests, giving $\mathcal{M} = 150 \pm 3$ kPa.

To measure the permeability, we follow the standard procedure and use Darcy's law (Beavers et al., 1975, Lanir et al., 1990, Lutz et al., 2021, Parker et al., 1987). We impose a known volumetric flow rate Q (in the range 1-3 ml/min) through the sponge using a syringe pump (AL-4000; WPI) while measuring the pressure upstream of the sponge, with a pressure transducer (40PC001B3A; Honeywell) referenced to the atmospheric pressure in the lab. To calculate the pressure drop across the sponge only, we also measure the pressure drop during flow through the empty chamber and subtract it from the pressure drop measured with the sponge. We impose three values of flux $q = Q/A_s$ and measure the resulting pressure difference ΔP for each. We then calculate the permeability k_0 as the slope of the q-$\Delta P/(\mu L)$ curve. An example data set shown in Figure 6.5 (left). We perform the measurement on the undeformed sponge and for two values of compressive strain (5% and 10%,), which we then convert to porosity. We repeat each measurement three times. The resultant permeability-porosity curve is shown in Figure 6.5, on the right. Error bars indicate the standard deviation over the three measurements. The relaxed permeability is $k_0 = 1.97 \pm 0.01 \times 10^{-12}$ m^2 (note that this standard deviation refers to a single sponge). We use the value of k_0 to calculate the permeability as function of porosity following Kozeny-Carman relation. The deformation-dependent

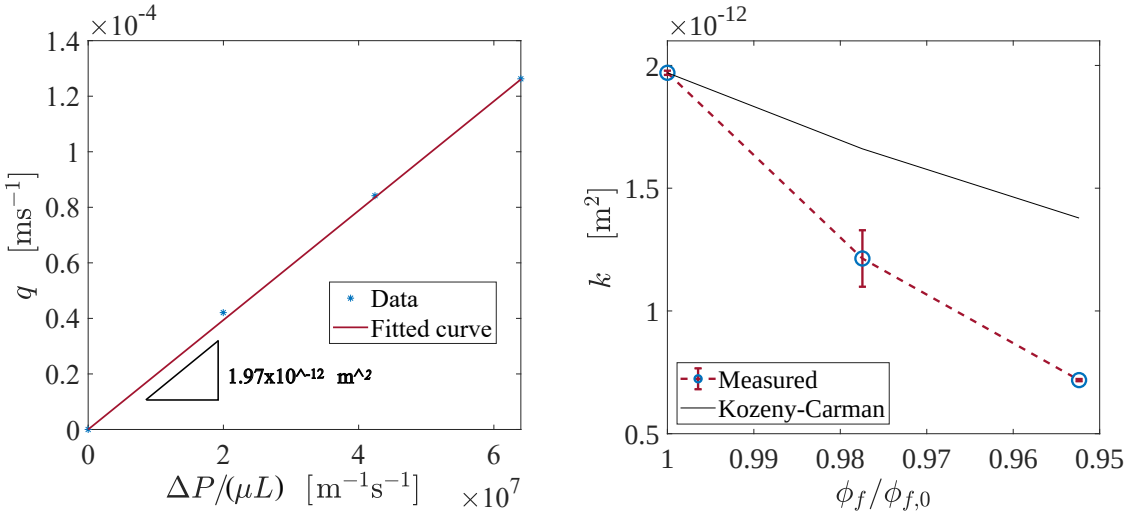

Figure 6.5: Left: set of flux *vs* normalised pressure drop measurements for a PDMS sponge. The permeability k is calculated as the slope of the fitted line. Right: permeability as a function of porosity. For each porosity value, three measurements are performed and averaged. Error bars indicate the standard deviation of the three measured values. The black line is calculated using Kozeny-Carman relation.

permeability data retrieved experimentally have lower values than the ones predicted with Kozeny-Carman, but they show similar trends.

The overall goal of the material characterisation is to derive the poroelastic timescale $T_{\mathrm{pe}} = \mu L^2/(k_0 \mathcal{M})$, determining the range of slow-loading and fast-loading. The fluid used in the experiments is water, with $\mu = 10^{-3}$ Pa s. With $L = 0.05$ m being the length of the sponge, and considering the approximate values $k_0 = 2 \times 10^{-12}$ m^2 and $\mathcal{M} = 150$ kPa, we obtain $T_{\mathrm{pe}} = 8.33$ s. Note that this value is relatively low. This means that observing the material in fast loading would require a very fast deformation applied at the piston. The speed of the piston is limited by the top operating speed of the actuator. This speed is nominally 4 mm/s, but we limit it to 1 mm/s during periodic loading, to avoid damage related to the repeated changes in direction. The largest amplitude we consider is $\tilde{A} = 0.1$, corresponding to $A = 5$ mm given the length of sponge. To study the fast-loading regime, with a maximum speed of 1 mm/s, the poroelastic timescale should be in the order of 10 s or larger. This implies that, with the poroelastic timescale typical of this study, our observations are limited to a material subject to slow loading and relatively fast loading (*i.e.* we cannot explore the range $\tilde{T} < 1$).

6.3 Semi-2D model

In the experiments, the applied load — and the resultant fluid and solid velocities — are assumed to induce a 1D poro-mechanical coupling, with advection and longitudinal hydrodynamic dispersion acting as in the 1D model formulated in Chapter 4. Molecular diffusion is assumed to remain

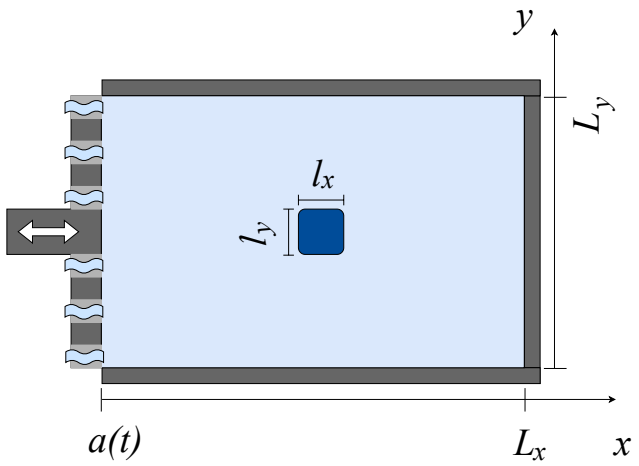

Figure 6.6: Schematic representation of the 2D domain of dimensions L_x and L_y. The medium experiences periodic, uniaxial loading by a permeable piston (left) so that fluid and solid motion occur only in the x-direction. Solute spreads in both directions from an initial blob of dimensions l_x and l_y in the middle of the sample (dark blue). The right, bottom and top boundaries are fixed and impermeable.

isotropic, driving the transport of solutes in all directions. Dispersion also has a transverse component, typically weaker than the longitudinal one. Hence, we formulate here a semi-2D model, where the poromechanical coupling is in one dimension and follows the formulations derived in Chapter 3, while the equations for solute transport are derived in two dimensions. Note that this model is formulated in Eulerian coordinates, since all the material properties are homogeneous.

6.3.0.1 Model problem

The two-dimensional soft porous medium has a relaxed longitudinal length L_x and transverse length L_y. The 1D poromechanical features are equivalent to the ones described in Chapter 3, with a relaxed porosity $\phi_{f,0}$, permeable left boundary located at $x = a(t)$, and impermeable right boundary located at $x = L_x$. In analogy with our experiments (see Section 6.2.2), the displacement applied at the piston follows a triangular wave, with $\dot{a}(t) = 2A/T$ and $-2A/T$ in the first and second halves of each cycle, respectively. The bottom and top boundaries (at $y = 0$ and $y = L_y$, respectively) are fixed and impermeable. In this configuration, we place a blob of solute of initial dimensions l_x and l_y in the centre of the domain. A schematic of this model problem is shown in Figure 6.6. Because the flow and deformation are uniaxial, the poromechanical problem is identical to that presented and analysed in Chapter 3.

6.3.0.2 2D solute transport

In 2D but with no flow in the y-direction, conservation of mass for the solute becomes:

$$\frac{\partial(\phi_f c)}{\partial t} + \frac{\partial}{\partial x}\left[(\phi_f c)v_f - \phi_f \mathcal{D}_x \frac{\partial c}{\partial x}\right] + \frac{\partial}{\partial y}\left[- \phi_f \mathcal{D}_y \frac{\partial c}{\partial y}\right] = 0, \tag{6.1}$$

where c is again the local solute concentration and $\mathcal{D}_x$ and $\mathcal{D}_y$ are now defined as

$$\mathcal{D}_x = \mathcal{D}_m + \mathcal{D}_{h,x} = \mathcal{D}_m + \alpha_L \mid v_f - v_s \mid \tag{6.2}$$

and

$$\mathcal{D}_y = \mathcal{D}_m + \mathcal{D}_{h,y} = \mathcal{D}_m + \alpha_T \mid v_f - v_s \mid, \tag{6.3}$$

with α_L and α_T the longitudinal and transverse dispersivities, respectively. Note that flow in the x-direction drives dispersion in both directions. Advection, on the contrary, only occurs longitudinally. The coefficient for molecular diffusion $\mathcal{D}_m$ is assumed to be isotropic. For simplicity, $\mathcal{D}_m$, α_L and α_T are all assumed to be constant, despite the hypothesis that they might be deformation-dependent. As we discuss in Chapter 7, we are planning to include the testing of this hypothesis in our future work.

As in our experiments, we consider a two-dimensional blob of solute that is initially located at the centre of the domain. The initial conditions for the 2D transport problem hence read:

$$\begin{aligned} c(x,y,0) = \frac{c_0}{2}\Big\{ &\{\tanh\left[s(x - L_x/2 - l_x/2)\right] - \tanh\left[s(x - L_x/2 + l_x/2)\right]\} \\ &\times\{\tanh\left[s(y - L_y/2 - l_y/2)\right] - \tanh\left[s(y - L_y/2 + l_y/2)\right]\} + 1\Big\}, \end{aligned} \tag{6.4}$$

where c_0 is the initial solute concentration, l_x and l_y are the initial longitudinal and transverse dimensions of the solute patch and s is a steepness parameter. The longitudinal boundary conditions (at the left and right boundaries) are

$$c(x = a, t) = 0 \quad \text{and} \quad \left.\frac{\partial c}{\partial x}\right|_{x=L_x} = 0. \tag{6.5}$$

The transverse boundary conditions (at the bottom and top boundaries) are

$$\left.\frac{\partial c}{\partial y}\right|_{y=0} = 0 \quad \text{and} \quad \left.\frac{\partial c}{\partial y}\right|_{y=L_y} = 0. \tag{6.6}$$

We make the problem dimensionless via the scaling

$$\begin{aligned} &\tilde{x} = \frac{x}{L_x},\ \tilde{y} = \frac{y}{L_x},\ \tilde{t} = \frac{t}{T_{\mathrm{pe}}},\ \tilde{c} = \frac{c}{c_0},\ \tilde{l_x} = \frac{l_x}{L_x},\ \tilde{l_y} = \frac{l_y}{L_x},\ \tilde{\alpha_L} = \frac{\alpha_L}{L_x},\ \tilde{\alpha_T} = \frac{\alpha_T}{L_x}, \\ &\tilde{\mathcal{D}_x} = \frac{\mathcal{D}_x}{\mathcal{D}_m} = 1 + \tilde{\alpha_L}\mathrm{Pe} \mid \tilde{v}_f - \tilde{v}_s \mid,\ \tilde{\mathcal{D}_y} = \frac{\mathcal{D}_y}{\mathcal{D}_m} = 1 + \tilde{\alpha_T}\mathrm{Pe} \mid \tilde{v}_f - \tilde{v}_s \mid . \end{aligned} \tag{6.7}$$

The dimensionless 2D transport problem reads:

$$\frac{\partial(\phi_f \tilde{c})}{\partial \tilde{t}} + \frac{\partial}{\partial \tilde{x}}\left[(\phi_f c)\tilde{v_f} - \phi_f \mathrm{Pe}^{-1}\tilde{\mathcal{D}_x}\frac{\partial \tilde{c}}{\partial \tilde{x}}\right] + \frac{\partial}{\partial \tilde{y}}\left[- \phi_f \mathrm{Pe}^{-1}\tilde{\mathcal{D}_y}\frac{\partial \tilde{c}}{\partial \tilde{y}}\right] = 0, \tag{6.8}$$

with initial conditions

$$\begin{aligned} \tilde{c}(\tilde{x},\tilde{y},0) = \frac{1}{2}\Big\{ &\{\tanh\left[\tilde{s}(\tilde{x} - 1/2 - \tilde{l_x}/2)\right] - \tanh\left[\tilde{s}(\tilde{x} - 1/2 + \tilde{l_x}/2)\right]\} \\ &\times\{\tanh\left[\tilde{s}(\tilde{y} - L_y/(2Lx) - \tilde{l_y}/2)\right] - \tanh\left[\tilde{s}(\tilde{y} - L_y/(2Lx) + \tilde{l_y}/2)\right]\} + 1\Big\}, \end{aligned} \tag{6.9}$$

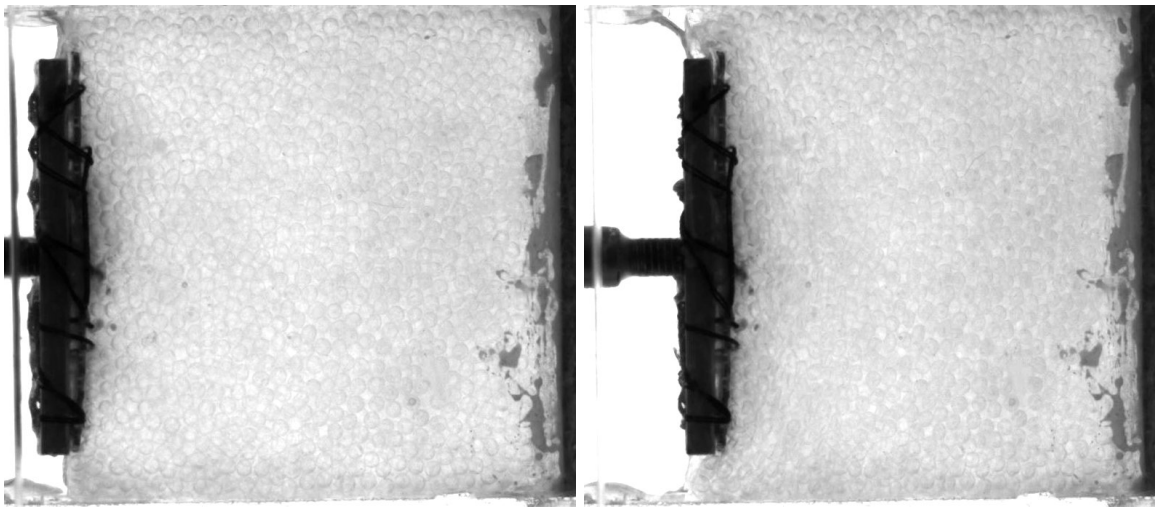

Figure 6.7: PDMS sponge in the relaxed configuration (left), and subject to compression with $\tilde{A} = 0.2$ (right). The pores can be used as markers for particle image velocimetry.

where we have taken $\tilde{s} = sL = 60$. The scaled boundary conditions at the left and right boundaries are

$$\tilde{c}(\tilde{a}, \tilde{t}) = 0 \quad \text{and} \quad \left.\frac{\partial \tilde{c}}{\partial \tilde{x}}\right|_{\tilde{x}=1} = 0, \tag{6.10}$$

while at the bottom and top boundary they are

$$\left.\frac{\partial \tilde{c}}{\partial \tilde{y}}\right|_{\tilde{y}=0} = 0 \quad \text{and} \quad \left.\frac{\partial \tilde{c}}{\partial \tilde{y}}\right|_{\tilde{y}=1} = 0. \tag{6.11}$$

This formulation for the solute transport model is coupled with the one-dimensional poromechanical model described in Chapter 3, which describes the evolution of ϕ_f, v_f, and v_s. We compare the predictions of this semi-2D model with our experimental results in Section 6.4.1.

6.4 Experimental results

6.4.1 Poromechanical coupling

We begin by assessing the poromechanical response of the material to periodic deformations. To do so, we impose a periodic deformation that has the form of a triangle wave in displacement with four combinations of amplitude and period: (i) small-amplitude and slow-loading ($A = 1$ mm, $T = 50$ s), (ii) small-amplitude and fast-loading ($A = 1$ mm, $T = 10$ s), (iii) large amplitude and slow-loading ($A = 5$ mm, $T = 50$ s) and (iv) large amplitude and fast-loading ($A = 1$ mm, $T = 50$ s). These cases are chosen to capture some of the main findings reported in Chapters 3 and 4. Note that, as mentioned above, the low value of T_{pe} limits the lower end of the loading periods that we can explore; with the PDMS sponges considered here, we can only characterise the slowest end of the fast-loading regime.

We perform particle image velocimetry (PIV) using the open-source software PIV-Lab (Thielicke and Sonntag, 2021, Thielicke and Stamhuis, 2014). We show an example of the undeformed and compressed PDMS sponge in Figure 6.7. In the sponges, the distribution of macroscopic pores provides a visual pattern that can be used to track the deformation of the material with respect to the relaxed configuration. We restrict the PIV analysis to a central region of interest in the sponge directly deformed by the piston, which is assumed to be distant enough from the top and bottom spacers. Figures 6.8 and 6.9 show the experimental (left) and numerical (right) solid velocities, normalised by $\tilde{v_s}^* = 2\tilde{A}/\tilde{T}$, for the slow-loading and fast-loading cases, respectively. The velocity of the piston is constant and to the right during the first half of the cycle and then constant and to the left during the second half of the cycle. Hence, in all plots, the solid velocity is positive during the first half of the cycle and negative during the second half of the cycle. The velocities are plotted in the laboratory (Eulerian) frame, and hence against x, because this is the frame in which PIV operates. Hence, the curves are not on top of each other because the piston is moving. The evolution of the normalised velocities during one loading cycle is captured by the model. For the slow-loading cases shown in Figure 6.8, the velocity decreases linearly in space from the value at the piston to zero at the right. The small-amplitude experimental lines are considerably noisy, as expected, given the small magnitude of the velocity imposed. In the fast-loading cases shown in Figure 6.9, the velocity profiles are slightly nonlinear, still decreasing in space from the value at the piston to zero. The variability observed in the experimental data is due to two main factors: the accuracy of the PIV measurements, which we estimate as the minimum velocity resolution (calculated as the ratio of the frame rate (frames per second) to the spatial resolution (pixels per mm), corresponding to 0.15 mm/s) and the "noisy" response of the material. The latter is related to the fact that PIV measures the local motion of the material, which is fairly complex as the pore geometry distorts. Note that the solid velocity calculated with PIV in the transverse direction is relatively random in space and about ten times smaller in magnitude than the longitudinal velocity. The deformation is hence considerably larger in the longitudinal direction. Moreover, the value of the solid velocity transverse component is biased by local changes at the microscale, thus providing an upper bound for the value of the fluid velocity which is expected to be significantly lower. Modelling the deformation as one-dimensional is therefore an appropriate approximation.

6.4.2 Solute transport

In this section, we observe the solute spreading experimentally and compare it with our theoretical model. We inject 20 μl of water dyed with Erioglaucine disodium salt (Alfa Aesar) in the middle of the sponge. The injection is performed with a syringe through an aperture in the right boundary. The needle is then retracted and the aperture is sealed, before images start being recorded. We trace the evolution of the solute profile by binarising each image based on an intensity threshold

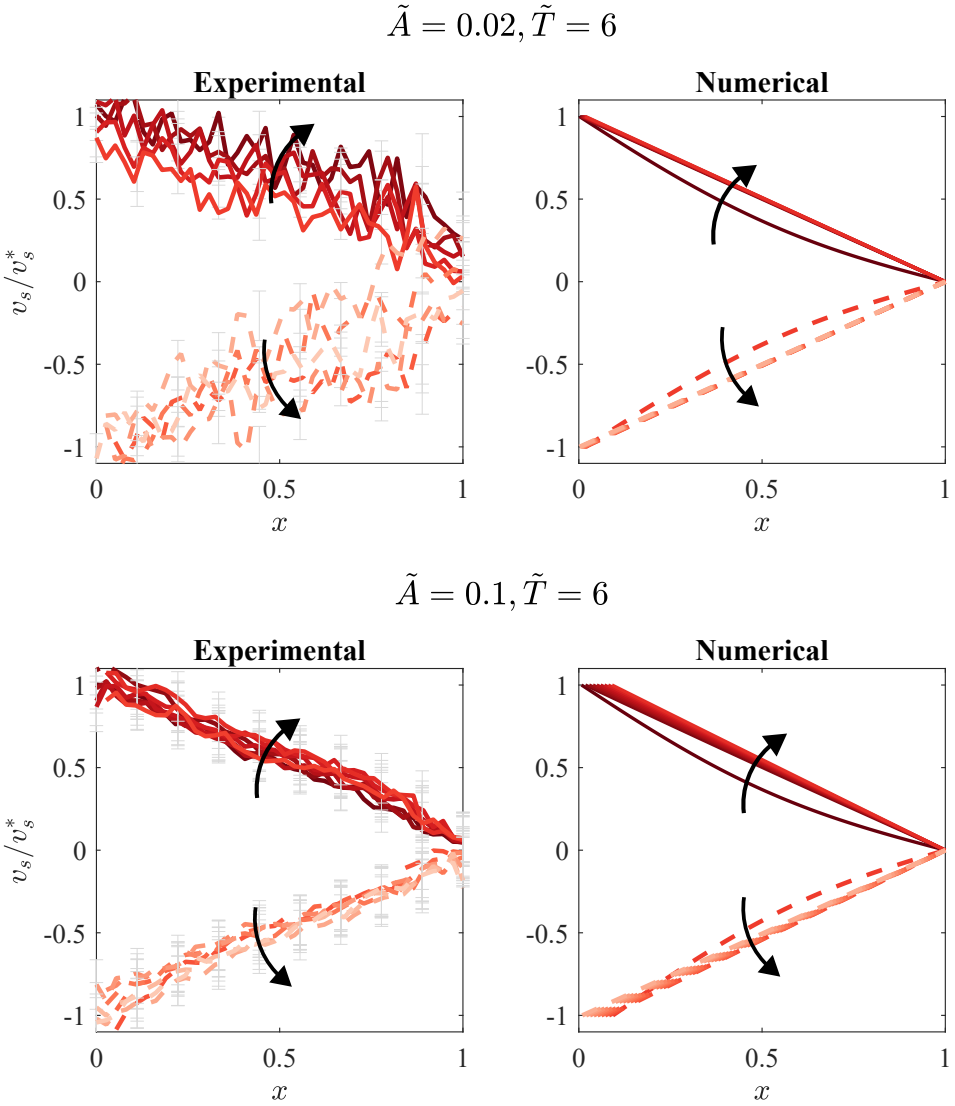

Figure 6.8: Evolution of the normalised experimental solid velocity obtained with PIV (left) and the respective normalised numerical solid velocity (right) for a sponge with $\phi_{f,0} = 0.7$. The loading period is in the slow regime, with $T = 50$ s corresponding to $\tilde{T} = 6$. The amplitude considered are $A = 1$ mm (top row) and $A = 5$ mm (bottom row), corresponding to $\tilde{A} = 0.02$ and $\tilde{A} = 0.1$ respectively. Values are shown at times $t = 3\tilde{T}$ to $4\tilde{T}$ in increments of $0.1\tilde{T}$ (dark to light). The time progression is indicated with black arrows. Error bars indicate the minimum PIV velocity resolution.

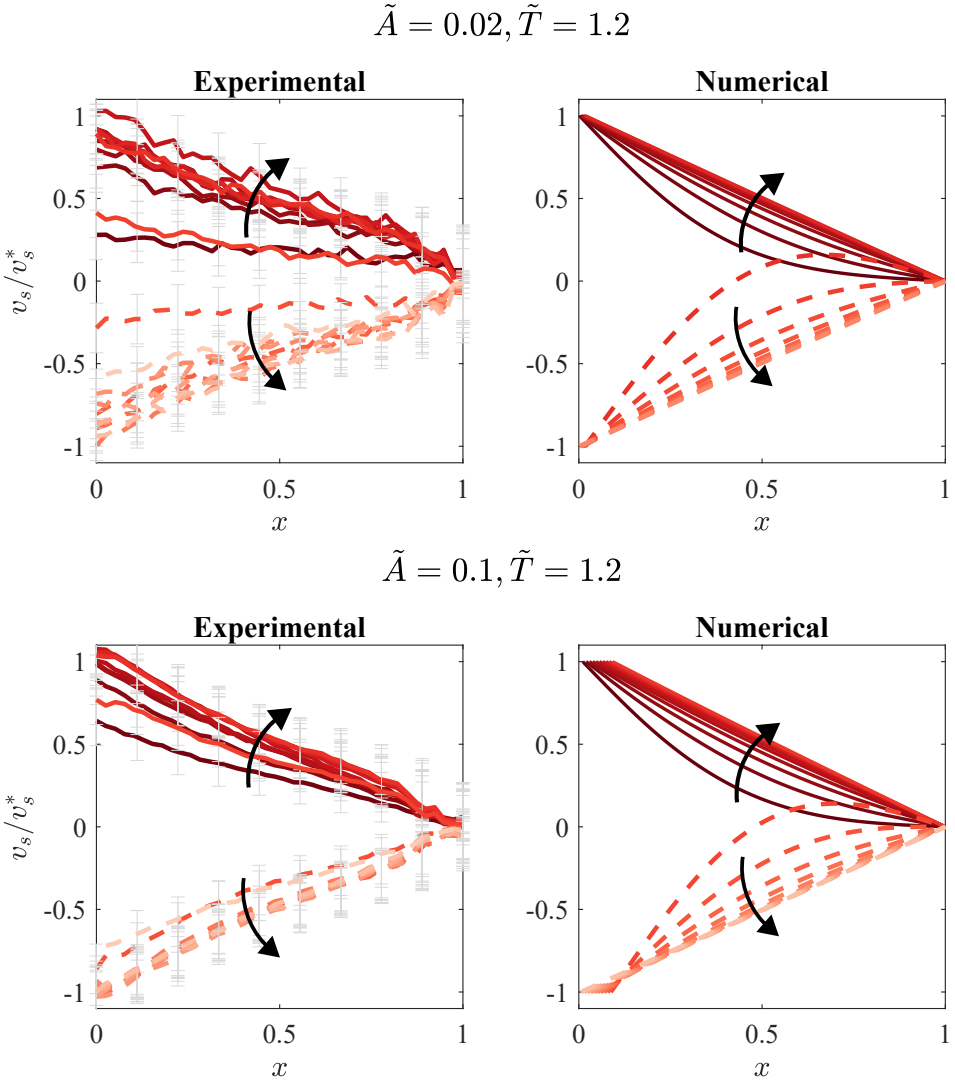

Figure 6.9: Evolution of the normalised experimental solid velocity obtained with PIV (left) and the respective normalised numerical solid velocity (right) for a sponge with $\phi_{f,0} = 0.7$. The loading period is in the fast regime, with $T = 10$ s corresponding to $\tilde{T} = 1.2$. The amplitude considered are $A = 1$ mm (top row) and $A = 5$ mm (bottom row), corresponding to $\tilde{A} = 0.02$ and $\tilde{A} = 0.1$ respectively. Values are shown at times $t = 3\tilde{T}$ to $4\tilde{T}$ in increments of $0.1\tilde{T}$ (dark to light). The time progression is indicated with black arrows. Error bars indicate the minimum PIV velocity resolution.

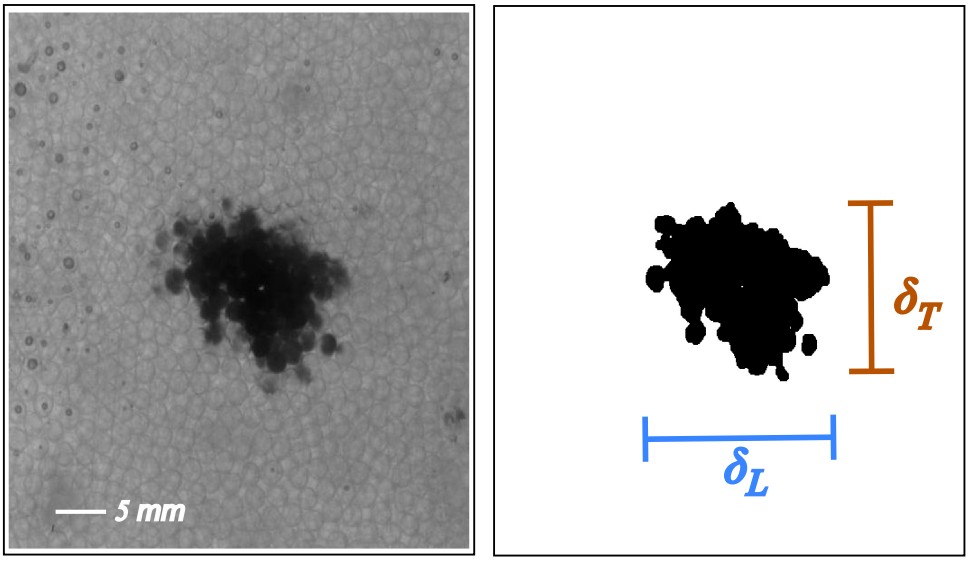

Figure 6.10: Example of raw image (left) and binarised image (right) for the tracking of the solute spreading. On the right, we indicate the longitudinal and transverse spreading lengths, δ_L and δ_T.

that captures the approximate outer edge of the profile. This simple method provides a qualitative analysis of the spreading of the solute over time. An example of a raw image and its binarised version is shown in Figure 6.10. For a more detailed analysis, the value of the solute concentration at each point in the domain can be linked to the attenuation of light intensity via the Beer-Lambert law (Mayerhöfer et al., 2020) after appropriate calibration. We do not perform this procedure here, but we discuss it in more detail in Chapter 7.

In analogy with Section 6.4.1, we consider five loading cases: (i) molecular diffusion only (where no load is applied), (ii) small-amplitude and slow-loading ($\tilde{A} = 0.02$, $\tilde{T} = 6$), (iii) small-amplitude and fast-loading ($\tilde{A} = 0.02$, $\tilde{T} = 1.2$), (iv) large amplitude and slow-loading ($\tilde{A} = 0.1$, $\tilde{T} = 6$) and (v) large amplitude and fast-loading ($\tilde{A} = 0.1$, $\tilde{T} = 1.2$). For each case, we observe the spreading of the initial blob of solute over a fixed total time $t = 500$ s (adjusting the number of cycles according to each $\tilde{T}$, with 10 cycles for $\tilde{T} = 6$ and 50 cycles for $\tilde{T} = 1.2$), and calculate the longitudinal and transverse spreading lengths of the solute, δ_L and δ_T (as shown in Figure 6.10, on the right). For both the shape and the lengths, the experimental and numerical data are compared. The spreading lengths in the model are calculated similarly to the travel distance in Chapter 4: we choose a threshold concentration c_δ and then find the leftmost and rightmost positions x_L and x_R where that concentration occurs. Then, $\delta_L(t) = |x_R(t) - x_L(t)|$. We calculate $\delta_L(t)$ analogously on the transverse direction. Once again, we take $c_\delta = 0.01$. In all the simulations, we fix $\phi_{f,0} = 0.7$.

We begin with the diffusion only case, which allows us to estimate the diffusion coefficient $\mathcal{D}_m$.

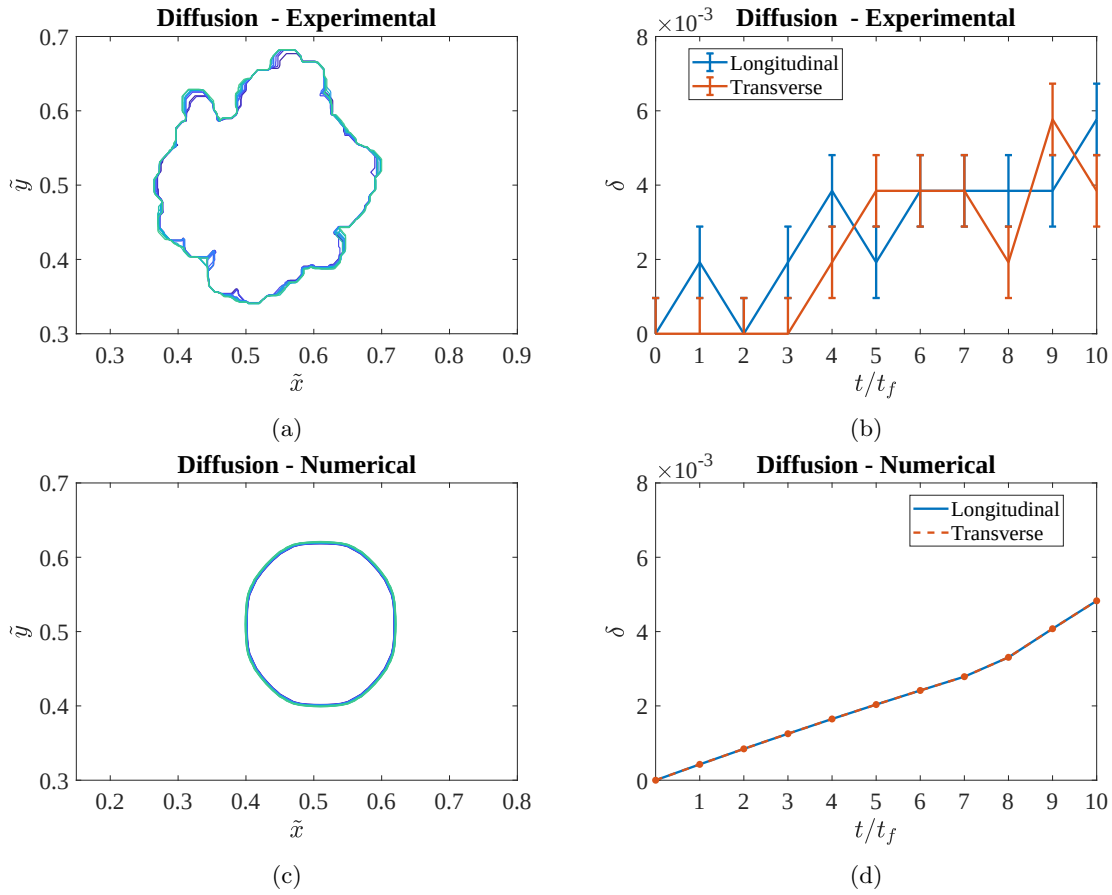

Figure 6.11: Experimental data (a and b) and numerical results (c and d) for the case of molecular diffusion only. The first column (a and c) shows the contours of the solute blob spreading in time (dark to light). The second column (b and d) shows the values of the longitudinal and transverse travel distance δ_L and δ_T at 10 fixed times between 0 and the final time t_f.

The coefficient of molecular diffusion is used as a fitting parameter to match of the final values of δ_L and δ_T (see Figure 6.11, panels b and d), suggesting $\tilde{\mathcal{D}_m} = 6 \times 10^{-7}$, which corresponds to $\mathcal{D}_m = 1.8 \times 10^{-10}$ m^2/s. This value is slightly larger than the ones reported for biological tissues and gels in Chapter 4, which is expected because of the larger pore size in the PDMS sponges. The overall spreading observed in this case is low, and the longitudinal and transverse travel distances coincide (as expected).

We now consider periodic loading. Figures 6.12 to 6.15 show the comparison between the spread measured experimentally and predicted numerically for cases (ii)-(v) respectively. The longitudinal and transverse dispersion coefficients are used as fitting parameters to match the respective values of δ in all loading cases, suggesting $\tilde{\alpha_L} = 5.5 \times 10^{-4}$ and $\tilde{\alpha_T} = 1.5 \times 10^{-4}$. This leads to a ratio α_L/α_T of approximately 5, which is in the range reported in the literature (Delgado, 2007). The dimensional values of the dispersion coefficients are $\alpha_L = 2.75 \times 10^{-2}$ mm and $\alpha_T = 7.5 \times 10^{-3}$ mm. These values are small compared to the pore size, but could be explained considering the size of

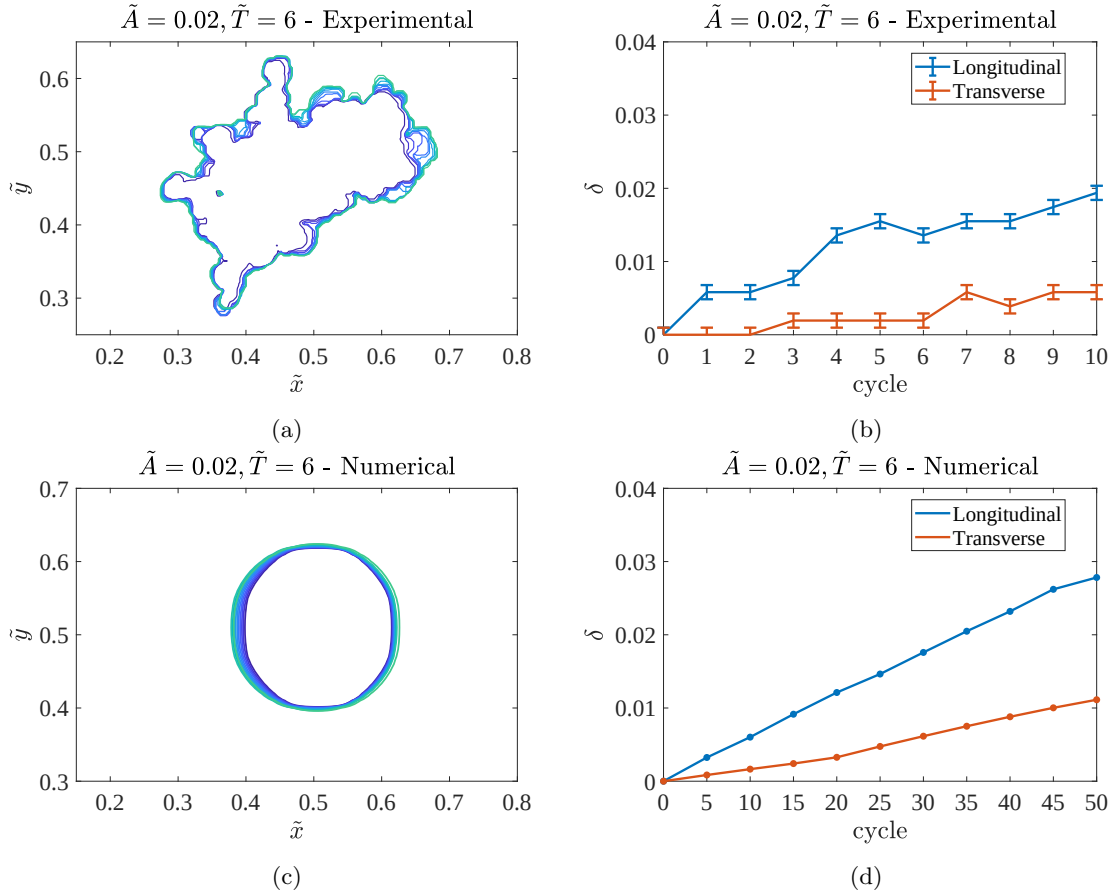

Figure 6.12: Experimental data (a and b) and numerical results (c and d) for the loading case $\tilde{A} = 0.02$, $\tilde{T} = 6$. The first column (a and c) shows the contours of the solute blob spreading in time (dark to light). The second column (b and d) shows the values of the longitudinal and transverse travel distance δ at 10 fixed times.

the pore throats (which is in the order of $0.25 - 0.4$ mm) and the fact that they are expected to be heterogeneous because of the irregular sphere packing.

Overall, we observe a good qualitative agreement between experiments and model for both the spreading of the solute blob and for the travel distance values. In all of the cases, the proportion between δ_L and δ_T retrieved from the images is captured in the model. We observe that the low-amplitude-slow-loading case (Figure 6.12) shows the smallest spreading, while the high-amplitude-faster-loading case shows the highest spreading, as expected. For small-amplitude-faster-loading and for high-amplitude-slow-loading (Figure 6.13 and 6.14, respectively), the ratio $2\tilde{A}/\tilde{T}$ is the same, suggesting the same spreading. The latter case, however, exhibits more longitudinal and transverse spreading than former, especially in the experimental data. In particular, in the small-amplitude-fast-loading case (Figure 6.13), the experimental value of δ_L is significantly lower than the numerical value. This could be related to the initial shape of the solute blob, which include an isolated pore on the right that might potentially induce errors in the calculation of the lengths from the binarised

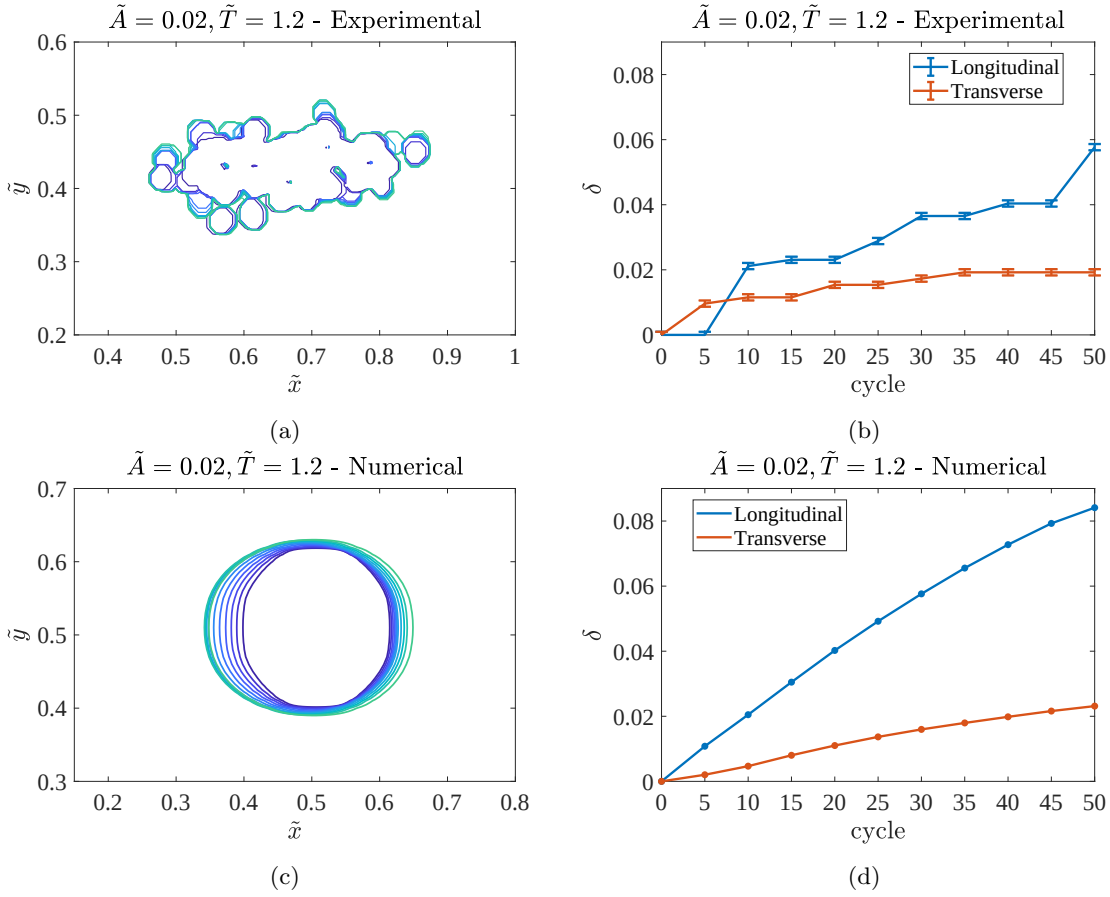

Figure 6.13: Experimental data (a and b) and numerical results (b and c) for the loading case $\tilde{A} = 0.02$, $\tilde{T} = 1.2$. The first column (a and c) shows the contours of the solute blob spreading in time (dark to light). The second column (b and d) shows the values of the longitudinal and transverse travel distance δ_L and δ_T at 10 fixed times.

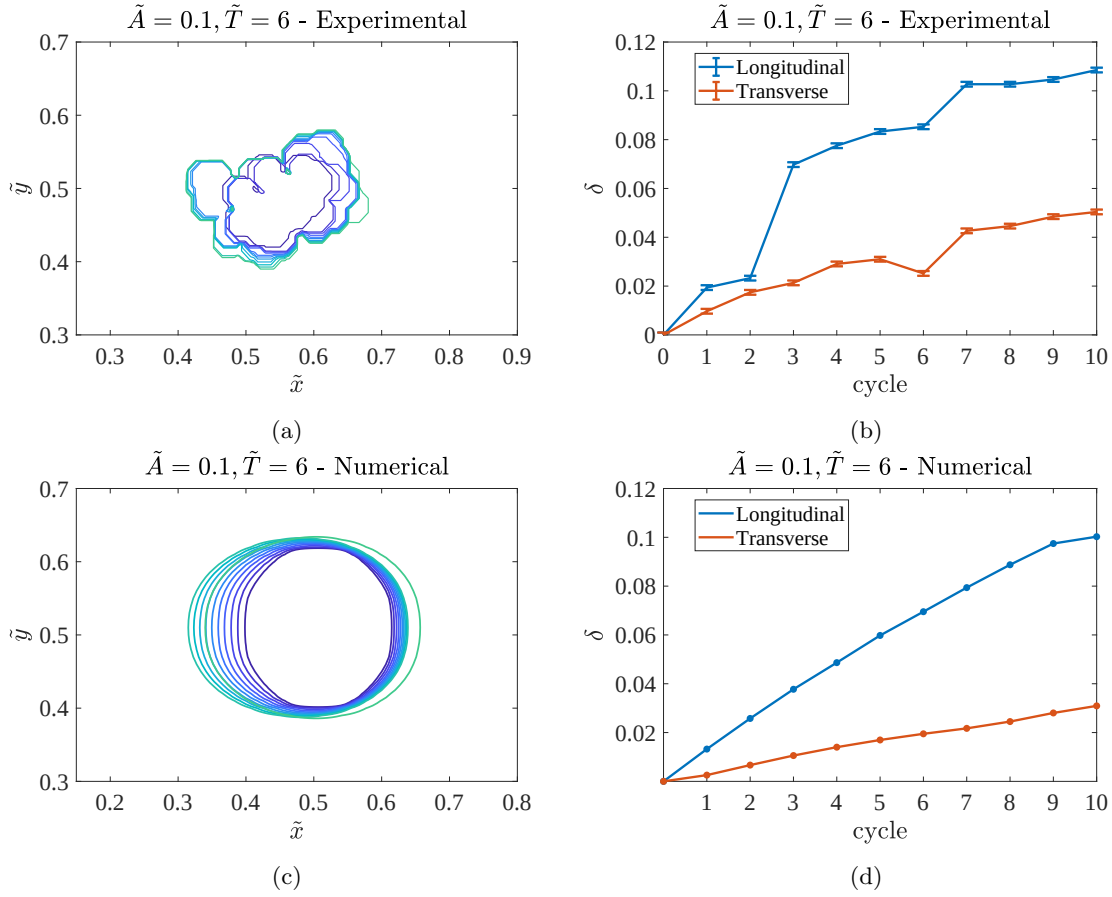

Figure 6.14: Experimental data (a and b) and numerical results (c and d) for the loading case $\tilde{A} = 0.1$, $\tilde{T} = 6$. The first column (a and c) shows the contours of the solute blob spreading in time (dark to light). The second column (b and d) shows the values of the longitudinal and transverse travel distance δ_L and δ_T at 10 fixed times.

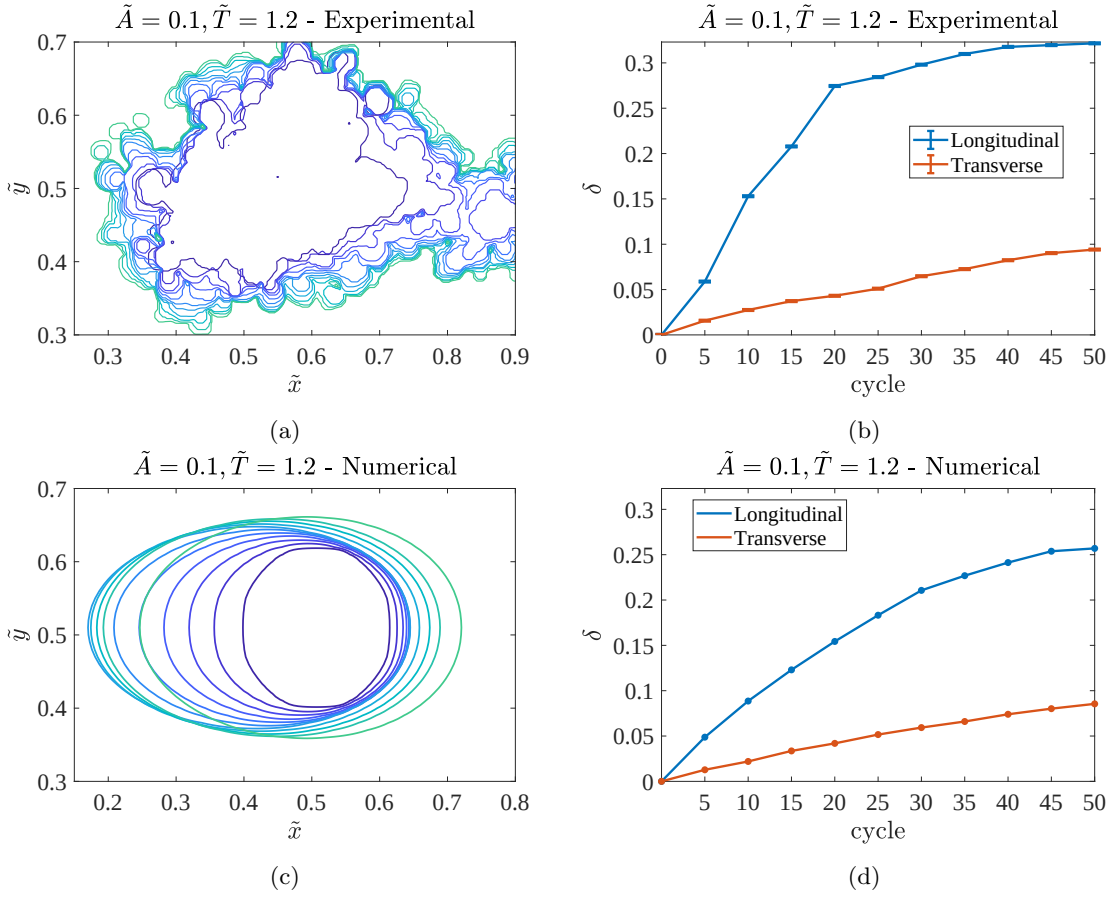

Figure 6.15: Experimental data (a and b) and numerical results (c and d) for the loading case $\tilde{A} = 0.1$, $\tilde{T} = 1.2$. The first column (a and c) shows the contours of the solute blob spreading in time (dark to light). The second column (b and d) shows the values of the longitudinal and transverse travel distance δ_L and δ_T at 10 fixed times.

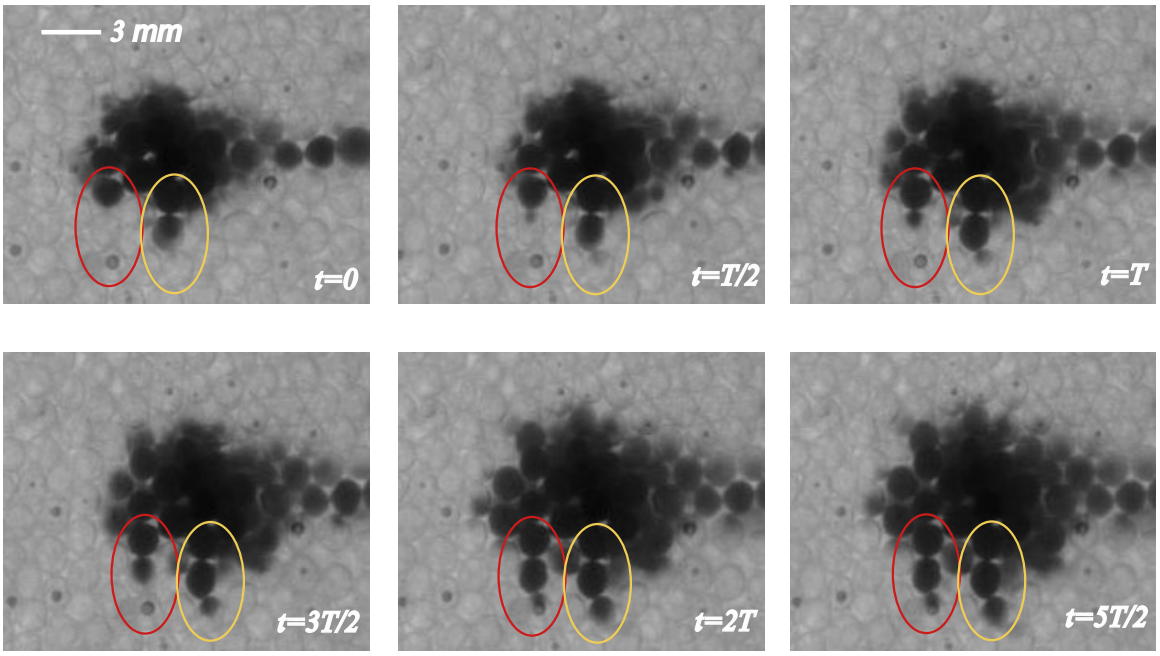

Figure 6.16: Sequence of solute spreading during periodic compression with amplitude $\tilde{A} = 0.1$. Two pore invasions are highlighted separately (red and yellow circles, respectively). The regions highlighted show jumps in the transverse spreading, resulting in discrete jumps in the relative travel distance calculated.

images.

The experimental values of δ are not seen to evolve smoothly over time. This is due to two main reasons: (i) we are not rigorously tracking concentration profiles, thus potentially introducing errors in the way we calculate δ, and (ii) the pore space in the PDMS results in discrete jumps as the dyed fluid enters each pore. In Figure 6.16, we show an example of this phenomenon: the solutes spread following the preferential paths suggested by pore network topography, rather than an isotropic continuous spread, and invade one pore at the time, resulting in step-like motion.

6.5 Conclusions

In this work, we presented proof-of-concept experimental findings on the impact of periodic loading on solute transport in soft porous media. Our results are the first direct observations of solute transport in a deforming porous medium; hence, here we merged the well established experimental background from two communities: the soft-poromechanics community, for the characterisation of the poromechanical response in soft porous media, and the rigid porous media community, for the quantification of Darcy-scale solute transport. Another goal of this study was to validate the numerical model formulated in Chapters 3 and 4.

We provided an experimental protocol for the fabrication and characterisation of the soft porous media employed in the study. In our protocol, we fabricate "sponges" by encasing a sacrificial sugar

structure in PDMS and then washing the sugar away once the PDMS has solidified. Specifically, we use sugar spheres, obtaining a network of interconnected spherical pores. Note that in this work we do not sinter the sugar granules in a humid environment; sintering would provide larger contact areas among the granules and would lead to a higher interconnectivity of the pores, thus allowing to tune the material properties. The PDMS sponges can be characterised with force-displacement and flow-pressure tests to measure the p-wave modulus and the permeability as a function of porosity. Through this characterisation, we estimated the poroelastic timescale, which is an essential parameter for our numerical simulations.

The experiments developed here can be reasonably modelled neglecting the material thickness and assuming uniaxial deformations. Hence, we formulated a semi-2D version of the model presented in Chapters 3 and 4, where the poromechanics is still uni-dimensional and the solute transport is two-dimensional. This means that we allow for isotropic diffusion and longitudinal and transverse dispersion coefficients, which are aligned with and perpendicular to the loading axis, respectively. The semi-2D model is the simpler and less computationally expensive than a fully 2D model.

We concluded by providing a experimental results and comparing them to the numerical data. We assessed the poromechanical response under periodic loading using PIV, showing good agreement between the numerically predicted and the experimentally calculated evolution of the solid velocity throughout the domain during one loading cycle. We then injected a blob of solute into the middle of the PDMS sponge and measure its evolution under different loading conditions, fixing the total time of observation. We started with the case of diffusion only — where no load is applied. In the comparison with the numerical model, we plotted the evolution of the blob shape and the longitudinal and transverse travel distances. We were hence able to estimate the value of the diffusion coefficient to be used in the model. The longitudinal and transverse dispersivities were estimated comparing the effect of different loading amplitudes and periods. We chose $\tilde{A} = 0.02$ and $\tilde{A} = 0.1$, to explore small and large deformations, and $\tilde{T} = 6$ and $\tilde{T} = 1.2$, to cover for relatively slow and fast loading (note that we do not currently have the possibility to explore the fast loading regime because of practical limitations of our equipment). The model and the experiments showed similar values and trends for the spreading.

The experimental validation for our semi-2D model coupling poromechanics and solute transport described in this chapter consists of a proof of concept. In this regard, several essential features of the experiments are well captured in our model; specifically, we demonstrate that hydrodynamic dispersion acts in dynamically loaded soft porous media and that the longitudinal component of dispersion is generally higher than the transverse one. Moreover, both components are seen to be strongly impacted by the amplitude and period of deformation. To our knowledge, these features have never been studied in soft porous media.

A more detailed analysis based on the concentration profiles will require numerous steps to achieve proper calibration of (i) the porosity distribution in the reference state, (ii) the porosity distribution in each deformed state, and (iii) the concentration-dependent attenuation of light. We discuss these points in details in the section regarding future work provided in Chapter 7.

Chapter 7

Discussion and conclusions

In this thesis, we have characterised the impact of large, periodic loading on deformation, fluid flow and solute transport in soft porous media. To do so, we have analysed a model that captures the coupling of poromechanics with solute transport in the context of several model problems.

In Chapter 2, we reviewed the general 3D formulation of large-deformation poroelasticity as prevented in MacMinn et al. (2016). This framework rigorously links large deformations to fluid flow for a generic soft porous medium.

In Chapter 3, we simplified the model to 1D and specified the constitutive choices for the deformation-dependent permeability (formulated with a Kozeny-Carman relation) and the elasticity law for the solid skeleton (for which we use Hencky hyperelasticity). We also formulated boundary conditions corresponding to periodic loading in confined compression. Through comparison with analytical solutions, we showed that the response of the medium depends primarily on whether the loading period T is large or small (ie, slow or fast, respectively) relative to the poroelastic timescale T_{pe}. Specifically, in slow loading, the deformation is uniform and quasi-static; in fast loading, as T decreases, the deformation is progressively more localised near the piston and the medium near the opposite boundary is increasingly less engaged in the deformation. We then performed a parameter study, to understand the impact of the initial porosity $\phi_{f,0}$, the loading amplitude A, and the loading period T, respectively, on the deformation and fluid flow. We showed that the impact of $\phi_{f,0}$ can be scaled out with an appropriate normalisation. In fast loading, increasingly large amplitudes lead to a more prominent asymmetry between the loading and the unloading phases of each cycle, with larger maximum magnitudes of deformation and fluid flow in loading than in unloading. Moreover, for fast loading, the propagation of the fluid flow throughout the domain is delayed relative to the loading, and the delay increases as T decreases.

In Chapter 4, we built on the results from Chapter 3 by studying the impact of periodic loading in confined compression on solute transport and mixing. Starting with the 1D poromechanical model formulated in Chapter 3, we incorporated a model for solute transport that accounts for advection, molecular diffusion, and hydrodynamic dispersion. We then focused on the problem of

solute spreading, where a strip of solute initially localised against the right boundary spreads over time. We illustrated the impact of periodic deformations on each of these mechanisms individually during one loading cycle. We then explored the impact of the model parameters on solute spreading after a number of cycles, beginning with the diffusion and dispersion coefficients. We also investigated the impact of the loading amplitude and period. For advection and diffusion only (*i.e.*, no dispersion), our results showed that solute transport and mixing are independent of T except for very fast loading, where they are steadily but weakly suppressed as A increases. Additionally including dispersion leads to considerably more transport and mixing in the parameter range considered here, and increasingly so as A increases. The solute travel distance depends strongly on T, with lower spreading in the slow-loading region progressively increasing in the fast-loading region up to a peak. For very fast loading, the increasingly strong localisation of the deformation increasingly suppresses transport as T further decreases.

In Chapter 5, we explored the scenario of a medium divided into two layers with different permeabilities. To account for this spatial variation in material properties, we reformulated the poromechanical and transport models from Chapters 3 and 4, respectively, in a Lagrangian reference frame. We then fixed the loading parameters (considering a large amplitude and a fast period) and compared the poromechanics and solute transport for three different media: a homogeneous medium and two examples of layered media. For all three media, we considered two loading scenarios: confined compression, as in Chapters 3 and 4, and also free-flow compression. We then focused on the problem of solute infiltration, where the left boundary of an initially "clean" medium is exposed to a constant external solute concentration. In both loading scenarios, the layers lead to a different distribution of deformation and fluid flow in each medium. As a result, solutes infiltrate at different rates in each case. We also considered simplified models for two tissues, articular cartilage and brain matter, comparing the poromechanics of healthy and pathological tissue (considering the structural changes induced by osteoarthritis and Alzheimer's disease, respectively).

In Chapter 6, we described an experimental campaign providing the first proof-of-concept observations of the coupling between deformation and solute transport in a soft porous medium. We then compared these findings to a quasi-2D version of our theoretical model. Our experimental efforts included the design, construction and testing of a confined compression set-up, the fabrication and characterisation of an appropriate model material, and an initial set of observation of the impact of different loading amplitudes and periods on the longitudinal and transverse spreading of a discrete solute blob within the medium. For comparison with theoretical results, we reformulated the model from Chapters 3 and 4 to couple one-dimensional poromechanics and two-dimensional solute transport, representative of the deformation and solute fluxes experienced by the material in confined compression. We found that larger amplitudes and shorter periods enhance solute spreading, as expected, thus confirming the crucial role of longitudinal and transverse hydrodynamic dispersion.

Moreover, we compared the spreading contours of the solute blob and the longitudinal and transverse spreading length estimated from the experiments to the ones predicted with our numerical model, showing good agreement.

Below, we provide an overview of the major limitations of this work, and comment on future work.

7.1 Limitations and future work

The model presented here (in all its versions) has some limitations. The 1D formulation employed in this work is simpler to interpret physically and less computationally expensive than a 2D or 3D model. However, the 1D nature of the model limits the loading conditions that can be studied, and prohibits the inclusion of most anisotropies, both in terms of the mechanical and structural properties of the medium and in terms of the nature of solute spreading. For example, a fully 2D model (with 2D poromechanics and 2D solute transport) could capture unconfined compression, which is common is biological scenarios.

Another limitation of this study is that we focus exclusively on periodic, displacement-driven deformations. This is limiting for two main reasons. First, some tissues are subject to stress or pressure-driven loading, which leads to a fundamentally different response, particularly in terms of displacement amplitude and stress amplitude. Second, displacement-driven deformation does not allow for large amplitudes at arbitrarily fast periods. Specifically, the permeability at the left boundary can vanish for sufficiently large A and/or small T, because the poroelastic diffusivity used here remains finite rather than diverging as $\phi_f \to 0$ (see Appendix A.1 and Hewitt et al. (2016b)).

Moreover, our model only considers a purely elastic behaviour of the solid skeleton, neglecting viscoelasticity. This is a limiting assumption for several biological tissues, where viscoelasticity plays an important role in the mechanical response of the solid phase.

Regarding the solute-transport part of the model, we have assumed that the solute is neutrally charged and small compared to the pore size. The former assumption is often not true for biological tissues; the mechanical and transport models could be extended to account for electrical interactions, but doing so is beyond the scope of this work. The second assumption has allowed us to neglect the hindrance between the molecules and the solid matrix, which complicates the problem for the need to include a relation between the molecule size and the radius of each pore, as extensively characterised (Ateshian and Weiss, 2013, Yao and Gu, 2007).

Moreover, we assume that the coefficients for molecular diffusion and hydrodynamic dispersion are independent of deformation. This is unlikely to be true and needs to be investigated experimentally. The experiments presented in Chapter 6 provide a promising avenue for characterising the deformation-dependence of these transport properties, but our results are currently limited to basic

proof of concept. The accuracy of the experimental results is hence limited and can be improved with the protocols described below for future work. We discuss these points in more detail below.

With regard to the model, a sensible next step would be to formulate a fully 2D version. This version would allow for the exploration of more scenarios, such as the loading case of unconfined compression, or the case of anisotropy. For example, 2D features could be introduced by imposing anisotropic boundary conditions for fluid outflow, even for a homogeneous and isotropic medium. Modifying the permeability of the boundaries could alter the main direction of the fluid velocity, and therefore also of the solute transport. We believe that the interaction of deformation and fluid flow could be also elucidated by comparing the case in which they are aligned (*i.e.*, confined compression) to the case in which they are nearly orthogonal. Anisotropy is also an intrinsic property of some media, in which case it can be modelled with tensorial material properties such as permeability and stiffness.

Experimentally, several important steps would be needed for the current protocol to provide precise quantitative data. In a liquid, the concentration of a visible solute in a quasi-2D system can be measured quantitatively via an initial calibration at known concentrations that can provide a unique relation between transmitted light intensity and concentration. The challenging aspect of tracking concentration profiles in a porous medium is the interpretation of the intensity values. When imaging concentrations in a porous medium (again in quasi-2D), local pixel intensity is influenced by both concentration and porosity. An important future improvement is hence to perform a calibration of the pore space by mapping the variations in intensity due to porosity at a known concentration and index-matching of the fluid (see, for example, (Basilio Hazas et al., 2023, Brouzet et al., 2022, Corapcioglu and Fedirchuk, 1999, McNeil et al., 2006, Sahu and Neufeld, 2023)). The light intensity can be then be related to concentration as in a pure fluid, via the Beer-Lambert law.

Another important task is the direct experimental measurement of all the transport properties, including the coefficient of molecular diffusion $\mathcal{D}_m$ and the longitudinal and transverse dispersivities α_L and α_T, all of which were only qualitatively estimated in this work. Quantitative measurement will require light-intensity calibration, as described above. Subsequently, the diffusivity $\mathcal{D}_m$ can be measured by observing the spreading of a solute blob, as done here only qualitatively. This measurement should be repeated for several different levels of uniform compression, to assess the deformation-dependence of $\mathcal{D}_m$. The dispersivities can be measured in a similar way, by imposing a known fluid flux and measuring the resultant longitudinal and transverse spreading of a solute blob. It is possible to isolate the dispersive flux from the diffusive one either using a non-diffusive tracer (similarly to what is described in (Souzy et al., 2016, 2020)) or by applying a sufficiently large flux that dispersion dominates diffusion on the timescale of observation (Rashidi et al., 1996). Note that this flux must be slow enough to avoid inducing any deformation in the medium. As with the diffusivity, the dispersivities should be measured in a series of uniformly compressed states to assess

their deformation dependence. The inclusion of deformation-dependent transport properties in the model would be relatively straightforward.

For a more extensive validation of the model presented in Chapters 3 and 4, smaller dimensionless loading periods should be tested in order to explore the localisation of the deformation near the piston. Smaller dimensionless periods are most readily achieved by increasing the poroelastic timescale of the system, such as by decreasing the stiffness or permeability of the PDMS sponges (via smaller sugar beads or a smaller ratio of PDMS crosslinker to base, respectively) or by using a fluid with a larger viscosity (*e.g.*, glycerol rather than water). A larger poroelastic timescale would allow for characterisation of the fast end of the periodic loading regimes with the same experimental apparatus.

Finally, the experimental protocol described for homogeneous media can be extended to the case of layered media, as modelled in Chapter 5. Layered PDMS sponges can be readily fabricated by using two different sizes of sugar beads, with smaller beads leading to a similar porosity but a smaller permeability. The organisation of the sugar beads in the casting mould thus allows direct control over the structure and properties of the resulting media.

7.2 Conclusions

Overall, we have used a relatively generic model to develop physical insight into solute transport in highly deformable porous media. The model is relatively simple, but can account for the impact of arbitrarily large, periodic deformations on the spreading of the solutes at the Darcy scale. By adapting the permeability and elasticity constitutive law (see Appendix A.1), the model can be representative of a wide spectrum of soft porous media, both homogeneous and layered. Our study on the purely poromechanical aspects of periodic loading could assist in the estimation of the poromechanical regime and the localisation effects relative to given loading parameters. This, coupled with the solute transport parameters, could provide a tool to estimate the relative importance of each transport mechanism.

Hence, with a relatively low computational cost, our model can be used to predict and control deformation and fluid flow localisation, and their effects on solute transport. In soft biological tissues and tissue-engineering constructs, these aspects are essential for cell survival. Large loads and fluid flows are needed for healthy development of many tissues, both for the mechanical stimulation of the cells (which activates mechanisms of mechanotransduction) and for the supply of nutrients and oxygen throughout the medium. However, an excessive localisation of the deformations could lead to cell death. Fluid-flow localisation could also limit the nutrient supply. For this reason, being able to fully understand the changes in the localisation of the poromechanical response from healthy to pathological conditions could provide a promising tool for improving treatments. Moreover, when designing new synthetic tissues, tuning the poromechanical response, either by changing the loading

parameters or by distributing the different tissue layers, could improve the cell response, and allow for specific optimisations of the poromechanics and solute transport distributions.

Appendix A

A.1 Constitutive laws

In our model, we consider Hencky elasticity as the constitutive law for the elastic solid. Hencky elasticity is a hyperelastic model commonly used for soft rubbers and polyurethane foams (Anand, 1979, Hencky, 1933, Xiao and Chen, 2002), and sometimes for soft biological tissues (*e.g.*, Fraldi et al., 2018, Marchesseau et al., 2010). In this appendix, we compare Hencky elasticity with two other hyperelastic models — Neo-Hookean and logarithmic Neo-Hookean — that are more commonly employed for soft tissues (*e.g.*, Ehlers et al., 2009, Sengers et al., 2004). This analysis suggests that our qualitative results also apply to these other elasticity laws.

The expressions $\sigma'(\phi_f)$ for Hencky elasticity and for linear elasticity are given in equations (3.14) and (3.20), respectively. The appropriate expressions for the Neo-Hookean and logarithmic Neo-Hookean constitutive laws are:

$$\sigma' = \Lambda(J-1)\mathbf{I} + \frac{\mathcal{G}}{J}\left(\mathbf{F}\mathbf{F}^T - \mathbf{I}\right) \tag{A.1}$$

and

$$\sigma' = \Lambda\left(\frac{\ln(J)}{J}\right)\mathbf{I} + \frac{\mathcal{G}}{J}\left(\mathbf{F}\mathbf{F}^T - \mathbf{I}\right) \tag{A.2}$$

respectively, where $J = (1-\phi_{f,0})/(1-\phi_f)$ and Λ and $\mathcal{G}$ are the Lamé constants, such that $\mathcal{M} = \Lambda + 2\mathcal{G}$. In 1D, equation (A.1) and equation (A.2) read, respectively

$$\sigma' = \Lambda(J-1) + \mathcal{G}\left(\frac{J^2-1}{J}\right), \tag{A.3}$$

and

$$\sigma' = \Lambda\frac{\ln(J)}{J} + \mathcal{G}\left(\frac{J^2-1}{J}\right). \tag{A.4}$$

In the first row of Figure A.1, we plot $\sigma'/\mathcal{M}$ against ϕ_f in compression for all four of these elasticity laws (linear, Hencky, Neo-Hookean and logarithmic Neo-Hookean). Note that the two Neo-Hookean models are characterised by an additional dimensionless parameter in confined compression, the ratio $\Lambda/\mathcal{G}$. All four curves have the same qualitative shape, although Hencky elasticity is noticeably stiffer than the other models during strong compression. However, these quantitative

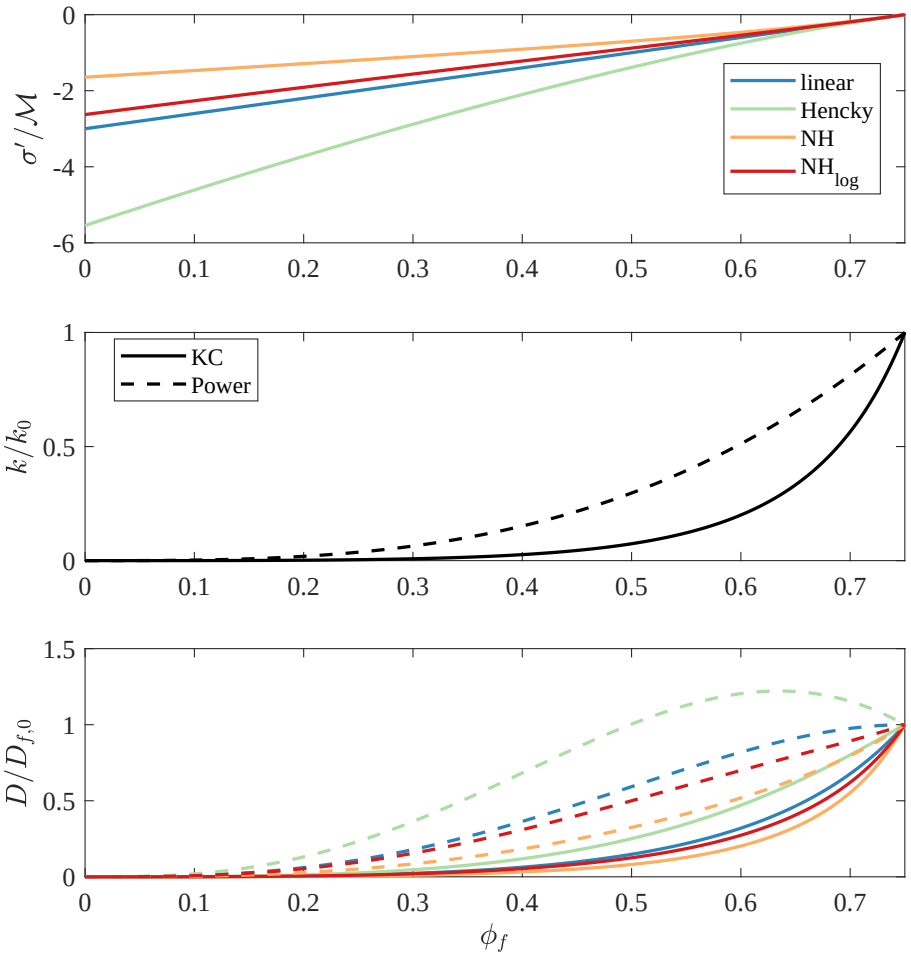

Figure A.1: Comparison of different constitutive properties: normalised effective stress $\sigma'(\phi_f)$ (first row), permeability $k(\phi_f)$ (second row), and poroelastic diffusivity $D_f(\phi_f) = (1-\phi_f)(k/\mu)\mathrm{d}\sigma'/\mathrm{d}\phi_f$ (third row) against ϕ_f for four different elasticity laws (linear, Hencky, Neo-Hookean, and logatithmic Neo-Hookean) and two different permeability laws (Kozeny-Carman and the power-law $k(\phi_f) = k_0\left(\phi_f/\phi_{f,0}\right)^3$). The relaxed porosity is $\phi_{f,0} = 0.75$ in all cases and we take $\Lambda/\mathcal{G} = 0.515$ in the two Neo-Hookean laws based on values reported in ref. (Ferguson et al., 2004).

differences are relatively unimportant because the permeability law forces the poroelastic diffusivity smoothly toward zero during strong compression in all cases (see below).

The permeability function used in our model follows the Kozeny-Carman formula (Equation 3.6), which is a normalised version of its form more commonly used for granular materials,

$$k(\phi_f) = \frac{d^2}{180} \frac{\phi_f^3}{(1-\phi_f)^2}, \tag{A.5}$$

where d is the characteristic pore or grain size. This formulation was initially derived analytically for a bundle of capillary tubes of diameter d (Kozeny, 1927) and then adapted to the case of granular beds and porous media (Carman, 1956, 1997). For deformable porous media, the Kozeny-Carman formula is consistent with the following poromechanical physical limits: the permeability vanishes as ϕ_f vanishes, and diverges as $\phi_f \to 1$.

In the second row of Figure A.1, we provide a comparison for two different permeability laws: Kozeny-Carman and a simpler power-law model given by

$$k(\phi_f) = k_0 \left(\frac{\phi_f}{\phi_{f,0}} \right)^3. \tag{A.6}$$

Both models are commonly used for soft tissues and gels (*e.g.*, Kozeny-Carman in refs. (Gao and Cho, 2022, Malandrino et al., 2014, Rahbari et al., 2017, Sacco et al., 2014) and power-law in refs. (Ehlers et al., 2009, Holmes and Mow, 1990, Sengers et al., 2004)) and the two curves have qualitatively similar shapes. Note that constant permeability $k(\phi_f) = k_0$ is rarely used for soft porous media and is considered non-physical, particularly for moderate to large deformations.

In the third row of Figure A.1, we compare the resulting poroelastic diffusivity $D_f(\phi_f)$ (Equation 3.13) for all eight combinations of these four elasticity laws with these two permeability laws. Most of these curves have the same qualitative shape, most importantly vanishing smoothly as $\phi_f \to 0$. The combination of Hencky elasticity with Kozeny-Carman permeability (solid green line) is roughly in the middle of this family of curves, suggesting that this combination is representative of the poromechanical behavior of many different soft porous media, thus supporting the qualitative generality of our results.

A.2 Early time evolution, penetration length, and periodic response to very fast loading

The macroscopic strain imposed on the medium is always of size A. For fast loading, this strain localises toward the left boundary, leading to local strains of size $\sim A/\sqrt{T}$ over a region of size $\sqrt{T}$ in the periodic state. Thus, the local strains can become large even when A is small, leading to large deviations from linear poroelasticity. These deviations are particularly large at early times, during which the deformations are localised to an even narrower region of size $\sqrt{t}$ (Figure A.2a), but they persist in the periodic state (Figure A.2c).

When the loading begins, the deformation propagates into the medium diffusively with penetration distance $\delta_{\text{et}} \sim \sqrt{t}$ until the deformation spans the domain (Figure A.2b). In the periodic state, the oscillations will be confined to a region of size $\sqrt{T}$. For very fast loading, $\sqrt{T} \ll 1$, the right portion of the medium will evolve toward a state of static compression (Figure A.2d).

A.3 Transition to the periodic regime

The linear-poroelastic solution in Section 3.2.8 includes a transient component that decays exponentially and a periodic component with period T. In this appendix, we illustrate and quantify the decay of the transient component and hence the convergence to the periodic regime for a large-deformation scenario. To do so, we solve the problem numerically for $\phi_{f,0} = 0.75$, $A = 0.2$, and for $T = 4\pi$, π, 0.2π, 0.12π, and 0.1π. This amplitude is the largest considered in this study, thus providing an upper bound for difference magnitudes. In each case, we calculate the root-mean-square (RMS) relative difference in $\phi_f(X,t)$ between the solution at time t and at time $t+T$.

Figure A.3 confirms the exponential decay of the transient for all five values of T (dashed black dashed). After this initial transition, the RMS relative difference for all curves oscillates around a mean value that is controlled by the relative error tolerance associated with time integration (see Figure A.8).

A.4 Impact of elasticity and permeability laws at large amplitudes

In Figure A.4, we compare different combinations of elasticity and permeability laws for a scenario involving large deformations and fast loading ($A = 0.09$, $T = 0.03\pi$). Specifically, we compare four cases: Hencky elasticity with Kozeny-Carman permeability (first column; same as the first column in Figure 3.5, but for a slightly lower amplitude), linear elasticity with Kozeny-Carman permeability (second column), Hencky elasticity with constant permeability (third column), and linear elasticity with constant permeability (fourth column). Note that the last column is still kinematically nonlinear because $D_f = 1 - \phi_f$ (see Equation 3.23) and the problem remains a moving-boundary problem. Even for constant permeability and linear elasticity, the fluid flux has a strong asymmetry between loading and unloading. This asymmetry is strongly enhanced by Kozeny-Carman permeability and very gently moderated by Hencky elasticity. The latter occurs because Hencky elasticity is stiffer than linear elasticity in compression.

A.5 Dispersive flux

In Figure A.5, we plot the flux $q_{\text{disp}}/q_{\text{diff}}$ for the cases that define the range considered in this study. In particular, the lowest value of $q_{\text{disp}}/q_{\text{diff}}$ is seen for the lowest amplitude and largest period

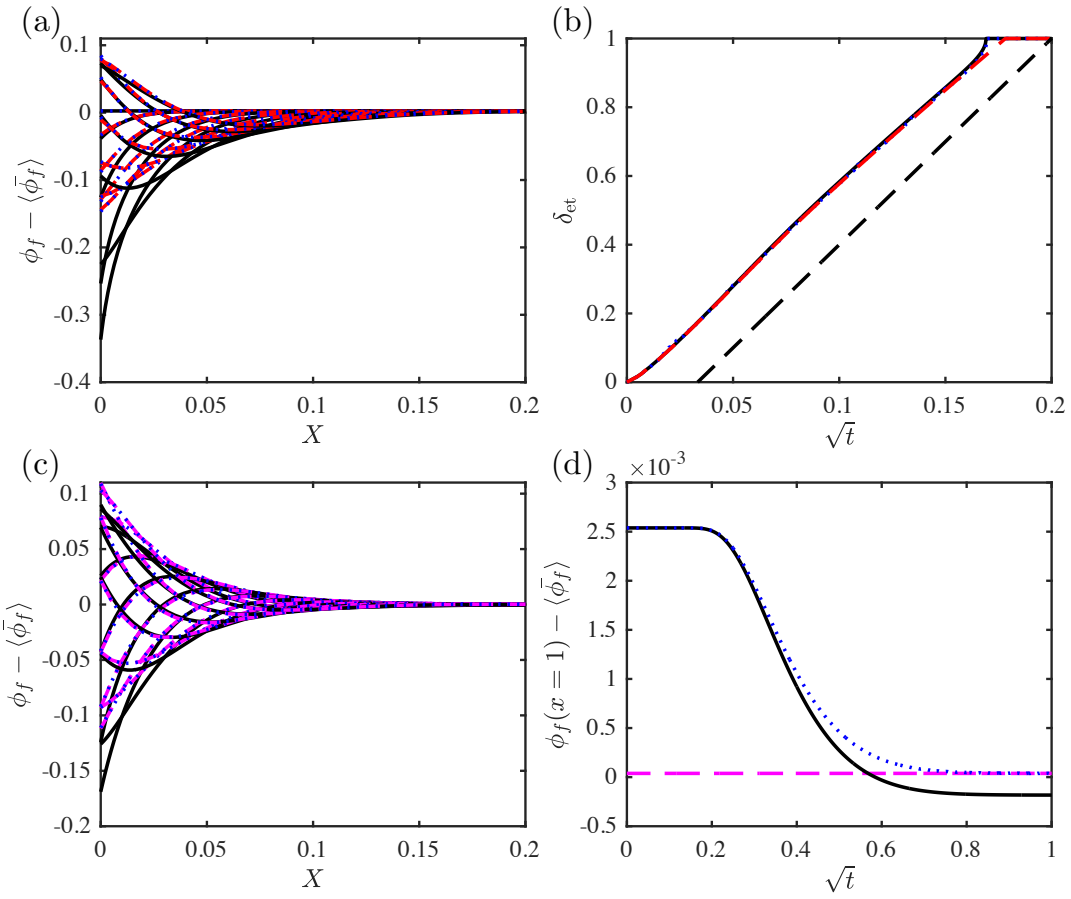

Figure A.2: Early time response for $\phi_{f,0} = 0.75$ at a small amplitude $A = 0.02$ and a very fast period $T = 0.001\pi$. We show $\Delta\phi_f$ as a function of the Lagrangian spatial coordinate X for several times t during (a) the first loading cycle and (c) one cycle in the periodic regime. We also show the evolution of (b) the penetration distance δ_{et} and (d) the change in porosity at the right boundary, $\Delta\phi_f(1,t)$, both against $\sqrt{t}$. All plots show the numerical solution (solid black) and the full linear-poroelastic solution (dotted blue). The top row includes the early-time linear-poroelastic solution (dashed red). The bottom row includes the very fast linear-poroelastic solution (dashed magenta). The latter is a constant in panel (d) because the very fast solution neglects the initial transient. Panel (b) also shows a linear trend in $\sqrt{t}$ for reference (dashed black).

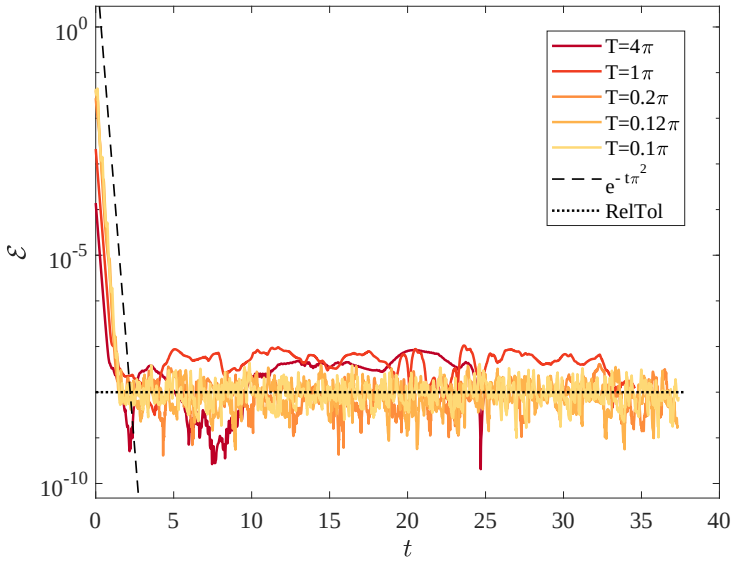

Figure A.3: The RMS relative difference between the $\phi_f(X,t)$ at time t and at time $t+T$ for $A = 0.2$, $\phi_{f,0} = 0.75$, and for five values of T (see the legend). The dashed black line indicates the exponential decay $e^{-t\pi^2}$ and the dotted black line indicates the relative tolerance selected for time integration, here set to 10^{-8} (see Figure A.8).

considered. The highest $q_{\text{disp}}/q_{\text{diff}}$ is observed both for large amplitudes and fast loading, and for moderate amplitude and very fast loading. Note that these fluxes are a consequence of the values chosen for Pe^{-1} and α.

A.6 Initial porosity and solute strip width

Table A.1 reports a summary of the baseline values and the explored values for $\phi_{f,0}$ and l. For the initial porosity, we consider values of fluid fractions that typically describe hydrogels or soft biological tissues. The other parameters highly vary depending on specific applications, and are hence mostly arbitrary. Results of varying $\phi_{f,0}$ and l are shown in Figure A.6 (respectively on the left and on the right). When decreasing the initial fluid fraction, stronger oscillations are observed. This is due to the impact of porosity in the relation between the fluid and the solid fractions described in Equation (3.18). For a lower porosity, in fact, the same solid velocity induces a higher fluid velocity than for a higher porosity. In this way, both advection and hydrodynamic dispersion are enhanced: the advective flux is in fact stronger for higher fluid velocity. However, at the end of each cycle, the final distance reached by the solute and the degree of mixing are only slightly higher for lower porosities. This is because, in the slow-loading regime considered here, fluid velocities are much lower than for fast-loading scenarios, and dispersive fluxes are only slightly predominant over molecular diffusion. The effect on hydrodynamic dispersion of a lower but uniform initial porosity is hence only slightly visible.

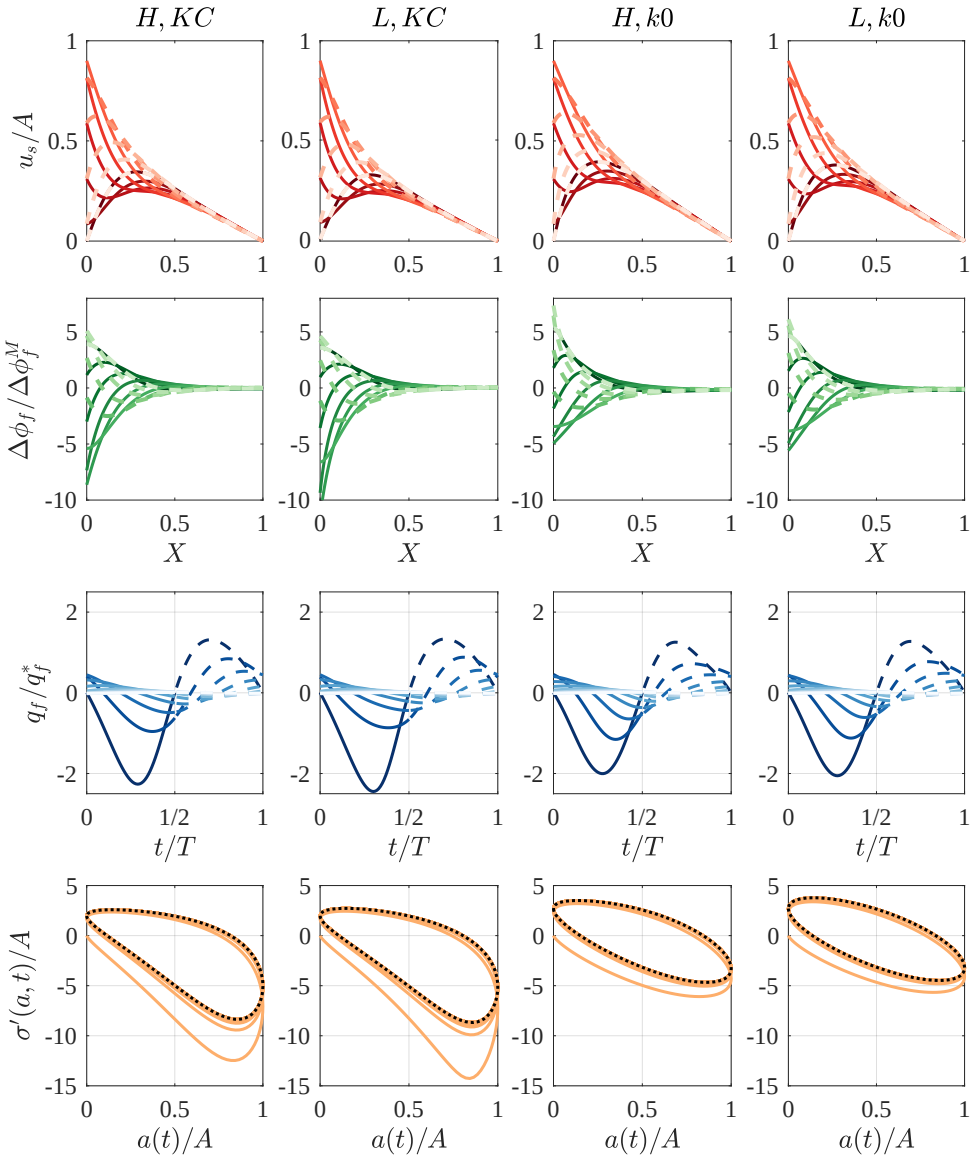

Figure A.4: As in Figure 3.5, but for a slightly lower amplitude ($A = 0.09$) and showing four different combinations of constitutive behavior: Hencky elasticity with Kozeny-Carman permeability (first column), linear elasticity with Kozeny-Carman permeability (second column), Hencky elasticity with constant permeability (thrid column), and linear elasticity with constant permeability (fourth column).

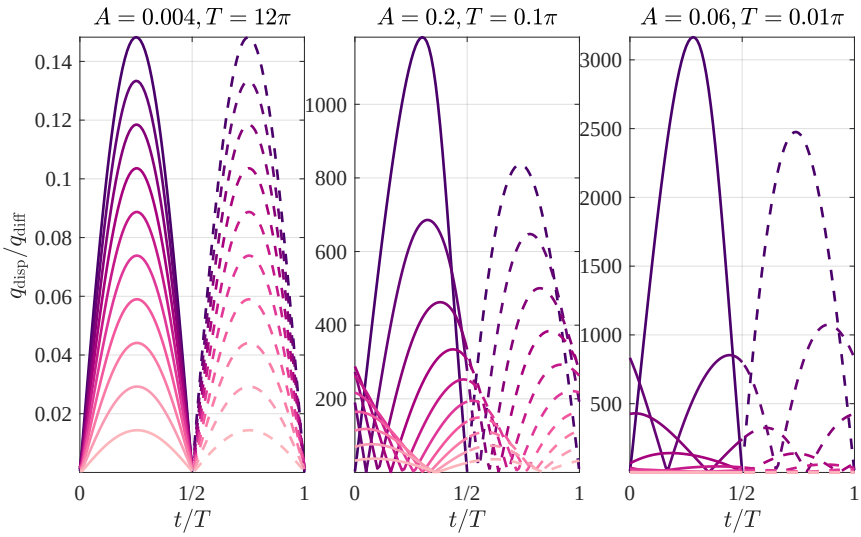

Figure A.5: Lowest (first column) and largest (second and third columns) values of $q_{\text{disp}}/q_{\text{diff}}$ considered in this study.

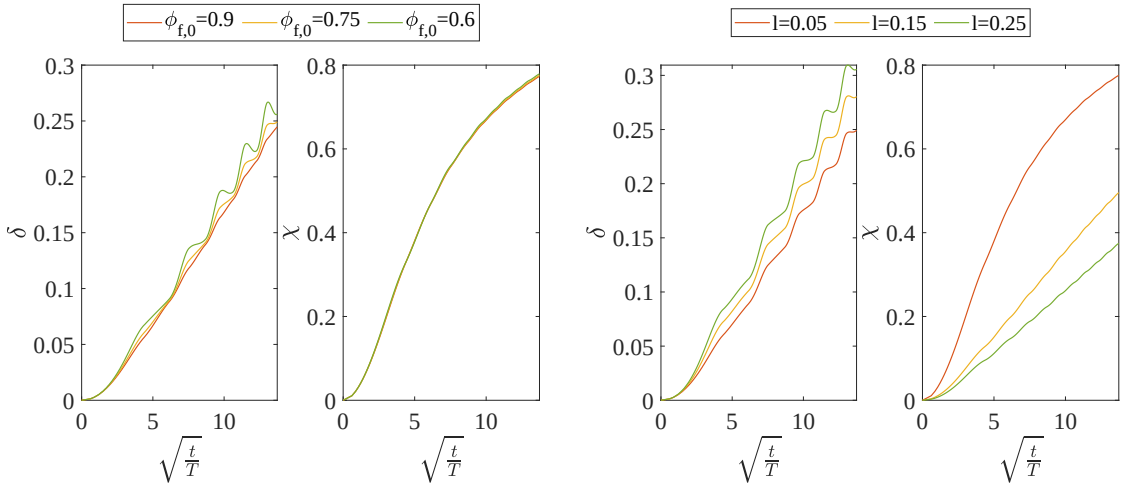

Figure A.6: Evolution of δ and χ over 5 cycles with different initial porosity $\phi_{f,0}$ (left) and initial solute stripe width l (right) values.

Parameter	Baseline value	Other values examined
$\phi_{f,0}$	0.75	0.60, 0.90.
l	0.05	0.15, 0.25.

Table A.1: Summary of the values of $\phi_{f,0}$ and l explored.

Increasing the initial solute amount leads to a sharp increase in the travel distance: this is generally expected because the total concentration of solute is higher and therefore all the transport mechanisms are amplified, as formulated in the concentration of mass. It is worth noticing, however, that a wider solute strip is associated to a lower degree of mixing: the variance of the solute at the end of the stimulation compared to the initial variance is in fact lower with more solute (see Equation 4.20).

A.7 Numerical methods

We solve our model numerically using Chebyshev spectral differences in space (Weideman and Reddy, 2000) in Chapter 3, and using compact finite differences in space in Chapter 4, Chapter 5 and Chapter 6. In all Chapters, we use implicit Runge-Kutta integration in time, which we achieve via `MATLAB`'s built-in solver `ODE15s` (Shampine and Reichelt, 1997). To handle the moving boundary, we rescale the spatial coordinate as

$$\xi = \frac{x-a}{1-a}, \tag{A.7}$$

thus mapping a general conservation law of the form

$$\frac{\partial \Omega}{\partial t} + \frac{\partial}{\partial x}[F(\Omega)] = 0 \tag{A.8}$$

on the domain $a(t) \leq x \leq 1$ to

$$\frac{\partial \Omega}{\partial t} - \left(\frac{1-\xi}{1-a}\right)\dot{a}\frac{\partial \Omega}{\partial \xi} + \left(\frac{1}{1-a}\right)\frac{\partial}{\partial \xi}[F(\Omega)] = 0 \tag{A.9}$$

on the domain $0 \leq \xi \leq 1$.

In Chapter 3, when solving equation (3.23), we then take $\Omega = \phi_f$ and

$$F(\phi_f) = -\tilde{D}_f(\phi_f)\frac{\partial \phi_f}{\partial \tilde{x}}. \tag{A.10}$$

For our spatial discretisation with Chebishev spectral differences, we perform a convergence analysis in the number of grid points N_x by calculating the RMS relative difference in $\phi_f(a,t)$ for each solution with respect the solution for $N_x = 1000$.

Figure A.7 illustrates the impact of A and T on the spatial accuracy of this numerical solution. Very small amplitudes and very slow periods are characterised by low differences that are of the order of the tolerance chosen for time integration (see Figure A.8). We choose $N_x = 300$ for all

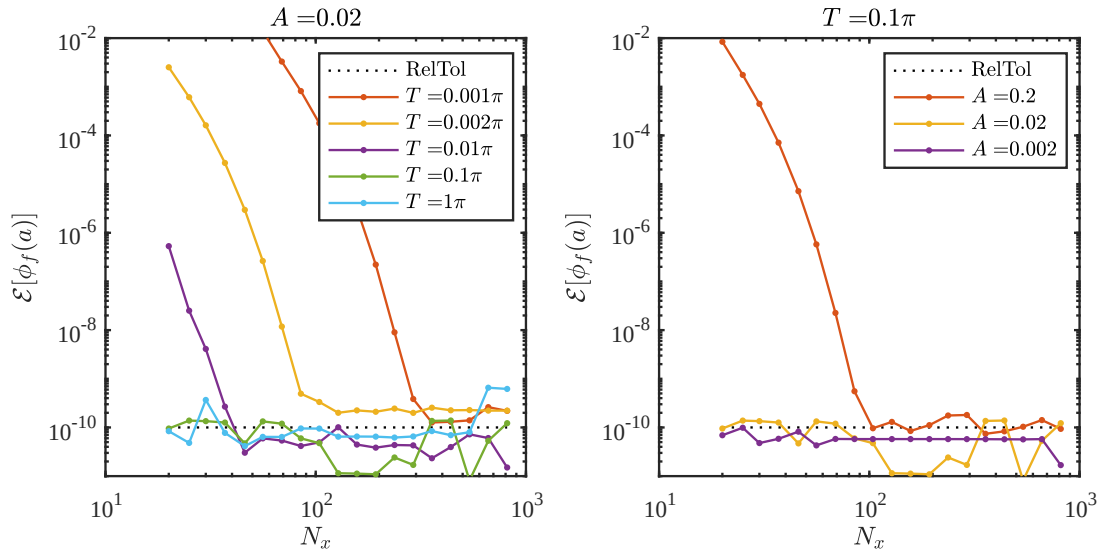

Figure A.7: Convergence analysis: RMS relative difference in $\phi_f(a,t)$ relative to the solution for $N_x = 1000$ when using Chebishev spectral differences. On the left, we fix $A = 0.02$ and consider different values of T, from very fast to slow. On the right, we fix $T = 0.1\pi$ and consider different values of A, from small to large.

simulations, associated with a maximum relative difference comparable to that of the relative error tolerance for time integration.

In Figure A.8, we consider the RMS relative difference in $\phi_f(X,t)$ between two consecutive cycles in the periodic regime for $A = 0.2$ and $T = 4\pi$, and for three values of the relative error tolerance for time integration. The results confirm that the RMS relative difference is limited by the relative error tolerance of the ODE solver, as expected. Throughout our analysis, we use a relative tolerance of 10^{-8}.

In Chapter 4, once again we take $\Omega = \phi_f$ and

$$F(\phi_f) = -\tilde{D}_f(\phi_f)\frac{\partial \phi_f}{\partial \tilde{x}}, \tag{A.11}$$

and couple it with:

$$F(\phi_f c) = (\phi_f \tilde{c})\tilde{v}_f - \phi_f \mathrm{Pe}^{-1}\tilde{\mathcal{D}}\frac{\partial \tilde{c}}{\partial \tilde{x}}. \tag{A.12}$$

For this solution, where we use compact finite differences, we repeat the convergence analysis in the number of grid points N_x (see Figure A.9), this time by calculating the RMS relative difference in $c(t, x = 1)$ for each solution with respect the solution for $N_x = 1000$. To balance between accuracy and computational time, we choose for all our simulations $N_x = 300$, associated with an error of less than 10^{-3}. We fix our tolerance value at 10^{-10}.

As a reference, the case of pure molecular diffusion is compared with an analytical solution for this problem (see Section A.8), resulting in good agreement between numerical and analytical results.

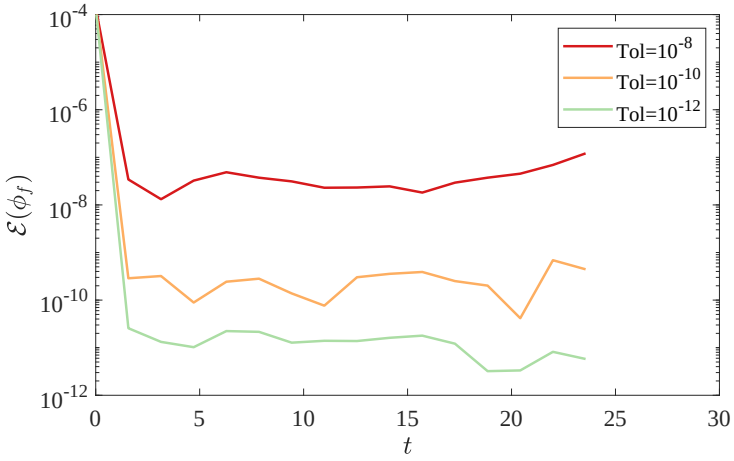

Figure A.8: RMS relative difference in $\phi_f(X,t)$ between two consecutive cycles in the periodic regime for $A = 0.2$ and $T = 4\pi$ and for three values of relative error tolerance for time integration.

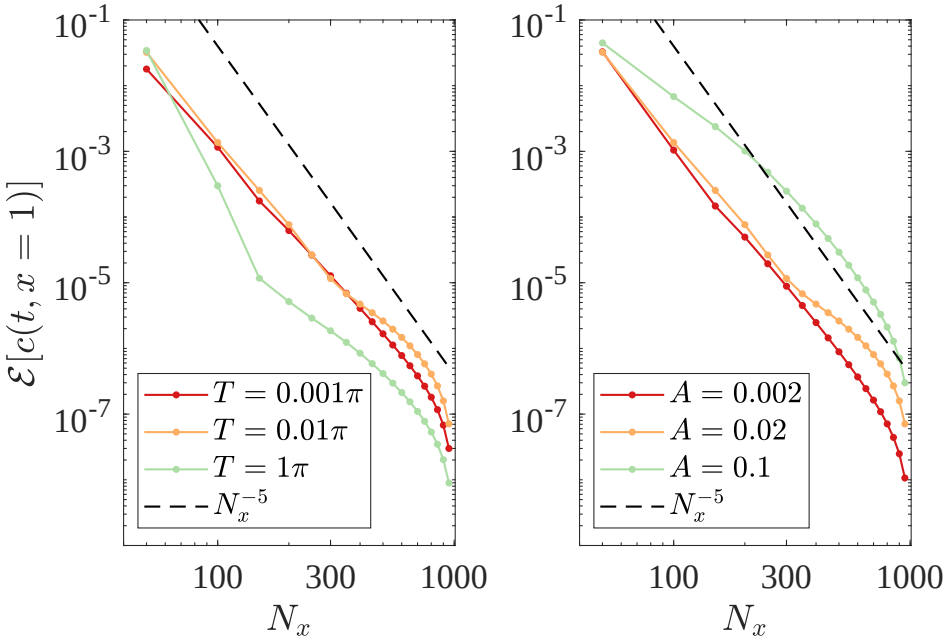

Figure A.9: Convergence analysis: RMS relative difference in $c(t, x = 1)$ relative to the solution for $N_x = 1000$ when using compact finite differences. On the left, we fix $A = 0.02$ and consider different values of T, from very fast to slow. On the right, we fix $T = 0.1\pi$ and consider different values of A, from small to large.

In Chapter 5, we take $\Omega = \Phi_f$ with

$$F(\Phi_f) = \frac{\partial W_f(\tilde{X}, \Phi_f)}{\partial \tilde{X}} \tag{A.13}$$

for the mechanics, and

$$F(\Phi_f \tilde{c}) = \tilde{c}\tilde{W}_f - \frac{1}{J}\phi_f \mathrm{Pe}^{-1}\tilde{\mathcal{D}}\frac{\partial \tilde{c}}{\partial \tilde{X}} \tag{A.14}$$

for solute transport. Based on the convergence analysis for this method shown in figure A.9, we fix once again $N_x = 300$.

In Chapter 6, we consider equation (A.11) for the 1D mechanics problem. The general conservation law for the 2D solute transport reads

$$\frac{\partial \Omega}{\partial t} + \frac{\partial}{\partial x}[F(\Omega)] + \frac{\partial}{\partial y}[G(\Omega)] = 0, \tag{A.15}$$

with

$$\Omega = \phi_f \tilde{c}, \tag{A.16}$$

$$F(\phi_f \tilde{c}) = (\phi_f \tilde{c})\tilde{v_f} - \phi_f \mathrm{Pe}^{-1}\tilde{\mathcal{D}}_x \frac{\partial \tilde{c}}{\partial \tilde{x}} \tag{A.17}$$

and

$$G(\phi_f \tilde{c}) = -\phi_f \mathrm{Pe}^{-1}\tilde{\mathcal{D}}_y \frac{\partial \tilde{c}}{\partial \tilde{y}}. \tag{A.18}$$

In this case, computational costs are considerably higher, so we fix $N_x = 150$ and $N_y = 100$, for which the error is larger but still acceptably small (in the order of 10^{-3}).

Since the models described in Chapter 5 and Chapter 6 are formulated with compact finite differences, for their convergence analysis we consider the data shown in figure A.9 relative to the model in Chapter 4.

A.8 Analytical solution for molecular diffusion

The analytical solution for the molecular diffusion problem in a semi-infinite medium, as formulated by Crank (1979), is:

$$c(x,t) = \frac{c_0}{2}\left[\mathrm{erfc}\left(\frac{l+x-1}{2\sqrt{Pe^{-1}t}}\right) + \mathrm{erfc}\left(\frac{l-x+1}{2\sqrt{Pe^{-1}t}}\right)\right]. \tag{A.19}$$

In Figure A.10, we compare the analytical solution to the numerical solution obtained with the method described in Appendix A.7. Note that we consider an initial solute profile that is smoother than the one for which the analytical solution is formulated. Hence, the two solutions show an initial discrepancy that vanishes with time, as the profile adjusts towards classical self similarity.

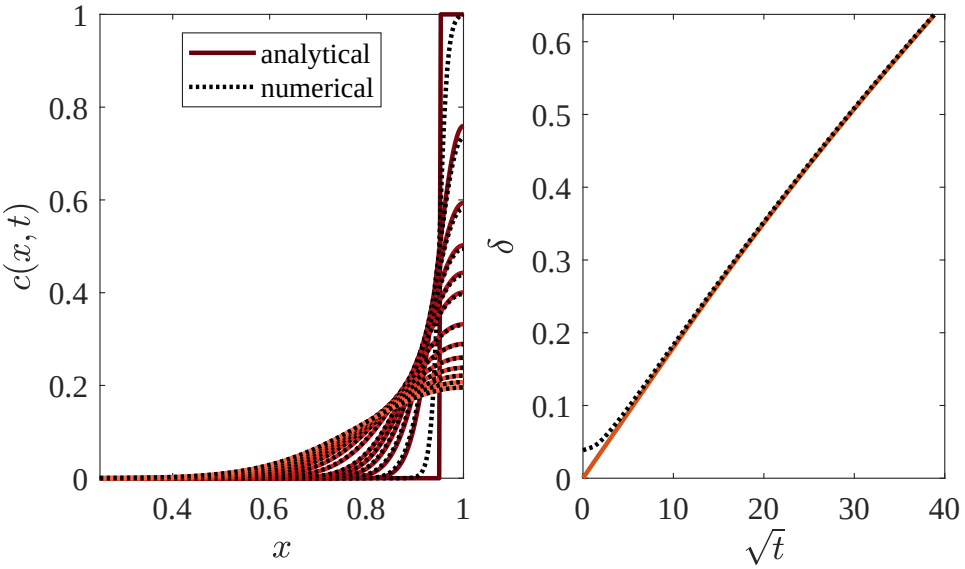

Figure A.10: Comparison between the analytical (red solid lines) and numerical (black dotted lines) solution for diffusion only. We show on the left the evolution of the concentration profiles $c(x,t)$ in time (dark to light) and on the right the evolution of δ over time.

Bibliography

M. B. Albro, N. O. Chahine, R. Li, K. Yeager, C. T. Hung, and G. A. Ateshian. Dynamic loading of deformable porous media can induce active solute transport. *Journal of Biomechanics*, 41(15): 3152–3157, 2008.

A. N. Alshawabkeh and N. Rahbar. Parametric study of one-dimensional solute transport in deformable porous media. *Journal of Geotechnical and Geoenvironmental Engineering*, 132(8):1001–1010, 2006.

P. Amrollahi and L. Tayebi. Bioreactors for heart valve tissue engineering: a review. *Journal of Chemical Technology & Biotechnology*, 91(4):847–856, 2015.

L. Anand. On H. Hencky's approximate strain-energy function for moderate deformations. *Journal of Applied Mechanics*, 46(1):78–82, 1979.

V. Arbabi, B. Pouran, H. Weinans, and A. A. Zadpoor. Transport of neutral solute across articular cartilage: The role of zonal diffusivities. *Journal of Biomechanical Engineering*, 137(7), 2015.

G. Ateshian. The role of interstitial fluid pressurization in articular cartilage lubrication. *Journal of Biomechanics*, 42:1163–76, 2009.

G. A. Ateshian and J. A. Weiss. Anisotropic hydraulic permeability under finite deformation. *Journal of Biomechanical Engineering*, 132(11):1–7, 2010.

G. A. Ateshian and J. A. Weiss. Finite element modeling of solutes in hydrated deformable biological tissues. In *Computer Models in Biomechanics: From Nano to Macro*, pages 231–249. Springer, 2013.

L. C. Auton and C. W. MacMinn. From arteries to boreholes: Transient response of a poroelastic cylinder to fluid injection. *Proceedings of the Royal Society A: Mathematical, Physical and Engineering Sciences*, 474(2216):20180284, 2018.

N. M. Bachrach, V. C. Mow, and F. Guilak. Incompressibility of the solid matrix of articular cartilage under high hydrostatic pressures. *Journal of Biomechanics*, 31(5):445–451, 1998.

M. Basilio Hazas, F. Ziliotto, J. Lee, M. Rolle, and G. Chiogna. Evolution of plume geometry, dilution and reactive mixing in porous media under highly transient flow fields at the surface water-groundwater interface. *Journal of Contaminant Hydrology*, 258:104243, 2023.

J. Bear. *Dynamics of fluids in porous media.* American Elsevier Publishing Company, 1972.

G. S. Beavers, T. A. Wilson, and B. A. Masha. Flow Through a Deformable Porous Material. *Journal of Applied Mechanics*, 42(3):598–602, 1975.

M. Berg, Y. Davit, M. Quintard, and S. Lorthois. Modelling solute transport in the brain microcirculation: is it really well mixed inside the blood vessels? *Journal of Fluid Mechanics*, 884:A39, 2020.

M. A. Biot. Theory of propagation of elastic waves in a fluid-saturated porous solid. i. low-frequency range. *The Journal of the Acoustical Society of America*, 28(2):168–178, 1956a.

M. A. Biot. Theory of propagation of elastic waves in a fluid-saturated porous solid. ii. higher frequency range. *The Journal of the Acoustical Society of America*, 28(2):179–191, 1956b.

L. Bojarskaite, D. M. Bjørnstad, A. Vallet, K. M. Gullestad Binder, C. Cunen, K. Heuser, M. Kuchta, K.-A. Mardal, and R. Enger. Sleep cycle-dependent vascular dynamics enhance perivascular cerebrospinal fluid flow and solute transport. *Nature Communications*, 14:953, 2023.

A. Bonazzi, B. Jha, and F. P. J. de Barros. Transport analysis in deformable porous media through integral transforms. *International Journal for Numerical and Analytical Methods in Geomechanics*, 45(3):307–324, 2021.

A. D. Bordoloi, D. Scheidweiler, M. Dentz, M. Bouabdellaoui, M. Abbarchi, and P. de Anna. Structure induced laminar vortices control anomalous dispersion in porous media. *Nature Communications*, 13(3820), 2022.

O. Borgman, R. Turuban, B. Géraud, T. Le Borgne, and Y. Méheust. Solute front shear and coalescence control concentration gradient dynamics in porous micromodel. *Geophysical Research Letters*, 50(5):e2022GL101407, 2023.

R. I. Borja and J. Choo. Cam-Clay plasticity, Part VIII: A constitutive framework for porous materials with evolving internal structure. *Computer Methods in Applied Mechanics and Engineering*, 309:653–679, 2016.

J. Bowles. *Foundation analysis and design.* McGraw-Hill, Inc, 1988.

H. Brenner and D. Edwards. *Macrotransport Processes.* Butterworth-Heinemann series in chemical engineering. Elsevier Science, 1993.

H. Brenner and K. Stewartson. Dispersion resulting from flow through spatially periodic porous media. *Philosophical Transactions of the Royal Society of London. Series A, Mathematical and Physical Sciences*, 297(1430):81–133, 1980.

C. Brouzet, Y. Méheust, and P. Meunier. co_2 convective dissolution in a three-dimensional granular porous medium: An experimental study. *Physical Review Fluids*, 7:033802, 2022.

J. O. D. Buijs, E. L. Ritman, and D. Dragomir-Daescu. Validation of a fluid-structure interaction model of solute transport in pores of cyclically deformed tissue scaffolds. *Tissue Engineering - Part C: Methods*, 16:1145–1156, 2010.

D. L. Butler, S. A. Goldstein, and F. Guilak. Functional tissue engineering: the role of biomechanics. *Journal of Biomechanical Engineering*, 122(6):570–575, 2000.

J. Cacheux, J. Ordonez-Miranda, A. Bancaud, L. Jalabert, D. Alcaide, M. Nomura, and Y. T. Matsunaga. Asymmetry of tensile versus compressive elasticity and permeability contributes to the regulation of exchanges in collagen gels. *Science Advances*, 9(31):eadf9775, 2023.

S. Cai and Z. Suo. Equations of state for ideal elastomeric gels. *Europhysics Letters*, 97(3):34009, 2012.

S. Camarero-Espinosa, B. Rothen-Rutishauser, E. J. Foster, and C. Weder. Articular cartilage: from formation to tissue engineering. *Biomaterals Science*, 4:734–767, 2016a.

S. Camarero-Espinosa, B. Rothen-Rutishauser, C. Weder, and E. J. Foster. Directed cell growth in multi-zonal scaffolds for cartilage tissue engineering. *Biomaterials*, 74:42–52, 2016b.

P. Carman. *Flow of gases through porous media*. Academic Press, New York, 1956.

P. Carman. Fluid flow through granular beds. *Chemical Engineering Research and Design*, 75: 150–166, 1997.

F. Catania, M. Massabó, M. Valle, G. Bracco, and O. Paladino. Assessment of quantitative imaging of contaminant distributions in porous media. *Experiments in Fluids*, 44:167–177, 2008.

A. Chen, W. Bae, R. Schinagl, and R. Sah. Depth- and strain-dependent mechanical and electromechanical properties of full-thickness bovine articular cartilage in confined compression. *Journal of Biomechanics*, 34(1):1–12, 2001.

A. H.-D. Cheng. *Poroelasticity*, volume 27 of *Theory and Applications of Transport in Porous Media*. Springer, 2016.

S.-J. Choi, T.-H. Kwon, H. Im, D.-I. Moon, D. J. Baek, M.-L. Seol, J. P. Duarte, and Y.-K. Choi. A polydimethylsiloxane (PDMS) sponge for the selective absorption of oil from water. *ACS Applied Materials & Interfaces*, 3(12):4552–4556, 2011.

M. Corapcioglu and P. Fedirchuk. Glass bead micromodel study of solute transport. *Journal of Contaminant Hydrology*, 36(3):209–230, 1999.

S. Cortez, A. Completo, and J. L. Alves. The influence of mechanical stimulus on nutrient transport and cell growth in engineered cartilage: A Finite element approach. *ECCOMAS Congress 2016 - Proceedings of the 7th European Congress on Computational Methods in Applied Sciences and Engineering*, 1(June):27–36, 2016.

J. Crank. *The mathematics of diffusion.* Oxford university press, 1979.

Y. Dabiri and L. P. Li. Influences of the depth-dependent material inhomogeneity of articular cartilage on the fluid pressurization in the human knee. *Medical Engineering and Physics*, 35(11): 1591–1598, 2013.

S. S. Datta, H. Chiang, T. S. Ramakrishnan, and D. A. Weitz. Spatial fluctuations of fluid velocities in flow through a three-dimensional porous medium. *Physical Review Letters*, 111:064501, 2013.

Y. Davit, H. Byrne, J. Osborne, J. Pitt-Francis, D. Gavaghan, and M. Quintard. Hydrodynamic dispersion within porous biofilms. *Physical Review E*, 87:012718, 2013.

P. de Anna, T. Le Borgne, M. Dentz, A. M. Tartakovsky, D. Bolster, and P. Davy. Flow intermittency, dispersion, and correlated continuous time random walks in porous media. *Physical Review Letters*, 110:184502, 2013.

P. de Anna, J. Jimenez-Martinez, H. Tabuteau, R. Turuban, T. Le Borgne, M. Derrien, and Y. Méheust. Mixing and reaction kinetics in porous media: An experimental pore scale quantification. *Environmental Science & Technology*, 48(1):508–516, 2014.

J. Delgado. Longitudinal and transverse dispersion in porous media. *Chemical Engineering Research and Design*, 85(9):1245–1252, 2007.

M. Dentz, T. Le Borgne, A. Englert, and B. Bijeljic. Mixing, spreading and reaction in heterogeneous media: A brief review. *Journal of Contaminant Hydrology*, 120-121:1–17, 2011.

M. Dentz, F. P. De Barros, T. Le Borgne, and D. R. Lester. Evolution of solute blobs in heterogeneous porous media. *Journal of Fluid Mechanics*, 853:621–646, 2018.

M. Dentz, J. J. Hidalgo, and D. Lester. Mixing in porous media: Concepts and approaches across scales. *Transport in Porous Media*, 146(1-2):5 – 53, 2023.

C. D. DiDomenico, A. Goodearl, A. Yarilina, V. Sun, S. Mitra, A. S. Sterman, and L. J. Bonassar. The effect of antibody size and mechanical loading on solute diffusion through the articular surface of cartilage. *Journal of Biomechanical Engineering*, 139(9):091005, 2017.

C. D. DiDomenico, Z. X. Wang, and L. J. Bonassar. Cyclic mechanical loading enhances transport of antibodies into articular cartilage. *Journal of Biomechanical Engineering*, 139(1):1–7, 2017.

C. D. DiDomenico, M. Lintz, and L. Bonassar. Molecular transport in articular cartilage — what have we learned from the past 50 years? *Nature Reviews Rheumatology*, 14:393–403, 2018.

W. Ehlers, N. Karajan, and B. Markert. An extended biphasic model for charged hydrated tissues with application to the intervertebral disc. *Biomechanics and Modeling in Mechanobiology*, 8(3): 233–251, 2009.

L. Fan, S. Pei, X. Lucas Lu, and L. Wang. A multiscale 3D finite element analysis of fluid/solute transport in mechanically loaded bone. *Bone Research*, 4:16032, 2016.

S. Federico and A. Grillo. Elasticity and permeability of porous fibre-reinforced materials under large deformations. *Mechanics of Materials*, 44:58–71, 2012.

S. Federico and W. Herzog. On the permeability of fibre-reinforced porous materials. *International Journal of Solids and Structures*, 45(7-8):2160–2172, 2008a.

S. Federico and W. Herzog. On the anisotropy and inhomogeneity of permeability in articular cartilage. *Biomechanics and Modeling in Mechanobiology*, 7(5):367–378, 2008b.

S. J. Ferguson, K. Ito, and L. J. Pyrak-Nolte. Fluid flow and convective transport of solutes within the intervertebral disc. *Journal of Biomechanics*, 37(2):213–221, 2004.

M. Fiori, S. Pramanik, and C. W. MacMinn. Flow and deformation due to periodic loading in a soft porous material. *Journal of Fluid Mechanics*, 974:A2, 2023a.

M. Fiori, S. Pramanik, and C. W. MacMinn. Flow and deformation due to periodic loading in a soft porous material - Example code. figshare, 2023b. https://dx.doi.org/10.6084/m9.figshare.24042162.

P. J. Fox. Coupled large strain consolidation and solute transport. i: Model development. *Journal of Geotechnical and Geoenvironmental Engineering*, 133(1):3–15, 2007a.

P. J. Fox. Coupled large strain consolidation and solute transport. ii: Model verification and simulation results. *Journal of Geotechnical and Geoenvironmental Engineering*, 133(1):16–29, 2007b.

M. Fraldi, S. Palumbo, A. Carotenuto, A. Cutolo, L. Deseri, and N. Pugno. Buckling soft tensegrities: Fickle elasticity and configurational switching in living cells. *Journal of the Mechanics and Physics of Solids*, 124, 2018.

G. Franceschini, D. Bigoni, P. Regitnig, and G. Holzapfel. Brain tissue deforms similarly to filled elastomers and follows consolidation theory. *Journal of the Mechanics and Physics of Solids*, 54 (12):2592–2620, 2006.

Y. C. Fung. *Biomechanics: mechanical properties of living tissues*. Springer Science & Business Media, 2013.

A. Gajo and R. Denzer. Finite element modelling of saturated porous media at finite strains under dynamic conditions with compressible constituents. *International Journal for Numerical Methods in Engineering*, 85(13):1705–1736, 2011.

X. Gao, Q. Zhu, and W. Gu. An Anisotropic Multiphysics Model for Intervertebral Disk. *Journal of Applied Mechanics*, 83(2):021011, 2015.

Y. Gao and H. J. Cho. Quantifying the trade-off between stiffness and permeability in hydrogels. *Soft Matter*, 18:7735–7740, 2022.

B. Gardiner, D. Smith, P. Pivonka, A. Grodzinsky, E. Frank, and L. Zhang. Solute transport in cartilage undergoing cyclic deformation. *Computer Methods in Biomechanics and Biomedical Engineering*, 10(4):265–278, 2007.

D. Gastaldi, M. Taffetani, R. Raiteri, and P. Vena. Effect of the anisotropic permeability in the frequency dependent properties of the superficial layer of articular cartilage. *Computer Methods in Biomechanics and Biomedical Engineering*, 21(11):635–644, 2018.

R. Gauvin, R. Parenteau-Bareil, D. Larouche, H. Marcoux, F. Bisson, A. Bonnet, F. A. Auger, S. Bolduc, and L. Germain. Dynamic mechanical stimulations induce anisotropy and improve the tensile properties of engineered tissues produced without exogenous scaffolding. *Acta Biomaterialia*, 7(9):3294–3301, 2011.

L. Gelhar. *Stochastic Subsurface Hydrology*. Prentice-Hall, 1993.

L. W. Gelhar and C. L. Axness. Three-dimensional stochastic analysis of macrodispersion in aquifers. *Water Resources Research*, 19(1):161–180, 1983.

L. W. Gelhar, C. Welty, and K. R. Rehfeldt. A critical review of data on field-scale dispersion in aquifers. *Water Resources Research*, 28(7):1955–1974, 1992.

F. Genna and A. Cividini. Finite element analysis of fluid phase nonlinearity effects on the undrained dynamic behaviour of nearly saturated porous media. *Soil Dynamics and Earthquake Engineering*, 8(4):189–201, 1989.

B. Ghanbarian, A. G. Hunt, R. P. Ewing, and M. Sahimi. Tortuosity in porous media: a critical review. *Soil science society of America journal*, 77(5):1461–1477, 2013.

F. Goirand, T. Le Borgne, and S. Lorthois. Network-driven anomalous transport is a fundamental component of brain microvascular dysfunction. *Nature Communications*, 12(7295), 2021.

P. Gouze, A. Puyguiraud, T. Porcher, and M. Dentz. Modeling longitudinal dispersion in variable porosity porous media: Control of velocity distribution and microstructures. *Frontiers in Water*, 3, 2021.

G. Grenier, M. Rémy-Zolghadri, D. Larouche, R. Gauvin, K. Baker, F. Bergeron, D. Dupuis, E. Langelier, D. Rancourt, F. A. Auger, and L. Germain. Tissue reorganization in response to mechanical load increases functionality. *Tissue Engineering*, 11(1-2):90–100, 2005.

W. Y. Gu, X. G. Mao, R. J. Foster, M. Weidenbaum, V. C. Mow, and B. A. Rawlins. The anisotropic hydraulic permeability of human lumbar anulus fibrosus: Influence of age, degeneration, direction, and water content. *Spine*, 24(23):2449–2455, 1999.

U. A. Gurkan, R. El Assal, S. E. Yildiz, Y. Sung, A. J. Trachtenberg, W. P. Kuo, and U. Demirci. Engineering anisotropic biomimetic fibrocartilage microenvironment by bioprinting mesenchymal stem cells in nanoliter gel droplets. *Molecular Pharmaceutics*, 11(7):2151–2159, 2014.

A. J. E. Haj, K. Hampson, and G. Gogniat. *Bioreactors for connective tissue engineering: design and monitoring innovations*, pages 81–93. Springer Berlin Heidelberg, 2009.

H. M. D. Harshani, S. A. Galindo-Torres, A. Scheuermann, and H. B. Muhlhaus. Experimental study of porous media flow using hydro-gel beads and led based PIV. *Measurement Science and Technology*, 28(1):015902, 2016.

Y. He, J. Qiu, J. Fu, J. Zhang, Y. Ren, and A. Liu. Printing 3D microfluidic chips with a 3D sugar printer. *Microfluidics and Nanofluidics*, 19(2):447–456, 2015.

H. Hencky. The law of elasticity for isotropic and quasi-isotropic substances by finite deformations. *Journal of Rheology*, 2(2):169–176, 1931.

H. Hencky. The Elastic Behavior of Vulcanized Rubber. *Rubber Chemistry and Technology*, 6(2): 217–224, 1933.

D. R. Hewitt, J. A. Neufeld, and N. J. Balmforth. Shallow, gravity-driven flow in a poro-elastic layer. *Journal of Fluid Mechanics*, 778:335–360, 2015.

D. R. Hewitt, J. S. Nijjer, M. G. Worster, and J. A. Neufeld. Flow-induced compaction of a deformable porous medium. *Physical Review E*, 93:023116, 2016a.

D. R. Hewitt, D. T. Paterson, N. J. Balmforth, and D. M. Martinez. Dewatering of fibre suspensions by pressure filtration. *Physics of Fluids*, 28(6):063304, 2016b.

J. Heyman, D. R. Lester, R. Turuban, Y. Méheust, and T. L. Borgne. Stretching and folding sustain microscale chemical gradients in porous media. *Proceedings of the National Academy of Sciences*, 117(24):13359–13365, 2020.

M. Holmes and V. Mow. The nonlinear characteristics of soft gels and hydrated connective tissues in ultrafiltration. *Journal of Biomechanics*, 23(11):1145–1156, 1990.

M. Holzner, V. L. Morales, M. Willmann, and M. Dentz. Intermittent lagrangian velocities and accelerations in three-dimensional porous medium flow. *Physical Review E*, 92:013015, 2015.

W. Hong, X. Zhao, J. Zhou, and Z. Suo. A theory of coupled diffusion and large deformation in polymeric gels. *Journal of the Mechanics and Physics of Solids*, 56(5):1779–1793, 2008.

J. Hrabe, S. Hrabětová, and K. Segeth. A model of effective diffusion and tortuosity in the extracellular space of the brain. *Biophysical journal*, 87(3):1606–1617, 2004.

J. Hu, Q. Chen, H. Zhu, L. Hou, W. Liu, Q. Yang, H. Shen, G. Chai, B. Zhang, S. Chen, Z. Cai, C. Wu, F. Hong, H. Li, S. Chen, N. Xiao, Z. xiang Wang, X. Zhang, B. Wang, L. Zhang, and W. Mo. Microglial piezo1 senses Aβ fibril stiffness to restrict Alzheimer's disease. *Neuron*, 111 (1):15–29.e8, 2023.

Y.-J. Hu, Y.-Y. Zhu, and C.-J. Cheng. Transient dynamic response of fluid-saturated soil under a moving cyclic loading. *Soil Dynamics and Earthquake Engineering*, 31(3):491–501, 2011.

J. Hwang, W. C. Bae, W. Shieu, C. W. Lewis, W. D. Bugbee, and R. L. Sah. Increased hydraulic conductance of human articular cartilage and subchondral bone plate with progression of osteoarthritis. *Arthritis & Rheumatism*, 58(12):3831–3842, 2008.

J. J. Iliff, M. Wang, Y. Liao, B. A. Plogg, W. Peng, G. A. Gundersen, H. Benveniste, G. E. Vates, R. Deane, S. A. Goldman, E. A. Nagelhus, and M. Nedergaard. A paravascular pathway facilitates csf flow through the brain parenchyma and the clearance of interstitial solutes, including amyloid β. *Science Translational Medicine*, 4(147):147ra111, 2012.

N. Inoue and A. A. Espinoza Orías. Biomechanics of intervertebral disk degeneration. *Orthopedic Clinics of North America*, 42(4):487 – 499, 2011.

G. M. Jensen. Biomechanics of the lumbar intervertebral disk: A review. *Physical Therapy*, 60(6): 765–773, 1980.

B. Jha, L. Cueto-Felgueroso, and R. Juanes. Quantifying mixing in viscously unstable porous media flows. *Physical Review E*, 84(6):066312, 2011.

Y. Kameo, T. Adachi, and M. Hojo. Transient response of fluid pressure in a poroelastic material under uniaxial cyclic loading. *Journal of the Mechanics and Physics of Solids*, 56(5):1794–1805, 2008.

M. R. Karim, T. Nogami, and J. G. Wang. Analysis of transient response of saturated porous elastic soil under cyclic loading using element-free Galerkin method. *International Journal of Solids and Structures*, 39(24):6011–6033, 2002.

J. V. Karpiak, Y. Ner, and A. Almutairi. Density gradient multilayer polymerization for creating complex tissue. *Advanced Materials*, 24(11):1466–1470, 2012.

R. T. Kedarasetti, P. J. Drew, and F. Costanzo. Arterial vasodilation drives convective fluid flow in the brain: a poroelastic model. *Fluids and Barriers of the CNS*, 19:34, 2020.

D. H. Kelley and J. H. Thomas. Cerebrospinal fluid flow. *Annual Review of Fluid Mechanics*, 55 (1):237–264, 2023.

B. Kim, J. Nikolovski, J. Bonadio, and D. J. Mooney. Cyclic mechanical strain regulates the development of engineered smooth muscle tissue. *Nature Biotechnology*, 17:979–983, 1999.

M. King, A. Baragwanath, M. Rosamond, D. Wood, and A. Gallant. Porous PDMS force sensitive resistors. *Procedia Chemistry*, 1(1):568–571, 2009. Proceedings of the Eurosensors XXIII conference.

J. Kozeny. Ueber kapillare leitung des wassers im boden. *Sitzungsberichte der Kaiserlichen Akademie der Wissenschaften*, 136(2a):271–306, 1927.

M. Kree and E. Villermaux. Scalar mixtures in porous media. *Physical Review Fluids*, 2:104502, 2017.

R. Krishnan, S. Park, F. Eckstein, and G. A. Ateshian. Inhomogeneous cartilage properties enhance superficial interstitial fluid support and frictional properties, but do not provide a homogeneous state of stress. *Journal of Biomechanical Engineering*, 125(5):569–577, 2003.

P. Kumar, B. Dey, and G. P. Raja Sekhar. Nutrient transport through deformable cylindrical scaffold inside a bioreactor: An application to tissue engineering. *International Journal of Engineering Science*, 127:201–216, 2018.

W. M. Lai, J. S. Hou, and V. C. Mow. A triphasic theory for the swelling and deformation behaviors of articular cartilage. *Journal of Biomechanical Engineering*, 113(3):245–258, 1991.

Y. Lanir, S. Sauob, and P. Maretsky. Nonlinear ffinite deformation response of open cell polyurethane sponge to fluid filtration. *Journal of Applied Mechanics*, 57(2):449–454, 1990.

J. Lee, J. Paek, and J. Kim. Sucrose-based fabrication of 3d-networked, cylindrical microfluidic channels for rapid prototyping of lab-on-a-chip and vaso-mimetic devices. *Lab Chip*, 12:2638–2642, 2012.

M. K. Lee, M. H. Rich, K. Baek, J. Lee, and H. Kong. Bioinspired tuning of hydrogel permeability-rigidity dependency for 3D cell culture. *Scientific Reports*, 5:1–7, 2015.

D. Lester, M. Trefry, and G. Metcalfe. Chaotic advection at the pore scale: Mechanisms, upscaling and implications for macroscopic transport. *Advances in Water Resources*, 97:175–192, 2016a.

D. R. Lester, G. Metcalfe, and M. G. Trefry. Is chaotic advection inherent to porous media flow? *Physical Review Letters*, 111(17):1–5, 2013.

D. R. Lester, M. Dentz, and T. Le Borgne. Chaotic mixing in three-dimensional porous media. *Journal of Fluid Mechanics*, 803:144–174, 2016b.

J. Levick. Flow through interstitium and other fibrous matrices. *Quarterly Journal of Experimental Physiology: Translation and Integration*, 72(4):409–437, 1987.

T. W. Lewis, P. Pivonka, and D. W. Smith. Theoretical investigation of the effects of consolidation on contaminant transport through clay barriers. *International Journal for Numerical and Analytical Methods in Geomechanics*, 33(1):95–116, 2009.

C. Li, R. I. Borja, and R. A. Regueiro. Dynamics of porous media at finite strain. *Computer Methods in Applied Mechanics and Engineering*, 193(36-38):3837–3870, 2004.

J. Li, Y. Hu, J. J. Vlassak, and Z. Suo. Experimental determination of equations of state for ideal elastomeric gels. *Soft Matter*, 8:8121–8128, 2012.

Y. Liang, B. Wen, M. A. Hesse, and D. DiCarlo. Effect of dispersion on solutal convection in porous media. *Geophysical Research Letters*, 45(18):9690–9698, 2018.

J. Liu, X. Li, J. Liu, and B. Han. Numerical Investigation of Transition Mechanism between the Two Kinds of Compressional Waves in Saturated Geotechnical Media. *International Journal of Geomechanics*, 19(3):1–9, 2019.

T. Lutz, L. Wilen, and J. Wettlaufer. A method for measuring fluid pressure and solid deformation profiles in uniaxial porous media flows. *Review of Scientific Instruments*, 92(2):025101, 2021.

C. W. MacMinn, E. R. Dufresne, and J. S. Wettlaufer. Fluid-driven deformation of a soft granular material. *Physical Review X*, 5:011020, 2015.

C. W. MacMinn, E. R. Dufresne, and J. S. Wettlaufer. Large Deformations of a Soft Porous Material. *Physical Review Applied*, 5(4):044020, 2016.

O. S. Madsen. Wave-induced pore pressures and effective stresses in a porous bed. *Géotechnique*, 28(4):377–393, 1978.

A. Malandrino, J. A. Planell, and D. Lacroix. Statistical factorial analysis on the poroelastic material properties sensitivity of the lumbar intervertebral disc under compression, flexion and axial rotation. *Journal of Biomechanics*, 42(16):2780–2788, 2009.

A. Malandrino, D. Lacroix, C. Hellmich, K. Ito, S. Ferguson, and J. Noailly. The role of endplate poromechanical properties on the nutrient availability in the intervertebral disc. *Osteoarthritis and Cartilage*, 22(7):1053–1060, 2014.

M. Maleki, K. Hashlamoun, W. Herzog, and S. Federico. Effect of structural distortions on articular cartilage permeability under large deformations. *Biomechanics and Modeling in Mechanobiology*, 19(1):317—334, 2020.

P. Manfredini, G. Cocchetti, G. Maier, A. Redaelli, and F. M. Montevecchi. Poroelastic finite element analysis of a bone specimen under cyclic loading. *Journal of Biomechanics*, 32(2):135–144, 1999.

S. Marbach and K. Alim. Active control of dispersion within a channel with flow and pulsating walls. *Physical Review Fluids*, 4:114202, 2019.

S. Marchesseau, T. Heimann, S. Chatelin, R. Willinger, and D. H. Fast porous visco-hyperelastic soft tissue model for surgery simulation: Application to liver surgery. *Progress in Biophysics and Molecular Biology*, 103(2):185–196, 2010.

G. Marini and S. J. Ferguson. Modelling the influence of heterogeneous annulus material property distribution on intervertebral disk mechanics. *Annals of Biomedical Engineering*, 42(8):1760–1772, 2014.

A. Maroudas. Physicochemical properties of cartilage in the light of ion exchange theory. *Biophysical Journal*, 8(5):575–595, 1968.

A. Maroudas. Distribution and diffusion of solutes in articular cartilage. *Biophysical Journal*, 10(5): 365–379, 1970.

A. Maroudas. Biophysical chemistry of cartilaginous tissues with special reference to solute and fluid transport. *Biorheology*, 12(3-4):233–248, 1975.

A. Maroudas and P. Bullough. Permeability of articular cartilage. *Nature*, 219(5):1260–1261, 1968.

S. Mattana, S. Caponi, F. Tamagnini, D. Fioretto, and F. Palombo. Viscoelasticity of amyloid plaques in transgenic mouse brain studied by brillouin microspectroscopy and correlative raman analysis. *Journal of Innovative Optical Health Sciences*, 10(06):1742001, 2017.

R. L. Mauck, M. A. Soltz, C. C. B. Wang, D. D. Wong, P.-H. G. Chao, W. B. Valhmu, C. T. Hung, and G. A. Ateshian. Functional tissue engineering of articular cartilage through dynamic loading of chondrocyte-seeded agarose gels . *Journal of Biomechanical Engineering*, 122(3):252–260, 2000.

R. L. Mauck, C. T. Hung, and G. A. Ateshian. Modeling of neutral solute transport in a dynamically loaded porous permeable gel: implications for articular cartilage biosynthesis and tissue engineering. *Journal of Biomechanical Engineering*, 125(5):602–614, 2003.

T. G. Mayerhöfer, S. Pahlow, and J. Popp. The bouguer-beer-lambert law: Shining light on the obscure. *ChemPhysChem*, 21(18):2029–2046, 2020.

J. McNeil, G. Oldenborger, and R. Schincariol. Quantitative imaging of contaminant distributions in heterogeneous porous media laboratory experiments. *Journal of Contaminant Hydrology*, 84 (1):36–54, 2006.

T. Mesallati, C. T. Buckley, T. Nagel, and D. J. Kelly. Scaffold architecture determines chondrocyte response to externally applied dynamic compression. *Biomechanics and Modeling in Mechanobiology*, 12(5):889–899, 2013.

M. Mishra, M. Martin, and A. De Wit. Differences in miscible viscous fingering of finite width slices with positive or negative log-mobility ratio. *Physical Review E*, 78(6):066306, 2008.

E. Moeendarbary, L. Valon, M. Fritzsche, A. R. Harris, D. A. Moulding, A. J. Thrasher, E. Stride, L. Mahadevan, and G. T. Charras. The cytoplasm of living cells behaves as a poroelastic material. *Nature Materials*, 12(3):253–261, 2013.

V. C. Mow, S. C. Kuei, W. M. Lai, and C. G. Armstrong. Biphasic creep and stress relaxation of articular cartilage in compression: Theory and experiments. *Journal of Biomechanical Engineering*, 102(1):73–84, 1980.

V. C. Mow, M. H. Holmes, and W. M. Lai. Fluid transport and mechanical properties of articular cartilage: a review. *Journal of Biomechanics*, 17(5):377–394, 1984.

M. C. Murphy, J. Huston III, C. R. Jack Jr, K. J. Glaser, A. Manduca, J. P. Felmlee, and R. L. Ehman. Decreased brain stiffness in Alzheimer's disease determined by magnetic resonance elastography. *Journal of Magnetic Resonance Imaging*, 34(3):494–498, 2011.

R. Neupauer, E. Roth, J. Crimaldi, D. Mays, and L. Sather. Demonstration of reversible dispersion in a darcy-scale push-pull laboratory experiment. *Transport in Porous Media*, 146, 2021.

K. W. Ng, R. L. Mauck, L. Y. Statman, E. Y. Lin, G. A. Ateshian, and C. T. Hung. Dynamic deformational loading results in selective application of mechanical stimulation in a layered, tissue-engineered cartilage construct. *Biorheology*, 43(3-4):497–507, 2006.

V.-H. Nguyen, T. Lemaire, and S. Naili. Poroelastic behaviour of cortical bone under harmonic axial loading: A finite element study at the osteonal scale. *Medical Engineering & Physics*, 32(4): 384–390, 2010.

J. Ni and X.-Y. Geng. Radial consolidation of prefabricated vertical drain-reinforced soft clays under cyclic loading. *Transportation Geotechnics*, 37:100840, 2022.

J. Ni, B. Indraratna, X.-Y. Geng, J. P. Carter, and Y.-L. Chen. Model of soft soils under cyclic loading. *International Journal of Geomechanics*, 15(4):04014067, 2015.

S. Oswald and W. Kinzelbach. Three-dimensional physical benchmark experiments to test variable-density flow models. *Journal of Hydrology*, 290(1):22–42, 2004.

F. Palombo, F. Masia, S. Mattana, F. Tamagnini, P. Borri, W. Langbein, and D. Fioretto. Hyperspectral analysis applied to micro-brillouin maps of amyloid-beta plaques in Alzheimer's disease brains. *Analyst*, 143:6095–6102, 2018.

S. Park, R. Krishnan, S. B. Nicoll, and G. A. Ateshian. Cartilage interstitial fluid load support in unconfined compression. *Journal of Biomechanics*, 36(12):1785–1796, 2003.

K. H. Parker, R. V. Mehta, and C. G. Caro. Steady Flow in Porous, Elastically Deformable Materials. *Journal of Applied Mechanics*, 54(4):794–800, 1987.

D. T. Paterson, T. S. Eaves, D. R. Hewitt, N. J. Balmforth, and D. M. Martinez. Flow-driven compaction of a fibrous porous medium. *Physical Review Fluids*, 4:074306, 2019.

M. Peroglio, D. Gaspar, D. I. Zeugolis, and M. Alini. Relevance of bioreactors and whole tissue cultures for the translation of new therapies to humans. *Journal of Orthopaedic Research*, 36(1): 10–21, 2018.

G. P. Peters and D. W. Smith. Solute transport through a deforming porous medium. *International Journal for Numerical and Analytical Methods in Geomechanics*, 26(7):683–717, 2002.

K. Piekarski and M. Munro. Transport mechanism operating between blood supply and osteocytes in long bones. *Nature*, 269:80–82, 1977.

D. M. Pierce, T. Ricken, and G. A. Holzapfel. A hyperelastic biphasic fibre-reinforced model of articular cartilage considering distributed collagen fibre orientations: continuum basis, computational aspects and applications. *Computer Methods in Biomechanics and Biomedical Engineering*, 16(12):1344–1361, 2013.

D. M. Pierce, M. J. Unterberger, W. Trobin, T. Ricken, and G. A. Holzapfel. A microstructurally based continuum model of cartilage viscoelasticity and permeability incorporating measured statistical fiber orientations. *Biomechanics and Modeling in Mechanobiology*, 15(1):229–244, 2016.

R. Poole, T. Kojima, T. Yasuda, F. Mwale, M. Kobayashi, and S. Laverty. Composition and structure of articular cartilage: A template for tissue repair. *Clinical Orthopaedics and Related Research*, 391:S26–S33, 2001.

R. Popescu, J. H. Prevost, G. Deodatis, and P. Chakrabortty. Dynamics of nonlinear porous media with applications to soil liquefaction. *Soil Dynamics and Earthquake Engineering*, 26(6):648–665, 2006.

L. Preziosi, D. Joseph, and G. Beavers. Infiltration of initially dry, deformable porous media. *International Journal of Multiphase Flow*, 22(6):1205 – 1222, 1996.

H. Pu, P. J. Fox, and C. D. Shackelford. Benchmark problem for large strain consolidation-induced solute transport. *Journal of Geotechnical and Geoenvironmental Engineering*, 144(3):1–4, 2018.

A. Rahbari, H. Montazerian, E. Davoodi, and S. Homayoonfar. Predicting permeability of regular tissue engineering scaffolds: scaling analysis of pore architecture, scaffold length, and fluid flow rate effects. *Computer Methods in Biomechanics and Biomedical Engineering*, 20(3):231–241, 2017.

M. Rashidi, L. Peurrung, A. Tompson, and T. Kulp. Experimental analysis of pore-scale flow and transport in porous media. *Advances in Water Resources*, 19(3):163–180, 1996.

M. K. Rasmussen, H. Mestre, and M. Nedergaard. Fluid transport in the brain. *Physiological Reviews*, 102(2):1025–1151, 2022.

B. Reynaud and T. M. Quinn. Anisotropic hydraulic permeability in compressed articular cartilage. *Journal of Biomechanics*, 39(1):131–137, 2006.

P. E. Riches, N. Dhillon, J. Lotz, A. W. Woods, and D. S. McNally. The internal mechanics of the intervertebral disc under cyclic loading. *Journal of Biomechanics*, 35(9):1263–1271, 2002.

M. Rolle, C. Eberhardt, G. Chiogna, O. A. Cirpka, and P. Grathwohl. Enhancement of dilution and transverse reactive mixing in porous media: Experiments and model-based interpretation. *Journal of Contaminant Hydrology*, 110(3):130–142, 2009.

E. J. Roth, D. C. Mays, R. M. Neupauer, L. J. Sather, and J. P. Crimaldi. Methods for laser-induced fluorescence imaging of solute plumes at the darcy scale in quasi-two-dimensional, refractive index-matched porous media. *Transport in Porous Media*, 136:879 – 898, 2021.

R. Sacco, P. Causin, P. Zunino, and M. T. Raimondi. A multiphysics/multiscale 2D numerical simulation of scaffold-based cartilage regeneration under interstitial perfusion in a bioreactor. *Biomechanics and Modeling in Mechanobiology*, 10:577–589, 2014.

P. G. Saffman. A theory of dispersion in a porous medium. *Journal of Fluid Mechanics*, 6:321 – 349, 1959.

C. K. Sahu and J. A. Neufeld. Experimental insights into gravity-driven flows and mixing in layered porous media. *Journal of Fluid Mechanics*, 956:A27, 2023.

D. A. Sánchez-Téllez, L. Téllez-Jurado, and L. M. Rodríguez-Lorenzo. Hydrogels for cartilage regeneration, from polysaccharides to hybrids. *Polymers*, 9(12):1–32, 2017.

K. Sano, Y. Ishida, and T. Aida. Synthesis of Anisotropic Hydrogels and Their Applications. *Angewandte Chemie - International Edition*, 57(10):2532–2543, 2018.

A. E. Scheidegger. General theory of dispersion in porous media. *Journal of Geophysical Research*, 66(10):3273–3278, 1961.

H. Schmidt, A. Shirazi-Adl, F. Galbusera, and H.-J. Wilke. Response analysis of the lumbar spine during regular daily activities—a finite element analysis. *Journal of Biomechanics*, 43(10):1849 – 1856, 2010.

B. G. Sengers, C. W. J. Oomens, and F. P. T. Baaijens. An integrated finite-element approach to mechanics, transport and biosynthesis in tissue engineering. *Journal of Biomechanical Engineering*, 126(1):82–91, 2004.

L. F. Shampine and M. W. Reichelt. The MATLAB ODE suite. *SIAM Journal on Scientific Computing*, 18(1):1–2, 1997.

K. M. Sharp, R. o. Carare, and A. Martin, Bryn. Dispersion in porous media in oscillatory flow between flat plates: applications to intrathecal, periarterial and paraarterial solute transport in the central nervous system. *Fluids and Barriers of the CNS*, 16(13), 2019.

J. F. Smith, T. P. J. Knowles, C. M. Dobson, C. E. MacPhee, and M. E. Welland. Characterization of the nanoscale properties of individual amyloid fibrils. *Proceedings of the National Academy of Sciences*, 103(43):15806–15811, 2006.

B. Sobac, M. Colombani, and Y. Forterre. On the dynamics of poroelastic foams. *Mécanique & Industries*, 12(03):231–238, 2011.

M. A. Soltz and G. A. Ateshian. Experimental verification and theoretical prediction of cartilage interstitial fluid pressurization at an impermeable contact interface in confined compression. *Journal of Biomechanics*, 31(10):927 – 934, 1998.

M. Souzy, P. Pham, and B. Metzger. Taylor's experiment in a periodically sheared particulate suspension. *Physical Review Fluids*, 1(4), 2016.

M. Souzy, H. Lhuissier, Y. Méheust, T. Le borgne, and B. Metzger. Velocity distributions, dispersion and stretching in three-dimensional porous media. *Journal of Fluid Mechanics*, 891, 2020.

M. E. Stender, R. A. Regueiro, and V. L. Ferguson. A poroelastic finite element model of the bone–cartilage unit to determine the effects of changes in permeability with osteoarthritis. *Computer Methods in Biomechanics and Biomedical Engineering*, 20(3):319–331, 2017.

C. T. Tan and G. M. Homsy. Simulation of nonlinear viscous fingering in miscible displacement. *The Physics of Fluids*, 31(6):1330–1338, 1988.

D. M. Tartakovsky and M. Dentz. Diffusion in porous media: Phenomena and mechanisms. *Transport in Porous Media*, 130(1):105–127, 2019.

G. I. Taylor. Dispersion of soluble matter in solvent flowing slowly through a tube. *Proceedings of the Royal Society of London. Series A. Mathematical and Physical Sciences*, 219(1137):186–203, 1953.

W. Thielicke and R. Sonntag. Particle image velocimetry for MATLAB: Accuracy and enhanced algorithms in pivlab. *Journal of Open Research Software*, 2021.

W. Thielicke and E. J. Stamhuis. Pivlab – towards user-friendly, affordable and accurate digital particle image velocimetry in matlab. *Journal of Open Research Software*, 2014.

A. Tomic, A. Grillo, and S. Federico. Poroelastic materials reinforced by statistically oriented fibres-numerical implementation and application to articular cartilage. *IMA Journal of Applied Mathematics*, 79(5):1027–1059, 2014.

M. Tran and B. Jha. Coupling between transport and geomechanics affects spreading and mixing during viscous fingering in deformable aquifers. *Advances in Water Resources*, 136:103485, 2020.

M. G. Trefry, D. R. Lester, G. Metcalfe, and J. Wu. Temporal fluctuations and poroelasticity can generate chaotic advection in natural groundwater systems. *Water Resources Research*, 55(4): 3347–3374, 2019.

D. E. Troyetsky, J. Tithof, J. H. Thomas, and D. H. Kelley. Dispersion as a waste-clearance mechanism in flow through penetrating perivascular spaces in the brain. *Scientific Reports*, 11(4595), 2021.

F. Urciuolo, G. Imparato, and P. A. Netti. Effect of dynamic loading on solute transport in soft gels implication for drug delivery. *AIChE Journal*, 54(3):824–834, 2008.

J. H. M. van Gils, E. van Dijk, A. Peduzzo, A. Hofmann, N. Vettore, M. P. Schützmann, G. Groth, H. Mouhib, D. E. Otzen, A. K. Buell, and S. Abeln. The hydrophobic effect characterises the thermodynamic signature of amyloid fibril growth. *PLOS Computational Biology*, 16(5):1–25, 2020.

B. L. Vaughan, P. A. Galie, J. P. Stegemann, and J. B. Grotberg. A poroelastic model describing nutrient transport and cell stresses within a cyclically strained collagen hydrogel. *Biophysical Journal*, 105(9):2188–2198, 2013.

A. T. Vuong, L. Yoshihara, and W. A. Wall. A general approach for modeling interacting flow through porous media under finite deformations. *Computer Methods in Applied Mechanics and Engineering*, 283:1240–1259, 2015.

L. C. Walker. Aβ plaques. *Free Neuropathology*, 1:31, 2020.

J. A. Weideman and S. C. Reddy. A MATLAB differentiation matrix suite. *ACM Transactions on Mathematical Software (TOMS)*, 26(4):465–519, 2000.

S. Whitaker. Diffusion and dispersion in porous media. *AIChE Journal*, 13:420–427, 1967.

S. Whitaker. *The Method of Volume Averaging*. Theory and Applications of Transport in Porous Media. Springer Netherlands, 1998.

F. Witt, G. N. Duda, C. Bergmann, and A. Petersen. Cyclic mechanical loading enables solute transport and oxygen supply in bone healing: An in vitro investigation. *Tissue Engineering - Part A*, 20(3-4):486–493, 2014.

S. Wognum, J. Huyghe, and F. Baaijens. Influence of osmotic pressure changes on the opening of existing cracks in 2 intervertebral disc models. *Spine*, 31:1783–8, 2006.

J. Wu, D. R. Lester, M. G. Trefry, and G. Metcalfe. When do complex transport dynamics arise in natural groundwater systems? *Water Resources Research*, 56(2):1–17, 2020.

J. Z. Wu, W. Herzog, and S. Federico. Finite element modeling of finite deformable, biphasic biological tissues with transversely isotropic statistically distributed fibers: toward a practical solution. *Zeitschrift fur Angewandte Mathematik und Physik*, 67(2), 2016.

H. Xiao and L. S. Chen. Hencky's elasticity model and linear stress-strain relations in isotropic finite hyperelasticity. *Acta Mechanica*, 157:51–60, 2002.

T. Yamamoto, H. L. Koning, H. Sellmeijer, and E. van Hijum. On the response of a poro-elastic bed to water waves. *Journal of Fluid Mechanics*, 87(1):193–206, 1978.

H. Yao and W. Y. Gu. Convection and diffusion in charged hydrated soft tissues: a mixture theory approach. *Biomechanics and Modeling in Mechanobiology*, 6(1-2):63–72, 2007.

C. Yaogeng, W. Wenshuai, D. Shenghu, W. Xu, C. Qun, and L. Xing. A multi-layered poroelastic slab model under cyclic loading for a single osteon. *BioMedical Engineering OnLine*, 17:97, 2018.

Y. Ye, G. Chiogna, O. A. Cirpka, P. Grathwohl, and M. Rolle. Enhancement of plume dilution in two-dimensional and three-dimensional porous media by flow focusing in high-permeability inclusions. *Water Resources Research*, 51(7):5582–5602, 2015.

D. Zhang and S. C. Cowin. Oscillatory bending of a poroelastic beam. *Journal of the Mechanics and Physics of Solids*, 42(10):1575–1599, 1994.

H. J. Zhang, D. S. Jeng, D. A. Barry, B. R. Seymour, and L. Li. Solute transport in nearly saturated porous media under landfill clay liners: A finite deformation approach. *Journal of Hydrology*, 479: 189–199, 2013.

L. Zhang. Solute transport in cyclic deformed heterogeneous articular cartilage. *International Journal of Applied Mechanics*, 3(3):507–524, 2011.

L. Zhang and A. Szeri. Transport of neutral solute in articular cartilage: effects of loading and particle size. *Proceedings of the Royal Society A: Mathematical, Physical and Engineering Sciences*, 461(2059):2021–2042, 2005.

L. Zhang and A. Z. Szeri. Transportation of neutral solute in deformable, anisotropic, soft tissue. *Computers and Mathematics with Applications*, 53(2):232–243, 2007.

L. Zhang and A. Z. Szeri. Transport of neutral solute in articular cartilage: Effect of microstructure anisotropy. *Journal of Biomechanics*, 41(2):430 – 437, 2008.

X. Zhao, L. Li, B. Li, J. Zhang, and A. Wang. Durable superhydrophobic/superoleophilic pdms sponges and their applications in selective oil absorption and in plugging oil leakages. *Journal of Materials Chemistry A*, 2:18281–18287, 2014.

L. Zhou, G. Zhuang, and G. Li. A facile method for the fabrication of glass-pdms-glass sandwich microfluidic devices by sacrificial molding. *Sensors and Actuators B: Chemical*, 261:364–371, 2018.

D. Zhu, S. Handschuh-Wang, and X. Zhou. Recent progress in fabrication and application of polydimethylsiloxane sponges. *Journal of Materials Chemistry A*, 5(32):16467–16497, 2017.

Y. Zhu, H. Wu, S. Sun, T. Zhou, J. Wu, and Y. Wan. Designed composites for mimicking compressive mechanical properties of articular cartilage matrix. *Journal of the Mechanical Behavior of Biomedical Materials*, 36:32–46, 2014.

R. A. Zimmerman and D. M. Tartakovsky. Solute dispersion in bifurcating networks. *Journal of Fluid Mechanics*, 901:A24, 2020.